國立臺灣大學工學院土木工程研究所

碩士論文

Department of Civil Engineering

College of Engineering

National Taiwan University

Master Thesis

協方差型隨機子空間識別法之應用

Application of Covariance Driven Stochastic Subspace

Identification Method

劉奕成

Yi-Cheng Liu

指導教授：羅俊雄 博士

Advisor: Chin-Hsiung Loh, Ph.D.

中華民國 100 年 6 月

June, 2011

國立臺灣大學碩士學位論文
口試委員會審定書

協方差型隨機子空間識別法之應用
Application of Covariance Driven
Stochastic Subspace Identification Method

　　本論文係劉奕成君（學號 R98521256）在國立臺灣大學土木工程學系碩士班完成之碩士學位論文，於民國 100 年 06 月 24 日承下列考試委員審查通過及口試及格，特此證明

口試委員：

羅　俊　雄	
（指導教授）	
莊　哲　男	
田　堯　彰	
鍾　立　來	

系主任　　呂　良　正

（簽名）

Acknowledgement

摘要

本研究目的是探討隨機子空間識別法（Stochastic Subspace Identification, SSI）在只有結構微震反應的量測下，於土木結構系統識別及損壞診斷上的應用範疇。在離線分析的應用上，可將於不同矩陣維度識別出之系統極點（system poles）繪製成穩定圖，以達正確識別結構震態的目的。在此研究的前半段，首先將對隨機子空間識別法搭配穩定圖的識別效果做研究，在不同情況諸如：訊號之雜訊、非線性、時變性與間隔緊密頻率等因素之甘擾下，比較各種隨機子空間識別法對此等甘擾因素之敏感度。接下來，協方差型隨機子空間識別法（Covariance driven Stochastic Subspace Identification, SSI-COV）將應用在廣州電視塔（Canton Tower）的系統識別工作，其為一座大型挑高細長結構，並為結構健康監測之標杆問題。除此之外，奇異譜分析法（Singular Spectrum Analysis, SSA）將以「前置子空間濾波器」的概念與協方差型隨機子空間識別法結合，名為「SSA-SSI-COV」識別法，除了能有效提昇資料解析能力，更提供一個能決定系統識別之最佳系統維度的做法。

研究的第二部份是針對系統震態參數之線上識別與損壞診斷技巧的開發，以遞迴式協方差型隨機子空間識別法（Recursive Covariance-driven Stochastic Subspace identification, RSSI-COV）為主體，並搭配延伸工具變項—投影近似子空間追蹤演算法（Extended Instrumental Variable – Projection Approximation Subspace Tracking algorithm, EIV-PAST）達成線上更新子空間的目地。另外，一個可供線上作業之子空間前置濾波器—「遞迴式奇異譜分析法（recursive Singular Spectrum, rSSA）」的開發與搭配，可有效減低雜訊對實地結構識別品質之影響，提昇線上分析的穩定性。此兩種子空間技術將透過時變性系統之數值模擬與實地試驗數據得到驗証，並從中取得可靠的識別模型控制參數。最後，它們將被應用在三個結構震態追縱的實驗上：（1）三層樓鋼構試體瞬時勁度折減之震動台實驗，（2）單層雙跨鋼筋混凝土結構之震動台試驗，此兩者皆以結構受到地震作用下之輸出反應做線上震態識別。最後，（3）橋樑沖刷實驗之損壞診斷與預警之應用。

關鍵詞： 隨機子空間識別、協方差型、系統識別、結構健康監測、遞歸式隨機子空間識別、遞歸式奇異譜分析、廣州電視塔

Abstract

In this research the application of output-only system identification technique known as Stochastic Subspace Identification (SSI) algorithms in civil structures is carried out. With the aim of finding accurate modal parameters of the structure in off-line analysis, a stabilization diagram is constructed by plotting the identified poles of the system with increasing the size of data matrix. A sensitivity study of the implementation of SSI through stabilization diagram is firstly carried out, different scenarios such as noise effect, nonlinearity, time-varying systems and closely-spaced frequencies are considered. Comparison between different SSI approaches was also discussed. In the following, the identification task of a real large scale structure: Canton Tower, a benchmark problem for structural health monitoring of high-rise slender structures is carried out, for which the capacity of Covariance-driven SSI algorithm (SSI-COV) will be demonstrated. The introduction of a subspace preprocessing algorithm known as Singular Spectrum Analysis (SSA) can greatly enhance the identification capacity, which in conjunction with SSI-COV is called the SSA-SSI-COV method, it also allows the determination of the best system order.

The objective of the second part of this research is to develop on-line system parameter estimation and damage detection technique through Recursive Covariance-driven Stochastic Subspace identification (RSSI-COV) approach. The Extended Instrumental Variable version of Projection Approximation Subspace Tracking algorithm (EIV-PAST) is taking charge of the system-related subspace updating task. To further reduce the noise corruption in field experiments, the data pre-processing technique called recursive Singular Spectrum Analysis technique (rSSA)

is developed to remove the noise contaminant measurements, so as to enhance the stability of data analysis. Through simulation study as well as the experimental research, both RSSI-COV and rSSA-SSI-COV method are applied to identify the dynamic behavior of systems with time-varying characteristics, the reliable control parameters for the model are examined. Finally, these algorithms are applied to track the evolution of modal parameters for: (1) shaking table test of a 3-story steel frame with instantaneous stiffness reduction. (2) Shaking table test of a 1-story 2-bay reinforced concrete frame, both under earthquake excitation, and at last, (3) damage detection and early warning of an experimental steel bridge under continuous scour.

Keywords: Stochastic Subspace Identification, Covariance Driven, System Identification, Structural Health Monitoring, Recursive Stochastic Subspace Identification, Recursive Singular Spectrum Analysis, Canton Tower

Contents

Table List

Figure List

Chapter 1
Introduction

1.1 Background

Structural health monitoring and damage detection in civil infrastructures is an issue that has attracted much attention in the last decades, a dense research work was carried out trying to prevent disasters caused by the agedness, deterioration and damage in structures. In recent years, there are painful example like the sudden collapse of I-35W Mississippi River Bridge on August 1, 2007, in the United States, with 13 dead and 144 injured as the victims; the collapse of Kao-Ping Bridge (高屏大橋) in Taiwan on August 27, 2000, with 30 injured, and the collapse of Ho-Feng Bridge (后豐大橋) in Taiwan on September 14, 2008, with 6 dead; the last two has occurd during the Typhoon struck and caused by the bridge pier scouring.

The raise in the safety concern on the civil infrastructures and the need of strategies and methods able to detect damage from the large scale civil structural systems and hence to make early warnings, is the reason that explains the intensive research activity in this challenging field over the last years.

The vibration-based damage detection is a global monitoring and assessment method [14], which has as its hypothesis that the global dynamic behavior of the structure is a function of the physical properties of the structure (mass, damping, and stiffness) whose changes will be reflected in the vibration signals, collect through sensors like: displacement transducers, velocity sensors, accelerometers…, etc. The statistical pattern recognition from the vibration signals is fundamental for the health

monitoring process [16]. Based on that point out in [44], it consists in a four-part process: (1) operational evaluation, (2) data acquisition, fusion and cleansing, (3) feature extraction and information condensation, and (4) statistical model development for feature discrimination.

The identification of damage can be grouped into two branches: the model-based and non-model-based [11, 14]. The construction of the mathematical model of dynamic systems from experimental data is the so-called system identification, different model-based identification approaches are available in classical literatures [24, 29, 43].

During the past few years, the subspace identification algorithms had been successfully applied on structural system identification. The subspace method can be classified into the Subspace Identification (SI) algorithm which uses both input and output data, and the Stochastic Subspace Identification (SSI) algorithm which is an output-only identification algorithm. The developments of these methods are based on concepts from linear algebra, system theory and statistics. There are two essential numerical tool for the subspace methods in linear algebra: Singular Value Decomposition (SVD) and the QR decomposition. Classical algorithms to perform such matrix decomposition tools are completely described in [18].

For large scale civil structures such as bridges, the input excitation to the structural system is unknown, the output-only Stochastic Subspace Identification (SSI) is suitable for the identification and monitoring of these structures excited by ambient vibrations. There are several varieties of SSI technique such as Covariance-driven (SSI-COV), Data driven (SSI-DATA), or combined with other methods like Expectation

Maximization technique (SSI-EM) [39, 42] and the Empirical Mode Decomposition (EMD) based stochastic subspace identification [52].

SSI-DATA algorithms were fully enhanced by Van Overschee and De Moor [47]. The core of output-only identification through SSI-DATA is the orthogonal projection carried out by LQ decomposition [47, 50], followed by the SVD used to extract the system subspace. There are variants of the Data-driven algorithm which correspond to a different choice of weighting matrices before factorizing the projection matrix. The well-known SSI-DATA algorithms include CVA, N4SID, MOESP and IV-4SID [27, 46, 48]. Application of the SSI-DATA algorithm to investigate the dynamic characteristics of a cable-stayed bridge had been studied in [49]. In [9] the algorithm was also applied to the identification of a Steel-Quake benchmark structure. In [55] the method is applied to identify the modal parameters of The Heritage Court Tower in Vancouver, Canada, and the Beichuan Bridge located in China, which has its arch made by concrete filled steel tube. The reference-based SSI algorithms were also developed in [36, 37, 38] and applied in the identification of a steel transmitter mast and a prestressed concrete bridge (the Z24-bridge in Switzerland).

As opposed to SSI-DATA, the SSI-COV algorithm avoids the computation of orthogonal projection, instead, it is replaced by converting raw time histories in an assemble of block covariances which is called Toeplitz matrix. The SSI-COV algorithm appears early as the Modified Instrumental Variable methhod, with applications in laboratory tests, such as the identification of a vertical steel clamped-free beam and modal analysis of a carrying bogie [7]. Other application can be found in the identification of offshore structures and rotating machinery [1] and an aircraft [2].

Different family of SSI-COV exist, a very famous identification algorithm is a combined approach of the Natural Excitation Technique (NExT) [23] and the Eigensystem Realization Algorithm (ERA) [25] to find modal parameters from ambient response. It is called as the Natural Excitation Technique and Eigensystem Realization Algorithm (NExT-ERA) [10] which has been applied to the identification and damage detection of a 4-story 2-bay steel IASC-ASCE Benchmark structure. The same algorithm is also applied to the identification of a cable stayed bridge in [53], where alternative form to construct the stabilization diagram [37] was proposed. Another similar approach exists: it is a combination of the Random Decrement method (RD) [4, 33] and ERA using Data Correlations (ERA/DC) [26]. This RD-ERA/DC algorithm is applied to the modal identification of Tsing Ma Bridge, located in Hong Kong [40]. Improvements were achieved by substituting random decrement functions by their cross-correlation in the assembling of the Hankel matrices.

Different from the off-line analysis, the output-only system identification and damage detection through on-line recursive algorithms has received considerable attention recently, it is suitable for long-term continuous monitoring systems and development of early warning systems. In the past few years, several recursive subspace identification algorithms have been proposed to update in an recursive fashion the main decomposition tools of the SSI algorithm: the LQ decomposition and SVD.

The updating of the LQ decomposition is done by means of Givens rotations [18], the SVD updating problem is circumvented by considering the similarities between recursive SSI and adaptive signal processing techniques for direction of arrival estimation [56], and only the column space of extended observability matrix is updated

4

[19, 20, 34]. The recursive stochastic realization by the classical Covariance-driven SSI algorithm (RSSI-COV) is proposed in [17], and the application for in-flight flutter monitoring is discussed in the paper. However, recursive Data-driven subspace algorithm is the most widely used method in the literature. Application for in-flight modal analysis of airplanes can be found in [13]. In [28] the RSSI-DATA is applied to the system identification of Donghai Bridge located in China. Damage detection example of the mentioned 4-story 2-bay steel IASC-ASCE Benchmark structure can be found in [12], and finally, application to the health monitoring and damage detection of a single pier subjected to scour, and to the 1-story 2-bay reinforced concrete frame can be found in [58].

Although the literature of SSI algorithms were reviewed, there is another useful output-only subspace tool called the Singular Spectrum Analysis (SSA), which is a novel non-parametric technique and it was firstly applied to extract tendencies and harmonic components in meteorological and geophysical time series [3]. Except the extraction of tendency, SSA can be applied to eliminate noise effect, or to detect the singularities, *e.g.*, to extract structural residual deformation [32].

The conjunction of SSA to SSI-COV will be the main contribution of this thesis. Although it is simply the addition of a pre-processing tool and no more, this action allows the determination of the best system order from the connection in-series of two SVD decomposition engine, and has greatly enhanced the identification quality and stability. Moreover, the recursive Singular Spectrum Analysis algorithm will be proposed in this thesis, which in conjunction with RSSI-COV method offers a very stable and accurate online tracking capacity.

1.2 Research Objectives

The objective of this research is to, first, enhance the Covariance-driven Stochastic Subspace Identification method (SSI-COV) to the named "Singular Spectrum Analysis–Covariance driven Stochastic Subspace identification method" (SSA-SSI-COV), validated both by numerical simulation and the application in system identification of Canton Tower, a benchmark problem for structural health monitoring of high-rise slender structures.

Second, develop the recursive Singular Spectrum Analysis method (rSSA), and in conjunction with the recursive Covariance-driven Stochastic Subspace Identification method to construct the named "recursive Singular Spectrum Analysis – Covariance driven Stochastic Subspace Identification method" (rSSA-SSI-COV), through a moving window approach. The method will be validated firstly by numerical simulation and later by application in the damage detection and health monitoring of laboratory experiments.

The organization of this thesis is briefly described as follows:

Chapter 2: The basic methodology of subspace identification algorithm is recalled through, firstly, the introduction of the dynamic model of a linear system, followed by the formulation of SSI-COV and SSI-DATA method, and finally, the Singular Spectrum Analysis (SSA) procedure will be described.

In system identification algorithms, it is important to distinguish the structure modes from the spurious modes because the order of the real system is always unknown. The alternatives to build the stabilization diagram will be introduced and compared one to

another. A comparison benefit-drawback and implementation issues will be discussed through a numerical simulation example and the identification of a laboratory test.

Chapter 3: A comprehensive numerical study and comparison between different SSI algorithms is carried out. Measurement noise effect and the addition of a noise which violates the SSI assumption is discussed. Identification of the simulated nonlinear signals, signals with time-varying frequency, signals with closely-spaced frequencies mixed with white noise is done to understand the performance of SSI algorithms under different scenarios of assumption violation and the mechanism to overcome this difficulties. The SSA-SSI-COV algorithm is introduced in this chapter to solve the identification problem of closely-spaced frequencies with added white noise.

Chapter 4: Application of SSI algorithms in system identification of the Canton Tower is discussed. The order determination procedure through the SSA-SSI-COV algorithm will be described. Comparison between different SSI approaches is made in this chapter. The procedure called decimation is although studied and applied to increase the convergence speed of the stabilization diagram.

Chapter 5: the derivation of Covariance-driven Recursive Stochastic Subspace Identification algorithm (RSSI-COV) can be found in this chapter. The Projection Approximation Subspace Tracking algorithm (PAST) and its Instrumental Variable extensions (EIV-PAST) is also described and implemented to RSSI-COV. To consider the noise contaminated data, a recursive pre-processing technique called recursive singular spectrum analysis technique (rSSA) is derived to enhance the accuracy and stability in the online tracking capability.

Chapter 6: the RSSI-COV method and the proposed rSSA-SSI-COV algorithm through a moving window approach are validated in this chapter by means of numerical simulation of a 6 DOF system, cases with sudden reduction and slow decreasing in system stiffness are studied. The effects of the selected RSSI model parameters in the online modal analysis, and the influence of time-varying frequencies in the selection of system order are also discussed.

Chapter 7: the RSSI-COV method and the proposed rSSA-SSI-COV algorithm through a moving window approach are applied to the monitoring and damage detection of, first, shaking table test of a 3-story steel structure with instantaneous stiffness reduction. Second, the shaking table test of a 1-story 2-bay reinforced concrete frame subjected to earthquake excitations with increasing intensity. Finally, application to the monitoring of a three pier and four span steel bridge under continuous scour is carried out.

Chapter 8: Summaries and suggestions for the use of the proposed algorithms will be given here. The potential research topics are indicated at the end.

Chapter 2
Stochastic Subspace Identification Methods

2.1 Introduction

In output-only characterization, the ambient response of a structure is recorded during ambient influence (*i.e.* without artificial excitation) by means of highly-sensitive velocity or acceleration sensing transducers. The Stochastic Subspace Identification (SSI) technique is a well known multivariate identification technique for output-only measurements. It was proved by several researchers to be numerically stable, robust to noise perturbation and suitable for conducting non-stationarity of the ambient excitations although its stationary assumption is violated [5, 37, 53].

The SSI-DATA algorithm was fully enhaced by Van Overschee and De Moor [47], while SSI-COV algorithm has as its antecedent the Eigensystem Realization Algorithm [25] for the free response of a structure, which are applied along with the Natural Excitation Technique (NExT) or Random Decrement (RD) functions. This chapter will begin with the introduction of the dynamic model of structures, followed by the stochastic properties and the system realization methods of each subspace algorithm.

2.2 Models of vibrating structures

2.2.1 Continuous-time state-space model

The Finite Element model of a linear time-invariant dynamic system can be expressed as:

$$\mathbf{M}\ddot{\boldsymbol{q}}(t) + \mathbf{C}_2\dot{\boldsymbol{q}}(t) + \mathbf{K}\boldsymbol{q}(t) = \boldsymbol{F}(t) = \mathbf{L}\boldsymbol{u}(t) \tag{2.1}$$

where $\mathbf{M}$, $\mathbf{C_2}$ and $\mathbf{K} \in \mathfrak{R}^{n \times n}$ are the mass, damping and stiffness matrix.

$q(t) \in \mathfrak{R}^n$ is the displacement vector at continuous time t.

$\dot{q}(t)$ is the velocity vector.

$\ddot{q}(t)$ is the acceleration vector with the same dimension as the displacement vector.

$F(t) \in \mathfrak{R}^n$ is the excitation vector.

$\mathbf{L} \in \mathfrak{R}^{n \times m}$ is the input location matrix.

$u(t) \in \mathfrak{R}^m$ is the vector describing m inputs as a function of time t.

n is the number of **DOF**s and m is the number of inputs.

The above second order differential equation can be rearranged into a first order differential equation known as the state-space model, which consist of two equations [24]:

The state equation:

$$\dot{x}(t) = \mathbf{A}_c x(t) + \mathbf{B}_c u(t) \tag{2.2}$$

where $x(t) = \begin{bmatrix} q(t) \\ \dot{q}(t) \end{bmatrix} \in \mathfrak{R}^{2n \times 1}$ is the state vector at continuous time t and therefore $\dot{x}(t) = \begin{bmatrix} \dot{q}(t) \\ \ddot{q}(t) \end{bmatrix}$. $\mathbf{A}_c$ is the so-called system matrix since it contains all the information related to the system ($\mathbf{M}$, $\mathbf{C_2}$, $\mathbf{K}$ in the equation of motion), and $\mathbf{B}_c$ is the definition of input matrix in the state equation. $\mathbf{A}_c$ and $\mathbf{B}_c$ are arranged as follows:

$$\mathbf{A}_c = \begin{bmatrix} \mathbf{0} & \mathbf{I} \\ -\mathbf{M}^{-1}\mathbf{K} & -\mathbf{M}^{-1}\mathbf{C_2} \end{bmatrix} \in \mathfrak{R}^{2n \times 2n} \quad , \quad \mathbf{B}_c = \begin{bmatrix} \mathbf{0} \\ \mathbf{M}^{-1}\mathbf{L} \end{bmatrix} \in \mathfrak{R}^{2n \times m} \tag{2.3}$$

The state equation which is a first order differential equation has the following

solution [57]:

$$x(t) = e^{\mathbf{A_c}(t-t_0)}x(t_0) + \int_{t_0}^{t} e^{\mathbf{A_c}(t-\tau)}\mathbf{B_c}u(\tau)d\tau \tag{2.4}$$

where the 1$^{\text{st}}$ term is the free vibration solution given an initial condition $x(t_0)$, and the 2$^{\text{nd}}$ term is a typical convolution integral. Through an eigen-analysis of the system matrix $\mathbf{A_c}$, the state equation can be decoupled through a coordinate transformation using the obtained complex eigenvectors.

$$\mathbf{A_c} = \mathbf{\Psi}\mathbf{\Lambda_c}\mathbf{\Psi}^{-1} \quad , \quad x(t) = \mathbf{\Psi}\eta(t) \tag{2.5}$$

where $\eta(t)$ is the generalized coordinate. $\mathbf{\Lambda_c} \in \mathfrak{R}^{2n \times 2n}$ is a diagonal matrix containing complex eigenvalues λ_i in the diagonal which appear in conjugate pairs, $\mathbf{\Psi} \in \mathfrak{R}^{2n \times 2n}$ are the complex eigenvectors. From the eigen-analysis $\mathbf{A_c}\mathbf{\Psi} = \mathbf{\Psi}\mathbf{\Lambda_c}$, one may find that they have the following structure:

$$\mathbf{\Lambda_c} = \begin{pmatrix} \mathbf{\Lambda} & \\ & \mathbf{\Lambda}^* \end{pmatrix} = \quad , \quad \mathbf{\Psi} = \begin{pmatrix} \mathbf{\Theta} & \mathbf{\Theta}^* \\ \mathbf{\Theta}\mathbf{\Lambda} & \mathbf{\Theta}^*\mathbf{\Lambda}^* \end{pmatrix} \tag{2.6}$$

In fact, it can be easily verified that $\mathbf{\Lambda}$ are the same eigenvalues and $\mathbf{\Theta}$ the same eigenvectors, *i.e.*, mode shapes, than those obtained by conducting eigen-analysis directly in the unforced equation of motion (2.1), but they cannot be used to decouple the equation of motion unless it is a proportionally damped system.

Then, the decoupled state equation can be written as follows:

$$\dot{\eta}(t) = \mathbf{\Lambda_c}\eta(t) + \mathbf{\Psi}^{-1}\mathbf{B_c}u(t) \tag{2.7}$$

Furthermore, to relate the obtained complex eigenvalues to a physical interpretation, a Taylor Expansion is required to decouple the free vibration term $e^{\mathbf{A_c}t}$ in (2.4), which is a matrix exponential:

11

$$e^{\mathbf{A}_c t} = \mathbf{I} + \mathbf{A}_c t + \frac{\mathbf{A}_c^2 t^2}{2!} + \frac{\mathbf{A}_c^3 t^3}{3!} + ... = \mathbf{\Psi}\left(\mathbf{I} + \mathbf{\Lambda}_c t + \frac{\mathbf{\Lambda}_c^2 t^2}{2!} + \frac{\mathbf{\Lambda}_c^3 t^3}{3!} + ...\right)\mathbf{\Psi}^{-1}$$
$$\Rightarrow e^{\mathbf{A}_c t} = \mathbf{\Psi} e^{\mathbf{\Lambda}_c t}\mathbf{\Psi}^{-1} = \mathbf{\Psi} diag\left(e^{\lambda_i t}\right)\mathbf{\Psi}^{-1}$$

(2.8)

where $diag(\cdot)$ is the diagonal operator. Therefore, considering only this free vibration term in (2.4) and having in mind that the complex eigenvalue has its real and imaginary part: $\lambda_i = \alpha_i + j\beta_i$, solution to the *i-th* mode free vibration is:

$$\eta_i(t) = e^{(\alpha_i + j\beta_i)(t-t_0)}\eta_i(t_0) = e^{\alpha_i(t-t_0)}[\cos\beta_i(t-t_0) + j\sin\beta_i(t-t_0)]\eta_i(t_0)$$

(2.9)

where the coordinate transformation shown in (2.5) has been applied to decouple the free vibration solution. Comparing (2.9) with the well-known free vibration solution of a SDOF system, the so-called *i-th* effective modal frequency ω_i' and effective damping ratio ζ_i' can be realized:

$$\omega_i' = \sqrt{\alpha_i^2 + \beta_i^2} = |\lambda_i| \quad , \quad \zeta_i' = \frac{\alpha_i}{\sqrt{\alpha_i^2 + \beta_i^2}} = \frac{-\alpha_i}{|\lambda_i|}$$

(2.10)

The effective modal frequency and damping ratio are exactly those obtained by normal mode approach if it is classical or proportional damping. In the case of non-proportional damping, ω_i' will be slightly different than the normal natural frequency, and ζ_i' can be called as the i-th effective attenuation rate [57].

One can note that ω_i' is actually the amplitude of the complex system pole, and ζ_i' is related to the phase. Hence, when a structural system is changed due to damage, the migration of system poles will be directly reflected by the computed effective modal frequency and damping ratio, which the term "effective" will be omitted hereafter.

The observation equation:

If only subsets of the n DOF can be measured, and considering that measurements are taken at l locations and the sensors can be either accelerometers, velocity or displacement transducers, the observation equation can be defined as:

$$\boldsymbol{y}(t) = \mathbf{C_a}\ddot{\boldsymbol{q}}(t) + \mathbf{C_v}\dot{\boldsymbol{q}}(t) + \mathbf{C_d}\boldsymbol{q}(t) \tag{2.11}$$

where $\boldsymbol{y}(t) \in \Re^{l}$ represents the l outputs. $\mathbf{C_a}$, $\mathbf{C_v}$ and $\mathbf{C_d} \in \Re^{l \times n}$ are the output location matrices corresponding to acceleration, velocity and displacement respectively.

To relate the output $\boldsymbol{y}(t)$ to the system state $\boldsymbol{x}(t)$, the equation of motion (2.1) can be used to eliminate $\ddot{\boldsymbol{q}}(t)$, and by arranging and grouping location matrices, the observation equation become:

$$\boldsymbol{y}(t) = \mathbf{C_c}\mathbf{x}(t) + \mathbf{D_c}\mathbf{u}(t) \tag{2.12}$$

where $\mathbf{C_c} = \left(\mathbf{C_d} - \mathbf{C_a}\mathbf{M}^{-1}\mathbf{K} \quad \mathbf{C_v} - \mathbf{C_a}\mathbf{M}^{-1}\mathbf{C_2} \right) \in \Re^{l \times 2n}$ is the output matrix, and $\mathbf{D_c} = \mathbf{C_a}\mathbf{M}^{-1}\mathbf{L} \in \Re^{l \times m}$ is the direct transmission matrix.

Although the eigenvectors of system matrix $\mathbf{A}$ contains mode shapes information as that shown in (2.6), however, there is no knowledge about the location of each DOF when the matrix $\mathbf{A}$ is identified, moreover, usually the number of modes, *i.e.*, order of the system extracted from measurement data is different than the number of sensors, thus, the system eigenvectors should be mapped to the sensor locations through the output location matrix $\mathbf{C_c}$:

$$\mathbf{V_c} = \mathbf{C_c}\boldsymbol{\Psi} \tag{2.13}$$

where $\mathbf{V_c}$ are the observed mode shapes.

2.2.2 Discrete-time state-space model

Since all data is sampled in discrete time, the above continuous time state-space model can be converted into a discrete time state-space model. By gathering together the state and observation equation:

$$\begin{aligned} x_{k+1} &= \mathbf{A}x_k + \mathbf{B}u_k \\ y_k &= \mathbf{C}x_k + \mathbf{D}u_k \end{aligned} \tag{2.14}$$

where $x_k = x(k\Delta t) = \begin{bmatrix} q_k^T & \dot{q}_k^T \end{bmatrix}^T$ is the discrete state vector containing the sampled displacements and velocities. u_k and y_k are sampled input excitation and output measurement. $\mathbf{A}$ is the system matrix, $\mathbf{B}$ is the input matrix, $\mathbf{C}$ is the observation matrix and $\mathbf{D}$, the direct transmission matrix, all in discrete-time. The relationships between these matrices in discrete-time and continuous time are the following [24]:

$$\mathbf{A} = e^{\mathbf{A}_c \Delta t} \quad , \quad \mathbf{B} = \mathbf{A}_c^{-1}\left(e^{\mathbf{A}_c \Delta t} - \mathbf{I}\right)\mathbf{B}_c \quad , \quad \mathbf{C} = \mathbf{C}_c \quad , \quad \mathbf{D} = \mathbf{D}_c \tag{2.15}$$

A basic assumption behind these relationships is that, the external perturbation is constant within a sampling period, *i.e.*, $u_k = u(k\Delta t)$ for the period of time $k\Delta t \le \tau < (k+1)\Delta t$. It is provided that the inverse of system matrix $\mathbf{A}_c$ exists.

The eigenvalues μ_i of the discrete-time system matrix $\mathbf{A}$ can be, therefore, related to the continuous-time eigenvalues by

$$\mu_i = e^{\lambda_i \Delta t} \Leftrightarrow \lambda_i = \frac{\ln(\mu_i)}{\Delta t} \tag{2.16}$$

Then, frequencies and damping ratios can be computed as mentioned before. Both the observation matrix and complex eigenvectors are not affected by the discretization in time, the above-mentioned equations can be used without any change.

14

This model is called the deterministic state-spaced model since both input and output are known.

2.2.3 Stochastic state-space model

Considering that there is always noise and perturbations both in the system (due to modelling inaccuracies) as in the measurementes, therefore (2.14) can be modified to its combined deterministic-stochastic state-space model:

$$
\begin{aligned}
\boldsymbol{x}_{k+1} &= \mathbf{A}\boldsymbol{x}_k + \mathbf{B}\boldsymbol{u}_k + \boldsymbol{w}'_k \\
\boldsymbol{y}_k &= \mathbf{C}\boldsymbol{x}_k + \mathbf{D}\boldsymbol{u}_k + \boldsymbol{v}'_k
\end{aligned}
\tag{2.17}
$$

The stochastic state-space model stems from the need of output-only system identification, situation under which both the input excitation as the noise terms are unknowns. Both the input terms and the noise terms are assumed to be a spatially white noise and they can be combined together as the process noise . Therefore, the discrete-time sthochastic state-space model can be simply stated as:

$$
\begin{aligned}
\boldsymbol{x}_{k+1} &= \mathbf{A}\boldsymbol{x}_k + \boldsymbol{w}_k \\
\boldsymbol{y}_k &= \mathbf{C}\boldsymbol{x}_k + \boldsymbol{v}_k
\end{aligned}
\tag{2.18}
$$

where $\boldsymbol{w}_k \in \mathfrak{R}^{2n \times 1}$ and $\boldsymbol{w}_k \in \mathfrak{R}^{l \times 1}$ are assumed to be zero mean, spatially white noise and with the following covariance matrices:

$$
E\left[\begin{pmatrix} \boldsymbol{w}_p \\ \boldsymbol{v}_p \end{pmatrix} \begin{pmatrix} \boldsymbol{w}_q^T & \boldsymbol{v}_q^T \end{pmatrix} \right] = \begin{pmatrix} \mathbf{Q} & \mathbf{S} \\ \mathbf{S}^T & \boldsymbol{R} \end{pmatrix} \delta_{pq}
\tag{2.19}
$$

where $E(\cdot)$ denotes expectation operator and δ_{pq} is the Kronecker delta ($\delta_{pq}=1$ if $p=q$, otherwise $\delta_{pq}=0$). p and q are arbitrary time instants.

One should note that if acceleration measurement is used, the direct transmission

term $\mathbf{D}\boldsymbol{u}_k$ is also considered by the stochastic model as a process noise. Reviewing expressions (2.11) and (2.12), if only velocity or displacement transducers are used, $\mathbf{C_c}$ = ($\mathbf{0}$ $\mathbf{C_v}$) or $\mathbf{C_c}$ = ($\mathbf{C_d}$ $\mathbf{0}$), and $\mathbf{C_a}$ = $\mathbf{0}$, the direct transmission matrix vanishes, therefore, theoretically the external excitation will not be measured.

In the case of structures subjected to ground motions such as earthquakes, $\mathbf{L}$ is an identity matrix, and $\boldsymbol{u}(t) = -\mathbf{M}\ddot{\boldsymbol{q}}_g(t)$, hence, quantities in the state vector shown in (2.2) will be relatives. If accelerometers are used and since it measures absolute accelerations, the ground acceleration should be added to the observation equation (2.12):

$$\boldsymbol{y}(t) = \mathbf{C_c}\boldsymbol{x}(t) + \mathbf{D_c}\boldsymbol{u}(t) = \mathbf{C_c}\boldsymbol{x}(t) + \mathbf{C_a}\mathbf{M}^{-1}\left[-M\ddot{\boldsymbol{q}}_g(t)\right] + \mathbf{C_a}\ddot{\boldsymbol{q}}_g = \mathbf{C_c}\boldsymbol{x}(t)$$

The $\mathbf{D_c}\boldsymbol{u}(t)$ term will be cancel out with the ground acceleration, *i.e.*, in the case of base excited structures, the acceleration measurements are free from the external noise contributed by $\mathbf{D_c}$ term. But this is not the case for structures excited by wind or other sources acting directly in the body of the structure, this externally imposed acceleration will be transmitted in the measurements as a measurement noise.

Properties of the stochastic state-space model is summarized in the following chart [37]:

The system state is a stochastic process and assumed to be stationary with zero mean:

$$E[\boldsymbol{x}_k\boldsymbol{x}_k^T] = \Sigma \quad , \quad E[\boldsymbol{x}_k] = \boldsymbol{0} \tag{2.20}$$

The noise terms are zero mean white noise and uncorrelated with the current system state:

$$E[\boldsymbol{x}_k\boldsymbol{w}_k^T] = \boldsymbol{0} \quad , \quad E[\boldsymbol{x}_k\boldsymbol{v}_k^T] = \boldsymbol{0} \tag{2.21}$$

The output covariance matrices $\mathbf{R}_i \in \mathfrak{R}^{l \times l}$ of arbitrary time lag i are defined as:

$$\mathbf{R}_i = E[\mathbf{y}_{k+i}\mathbf{y}_k^T] \tag{2.22}$$

The "next-step – output" covariance matrix $\mathbf{G} \in \mathfrak{R}^{2n \times l}$ is defined as:

$$\mathbf{G} = E[\boldsymbol{x}_{k+1}\boldsymbol{y}_k^T] \tag{2.23}$$

From the stationarity, spatially white noise assumption and the previous definitions, following properties can be deduced:

$$\boldsymbol{\Sigma} = \mathbf{A}\boldsymbol{\Sigma}A^T + \mathbf{Q} \tag{2.24a}$$

$$\mathbf{R}_0 = \mathbf{C}\boldsymbol{\Sigma}C^T + \mathbf{R} \tag{2.24b}$$

$$\mathbf{G} = \mathbf{A}\boldsymbol{\Sigma}C^T + \mathbf{S} \tag{2.24c}$$

From the stochastic state-space model and applying stochastic properties shown in (2.24), the most important property can be deduced:

$$\mathbf{R}_i = \mathbf{C}\mathbf{A}^{i-1}\mathbf{G} \tag{2.25}$$

This last will be the key property to derive the Covariance-driven SSI algorithm.

2.3 Covariance-driven Stochastic Subspace Identification (SSI-COV)

The SSI-COV stems from the need to solve the problem through identifying a stochastic state-space model (matrices **A** and **C**) from output-only data. The first step is to gather the measurement vectors in a Hankel Data matrix:

$$\mathbf{H}_{1,2i} \equiv \frac{1}{\sqrt{N}}\begin{bmatrix} y_1 & y_2 & \cdots & y_j \\ y_2 & y_3 & \cdots & y_{j+1} \\ \vdots & \vdots & & \vdots \\ y_i & y_{i+1} & \cdots & y_{i+j-1} \\ y_{i+1} & y_{i+2} & \cdots & y_{i+j} \\ y_{i+2} & y_{i+3} & \cdots & y_{i+j+1} \\ \vdots & \vdots & & \vdots \\ y_{2i} & y_{2i+1} & \cdots & y_{2i+j-1} \end{bmatrix} = \begin{bmatrix} \mathbf{Y}_p \\ \mathbf{Y}_f \end{bmatrix} \tag{2.26}$$

where $\mathbf{Y}_p$ denotes the past measurements and $\mathbf{Y}_f$ denotes for the future measurements. It can be easily find that the block Toeplitz matrix can be obtained by a multiplication between future and transpose of past measurements:

$$\mathbf{T}_{1/i} = \begin{bmatrix} \mathbf{R}_i & \mathbf{R}_{i-1} & ... & \mathbf{R}_1 \\ \mathbf{R}_{i+1} & \mathbf{R}_i & ... & \mathbf{R}_2 \\ ... & ... & ... & ... \\ \mathbf{R}_{2i-1} & \mathbf{R}_{2i-2} & ... & \mathbf{R}_i \end{bmatrix} = \mathbf{Y}_f \left(\mathbf{Y}_p \right)^T \tag{2.27}$$

where $\mathbf{R}_i$ is the block output covariance with time lag i defined in (2.22).

Through the stochastic property in (2.25), the Toeplitz matrix can be factorized into the extended observability matrix $\mathbf{O}_i \in \mathfrak{R}^{li \times 2n}$ and the reversed extended stochastic controllability matrix $\mathbf{\Gamma}_i \in \mathfrak{R}^{2n \times li}$, as shown below:

$$\mathbf{T}_{1/i} = \mathbf{O}_i \mathbf{\Gamma}_i = \begin{bmatrix} \mathbf{C} \\ \mathbf{CA} \\ ... \\ \mathbf{CA}^{i-1} \end{bmatrix} \begin{bmatrix} \mathbf{A}^{i-1}\mathbf{G} & ... & \mathbf{AG} & \mathbf{G} \end{bmatrix} \tag{2.28}$$

where i is the order of the Toeplitz matrix, *i.e.*, number of block rows and columns it constitutes. Singular Value Decomposition (SVD) is the tool used to perform the above mentioned factorization:

$$\mathbf{T}_{1/i} = \mathbf{USV}^T = \begin{pmatrix} \mathbf{U}_1 & \mathbf{U}_2 \end{pmatrix} \begin{pmatrix} \mathbf{S}_1 & 0 \\ 0 & 0 \end{pmatrix} \begin{pmatrix} \mathbf{V}_1^T \\ \mathbf{V}_2^T \end{pmatrix} = U_1 S_1 V_1^T \tag{2.29}$$

where $\mathbf{U} \in \mathfrak{R}^{li \times li}$ and $\mathbf{V} \in \mathfrak{R}^{li \times li}$ are orthonormal matrices, l are the number of outputs, and $\mathbf{S}$ is a diagonal matrix containing positive singular values in descending order. Comparing (2.28) and (2.29), the matrix $\mathbf{O}_i$ in which contains the system matrices ($\mathbf{A}$ and $\mathbf{C}$) can be computed by splitting the SVD in two parts:

$$\mathbf{O}_i = \mathbf{U}_1\,\mathbf{S}_1^{1/2} \qquad\qquad \mathbf{\Gamma}_i = \mathbf{S}_1^{1/2}\,\mathbf{V}_1^{T} \tag{2.30}$$

From $\mathbf{O}_i$ matrix, the system matrices ($\mathbf{A}$ and $\mathbf{C}$) can be obtained easily. In MATLAB notation, the $\mathbf{C}$ matrix is just the first block of $\mathbf{O}_i$:

$$\mathbf{C} = \mathbf{O}_i(1\!:\!l,:) \tag{2.31}$$

System matrix $\mathbf{A}$ can be computed by exploiting the shift structure of the extended observability matrix $\mathbf{O}_i$:

$$\begin{bmatrix} \mathbf{CA} \\ \mathbf{CA}^2 \\ \vdots \\ \mathbf{CA}^{i-1} \end{bmatrix} = \begin{bmatrix} \mathbf{C} \\ \mathbf{CA} \\ \vdots \\ \mathbf{CA}^{i-2} \end{bmatrix} \mathbf{A} \tag{2.32}$$

therefore,

$$\mathbf{A} = \mathbf{O}_i\big(1\!:\!l(i-1),:\big)^{\dagger}\,\mathbf{O}_i\big(l+1\!:\!li,:\big) \tag{2.33}$$

where $(\cdot)^{\dagger}$ denotes pseudo-inverse. Then, by conducting eigenvalue decomposition on the system matrix $\mathbf{A}$, after the eigenvalues are converted to a continuous-time poles with (2.16), modal frequencies and damping ratios can be computed with (2.10). The observed mode shapes can be obtained by applying (2.13).

2.4 Data-driven Stochastic Subspace Identification (SSI-DATA)

As opposite to SSI-COV, the Data-driven algorithm (SSI-DATA) avoids the calculation of covariance. Instead, the data reduction step is accomplished by projecting the row space of the future outputs into the row space of past outputs. Covariance and orthogonal projection are closely related, in that they are both intended to eliminate uncorrelated noise contributions. From the data structure shown in (2.26) the orthogonal

projection can be defined as follows:

$$\mathbf{Y}_f / \mathbf{Y}_p \equiv \mathbf{Y}_f \mathbf{Y}_p^T \left(\mathbf{Y}_p \mathbf{Y}_p^T \right)^{\dagger} \mathbf{Y}_p = \mathbf{P}_i \tag{2.34}$$

where $\mathbf{Y}_f$ and $\mathbf{Y}_p$ are defined as (2.26), $(\cdot)^{\dagger}$ denotes pseudo-inverse, and $\mathbf{P}_i \in \mathfrak{R}^{li \times j}$ is the orthogonal projection matrix. The main theorem of stochastic subspace identification [47] implies that the extended observability matrix $\mathbf{O}_i$ can be found from the result of orthogonal projection:

$$\mathbf{P}_i = \mathbf{O}_i \hat{\mathbf{X}}_i \tag{2.35}$$

where $\hat{\mathbf{X}}_i \in \mathfrak{R}^{2n \times j}$ is the estimated state sequence in stochastic system which is equal to the estimates from the forward non-steady state Kalman filter [47].

$$\hat{\mathbf{X}}_i = \begin{pmatrix} x_i & x_{i+1} & ... & x_{i+j-2} & x_{i+j-1} \end{pmatrix} \tag{2.36}$$

Instead of (2.34), the orthogonal projection can be performed by a numerically robust and stable tool called LQ decomposition (this is, actually, the transpose version of the well-known QR decomposition), which is applied directly on the Hankel data matrix:

$$\mathbf{H}_{1,2i} = \begin{pmatrix} \mathbf{H}_{1,i} \\ \mathbf{H}_{i+1,i+1} \\ \mathbf{H}_{i+2,2i} \end{pmatrix} \begin{matrix} li \\ l \\ l(i-1) \end{matrix} \quad \begin{matrix} li & l & l(i-1) & j \end{matrix} \\ \begin{pmatrix} \mathbf{L}_{11} & \mathbf{0} & \mathbf{0} \\ \mathbf{L}_{21} & \mathbf{L}_{22} & \mathbf{0} \\ \mathbf{L}_{31} & \mathbf{L}_{32} & \mathbf{L}_{33} \end{pmatrix} \begin{pmatrix} \mathbf{Q}_1^T \\ \mathbf{Q}_2^T \\ \mathbf{Q}_3^T \end{pmatrix} = \mathbf{LQ} \tag{2.37}$$

where $\mathbf{L}$ is a lower triangular matrix, and $\mathbf{Q}$ is an orthogonal matrix. $\mathbf{L}_{ij}$ are partitions of the lower triangular matrix and $\mathbf{Q}_{ij}$ are partitions of the $\mathbf{Q}$ matrix.

$$\mathbf{P}_i = \mathbf{O}_i \hat{\mathbf{X}}_i = \begin{pmatrix} \mathbf{L}_{21} \\ \mathbf{L}_{31} \end{pmatrix} \mathbf{Q}_1^T \in \mathfrak{R}^{li \times j} \tag{2.38}$$

The proof of the above equation can be found in [50], *i.e.*, the desired column

20

space of $\mathbf{O}_i$ can be obtained directly from the column space $\begin{pmatrix} \mathbf{L}_{21} \\ \mathbf{L}_{31} \end{pmatrix}$. This is the key of why these algorithms are called "subspace" identification algorithms. They retrieve system matrix as the subspace of the projection matrix. If only system matrices ($\mathbf{A},\mathbf{C}$) are required, the SVD shown in (2.29) and its subsequent equations can be applied to $\begin{pmatrix} \mathbf{L}_{21} \\ \mathbf{L}_{31} \end{pmatrix}$ to determine the system order by separating the system subspace (non-zero singular values) from the noise subspace, which corresponds to vanishing singular values, and from now on, everything can be computed as that outlined in SSI-COV.

Estimating the noise covariances: $\mathbf{Q}$, $\mathbf{R}$ and $\mathbf{S}$

The Kalman filter state sequence $\hat{\mathbf{X}}_i$ can be determined from the projection matrix by:

$$\hat{\mathbf{X}}_i = \mathbf{O}_i^{\lambda} \mathbf{P}_i \tag{2.39}$$

where $\mathbf{O}_i$ is obtained by applying (2.29) and (2.30), $(\cdot)^{\lambda}$ denotes for pseudo-inverse.

The Hankel data matrix can be split in a different way:

$$\mathbf{H}_{1,2i} \equiv \left(\frac{\mathbf{H}_{1,i+1}}{\mathbf{H}_{i+2,2i}} \right) \equiv \left(\frac{\mathbf{Y}_p^+}{\mathbf{Y}_f^-} \right) \tag{2.40}$$

where $\mathbf{Y}_p^+$ and $\mathbf{Y}_f^-$ are obtained by displacing the first block row of the future outputs to the past outputs as its last block row. Similar to the main theorem of the orthogonal projection [47], it can be realized that:

$$\mathbf{P}_{i-1} = \mathbf{Y}_f^- / \mathbf{Y}_p^+ \equiv \mathbf{Y}_f^- \mathbf{Y}_p^{+T} \left(\mathbf{Y}_p^+ \mathbf{Y}_p^{+T} \right)^{\lambda} \mathbf{Y}_p^+ = \mathbf{O}_{i-1} \hat{\mathbf{X}}_{i+1} \tag{2.41}$$

where $\mathbf{O}_{i-1}$ is the same as $\mathbf{O}_i$ but deleting the last l rows.

Similarly to (2.38), $\mathbf{O}_{i-1}$ computed in a numerically stable way is in terms of the LQ

21

partitions:

$$\mathbf{P}_{i-1} = \mathbf{O}_{i-1}\hat{\mathbf{X}}_{i+1} = \begin{pmatrix} \mathbf{L}_{31} & \mathbf{L}_{32} \end{pmatrix} \begin{pmatrix} \mathbf{Q}_1^T \\ \mathbf{Q}_2^T \end{pmatrix} \in \mathfrak{R}^{l(i-1)\times j} \tag{2.42}$$

Since $\mathbf{O}_{i-1}$ can be computed just deleting the last l rows, $\mathbf{P}_{i-1}$ is calculated by the LQ decomposition, then, the shift Kalman state sequence can be determined by doing pseudo-inverse to $\mathbf{O}_{i-1}$:

$$\hat{\mathbf{X}}_{i+1} = \mathbf{O}_{i-1}^{\lambda}\mathbf{P}_{i-1} \tag{2.43}$$

The sequence $\hat{\mathbf{X}}_{i+1}$ as $\hat{\mathbf{X}}_i$ can be substituted into the stochastic state-space model:

$$\begin{pmatrix} \hat{\mathbf{X}}_{i+1} \\ \mathbf{H}_{i+1,i+1} \end{pmatrix} = \begin{pmatrix} \mathbf{A} \\ \mathbf{C} \end{pmatrix}\hat{\mathbf{X}}_i + \begin{pmatrix} \boldsymbol{\rho}_w \\ \boldsymbol{\rho}_v \end{pmatrix} \tag{2.44}$$

Both $\hat{\mathbf{X}}_{i+1}$, $\hat{\mathbf{X}}_i$ and $\mathbf{H}_{i+1,i+1}$ are sequences of length j, (2.44) is in fact, a typical least square formulation and the system matrices $(\mathbf{A},\mathbf{C})$ can be determined either by doing pseudo-inverse to $\hat{\mathbf{X}}_i$ or by the typical QR decomposition. After estimates of $(\mathbf{A},\mathbf{C})$ are determined, the residual sequence, *i.e.*, the process noise sequence $\boldsymbol{\rho}_w$ and $\boldsymbol{\rho}_v$ can be easily calculated:

$$\begin{pmatrix} \boldsymbol{\rho}_w \\ \boldsymbol{\rho}_v \end{pmatrix} = \begin{pmatrix} \hat{\mathbf{X}}_{i+1} \\ \mathbf{H}_{i+1,i+1} \end{pmatrix} - \begin{pmatrix} \hat{\mathbf{A}} \\ \hat{\mathbf{C}} \end{pmatrix}\hat{\mathbf{X}}_i \tag{2.45}$$

Then, the required noise covariances can be determined from $\boldsymbol{\rho}_w$ and $\boldsymbol{\rho}_v$. This algorithm guarantees the positive realness of the identified error covariances [47]:

$$\begin{pmatrix} \hat{\mathbf{Q}} & \hat{\mathbf{S}} \\ \hat{\mathbf{S}}^T & \hat{\boldsymbol{R}} \end{pmatrix} = \left[\begin{pmatrix} \boldsymbol{\rho}_w \\ \boldsymbol{\rho}_v \end{pmatrix} \begin{pmatrix} \boldsymbol{\rho}_w^T & \boldsymbol{\rho}_v^T \end{pmatrix} \right] \tag{2.46}$$

2.5 Singular Spectrum Analysis (SSA)

SSA [65] is a novel non-parametric technique used in the analysis of time series based on multivariate statistics. This method was firstly applied to extract tendencies and harmonic components in meteorological and geophysical time series [3]. Except the extraction of tendency, SSA can be applied to eliminate noise effect, or to detect the singularities, *e.g.*, to extract structural residual deformation [32]. Basically, this method is capable of decomposing the original series into a summation of principal components, so that each component in this sum can be identified as a tendency, periodic components (stationary), nontationary signal or noise.

The SSA procedure starts from: (1) Embedding: generate a Hankel matrix from the time series itself by sliding a window that is shorter in length than the original series. Firstly, let $\mathbf{Y} = (y_1, y_2, \ldots, y_N)$ be the time series of length N. And let L be the window length or number of block rows of the Hankel matrix, which is an integer in $1 < L < N$. Each sliding window vector X_j with length of L would then be derived: $X_j = \{ y_j, y_{j+1}, \ldots, y_{j+L-1} \}^T$, $j = 1, 2, \ldots, K$, where $K = N-L+1$ is the number of columns. The matrix $\mathbf{X} = [X_1, X_2, \ldots, X_K]$ is a Hankel data matrix (or called trajectory matrix):

$$\mathbf{X} = \begin{bmatrix} y_1 & y_2 & \cdots & y_K \\ y_2 & y_3 & \cdots & y_{K+1} \\ \vdots & \vdots & & \vdots \\ y_L & y_{L+1} & \cdots & y_N \end{bmatrix} \tag{2.47}$$
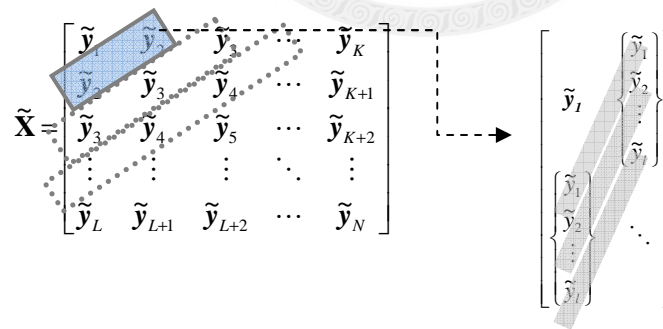
(2) Singular Value Decomposition: the Hankel matrix can be represented in the form: $\mathbf{X} = \mathbf{E}_1 + \mathbf{E}_2 + \ldots + \mathbf{E}_d$, where d is the number of non-zero eigenvalues of the $L \times L$ sample covariance matrix $\mathbf{S}_{\text{COV}} = \mathbf{X} \cdot \mathbf{X}^T$. The *i-th* elementary matrix, or called *i-th* eigentriple, are given by $\mathbf{E}_k = \sqrt{\lambda_k}\, \mathbf{u}_k \mathbf{v}_k^T = s_k \mathbf{u}_k \mathbf{v}_k^T$ where $\lambda_1, \lambda_2, \ldots \lambda_d$ are the non-zero eigenvalues of

$\mathbf{S}_{\text{COV}}$, in descending order, $\boldsymbol{u}_1$, $\boldsymbol{u}_2$, …, $\boldsymbol{u}_d$ are the corresponding eigenvectors, and vectors $\boldsymbol{v}_k$ are derived by $\boldsymbol{v}_k = \mathbf{X}^T \cdot \boldsymbol{u}_k / \sqrt{\lambda_k}$, $k = 1, 2, …, d$.

$$\mathbf{X} = \mathbf{USV}^T = \begin{pmatrix} \boldsymbol{u}_1 & \boldsymbol{u}_2 & \cdots & \boldsymbol{u}_d & \cdots & \boldsymbol{u}_L \end{pmatrix} \begin{pmatrix} s_1 & & & & & \\ & s_2 & & & & \\ & & \ddots & & & \\ & & & s_d & & \\ & & & & \ddots & \\ & & & & & s_L \end{pmatrix} \begin{pmatrix} \boldsymbol{v}_1^T \\ \boldsymbol{v}_2^T \\ \vdots \\ \boldsymbol{v}_d^T \\ \vdots \\ \boldsymbol{v}_L^T \end{pmatrix} = \sum_{k=1}^{d} s_k \boldsymbol{u}_k \boldsymbol{v}_k^T \quad (2.48)$$

(3) Grouping: the plot of the singular values in descending order is called the singular spectrum and is essential in deciding the index from where to truncate the summation. Finally, decide a parameter r to reconstruct an approximate matrix of $\mathbf{X}$, *i.e.* $\tilde{\mathbf{X}} \approx \mathbf{E}_1 + \mathbf{E}_2 + … + \mathbf{E}_r$, r does not need to be equal to the number of non-zeros singular values d.

(4) Averaging: the elements along the anti-diagonals of $\mathbf{X}$ are the same originally, however, after $\tilde{\mathbf{X}}$ is reconstructed, these may become slightly different, therefore, these entries are averaged to reconstruct signal:

$$\tilde{\mathbf{X}} = \begin{bmatrix} \tilde{y}_1 & \tilde{y}_2 & \tilde{y}_3 & \cdots & \tilde{y}_K \\ \tilde{y}_2 & \tilde{y}_3 & \tilde{y}_4 & \cdots & \tilde{y}_{K+1} \\ \tilde{y}_3 & \tilde{y}_4 & \tilde{y}_5 & \cdots & \tilde{y}_{K+2} \\ \vdots & \vdots & \vdots & \ddots & \vdots \\ \tilde{y}_L & \tilde{y}_{L+1} & \tilde{y}_{L+2} & \cdots & \tilde{y}_N \end{bmatrix} \longrightarrow \begin{bmatrix} \tilde{y}_I & \begin{Bmatrix} \tilde{y}_1 \\ \tilde{y}_2 \\ \vdots \\ \tilde{y}_I \end{Bmatrix} \\ \begin{Bmatrix} \tilde{y}_1 \\ \tilde{y}_2 \\ \vdots \\ \tilde{y}_I \end{Bmatrix} & \ddots \end{bmatrix} \quad (2.49)$$

It is proved in [65] that averaging the signal along the anti-diagonals of the approximate matrix $\tilde{\mathbf{X}}$, makes minimum the Frobenius norm of the error between $\tilde{\mathbf{X}}$ and the Hankel matrix assembled by the reconstructed signal, *i.e.*, the averaging leads to the optimal signal reconstruction in terms of the principal components.

2.6 Pole discrimination: the stabilization diagram

2.6.1 Alternatives to build the stabilization diagram

In real world applications, noise and perturbations are always present at any measurement, and there is no prior information about the number of modes can be extracted from the data, *i.e.*, there are always uncertainties in the determination of system order. Therefore, a stabilization diagram is used to discriminate between noise or spurious poles and true system poles. Based on the procedure of SSI-COV, there are several ways to build the stabilization diagram:

1st version: Decide first the maximum dimension of the Toeplitz matrix shown in (2.27), perform SVD, and let the order of system matrix **A** increases from a lower value till reaching the maximum dimension of the Toeplitz matrix defined by the user.

The advantage of this version is that only once has to be done the SVD; less time is consumed in the construction of the stabilization diagram. The drawback is that, there is no clear criterion to ensure that the chosen maximum dimension is sufficient or not to reveal true system information. While the order of system matrix **A** is increasing, more noise information will be included in the system matrix **A**, consequently, more noise or spurious poles will appear on the diagram. For this purpose, modal transfer norm [41] was introduced in addition, to clear out the large number of spurious poles at higher orders thus clarifying the stabilization diagram. But again, a threshold level has to be defined for the modal transfer norm. The concept behind this version to construct the stabilization diagram is that, even including more spurious poles in the system matrix **A**, the true modes (frequency, damping, mode shape) extracted by eigen-decomposition will remain stable.

2nd version: Determine the order of system matrix **A** by observing the variation of the

singular values, and then, increase the size of the Toeplitz matrix both rows and

columns holding the order of system matrix unchanged. It is important to note that if

full sensors are used to compute the covariance as usually does, the formed covariance

block is a square matrix, for convenience, this version will be called the "square Toepliz

matrix" because the shape of Toeplitz matrix remains squared. The main drawback of

this alternative is, first, more time consuming, and second, the system matrix order must

be defined previously. For field measurement data, generally there is no clear gap on the

distribution of singular values as that appearing in numerical simulation. The advantage

of this version is that, one do not have to try at the beginning the maximum Toeplitz

matrix size, since the required size to achieve good results may vary from case to case.

Increase of the Toeplitz matrix dimension means a larger subspace dimension and

also more data to extract the orthonormal base which spans the system-related

information, therefore, a better separation between signal and noise can be achieved.

Moreover, this also means an increment of the extended observability matrix order,

since the system matrix **A** is extracted by taking advantage of the shift structure of

matrix O_i as shown in equation (2.32). Evidently, the pseudo-inverse of O_i is a

numerically stable way to determine the system matrix **A** by least square, *i.e.*, a

convergent estimate of modal parameters is expected by increasing the Toeplitz matrix

order.

Both SSI-DATA and SSI-COV, the system information is extracted by applying

SVD to the projection matrix and Toeplitz matrix respectively. If the Hankel data matrix

in (2.26) has the same number of rows in both past Y_p and future Y_f measurements, the

resultant $\begin{pmatrix} \mathbf{L}_{21} \\ \mathbf{L}_{31} \end{pmatrix}$ term in (2.38) and Toeplitz matrix is square; however, if different

number of rows is chosen for $\mathbf{Y}_p$ and $\mathbf{Y}_f$, *e.g.*, if only number rows of $\mathbf{Y}_f$ is increased

keeping number of rows of $\mathbf{Y}_p$ constant, both $\begin{pmatrix} \mathbf{L}_{21} \\ \mathbf{L}_{31} \end{pmatrix}$ and Toeplitz matrix will become a

rectangular matrix. This constitutes the alternative form to construct the stabilization

diagram, which is presented as follows:

3rd version: This is a modification of the second version. Since Toeplitz matrix has not

necessary to be a square matrix, an alternative way to construct the stabilization diagram

is to increment only block rows of the Toeplitz matrix by keeping number of block

columns and system matrix $\mathbf{A}$ order constant [53]. For convenience, this version is

called as the "rectangular Toeplitz matrix" because it only increments rows but not

columns. The advantage of this method is that, it conserves the data addition property of

the stabilization diagram in a least square sense (it is much faster than the 2nd version).

The difficulty on the choice of number of block columns constitutes the main

drawback of this method, because this latter will determine the number of components

the Toeplitz matrix will be decomposed by SVD. In the presence of noise, if the number

of columns of the Toeplitz matrix is lower than the required, it will lead to an unstable

diagram and a poor estimation of modal parameters. On the contrary, the use of square

Toeplitz matrix has not to worry about the noise effect and the determination of number

of columns, since the presence of noise will only delay the outcome of a stable diagram.

Having reviewed the advantages and drawbacks of each way to construct the

stabilization diagram, the use of rectangular Toeplitz matrix (3rd version) may be

recommended for systems with prior knowledge about the noise content, however, for

identification task in first time, the use of square Toeplitz matrix (2nd version) is

recommended although it implies more time consuming.

Stabilization criteria

A typical stabilization diagram is shown in **Figure 2-2**. It is implemented by comparing the poles obtained between two consecutive matrix order, from lowest to highest, and applying stabilization criteria to modal frequencies, damping ratios and mode shapes, to discriminate if a pole is stable or not.

The chosen stability criteria are referenced from [37] and is defined as follows:

$$\text{Modal frequency: } \frac{\left|f^{(i+1)}-f^{(i)}\right|}{f^{(i)}}\times100\% \leq 1\%$$

$$\text{Modal damping ratio: } \frac{\left|\zeta^{(i+1)}-\zeta^{(i)}\right|}{\zeta^{(i)}}\times100\% \leq 5\% \tag{2.50}$$

$$\text{Mode shape: } \left(1-MAC(i,i+1)\right)\times100\% \leq 3\%$$

where i is the number of block rows of $\mathbf{Y}_f$ in (2.26), which determines the Toeplitz or projection matrix order, and *MAC* is the Modal Assurance Criterion, which is nothing else than the squared correlation between two mode shape vectors:

$$MAC(i,i+1)=\frac{(\boldsymbol{v}^{(i+1)H}\boldsymbol{v}^{(i)})^2}{(\boldsymbol{v}^{(i+1)H}\boldsymbol{v}^{(i+1)})(\boldsymbol{v}^{(i)H}\boldsymbol{v}^{(i)})} \tag{2.51}$$

where the subscript ^{H} denotes Hermitian transpose, $\boldsymbol{v}$ is the given mode shape vector, and *MAC* is a scalar between zero and unity.

The system poles are generally more stable in terms of its modal frequency as the matrix order is increased, followed by mode shape, and damping ratio is the more unstable quantity. Therefore, firstly, the poles are discriminated based on the modal

frequency, the frequency stable poles are grouped and marked in the diagram as a blue circle "o". Later, from the group of frequency stable poles, mode shape and damping ratio stable poles are discriminated, and they are represented by a green cross "+" and red "**x**" respectively. This means that, if a pole appears in the diagram as an assembly of this three symbols ("**O**", "+" and "**x**"), it is stable either in frequency and mode shape, as in damping ratio.

2.6.2 Comparison of stabilization diagram alternatives and influence of the model order determination

The 1st alternative has been studied and applied in [37], although it is the fastest way to construct the stabilization diagram, however, higher the order in the stabilization diagram, noisier is the system matrix and more spurious poles appear in the diagram. Otherwise, the 2nd and 3rd version to construct the stabilization diagram have more statistical meaning, because by increasing the order of stabilization diagram, more accurate modal parameter solution is expected due to the convergent property explained before. The following are comparisons between the 2nd and 3rd version considering the problem of model order determination.

2.6.2.1 *Simulation example: 6-DOF simulation study.*

The simulation example consists in a lumped mass model and a shear building type stiffness matrix. The system natural frequencies are:

f = [1.0107 , 2.2795 , 3.9280 , 5.4433 , 7.5773 , 8.2290] Hz

Rayleigh damping was assumed for the derivation of damping matrix, the assumed damping ratio for each mode are:

$\xi = [0.0351 , 0.0299 , 0.010 , 0.0087 , 0.0105 , 0.0058],$

Response is generated using discrete time deterministic state-space model having a spatially white noise as the input, and measured at each DOF. Measurement noise can be added after the system response is obtained. **Figure 2-1** shows the noise free velocity measurement at 6th DOF, the sampling rate is 200 Hz and the total generated data length was 15000 points, which is equal to 75 sec.

Figure 2-2 shows a comparison between the stabilization diagram using square and rectangular Toeplitz matrix for noise free data. 10000 data points were windowed to form the covariance matrices. Since this is a 6 DOF simulation example, there is no choice but to define system order as 12.

The 3rd version only uses 2 block columns but let the block rows increase; SVD of Toeplitz matrix with 2 block columns have only 12 singular values since 6 sensors are used, this means that the order of matrix **A** is the same as the number of columns. Clearly one can see in **Figure 2-2** that there is no difference between the two versions and the identified modal parameters are very stables at the beginning, because extra principal components were not needed since this is a noise free case.

For the same system but considering acceleration measurements, as mentioned in section 2.2.1, equation (2.12) shows that the external excitation is directly transmitted into the acceleration measurements. A plot of this noisy signal from 6th DOF is shown in **Figure 2-3**. The input is generated by a 0 decibel (dB) spatially white noise, after multiplied by the direct transmission term it is equivalent to a noise to signal ratio of 0.456, i.e., 45.6% in RMS sense (ratio of Frobenius norm between noise and response data). Under this type of noise which is correlated with output, an insufficient Toeplitz

matrix size will lead to a poor estimate of the lower modes. These results are shown in **Figure 2-4**.

On the contrary, although it is more time consuming the use of the square Toeplitz matrix, one has not to worry about the noise and the determination of number of columns, as shown in the **Figure 2-5**, noise in the measurement data will only delay the emergence of a stable diagram. This explains why SSI-COV technique is robust against non-stationarity even its assumptions were violated, the essence of SSI-based algorithms is SVD, the larger the size of Toeplitz matrix, or projection matrix in case of SSI-DATA, the greater is the subspace dimension, more covariance data will be used by SVD to determine the system-related orthonormal base which span the Toeplitz matrix, *i.e.*, a better fitting of the system information can be achieved.

The simulation results are summarized in **Table 2-1**. For the noise free case, only excitation level of 50 dB is considered and correct results were obtained just at the beginning of the stabilization diagram, *e.g.*, at 10 block rows using square Toeplitz matrix, moreover, answers picked from different number of rows are accurate enough. In the case of noisy measurements due to the directly transmitted excitation acceleration, three levels of excitation power were considered: 0 dB, 10 dB and 50 dB. Answers obtained using square Toeplitz matrix always converge to the correct solution, however, in the case of rectangular Toeplitz matrix, if the number of block columns are insufficient as mentioned before, lower mode answers are quite wrong or does not appear.

As conclusions from the numerical simulation, it is important to note that SSI algorithm cannot recover the exact answer even for a simulated and noise free

measurements due to its stochastic assumption, which switches from a input-output model to an output-only model. A good estimate of frequency can be always achieved by increasing the size of square Toeplitz matrix despite higher noise content in the data, *i.e.*, convergence to the true answer. However, damping estimate seems to be quite sensible to noise and some deviations are significant.

2.6.2.2 *Experimental example: identification of a 6-story steel frame from shaking table test*

The 6-story steel frame shaking table test was carried out at National Center for Research on Earthquake Engineering (NCREE), Taiwan, at August 2007. The structure and the sensor placement are shown in **Figure 2-6**. Accelerometers are placed at the center of each floor. Dimension of the columns are 150 x 25 mm (rectangular). Beams(L shape): 50x50x5 mm. Floor slab : 1000 x 1500 x 20 mm. Base plate : 1700 x 1700 x 20 mm. The mass on each floor (lumped mass) is 862.85 kg (include bracing).

Response data of the structure subjected to a white noise ground excitation of 50 gal is used for system identification. A plot of the measured acceleration response in the 6th floor is shown in **Figure 2-7**, signals looks quite clear and is similar to that shown in **Figure 2-1**. This verifies the fact that, for the base-excited structure, the $\mathbf{D}u_k$ term in (2.12) will cancel out with the ground acceleration to obtain a "noise free" absolute acceleration measurement. Based on the previous simulation results, rectangular Toeplitz matrix with reduced number of block columns should be able to identify system poles correctly. For the identification purpose, data of all 6 sensors are used simultaneously, Total data length is 11800 points but only 8000 points was windowed to form covariance. The sampling rate is 200 Hz.

In this simple case, intuitively, a 6 story steel frame can be modeled as a 6 DOF system, therefore the order of system matrix A can be determined as 12. A plot of singular values can be a good indicator of the order that one may choose, which is shown in the **Figure 2-8**.

Figure 2-9 shows the result obtained using both square and rectangular Toeplitz. The result is consistent with that obtained in the simulation example: for this almost noise free measurements, accurate results are obtained even using only 2 block columns (corresponding to 12 singular values to match the system order, no extra components used for noise).

In order to verify the performance of stabilization diagram in case of underestimation or overestimation of the system order, different cases were analyzed and shown in **Figure 2-10**.

Conclusion obtained from **Figure 2-10** are that, when rectangular Toeplitz matrix is used, underestimation of system order leads to incorrect results for those modes corresponding to the selected singular values, however, correct answers can be achieved using square Toeplitz matrix for the same case. On the other side, overestimation do not consist any problem for both ways to construct the stability diagram. Having in consideration the error tolerance requirement in the selection of model order, specially for field data collected from full-scale real structures, square Toeplitz matrix seems to be more suitable for an accurate and reliable system identification.

Chapter 3
Simulation study of SSI-based algorithms

A comprehensive numerical simulation task was carried out to understand the sensitivity of SSI-based algorithms subject to different perturbation factors and with special attention in their effects on the stabilization diagram.

3.1   Noise effect in the identification of modal parameters

In this section, comparison will be made for different SSI-based algorithms under noise effect. The same 6-DOF system of section 2.9.2 is used here again, which has well spaced frequencies.

3.1.1   Addition of a spatially white noise (from 50% to 200%)

In this part, a spatially white noise was added after the system response was generated. **Figure 3-1** shows a segment of the 6th DOF measurement with 100% noise added in terms of percentage of signal RMS. **Figure 3-2** and **Figure 3-3** Show the stabilization diagram for the case of 100% and 200% respectively. A total of 8000 points (sampling rate 200 Hz) were used for identification, the numerical results were picked when the matrix order is 80 block rows. The order ic is defined as half of the order of Hankel data matrix i, for pseudo-inputs in the case of PEM/SSI (**Appendix B**).

Clearly one can see that there is not any problem for SSI-based algorithms to identify accurately the modal frequencies, since the first step of these algorithms either covariance or projection can cancel out almost all added white noise once at all. Therefore, even adding 200% of noise in RMS sense (noise to signal ratio), which is quite exaggerated, error of the identified frequencies is less than 4% for the 1st mode

and less than 1.5% for the remaining modes, as it is shown in **Table 3-1**. On the

contrary of modal frequencies, damping ratio is very sensible to the addition of any type

of noise even it is very small, as shown in **Table 3-2**, the error can be so large that

reaches 100%.

The stabilization pattern of SSI-COV and SSI-DATA are similar. PEM/SSI

algorithm makes stabilization start slightly earlier for lower modes, however, the

number of rows to reveal a total stable diagram is similar to that of SSI-DATA and

SSI-COV. Therefore, one can conclude that these three algorithms together with

stabilization diagram perform quite well under the addition of white noise, because

noise assumptions of the stochastic state-space model were satisfied.

3.1.2 Addition of a white noise correlated with output (violation to SSI assumption)

For the same system and considering the same acceleration measurements shown

in **Figure 2-3**, the type of added noise is the input multiplied by the direct transmission

term and thus, it is correlated with output through the system matrix. It is equivalent to a

noise to signal ratio of 0.456, *i.e.*, 45.6% in terms of RMS.

Results using SSI-COV, SSI-DATA and PEM/SSI are shown in **Figure 3-4.** Even

a noise correlated with output measurement is added which violates the SSI

assumptions, by increasing the order of projection or covariance matrix up to a certain

level, frequencies can be accurately identified with stability diagram. But this is not the

case for PEM/SSI, the reason of the loss of stability for the lowest mode is mainly due

to the second projection, which tries to double fit the future measurements. Since in this

case the SSI assumptions were violated, the second fitting rather is trying to include the

undesired noise in the projection, therefore, the first mode was perturbed and cannot be

35

identified correctly. On the other side, lower modes are the most affected by the noise effects and take more time to stabilize meanwhile the matrix order increase.

Since there is always uncertainty about the ambient noise or perturbations, one may conclude from this simulation experience that, the way to improve the noise robustness of SSI algorithm, is more convenient a pre-processing filter to firstly eliminate the perturbation factors than the post-processing approach as the case of PEM/SSI. Hence, in the next sections, the pre-processing tool known as SSA will be introduced.

3.2 Nonlinearity in the signal

There is always some nonlinearity present in real world civil structures, therefore, after the study of the influence of noise in the measurements, another question to answer is: what outcome will be obtained by a linear system identification technique to identify a system with certain nonlinearity? And, whether the stabilization diagram works or not due to the presence of this nonlinearity?

To make simulation example possible, Duffing model [8] was considered to simulate a nonlinear SDOF system. Duffing model assume a cubic stiffness function, k_3u^3, which is added to the linear stiffness term in the equation of motion, where u is the displacement. A positive value of k_3 indicates hardening phenomenon and a negative value, softening. Considering that softening is more common in civil infrastructures, a set of negative values of k_3 will be used in the modeling.

Newmark-beta method and a white noise input was used to generate the system response. Since there is an extra nonlinear term in the equation of motion, an iterative

procedure had to be used to approximate the secant stiffness [22] as shown in **Figure 3-5**. First, the tangent stiffness ($k_{tang} = k + 3k_3u_i^2$, where "i" is the i-th step) was used as initialization, after found u_{i+1}, the secant stiffness can be calculated from u_i and u_{i+1}, but again, this secant stiffness is used to compute the next step $u_{i+1}^{(1)}$ and so on, until the difference between $u_{i+1}^{(m)}$ and $u_{i+1}^{(m+1)}$ is less than the specified convergence tolerance. The same tolerance applies to the estimated next step velocity and acceleration. Here, the tolerance is specified as the difference between $m+1^{th}$ and m^{th} iteration, which must be less than 0.01%.

Three natural frequencies were used in the simulation with different values of k_3, this is shown in **Table 3-3**. Moreover, 1% damping ratio was assumed.

Figure 3-6 shows a comparison between the generated signal of a system of 0.1 Hz. Clearly due to the softening effect (frequency became lower in some time instants) the acceleration response is delayed with respect to the signal of a linear system. **Figure 3-7** shows the comparison between the computed nonlinear (Duffing) and linear restoring force.

Figure 3-8 shows the comparison of stabilization diagram constructed using SSI-COV, SSI-DATA for different frequencies, and one example for PEM/SSI. The diagram shows convergent properties, and the identified frequencies are slightly lower than the natural frequency of the original linear system as shown in **Table 3-4**. This result was expected because SSI algorithms is just finding a best fit of the nonlinear signal to a linear system, and since it is a softening model we are dealing with, the obtained equivalent frequency is reasonable to be slightly lower than the corresponding linear frequency.

With these results one can conclude that SSI-based algorithms can identify an equivalent linear system from nonlinear signals effectively. Nonlinearity of the signal does not interfere the stabilization diagram.

3.3 Closely-spaced frequencies blended with signals of a time-varying system

In this section, two closely-spaced frequencies sine waves were generated, but it is blended with a signal with time-varying frequency. No noise was added in this simulation experiment, and the frequencies are close enough: $f_1 = 7.99$ Hz and $f_2 = 8.00$ Hz, the time varying term is "$\sin(t^2)$" which is shown below. The sampling rate is 100 Hz, the total data length was 1000 points. The signal together with the result from recursive frequency tracking using RSSI-COV is shown in **Figure 3-9**. Note that the first 100 points is the window length to initiate the recursive algorithm.

$$y = \sin 2\pi f_1 t + \sin 2\pi f_2 t + \sin t^2 \tag{3.1}$$

Although it is not appropriate to use linear SSI algorithm and stabilization diagram to identify time-varying systems for which is more convenient a recursive algorithm, the purpose is to understand the behavior of SSI and stability diagram in the presence of time-varying frequencies. **Figure 3-10** and **Figure 3-11** shows the stabilization diagram constructed using SSI-COV and SSI-DATA for different system orders, **Figure 3-12** shows the diagram for PEM/SSI.

These figures is showing that the closely-spaced frequencies appear as a single frequency if insufficient system order was chosen, as the system order increases to a sufficient level, two close-spaced frequencies will be revealed, but to make it stable

from the beginning to at least 100 block rows, the system order must be at least 26. Although the stabilization behavior is different between SSI-COV and SSI-DATA since the first uses correlation and the second, projection, SVD is the main reason of the mentioned phenomena, *i.e.*, SVD is the tool used to extract the observability matrix: when the system order is only 4 or 6, only the first 4 or 6 orthonormal vectors was chosen and the closely-spaced frequency information cannot be recovered, because there are time-varying frequencies with the same power which contains, in other words, "a lot of frequencies" within the data being analyzed. Consequently, the closely-spaced frequencies cannot be revealed until the selected system order is enough to cover all the orthonormal vectors which span the system-related information.

Furthermore, as the data matrix order increases, in more orthonormal vectors and with larger dimensions the signal time-varying frequencies will be decomposed, then, more "equivalent frequencies" appear in the diagram to fit this time-varying signal, as shown in **Figure 3-10 d**), but these poles are not stable. When the system order is insufficient, two closely-spaced frequencies will be perturbed at higher number of rows due to the finer decomposition of the time-varying signal. Thus, the required system order to include all information is higher as well as the number of block rows increases. In our case, a system order of 26 was enough to cover up to 100 rows.

Since this simulated signal is a sine wave with zero damping, this can be treated as free vibration of a idealized undamped system. As mentioned in the theoretical framework, terms in the extended observability matrix $\mathbf{O}_i$ is actually a sequence of observed free vibration of the system. Whether is covariance used in SSI-COV or orthogonal projection in SSI-DATA, the main objective is to cancel out the random input excitation which is represented by process noise in stochastic state-space model.

In this case of sine waves, there is no input and hence, covariance or projection is not required here as it is shown in the following expressions:

$$\mathbf{Y}_p = \mathbf{O}_i \mathbf{X}_p + \mathbf{\Pi} \mathbf{U}_p \tag{3.2}$$

where

$$\mathbf{Y}_p = \begin{bmatrix} y_1 & y_2 & y_3 & \cdots & y_j \\ y_2 & y_3 & y_4 & \cdots & y_{j+1} \\ y_3 & y_4 & y_5 & \cdots & y_{j+2} \\ \vdots & \vdots & \vdots & \cdots & \vdots \\ y_i & y_{i+1} & y_{i+2} & \cdots & y_{i+j} \end{bmatrix} \qquad \mathbf{O}_i = \begin{bmatrix} \mathbf{C} \\ \mathbf{CA} \\ \mathbf{CA}^2 \\ \vdots \\ \mathbf{CA}^{i-1} \end{bmatrix}$$

$$\mathbf{X}_p = \begin{bmatrix} x_1 & x_2 & x_3 & \cdots & x_j \end{bmatrix}$$

and

$$\mathbf{\Pi} = \begin{bmatrix} \mathbf{D} & \mathbf{0} & \mathbf{0} & \cdots & \mathbf{0} \\ \mathbf{CB} & \mathbf{D} & \mathbf{0} & \cdots & \mathbf{0} \\ \mathbf{CAB} & \mathbf{CB} & \mathbf{D} & \cdots & \mathbf{0} \\ \vdots & \vdots & \vdots & & \vdots \\ \mathbf{CA}^{i-2}\mathbf{B} & \mathbf{CA}^{i-3}\mathbf{B} & \mathbf{CA}^{i-4}\mathbf{B} & \cdots & \mathbf{D} \end{bmatrix} \qquad \mathbf{U}_p = \begin{bmatrix} u_1 & u_2 & u_3 & \cdots & u_j \\ u_2 & u_3 & u_4 & \cdots & u_{j+1} \\ u_3 & u_4 & u_5 & \cdots & u_{j+2} \\ \vdots & \vdots & \vdots & & \vdots \\ u_i & u_{i+1} & u_{i+2} & \cdots & u_{i+j} \end{bmatrix}$$

with $\mathbf{U}_p = \mathbf{0}$

$$\tag{3.3}$$

where $\mathbf{U}_p$ is the past input, $\mathbf{X}_p$ is the past Kalman filter, and the other variables are the same as defined in chapter 2. The expression is deduced from discrete-time deterministic state-space model [47], SVD can be applied directly to the Hankel data matrix and correct answer can be obtained. This result is shown in **Figure 3-13**.

From **Figure 3-13** one can realize that, without any noise cancellation procedure, the time-varying signal is "literally" fitted with "a lot of equivalent linear frequencies", and the respective diagram is approximately stable.

The effect of doing first covariance by SSI-COV is effective to distinguish the signals with time-varying frequency from the signal with time-invariant characteristic because together with the stabilization diagram, the poles of time-varying frequencies

"split" continuously as the number of block rows increases and do not stabilize, as that shown in **Figure 3-10 d**). This continuous splitting phenomenon is a useful way to identify the presence of time-varying signals when SSI-COV is used.

3.4 Preprocessing with SSA and noise effect in closely-spaced frequencies

So far all analysis presented in section 3.3 were done for a noise free signal. In this section, white noise will be added to the signal to test the ability of SSI-based algorithms to identify closely-spaced frequencies. Unfortunately, after adding 5% noise neither SSI-COV nor SSI-DATA are able to identified the close frequencies. The results is shown in **Figure 3-14**. Later on, the subspace preprocessing tool known as SSA will be introduced to address this noise perturbation problem.

To focus only in the noise effect in closely-spaced frequencies, the time-varying signal is removed and the result is shown in section 3.4.1.

3.4.1 Sinusoidal waves

Consider the case of a signal constituted by 7.99 Hz and 8.00 Hz sine waves with added 10% noise, which is shown in **Figure 3-15**. 15000 points were generated with a sampling rate of 200 Hz, 10000 points were used in covariance for SSI-COV, and similarly, 10000 columns form Hankel matrix for SSI-DATA. Since SVD does not decompose signal according to frequency components, although theoretically a system order of 4 is enough for 2 frequencies, after several trial and error, system order was chosen as 8 in this noisy case, and the resulting stabilization diagram is shown in **Figure 3-16**. The diagram starts to converge and stabilize up to approximately 260 rows in

SSI-COV, but for SSI-DATA the diagram is still not stable. However, both resultant diagram spinning around and converges very slowly to the correct answer, the required number of rows is approximately about 400 rows.

The identified frequencies are: 7.9946 Hz and 8.0040 Hz; damping ratios are: 0.00057 and 0.00455 for SSI-COV. For SSI-DATA, the identified frequencies are: 7.9966 Hz and 7.9794 Hz; damping ratios are: 0.0003 and -0.0009.

Here we can conclude that a small level of noise can interfere severely in the identifiability of closely-spaced frequencies. PEM/SSI was proven in previous sections to be very sensible to noise contamination, thus, the use of SSA before SSI is an option to, filter out first the noise contamination and then the identification quality of the stabilization diagram can be improved. **Figure 3-17** shows the variation of singular values (singular spectrum) obtained in SSA: **a)** is the singular values obtained by the SVD of a Hankel matrix of 200 by 5000, there are in total 200 singular values. One can note that in **a)** there are only 2 singular values separated from the remains, *i.e.*, the decomposition order is not enough to separate the two close frequencies from noise. On the contrary, when the size of Hankel matrix is increased to a 1000 by 3000 matrix as shown in **b)**, the noisy signal data is decomposed into 1000 components, and effectively 4 singular values were separated from the remains, *i.e.*, the 2 close frequencies are extracted.

The stabilization shown in **Figure 3-18** shows the stabilization diagram for the cases **a)** and **b)**: only one frequency appears in **a)** meanwhile two close frequencies were revealed in **b)**, the identified frequencies and damping ratios at 100 rows are: 7.9949 Hz, 8.0278 Hz, and 0.00028, 0.0167 respectively (original damping ratio is zero). This result

shows that SSA-SSI-COV is an effective algorithm to treat noisy measurements and to improve the identification quality.

3.4.2 Response of a 2-DOF system subjected to white noise excitation

In fact, sine waves will never be measured in real world structures subjected to ambient excitations, thus, to complete the research in closely-spaced frequencies contaminated with noise, a 2 DOF system was created with the following properties:

M = [1   0; 0   1];

C = [0.1141   -0.0710 ; -0.0710   0.1141];

K = [5   -0.35 ; -0.35   5];

Natural frequencies = [0.3432   0.3681];

Damping ratios = [0.01   0.04];

15000 data points were generated, sampling rate is 50 Hz, a plot of the generated acceleration measurements in the 2nd DOF is shown in **Figure 3-19**, the noisy measurement shown in **Figure 3-19 b)** is due to the direct transmitted acceleration of external excitation, and it is equivalent to 128.86% of noise in terms of RMS of the signal.

Both SSI-COV and SSI-DATA do not have any problem to identify close frequencies when the signal is noise free and the system was excited by a white noise input as shown in **Figure 3-20**.

For noisy acceleration measurements shown in **Figure 3-19 b)**, the close frequencies shows convergent property up to 60 rows and seems to be stable after 120

rows when SSI-COV is used. This is shown in **Figure 3-21 a)**. The result obtained using SSI-DATA is better for the singles generated by state-space model than pure sine waves with added noise; up to 60 rows the poles are stables. This can be explained because SSI-DATA derivation is based on the same state-space model and under the assumption of a continuous white noise excitation.

To improve the stability of the diagram and enhance the identification quality with a reduced number of rows, which means a significant reduction in computation effort, the pre-processing tool SSA can be used in conjunction with SSI-COV. The Hankel matrix to be decomposed by SSA was decided to be 800 block rows (totally 1600 rows with 2 sensor) by 3000 columns, the variation of singular values is shown in **Figure 3-22**, and a comparison of the reconstructed signal with the noise free signal is shown in **Figure 3-23**.

Although SSA could not recover exactly the noise free signal as shown in **Figure 3-24**, however, it conserves the required information to perform a good SSI-COV identification: 3500 points were used in covariance, and rows were increased from 2 to 100, system order is determined to be 4. A comparison between different possible choices of singular values was made in this figure.

Through **Figure 3-24** one can realize that even with only 4 singular values, the information is sufficient to let SSI-COV able to identify the system frequencies, but it is not for damping ratio, this is observed in **Table 3-5**.

As a conclusion for this example, from the different choices shown above, 8 singular values chosen from SSA is the optimum in terms of the obtained modal parameters. Selecting more singular values than the amount in need will introduce extra

noise components in the filtered signal and hence, the stabilization became worse; on the other side, although insufficient singular values is leading to negative damping ratio estimates (unstable systems poles), both the stability diagram and the frequency estimate has the same quality and accuracy. From this point, there should be a best choice of singular values at SSA step, which leads to the best estimate of modal parameters through SSI-COV. Furthermore, below this critical number, the stabilization diagram will be always stable and with the same accuracy whatever the number of singular values chosen.

The unique drawback of the use of SSA before SSI-COV is the uncertainty about the damping ratio estimate, since it seems to be always lower than the true damping ratio. The reason is that, the information extracted by SSA is sufficient to obtain an accurate estimate of the frequency, but a great portion of the signal was filtered out loosing in this way the possibility to obtain a reliable damping ratio estimate. However, anyway, as what is shown in previous sections, the damping ratio obtained by SSI-based algorithms from ambient vibrations is generally bad due to the noise interference.

After these simulation studies, SSA-SSI-COV has been proven to be very effective to deal with noisy measurements, accuracy and stability diagram are also improved. In section 4, the application of SSA-SSI-COV in the identification task of a real and complex structure leads to a very practical way to determine the system order.

Chapter 4

Application of SSI to the identification of Canton Tower

The Canton Tower is located at Guangzhou, China. It is a super high-rise tube-in-tube structure with a height of 610 m, as shown in **Figure 4-1**. This structure comprises a reinforced concrete inner tube and a steel outer tube with concrete-filled tube (CFT) columns. There are 37 floors connecting the inner tube and the outer tube. The outer tube consists of 24 CFT columns, uniformly spaced in an oval while inclined in the vertical direction. The inner tube is an oval shape but with constant dimension of 14m by 17m in plan, but its centroid differs from the centroid of the outer tube. The Hong Kong Polytechnic University is in charge of the implementation of the long-term SHM both during the construction as in the service stage. More details can be found in references [35, 63, 64]. The data were recorded from 18:00 pm on 19 January 2010 to 18:00 pm on 20 January 2010, lasting 24 hours. I The acceleration, wind direction, wind speed and ambient temperature were measured during the period.

Twenty uni-axial accelerometers (Tokyo Sokushin AS-2000C) were employed for vibration measurements, the frequency range is DC-50 Hz (3dB), amplitude range ±2 g, and the sensitivity 1.25 V/g. They were installed at eight levels as shown in Figure 1, the 4th level and the 8th level were equipped with four uni-axial accelerometers, two for measurement of the horizontal acceleration along the long-axis of the inner structure and the other two for the short-axis. At the other six levels, each section was equipped with two uni-axial accelerometers, one along the long-axis of the inner structure and the other along the short-axis of the inner structure. **Figure 4-1** also shows a plan of the section and the measurement direction of acceleration. The sensors were fixed to the shear wall of the inner structure via a steel angle. The sampling frequency of the

acceleration and wind data was 50 Hz. **Figure 4-2** shows the acceleration measurement at the first minutes of the 1st and 20th sensor which are located at a lower and a higher place of the tower respectively. Signals of the 20th sensor appear to contain a long period signal (about 2 seconds) as compared to the measurement of 1st sensor.

4.1 Frequency Domain Decomposition (FDD)

Before applying the SSI analysis, the FDD (**Appendix A**) was used to identify the possible number of modes contain in the response measurements. The FDD spectrum was calculated using the first 131072 points (43.69 minutes data) starting from 18:00 pm on 19 January 2010, Welch's periodogram [54] was used to estimate the power spectrum density function with a window length of 8192 points and an overlap of 4096 points which leads to a power spectrum estimate obtained by averaging a total 31 Fourier spectrums. Since the sampling rate is 50 Hz, the used of window length of 8192 points leads to a frequency resolution of 0.006 Hz. The result of FDD spectrum is shown in **Figure 4-3**.

4.2 SSI-COV and SSI-DATA

To construct the stabilization diagram using SSI-COV, the first 18000 points (6 minutes data starting from 18:00 pm on 19 January 2010) were used in the covariance, and the size of square Toeplitz matrix increases from 5 to 300 block rows, all 20 sensors were used in the computation. By observing the variation of singular values shown in **Figure 4-4**, there is not any significant gap between the extracted singular values. There is no clear criterion to determine the system order based on the singular spectrum in SSI-COV. As an extra help, one can count the number of peaks appearing in FDD spectrum multiplied by two to get an estimate of the system order, *i.e.*, number of singular values to be chosen. In our case, 90 singular values were chosen.

In the case of SSI-DATA, a 8000 columns Hankel data matrix with rows i increasing from 20 to 280 block rows (the actual maximum number of rows is $2 \times i \times l$ = 11200 rows) are used to identify the modal parameters of Canton Tower. The system order is chosen as the same as SSI-COV.

Based on the experience of simulation examples, either with SSI-COV or SSI-DATA, a stable diagram will take time in reveal for noisy acceleration measurements, and this occurs as it is expected, the stabilization diagram constructed using SSI-COV is shown in **Figure 4-5 a)**, ranging from 0 to 1 Hz, and the outcome for SSI-DATA is shown in **b)**. The diagram from 1 Hz to 5 Hz is shown in **Figure 4-5 c)** and **d)** for SSI-COV and SSI-DATA respectively. A peculiarity of this diagram is that the spectrum of the 1st singular value calculated by FDD is plotted at the background of the diagram for comparison purpose. The identified modal parameters are shown in **Figure 4-6** and **Figure 4-7**, "**f**" indicates frequency, "**d**" indicates damping ratio; the plots are the complex modes identified by SSI-COV and SSI-DATA for the first 18 modes. The "**R**" term represents the correlation coefficient between real part and imaginary part of complex modes, this serves as an indicator of the almost-proportionality of the structure damping, *i.e.*, if **R** is near to the unit, damping of the structure is almost totally proportional and the phase angle of complex mode shapes are in phase (0°) or out-of-phase (180°).

The first two close frequencies: 0.0404 and 0.0409 Hz have a damping ratio much higher than the usual for civil structures, and their complex mode shapes are quite sparse besides that the second pole is not stable, hence, this two poles can be discarded and they probably correspond to the dominant wind frequency since the wind spectrum has its peak around 0.1 Hz.

On the other side, SSI-DATA could not find the first mode which is 0.0902 Hz based on the identification result of SSI-COV. However, although SSI-COV could identify the 1st mode, its complex mode shape is a little more scattered comparing with other identified modes which are almost a straight line. The especial difficulty to find the first mode may be explained by the fact that the dominant wind frequency identified here is very close to the first mode, therefore, this latter is likely to be affected by the wind frequency as well as the noise content, thus, from the simulation experience the lowest mode is the most affected by the noise.

Besides that, SSI-DATA could only found three stable frequencies: 0.365, 0.477 and 0.519 Hz meanwhile SSI-COV found five in that range. The difficulty to identify these frequencies may be explained based on the conclusions obtained in previous simulation results: closely-spaced frequencies with noise in the measurements are hard to be identified, if the noise effect is strong and unable to be filtered out first, generally only one equivalent frequency can be identified. Although SSI-COV shows to be able to separate these close frequencies, huge Toeplitz matrix size is required to achieve a good segregation between system information and noise, *i.e.*, excessive time was consumed in computation.

4.3 SSA-SSI-COV

4.3.1 Implementation

In this section, SSA will be used as a pre-processing tool in the sense of a "subspace filter", to extract first the principal components from the measurements, thus, to enhance the stability of SSI-COV. The SSA-SSI-COV procedure is listed as follows:

1. Assemble Hankel Data matrix (100~200 block rows are recommended). The number

of columns will determine the available data point to construct the oncoming Toeplitz matrix. Usually the number of columns should be much larger than the number of block rows. The number of rows will determine the number of principal components the signal to be decomposed.

2. Perform SVD to the Hankel Data matrix in the step of SSA, from the singular spectrum (plot of the singular values) obtained in SSA, a preliminary set of principal components can be selected to reconstruct the signal.

3. Reconstruct the signal and repeat it for the set of choices of SV.

4. Construct Toeplitz matrix from the reconstructed signals, as it is done in SSI-COV.

5. Conduct SVD to the Toeplitz matrices and plot the singular spectrum (The size of Toeplitz matrix could be the largest number of block rows that will be reached in the stabilization diagram. 100~200 block rows is recommended for field noisy measurements).

6. Repeat step 4 and step 5 for the set of choices of SV from SSA.

7. Go from large to small number of components (SV) selected from SSA, and seek for the one whose singular spectrum in SSI-COV has a remarkable change of slope.

8. The best system order will be within the start and end of the change of slope, and the stabilization diagram can be constructed for pole discrimination.

The introduction of SSA before SSI-COV enables the determination of system order, which is totally subjective if SSI algorithms are used alone. The above described procedure will be demonstrated in the following Canton Tower identification task.

4.3.2 Canton Tower identification through SSA-SSI-COV

Application of SSA-SSI-COV to the measurements of Canton Tower was studied. In performing the SSA, 20 sensors measurements in form of vector were placed at once in Hankel data matrix with the following dimensions: 340 block rows (totally 6800 rows) by 15000 columns. The outcome singular spectrum is shown in **Figure 4-8**. It is difficult to select a suitable number of singular values from this figure because there is not any gap on the distribution of singular values obtained by SSA.

In the implementation of SSA-SSI-COV there are two parameters to be determined: the first one is the number of Singular Values (SV) to be chosen by conducting the SSA, and the other is the system order to be determined in the SSI-COV analysis. From the experience gathered by working on the data of Canton Tower, a specific number of SV in SSA step leads to a change of slope in the singular spectrum obtained in SSI-COV (one can call it the first critical number of components). This is shown in **Figure 4-9 b)**. If the selected number of SV in the step of SSA continues decreasing, up to a second critical point the change of slope will become very sharp, almost a vertical jump, as in the case of 95SV shown in **Figure 4-9 d)**. This latter phenomenon will remain as the number of SV chosen in SSA continues decreasing as that shown in **e)** and **f)**. In this second critical point, usually the number of SV in the SSA step will be very closer to the system order, where is an almost vertical jump. From experience, the second critical point gives the best identification results, but those not well excited or highly contaminated modes will be also filtered out.

Different stabilization diagrams were made for comparison purpose. **Figure 4-10** shows the result for different choices of SV, ranging from 0 Hz to 1 Hz. In the beginning, 312 SV were chosen from SSA, the jump in the singular spectrum of

SSI-COV is almost imperceptible and only a few modes appear in the stability diagram. When a smaller number of SV is selected, *e.g.*, 136 SV in SSA step, as shown in **Figure 4-9 b)**, the change of slope is a little more remarkable (this can be considered as approximately the first critical point), and the stabilization diagram shown in **Figure 4-10 c)** was improved. If one keep reducing the selected SV in SSA step, the diagram become more stable and starts earlier. However, in the case of **Figure 4-10 d)** when 95 SV were chosen, the 1st mode has been filtered out although a stable diagram starts even earlier than **Figure 4-10 c)** in which 136 SV were selected. Finally, as discussed above in the simulation section, although the number of SV selected are fewer than the required as in the case of **Figure 4-10 e)** and **f)**, certain modes will not be discarded, but the diagram is totally stable just at the beginning, *i.e.*, correct answers were found at a few block rows; in other words, these totally stable modes are free from noise perturbation after the pre-processing with SSA.

To understand the absence of the 1st mode when 95 SV are extracted from SSA. The Fourier Spectrum of the response data is shown in **Figure 4-11**. Title of the figure indicates sensor number. In the case of 95 SV, the major peaks are covered, but the peak corresponding to the first mode was almost totally filtered out, which is originally very small comparing to others and looks fuzzy and blended with the noise frequency. By increasing the number of selected SV to 136 (**Figure 4-12**), in this case, the peak corresponding to the 1st mode is conserved, however, the noise filtering is not as good as it is the case of 95 SV. Therefore, 95 SV is slightly better in terms of stability diagram tan 136 SV. Comparing **Figure 4-11** and **Figure 4-12**, one can note that there is another peak at 1.2 Hz just filtered out by SSA using 95 SV.

The stabilization diagram with frequency ranging from 1 to 5 Hz is shown in

Figure 4-13 a) and **b)**, for the cases of 136 and 95 SV respectively. Finally, complex mode shapes together with the modal frequency and damping ratio are shown in **Figure 4-14** and **Figure 4-15** respectively. A summary and comparison of the identified system modal frequencies with the Finite Element Model of the structure is shown in **Table 4-1**.

Similar to the outcome from SSI-COV, the first two identified frequencies by SSA-SSI-COV: 0.0345 Hz and 0.0465 Hz (using 95 SV), which are probably wind frequencies, whose mode shapes plotted in complex plane appear without any regularity. Although the fundamental mode was found by extracting 136 SV, unlike the other modes which appear almost in a straight line (meaning that the structure has almost-proportional damping) this 1st mode is the unique which has the lowest value of **R** excepting the wind modes, which is equal to 0.7. Here one can conclude that, from the several choices of SV from SSA, the use of 95 SV leads to the best stability. But to achieve a better identification quality of the 1st mode shape, a larger Toeplitz matrix size may be needed.

4.3.3 Canton Tower identification through SSA-SSI-DATA

A unique remaining question is that, if SSA can be combined with other SSI algorithm as a pre-processing tool, such as SSI-DATA? The stabilization diagram using SSA-SSI-DATA is shown in **Figure 4-16**. From this result one can conclude that SSA serves as a preprocessing tool only in conjunction with SSI-COV but not for SSI-DATA. The result obtained by SSA-SSI-DATA is worse than that applying directly SSI-DATA. This may be explained by the fact that, the orthogonal projection used in SSI-DATA is trying to find the best fit by least square of the future measurements in terms of the past data. However, the principal components recovered by SSA used for reconstruction of

the signal may provide a bad fitting in the projection and worse results were obtained.

4.4 Low pass filter with SSI-COV

As it can be observed from the Fourier Spectrum of the acceleration measurement of sensor No. 19 shown in **Figure 4-17**, there is a wide band measurement noise distributed in the high frequency range (comparing to the structure fundamental mode, after 5 Hz can be considered as high frequency). Low-pass filter is commonly used to reduce the noise effect in system identification. Here the use of low-pass filter and its effect in stabilization diagram is evaluated.

A Butterworth IIR (Infinite Impulse Response) filter of order 10 and cutoff frequency of 5 Hz is used to low-pass the signal trying the eliminate the measurement noise. To avoid phase shifting effect in the filtering process, the data was filtered twice: the filtered data is reversed and passed again by the same filter to cancel out all phase shift caused by the Butterworth IIR filter. The frequency response function of 10th order Butterworth filter with cutoff frequency of 5 Hz is shown in **Figure 4-18**. The frequency axis is normalized, the normalized cutoff frequency corresponds to 0.2 of the original Nyquist frequency which is 25 Hz. A segment of the filtered signal is shown in **Figure 4-19**, one can see that the high frequency noise content was reduced after filtering.

The stabilization diagram constructed using both SSI-COV and SSI-DATA are shown in **Figure 4-20**. However, after low-passing the acceleration data, neither SSI-COV nor SSI-DATA were able to realize the fundamental mode of the structure at a similar matrix order than that used in by SSA-SSI-COV. The mode corresponds to 0.4243 Hz was also missed by SSI-DATA and the diagram of the same mode is not stable. Therefore, although high frequency noise can be filtered out, the noise content below 5 Hz still exists and continues perturbing the identification of these

closely-spaced frequencies. From this evaluative comparison, when SSI-COV is used, one may prefer SSA as pre-processing tool than low-pass filter, thus, besides the better noise filtering performance achieve by SSA, it is a practical way to determine the system order.

Finally, to complete the modal information, the three dimensional plot of examples of the identified mode shapes with SSI-COV are shown from **Figure 4-21** to **Figure 4-24**, from the first mode to the 24-th mode. The corresponding first 18 complex mode shapes are shown in **Figure 4-6** and **Figure 4-7**, which are the system poles extracted from the 300-th block row.

4.5 Improve the identification convergence speed with decimation

In addition to the SSA-SSI-COV algorithm which pre-process the noisy data and allows to realize all identifiable modes, the convergence of time domain system identification algorithms can be easily improved by "decimation", which is a two-step process: low-pass anti-aliasing filter and downsampling, thus, the choice of a proper sampling rate is an important issue in system identification [29,66]. The Nyquist frequency gives the lower bound for the sampling rate meanwhile the upper bound is determined by the numerical instability due to truncation and round-off errors in a digital computer. It is shown in [67] that the poles of the transfer function of a discrete-time system approach to one on the unit circle as the sampling interval becomes very small, which leads to numerical instability in the computation especially when the data is noise contaminated. In [68] a sampling rate between 10 times to 50 times the closed loop system bandwidth is recommended for the digital implementation of feedback systems.

The Canton Tower is a very flexible and long period structure with about 0.09 Hz

for its first mode, and there are 9 modes below 1 Hz. It is possible that a sampling rate of 50 Hz is too high for a fast convergence of these modes below 1 Hz through the use of stabilization diagram especially for the 1st mode.

Three downsampling factors were chosen for comparison: 2, 5, and 10, which will reduce the original sampling rate (50 Hz) to 25 Hz, 10 Hz and 5 Hz respectively. To avoid aliasing, a low-pass filter must be used as an anti-aliasing filter to reduce the bandwidth of signal before it is downsampled, *i.e.*, the signal are firstly low-passed by a Butterworth 10th order filter with cut-off frequencies of 12.5 Hz, 5 Hz and 2.5 Hz corresponding to the respective Nyquist frequency. The same 400 seconds data length is downsampled for identification, thus, there are only 2000 points available for the case with sampling rate of 5 Hz, 4000 points for 10 Hz and 10000 points for 25 Hz. The system order is defined to be 60 when the data is downsampled to 5 Hz, and 90 when it is downsampled to 25 Hz and 10 Hz. The outcome stabilization diagram is shown in **Figure 4-25** for the frequency ranging from 0 to 1 Hz. It is clear from **a)** that with the data downsampled to 25 Hz, it is still costly to reveal a stable diagram for the 1st mode; however, a stable diagram appears for all modes with few block rows when the data is downsampled to **b)** 10 Hz and **c)** 5 Hz, although for this latter not all modes were identified. **Figure 4-26** shows the stability diagram for the frequency range between 1 to 6 Hz. Examples of complex modes shapes identified with different sampling rates are shown in **Figure 4-27** for modes 1~10 (the wind modes are not shown), the same as those obtained in section 4.2 and 4.3 by SSI-COV and SSA-SSI-COV under a sampling rate of 50 Hz, these complex modes appear almost in a straight line, thus, the mode shape quality is not affected by a proper decimation.

Finally, the identified modal frequencies and damping ratios are summarized in

Table 4-2, one can note that the identified frequencies are the same as that obtained with the original sampling rate, only the identified damping ratio for 1st mode (about 1%) is much lower than that identified through SSI-COV and SSA-SSI-COV using the original sampling rate of 50 Hz. From this analysis, it is concluded that a sampling rate of 10 Hz is suitable for identification and monitoring of Canton Tower which implies a significant reduction in computation effort. If only lower modes are interested, the sampling rate can be even reduced to 5 Hz and the convergence is even faster.

Chapter 5

Recursive Stochastic Subspace Identification algorithms

Different from the off-line analysis, the on-line system identification and damage detection, based on vibration data measured from the structural health monitoring system has received considerable attention recently. In this section, the Covariance-driven Recursive Stochastic Subspace Identification algorithm (RSSI-COV) is discussed, for later, to be used to estimate system modal parameters from the response measurements of time-varying systems. To consider the noise contaminated data, a recursive pre-processing technique called recursive singular spectrum analysis technique (rSSA) is introduced to enhance the accuracy and stability in the online tracking capability.

5.1 Recursive Covariance-driven Stochastic Subspace Identification algorithm (RSSI-COV)

For online application of SSI-COV, instead of arranging the block covariances in the so-called Toeplitz matrix as shown in (2.27), these must adopt the form of a Hankel Covariance matrix, which is the way it is outlined in NExT-ERA [10]. From the same stochastic properties shown in (2.25), the Hankel Covariance matrix has the following factorization properties:

$$\mathbf{H}^{cov} = \begin{bmatrix} \mathbf{R}_1 & \mathbf{R}_2 & ... & \mathbf{R}_i \\ \mathbf{R}_2 & \mathbf{R}_3 & ... & \mathbf{R}_{i+1} \\ ... & ... & ... & ... \\ \mathbf{R}_i & \mathbf{R}_{i+1} & ... & \mathbf{R}_{2i-1} \end{bmatrix} = \mathbf{O}_i \mathbf{\Omega}_i = \begin{bmatrix} \mathbf{C} \\ \mathbf{CA} \\ ... \\ \mathbf{CA}^{i-1} \end{bmatrix} \begin{bmatrix} \mathbf{G} & \mathbf{AG} & ... & \mathbf{A}^{i-1}\mathbf{G} \end{bmatrix} \qquad (5.1)$$

where $\mathbf{O}_i \in \Re^{li \times 2n}$ is the same observability matrix and $\mathbf{\Omega}_i \in \Re^{2n \times li}$ is the stochastic controllability matrix, which is similar to $\mathbf{\Gamma}_i$ shown in (2.28) but with its entries in reversed order. The observability matrix can be obtained by applying SVD to the Hankel covariance matrix, and then the system matrices and modal parameters can be extracted in the same manner than that presented in SSI-COV off-line analysis. The Hankel Covariance matrix can be constructed by arranging the output measurement data vectors as follows:

$$
\boldsymbol{y}_k^+ \equiv \begin{bmatrix} \boldsymbol{y}_{k-i+1} \\ \boldsymbol{y}_{k-i+2} \\ \cdots \\ \boldsymbol{y}_k \end{bmatrix}, \boldsymbol{y}_k^{-T} \equiv \begin{bmatrix} \boldsymbol{y}_{k-i}^T & \boldsymbol{y}_{k-i-1}^T & \cdots & \boldsymbol{y}_{k-2i+1}^T \end{bmatrix} \tag{5.2}
$$

where $\boldsymbol{y}_k \in \Re^{l \times 1}$ is the output measurement vector. $\boldsymbol{y}_k^+ \in \Re^{il \times 1}$ and $\boldsymbol{y}_k^{-T} \in \Re^{1 \times il}$. l is the number of sensors and i is number of block rows which forms the Hankel covariance matrix. One can find easily that the latter can be built by the following expression:

$$
\mathbf{H}_N^{cov} = E[\boldsymbol{y}_k^+ \boldsymbol{y}_k^{-T}] = \frac{1}{\tilde{p}} \sum_{k=2i}^N \boldsymbol{y}_k^+ \boldsymbol{y}_k^{-T}
$$

$$
= \begin{bmatrix} \boldsymbol{y}_{i+1} & \boldsymbol{y}_{i+2} & \cdots & \boldsymbol{y}_{N-i+1} \\ \boldsymbol{y}_{i+2} & \boldsymbol{y}_{i+3} & \cdots & \boldsymbol{y}_{N-i+2} \\ \vdots & \vdots & & \vdots \\ \boldsymbol{y}_{2i} & \boldsymbol{y}_{2i+1} & \cdots & \boldsymbol{y}_N \end{bmatrix} \begin{bmatrix} \boldsymbol{y}_i^T & \boldsymbol{y}_{i-1}^T & \cdots & \boldsymbol{y}_1^T \\ \boldsymbol{y}_{i+1}^T & \boldsymbol{y}_i^T & \cdots & \boldsymbol{y}_2^T \\ \vdots & \vdots & & \vdots \\ \boldsymbol{y}_{N-i}^T & \boldsymbol{y}_{N-i-1}^T & \cdots & \boldsymbol{y}_{N-2i+1}^T \end{bmatrix} = \mathbf{Y}_k^+ \mathbf{Y}_k^{-T} \tag{5.3}
$$

where k is ranging over the entire set of available data and $\tilde{p}$ is an optional normalization parameter. As multiplying $\mathbf{H}_N^{cov}$ by a constant does not affect the obtained matrices $\mathbf{A}$ and $\mathbf{C}$, $\tilde{p}$ can be set to 1 without further influence on the obtained models. Since the order of the Hankel Covariance matrix is "i" with data length N, then, the Hankel Covariance matrix (which is a square matrix since the same order is used for rows and columns) can be calculated as the summation over N-$2i$+1 rank-one matrices formed by $\boldsymbol{y}_k^+ \boldsymbol{y}_k^{-T}$, and later a new incoming data point N+1 will be converted into a

new rank-one matrix adding to the existing Hankel Covariance matrix.

There are three possibilities to formulate the adaptive Hankel matrix for RSSI-COV [17]:

1. *Exponential forgetting:* The old data is multiplied by a forgetting factor μ when a new data is added.

$$\mathbf{H}_{N+1}^{\text{cov}} = \mu \mathbf{H}_N^{\text{cov}} + y_{N+1}^{+} \left(y_{N+1}^{-} \right)^T \tag{5.4}$$

2. *Sliding window:* This formulation require 2 step calculation for each incoming new data. The oldest data is removed from the window (downdating) and a new data is incorporated (updating). Let the window length be *L*:

$$\mathbf{H}_N^{\text{cov}} = E\left[y_k^{+} y_k^{-T} \right] = \frac{1}{p} \sum_{k=N-L+2i}^{N} y_k^{+} y_k^{-T} \tag{5.5a}$$

$$\mathbf{H}_{N+1}^{\text{cov}} = \mathbf{H}_N^{\text{cov}} + y_{N+1}^{+} \left(y_{N+1}^{-} \right)^T - y_{N-L+2i}^{+} \left(y_{N-L+2i}^{-} \right)^T \tag{5.5b}$$

3. *Combined approach:* It is the application of forgetting factor in updating as well as in downdating.

$$\mathbf{H}_{N+1}^{\text{cov}} = \mu \mathbf{H}_N^{\text{cov}} + y_{N+1}^{+} \left(y_{N+1}^{-} \right)^T - \mu^{N-2i+1} y_{N-L+2i}^{+} \left(y_{N-L+2i}^{-} \right)^T \tag{5.6}$$

where the superscript *N-2i+1* above the forgetting factor μ is because $\mathbf{H}_N$ is formed by the summation over *N-2i+1* rank-one matrices formed by $y_k^{+} y_k^{-T}$, and since the Hankel Covariance matrix is updated first, the rank-one matrix "$y_{N-L+2i}^{+} \left(y_{N-L+2i}^{-} \right)^T$" to be downdated should be multiplied by the corresponding forgetting factor to the power of *N-2i+1*.

The software library LAPACK is used in MATLAB to compute SVD of the Hankel Covariance matrix in an off-line manner, which uses the classical algorithms

like Householder reflections and QR algorithms [18], but it is very costly in the computation effort since it takes $O(ab^2)$ floating point operations to compute SVD[45], where a is the number of rows and b is number of columns of the matrix. It is not suitable for online applications. The need of a recursive fashion to update SVD was firstly found in the field of sensor array signal processing, in which the subspace estimation plays an important role and the online tracking of the direction of arrival (DOA) of the plane waves is the main issue. As a consequence, a new approach called Projection Approximation Subspace Tracking (PAST) was initially developed by Bin Yang [56], who takes advantage of a mathematical lemma to find the required column subspace as an unconstrained optimization problem. Later the algorithm is modified to its Extended Instrumental Variable version (EIV-PAST) by Gustafsson [20], which is a suitable algorithm for the structure of SSI-COV [17]. It is important to mention that PAST is not the unique algorithm to track the time varying subspace, it is classified in the category of the unconstrained quadratic optimization problem [34]. In the following, a brief description of PAST, its extension to EIV-PAST and implementation to recursive SSI-COV will be described.

5.1.1 Projection Approximation Subspace Tracking (PAST)

The PAST is originally a fast dominant-eigenvectors updating algorithm which is based on the following unconstrained cost function:

$$V(\mathbf{W}) = E\left\| z(t) - \mathbf{W}\mathbf{W}^H z(t) \right\|^2 = Tr\left\{ \mathbf{C_z} - 2\mathbf{W}^H \mathbf{C_z}\mathbf{W} + \mathbf{W}^H \mathbf{C_z}\mathbf{W}\mathbf{W}^H \mathbf{W} \right\} \qquad (5.7)$$

where $z(t) \in \Re^{m \times 1}$ is a random vector, $\|\cdot\|$ denotes the Euclidean vector norm. E{·} and Tr{·} are the expectation and trace operator respectively. $\mathbf{C_z}$ is the signal covariance matrix defined as $\mathbf{C_z} = E[z(t)z^T(t)]$. The superscript [H] denotes Hermitian transpose, $\mathbf{W}$

is a matrix with suitable dimensions. In our case, the covariance of vibration signals is real, the desired column subspace $\mathbf{W}$ is also real, therefore the Hermitian transpose can be treated as the usual matrix transpose. The cost function is known as Yang's criterion, and there is a mathematical statement with respect to the matrix $\mathbf{W}$:

Theorem 1[20]*:* The matrix $\mathbf{W}$ is a stationary point of $V(\mathbf{W})$ if and only if $\mathbf{W} = \overline{\mathbf{U}}\mathbf{T}$, where $\overline{\mathbf{U}} \in \mathfrak{R}^{m \times r}$ has orthonormal columns and contains any r distinct eigenvectors of $\mathbf{C_z}$. All stationary points of $V(\mathbf{W})$ are saddle points, except when $\overline{\mathbf{U}}$ contains the r dominant eigenvectors, *i.e.*, $\overline{\mathbf{U}} = \overline{\mathbf{U}}'$. In this case, $V(\mathbf{W})$ attains the global minimum. Here, $\mathbf{T} \in \mathfrak{R}^{r \times r}$ is an arbitrary unitary matrix. Proof can be found in [56].

Avoiding the cumbersome mathematical derivations of the proof, more intuitively, the cost function is trying to minimize the error between the "transformed" or "filtered" signal $\bar{z}(t) = \overline{\mathbf{U}}'\overline{\mathbf{U}}'^T z(t)$ and $z(t)$, through a transformation matrix composed by the dominant eigenvectors of the signal covariance matrix $\mathbf{C_z}$, *i.e.*, $\overline{\mathbf{U}}'\overline{\mathbf{U}}'^T$. Usually the computed dominant eigenvectors are orthonormal, thus, $\overline{\mathbf{U}}'\overline{\mathbf{U}}'^T$ is actually an orthogonal projection matrix as it is defined in linear algebra, and $\bar{z}(t)$ is the projection of the noisy signal into the signal subspace, thus, noise will be filtered out by this orthogonal projection. In fact, this "subspace filtering" concept was the original idea of Bin Yang to eliminate the measurement noise, which later will be implemented in recursive SSA.

Based on *Theorem 1*, instead of solving the Eigen-Decomposition problem through classical approaches, the unconstrained cost function only tries to update the dominant eigenvectors of the signal covariance matrix $\mathbf{C_z}$. For time-varying systems, the dominant

62

eigenvectors $\overline{\mathbf{U}}'$ changes with time, the criterion can be modified by introducing a forgetting factor:

$$V\left[\mathbf{W}\left(t\right)\right] = \sum_{k=1}^{t} \mu^{t-k} \left\| z\left(k\right) - \mathbf{W}\left(t\right)\mathbf{W}^{H}\left(t\right)z\left(k\right) \right\|^{2} \tag{5.8}$$

where μ denotes the forgetting factor used in the summation to give different weights to the random vector $z(k)$ in the summation, and the expectation in (5.7) is replaced by the summation. Also the definition of $\mathbf{C_z}$ has to be replaced by

$$\mathbf{C_z}\left(t\right) = \sum_{k=1}^{t} \mu^{t-k} z\left(k\right)z^{H}\left(k\right) \tag{5.9}$$

However, the inconvenience found in the cost function is that, as shown in equation (5.7), after expand the cost function, it is a fourth order matrix equation to be solved. To adapt the solution to a Recursive Least Square (RLS) approach, an "approximation" is introduced:

$$\boldsymbol{h}\left(k\right) = \mathbf{W}^{H}\left(k-1\right)z\left(k\right) \tag{5.10}$$

which replace $\mathbf{W}^{H}\left(t\right)z\left(k\right)$ in (5.8). The assumption under this approximation is that there is not a drastic subspace change from a point to another, *i.e.*, signal subspace is slow varying comparing to the sampling rate of data point.

With this assumption, since the dominant subspace $\mathbf{W}^{H}(k-1)$ is already known from the previous step k-1, the original cost function is converted to a quadratic criterion:

$$\overline{V}\left[\mathbf{W}\left(t\right)\right] = \sum_{k=1}^{t} \mu^{t-k} \left\| z\left(k\right) - \mathbf{W}\left(t\right)\boldsymbol{h}\left(k\right) \right\|^{2} \tag{5.11}$$

which is a typical optimization function in Least Square problems and can be minimized by:

$$\mathbf{W}\left(t\right) = \overline{\mathbf{U}}'\left(t\right) = \mathbf{C}_{zh}\left(t\right)\mathbf{C}_h^{-1}\left(t\right) \tag{5.12}$$

where $\mathbf{C}_{zh}$ is the covariance matrix formed by z(k) and h(k):

$$\mathbf{C}_{zh}\left(t\right) = \sum_{k=1}^{t}\mu^{t-k}z(k)h^H\left(k\right) = \mu\mathbf{C}_{zh}\left(t-1\right) + z(t)h^H\left(t\right) \tag{5.13}$$

$$\mathbf{C}_h\left(t\right) = \sum_{k=1}^{t}\mu^{t-k}h(k)h^H\left(k\right) = \mu\mathbf{C}_h\left(t-1\right) + h(t)h^H\left(t\right) \tag{5.14}$$

Thus, when there is a new incoming data at instant t, the matrix inversion lemma can be applied to (5.14) and the well-known RLS algorithm can be easily derived for updating $\mathbf{W}(t)$.

5.1.2 Instrumental Variable Projection Approximation Subspace Tracking (IV-PAST)

Since PAST by Bin Yang was formulated originally to treat antenna signals corrupted with additive noise through a subspace approach [56]. However, from the derivations and assumptions shown in section 2: in output-only SSI, the input source $\mathbf{B}u_k$ is unknown, which together with system noise are assumed to be a stationary and spatially white noise, *i.e.*, instead of a simple additive noise, it is rather the source of the system response. For this type of noise, it was proved in [43] that the normal least square formulation will lead to a biased solution and it is not appropriate to handle this type of problem; instead, an **Instrumental Variable** (IV) approach must be used. Since the instruments must be uncorrelated with noise, usually the same output measurement but with a time lag "i" can be chosen for this purpose. The modification of PAST to IV-PAST and later Extended IV-PAST was proposed by Gustafsson [20].

By introducing the instrument $\xi(t) \in \Re^{m \times 1}$, the least square solution to the

objective function in (5.11) becomes the following equation:

$$\sum_{k=1}^{t} \mu^{t-k}[z(k)\boldsymbol{\xi}^{H}(k) - \mathbf{W}(t)\boldsymbol{h}(k)\boldsymbol{\xi}^{H}(k)] = \mathbf{C}_{z\xi}(t) - \mathbf{W}(t)\mathbf{C}_{h\xi}(t) = 0 \qquad (5.15)$$

Again, the summation over the multiplication of the signal $z(k)$ and instrument $\boldsymbol{\xi}(k)$ weighted by the forgetting factor, can replace by the respective cross-covariance matrices $\mathbf{C}_{z\xi}(t)$ and $\mathbf{C}_{h\xi}(t)$, which are defined and updated by:

$$\mathbf{C}_{z\xi}(t) = \sum_{k=1}^{t} \mu^{t-k} z(k)\boldsymbol{\xi}^{H}(k) = \mu\mathbf{C}_{z\xi}(t-1) + z(t)\boldsymbol{\xi}^{H}(t) \qquad (5.16)$$

$$\mathbf{C}_{h\xi}(t) = \sum_{k=1}^{t} \mu^{t-k} \boldsymbol{h}(k)\boldsymbol{\xi}^{H}(k) = \mu\mathbf{C}_{h\xi}(t-1) + \boldsymbol{h}(t)\boldsymbol{\xi}^{H}(t) \qquad (5.17)$$

Then, by inverting $\mathbf{C}_{h\xi}(t)$ the matrix $\mathbf{W}(t)$ can be found:

$$\mathbf{W}(t) = \overline{\mathbf{U}}'_{IV}(t) = \mathbf{C}_{z\xi}(t)\mathbf{C}_{h\xi}^{-1}(t) \qquad (5.18)$$

The same matrix inversion lemma can be applied to (5.18) and the same RLS-like algorithm can be formulated for IV-PAST.

5.1.3 Extended Instrumental Variable Projection Approximation Subspace Tracking (EIV-PAST)

The inconvenience one may found in IV-PAST is that, to let the inverse of the cross-covariance matrix exist, the length of the instrument vector must have the same size as the measurement vector z(t). Another problem one may found in practice is that the cross-covariance matrix may be ill-conditioned for which is not amenable the inversion. The Extended Instrumental Variable was derived to solve this problem and make further stable the inversion process. Then, the cost function to be minimized can be replaced by its corresponding EIV formulation:

$$\overline{V}[\mathbf{W}(t)] = \left\| \sum_{k=1}^{t} \mu^{t-k} z(k) \xi^H(k) - \mathbf{W}(t) \sum_{k=1}^{t} \mu^{t-k} h(k) \xi^H(k) \right\|_F^2 = \left\| \mathbf{C}_{z\xi}(t) - \mathbf{W}(t) \mathbf{C}_{h\xi}(t) \right\|_F^2 \quad (5.19)$$

where the subscript $_F$ denotes the Frobenius norm defined as $\sqrt{tr(\sigma\sigma^H)}$. $\mathbf{C}_{z\xi}(t)$ and $\mathbf{C}_{h\xi}(t)$ are the same as that defined in (5.16) and (5.17).

The least square solution of (5.19) is readily found to be:

$$\mathbf{W}(t) = \overline{\mathbf{U}}'_{EIV}(t) = \mathbf{C}_{z\xi}(t) \mathbf{C}_{h\xi}^T(t) \left[\mathbf{C}_{h\xi}(t) \mathbf{C}_{h\xi}^T(t) \right]^{-1} \quad (5.20)$$

The difference between (5.15) and (5.20) is the effect of the extra-added Frobenius norm, which is able to fulfill the need of Recursive Least Square (RLS) via matrix inversion lemma, to treat the case of non-square matrices due to the use of instruments of different length, or, to obtain a better numerical stability in the recursion. A complete derivation and formulas for the EIV-RLS algorithm can be found in [43].

5.1.4 Adaptation of EIV-PAST to RSSI-COV

Since covariance driven subspace can be considered as an **SVD**-enhanced Instrumental-Variable (IV) method [37], one may think that the IV-PAST algorithm is suitable to perform the SVD-updating task, or better said, the observability matrix $\mathbf{O}_i$ (column subspace of the Hankel covariance matrix) updating task, which is not true.

Let the random vector $z(t)$ in IV-PAST formulation be replaced by the corresponding data vector in (5.2), which is $y_k^+ \in \Re^{il \times 1}$; on the other side, the substitution of the instrument $\xi(t)$ is evidently $y_k^{-T} \in \Re^{1 \times il}$. IV Solution to the cost function will become:

$$\sum_{k=t-L+2i}^{t}[\mathbf{y}_k^+ \mathbf{y}_k^{-T} - \mathbf{W}(t)\overline{\mathbf{h}}(k)\mathbf{y}_k^{-T}] = \mathbf{H}_t^{\text{cov}} - \mathbf{W}(t)\overline{\mathbf{H}}_t^{\text{cov}} = 0 \qquad (5.21)$$

where $\overline{\mathbf{h}}(k) = \mathbf{W}^H(k-1)\mathbf{y}_k^+$ is the above mentioned approximation, $\mathbf{H}_t^{\text{cov}} = \dfrac{1}{p}\sum_{k=t-L+2i}^{t} \mathbf{y}_k^+ \mathbf{y}_k^{-T}$ is the definition of Hankel covariance matrix in a moving window formulation (forgetting factor defined as the unit), and $\overline{\mathbf{H}}_t^{\text{cov}} = \sum_{k=t-L+2i}^{t}\overline{\mathbf{h}}(k)\mathbf{y}_k^{-T}$.

Similar to (5.18), the dominant eigenvectors can be found by

$$\mathbf{W}(t) = \overline{\mathbf{U}}_{IV}'(t) = \mathbf{H}_t^{\text{cov}}\left(\overline{\mathbf{H}}_t^{\text{cov}}\right)^{-1} \qquad (5.22)$$

However, either PAST or IV-PAST algorithm was derived to update dominant eigenvectors of the covariance matrix, the relationship between Eigen-Decomposition (ED) and SVD of the Hankel covariance matrix is preferred to be revised. The SVD of a Hankel Covariance matrix is defined as:

$$\mathbf{H}^{\text{cov}} = \mathbf{U}\mathbf{S}\mathbf{V}^T = \begin{pmatrix} \mathbf{U}_1 & \mathbf{U}_2 \end{pmatrix}\begin{pmatrix} \mathbf{S}_1 & 0 \\ 0 & 0 \end{pmatrix}\begin{pmatrix} \mathbf{V}_1^T \\ \mathbf{V}_2^T \end{pmatrix} \qquad (5.23)$$

where $\mathbf{U}$ and $\mathbf{V}$ are orthonormal matrices, $\mathbf{S}$ is a diagonal matrix containing the singular values. But the column subspace $\mathbf{U}$ can be also obtained from the ED of the Hankel Covariance matrix multiplied by its transpose:

$$\mathbf{H}^{\text{cov}}\mathbf{H}^{\text{cov}T} = \mathbf{U}\mathbf{S}\mathbf{V}^T\mathbf{V}\mathbf{S}^T\mathbf{U}^T = \mathbf{U}\overset{\frown}{\left(\mathbf{S}\mathbf{S}^T\right)}\mathbf{U}^T = \mathbf{U}\left(\mathbf{S}\mathbf{S}^T\right)\mathbf{U}^{-1} \qquad (5.24)$$

(where the brace above $(\mathbf{S}\mathbf{S}^T)\mathbf{U}^T$ is labeled "Symmetric matrix")

From the relationships shown above, the desired observability matrix $\mathbf{O}_i$ is the same as the column subspace $\mathbf{U}_1$ extracted from Hankel Covariance matrix using SVD. However, if *Theorem 1* is reviewed, after solving (5.21) by least square, the obtained dominant eigenvector $\mathbf{W}(t) = \overline{\mathbf{U}}_{IV}'(t)$ is the eigenvector of the Hankel Covariance

matrix, it is NOT the desired column subspace. This latter must be computed via ED of the Hankel Covariance matrix multiplied by its transpose as shown in (5.24), *i.e.*, the desired column subspace can be updated as the dominant eigenvectors of the "Covariance of Hankel Covariance matrix".

Fortunately there is **EIV-PAST** whose Frobenius norm is just satisfying this requirement. Again, substituting the random vector $z(t)$ and the instrument $\xi(t)$ by the corresponding data vector in (5.2), the objective function of **EIV-PAST** to be minimized will become:

$$\overline{V}\big[\mathbf{W}(t)\big] = \left\| \sum_{k=t-L+2i}^{t} \boldsymbol{y}_k^+ \boldsymbol{y}_k^{-T} - \mathbf{W}(t) \sum_{k=t-L+2i}^{t} \overline{\boldsymbol{h}}(k) \boldsymbol{y}_k^{-T} \right\|_F^2 = \left\| \mathbf{H}_t^{\text{cov}} - \mathbf{W}(t) \overline{\mathbf{H}}_t^{\text{cov}} \right\|_F^2 \qquad (5.25)$$

where the moving window approach is adopted again. Similar to (5.20), the least square solution to (5.25) is the follows:

$$\mathbf{W}(t) = \mathbf{U}_1(t) = \left(\mathbf{H}_t^{\text{cov}} \overline{\mathbf{H}}_t^{\text{cov}T} \right) \left(\overline{\mathbf{H}}_t^{\text{cov}} \overline{\mathbf{H}}_t^{\text{cov}T} \right)^{-1} \qquad (5.26)$$

Comparing (5.22) and (5.26), the first one is computing the dominant eigenvectors of the Hankel Covariance matrix, on the contrary, (5.26) is computing the dominant eigenvectors of $\mathbf{H}_t^{\text{cov}} \overline{\mathbf{H}}_t^{\text{cov}T}$ as that shown in (5.24), *i.e.*, the desired columns subspace $\mathbf{U}_1(t)$ of the Hankel Covariance matrix.

Hence, the so-called Extended Instrumental Variable Recursive Least Square (EIV-RLS) algorithm can be applied to solve the EIV-PAST problem, which fulfills the SVD-updating requirement of RSSI-COV to track the time-varying subspace $\mathbf{U}_1(t)$. The explicit formulas to be implemented in RSSI-COV are shown below. Complete derivation of these formulas of EIV-RLS algorithm can be found in [43].

1. From an initial SVD the recursive algorithm can be initialized with $\mathbf{U}_1(t)$, $\mathbf{P}(t)$ and $\overline{\mathbf{H}}_t$:

$$\overline{\mathbf{H}}_t = \mathbf{U}_1^T(t)\mathbf{H}_t \quad \& \quad \mathbf{P}(t) = \left[\overline{\mathbf{H}}_t\overline{\mathbf{H}}_t^T\right]^{-1} \tag{5.27a}$$

2. Given a new incoming data vector $\mathbf{y}_{t+1}$, $\mathbf{U}_1(t+1)$, $\mathbf{P}(t+1)$, $\mathbf{H}_{t+1}$ and $\overline{\mathbf{H}}_{t+1}$ can be updated and downdated using the following algorithm:

Updating:

$$\overline{\mathbf{h}}(t+1)^* = \mathbf{U}_1^T(t)\mathbf{y}_{t+1}^+ \quad , \quad \mathbf{w}(t+1)^* = \overline{\mathbf{H}}_t\mathbf{y}_{t+1}^- \tag{5.27b}$$

$$\mathbf{v}(t+1)^* = [\mathbf{H}_t\mathbf{y}_{t+1}^- \quad \mathbf{y}_{t+1}^+] \tag{5.27c}$$

$$\mathbf{\psi}(t+1)^* = [\mathbf{w}(t+1)^* \quad \overline{\mathbf{h}}(t+1)^*] \tag{5.27d}$$

$$\mathbf{\Lambda}(t+1)^* = \frac{1}{\mu^2}\begin{bmatrix} -(\mathbf{y}_{t+1}^-)^T\mathbf{y}_{t+1}^- & \mu \\ \mu & 0 \end{bmatrix} \tag{5.27e}$$

$$\mathbf{K}(t+1)^* = \left[\mu^2\mathbf{\Lambda}(t+1)^* + \mathbf{\psi}(t+1)^{*T}\mathbf{P}(t)\mathbf{\psi}(t+1)^*\right]^{-1}\mathbf{\psi}(t+1)^*\mathbf{P}(t) \tag{5.27f}$$

$$\mathbf{U}_1(t+1)^* = \mathbf{U}_1(t) + [\mathbf{v}(t+1)^* - \mathbf{U}_1(t)\mathbf{\psi}(t+1)^*]\mathbf{K}(t+1)^* \tag{5.27g}$$

$$\mathbf{P}(t+1)^* = \frac{1}{\mu^2}\left[\mathbf{P}(t) - \mathbf{P}(t)\mathbf{\psi}(t+1)^*\mathbf{K}(t+1)^*\right] \tag{5.27h}$$

$$\overline{\mathbf{H}}_{t+1}^* = \mu\overline{\mathbf{H}}_t + \overline{\mathbf{h}}(t+1)^*\left(\mathbf{y}_{t+1}^-\right)^T \tag{5.27i}$$

$$\mathbf{H}_{t+1}^* = \mu\mathbf{H}_t + \mathbf{y}_{t+1}^+\left(\mathbf{y}_{t+1}^-\right)^T \tag{5.27j}$$

Several numerical studies of time varying systems subjected to white noise excitation were carried out to test the performance of RSSI-COV. Results show that for the SSI algorithms, forgetting factor leads to severe problems in the tracking of modal parameters. Since forgetting factor is introducing different weightings to the data meanwhile Hankel covariance matrix is being formed, the ability of this step to cancel out the random components no longer works. Moving window approach with forgetting factor set to one is adopted in this work since it better matches the assumptions of SSI-COV. The use of a moving window implies the same procedure shown above has to be done twice to complete the subspace updating for each new incoming data: after adding the new incoming data (updating), the oldest data has to be subtracted from the moving window (downdating). The same formulas shown above can be applied for downdating by setting forgetting factor μ equals to one, the data vectors y^+_{t+1} and $y^{-\,T}_{t+1}$ should be replaced by the oldest data vector in the moving window, *i.e.*, if the moving window length is L, these become: y^+_{t-L+2i} and $y^{-}_{t-L+2i}{}^T$. Moreover, several sign changes in the last four formulas have to be introduced for downdating:

Downdating:

$$\overline{h}(t+1) = \mathbf{U}_1^T(t+1)^* y^+_{t-L+1} \quad , \quad w(t+1) = \overline{\mathbf{H}}^*_{t+1} y^-_{t-L+1} \tag{5.28a}$$

$$\mathbf{v}(t+1) = [\mathbf{H}^*_{t+1} y^-_{t-L+1} \quad y^+_{t-L+1}] \tag{5.28b}$$

$$\boldsymbol{\psi}(t+1) = [w(t+1) \quad \overline{h}(t+1)] \tag{5.28c}$$

$$\boldsymbol{\Lambda}(t+1) = \frac{1}{\mu^2} \begin{bmatrix} -\left(y^-_{t-L+1}\right)^T y^-_{t-L+1} & \mu \\ \mu & 0 \end{bmatrix} \tag{5.28d}$$

$$K(t+1) = \left[\mu^2 \Lambda(t+1) + \psi(t+1)^T P(t+1)^* \psi(t+1)\right]^{-1} \psi(t+1) P(t+1)^* \qquad (5.28e)$$

$$U_1(t+1) = U_1(t+1)^* - \left[v(t+1) - U_1(t+1)^* \psi(t+1)\right] K(t+1) \qquad (5.28f)$$

$$P(t+1) = \frac{1}{\mu^2}\left[P(t+1)^* + P(t+1)^* \psi(t+1) K(t+1)\right] \qquad (5.28g)$$

$$\overline{H}_{t+1} = \mu \overline{H}_{t+1}^* - \overline{h}(t+1)\left(y_{t-L+1}^-\right)^T \qquad (5.28h)$$

$$H_{t+1} = \mu H_{t+1}^* - y_{t-L+1}^+ \left(y_{t-L+1}^-\right)^T \qquad (5.28i)$$

Since the updating task is done for the time-varying column subspace $U_1(t)$ from the formulas shown above, the system information can be then extracted from $U_1(t)$ as previously discussed in section 2.3, for each time instant.

5.2 Recursive Singular Spectrum Analysis (rSSA)

To be able to apply SSA in online filtering of vibration measurements, an on-line version of the algorithm that describe the current signal structure at each time instant is required. As mentioned before in section 2.7, the first step is to assemble the measurement data in a Hankel data matrix of N data points $X(N)$ as shown in (2.47). Although a forgetting factor $0<\lambda<1$ can be applied to gives different weights to the data in terms of its age, through several simulation studies have been carried out, one conclude again that for subspace-based algorithms, the moving window approach should be adopted. The number of block rows is i' and is kept constant meanwhile a new data point is added as a new column appended to the moving window Hankel matrix:

$$\mathbf{X}(N+1) = \begin{bmatrix} y_{N\text{-}L\,'+1} & y_{N\text{-}L\,'+2} & \cdots & y_{N-i'+1} & y_{N-i'+2} \\ y_{N\text{-}L\,'+2} & y_{N\text{-}L\,'+3} & \cdots & y_{N-i'+2} & y_{N-i'+3} \\ \cdots & \cdots & \cdots & \cdots & \cdots \\ y_{N\text{-}L\,'+i'} & y_{N\text{-}L\,'+i'+1} & \cdots & y_{N} & y_{N+1} \end{bmatrix} \tag{5.29}$$

$$= \begin{bmatrix} X_{N-L'+i'} & X_{N-L'+i'+1} & \cdots & X_{N} \mid X_{N+1} \end{bmatrix} = \begin{bmatrix} \mathbf{X}(N) \mid X_{N+1} \end{bmatrix}$$

where $\mathbf{X}(N) \in \Re^{il \times K}$, l is the number of sensors, i' is the sliding window vector order, *i.e.*, number of block rows of the Hankel data matrix; L' is the length of moving window, $K'=L'-i'+1$ is the number of columns, with $K' > i'$. For convenience, the subscript notation for the sliding window vector is different than that used in off-line SSA, which becomes now $X_{N\text{-}L'+i'+j}$, $j =0,1,2, ..., K'$.

Similar to that shown in (5.24), by applying SVD to the Hankel data matrix $\mathbf{X}(N+1)$, the left singular vectors $\mathbf{U}$ can be computed via Eigen-Decomposition (ED) of the covariance of sliding window vectors:

$$\mathbf{C}_{SSA}(N+1) = \sum_{j=1}^{K} X_{N-L'+i'+j} X_{N-L'+i'+j}^{T} = \mathbf{X}(N)\mathbf{X}^{T}(N) + X_{N+1} X_{N+1}^{T} - X_{N-L'+i'} X_{N-L'+i'}^{T} \tag{5.30}$$

where $\mathbf{C}_{SSA}(N+1)$ is the covariance matrix of the sliding window vector $X_{N\text{-}L'+i'+j}$.

To make rSSA algorithm possible, only the left singular vectors corresponding to the non-zero singular values of $\mathbf{X}(N+1)$ will be used and updated as on-line filters: since they correspond to the column subspace which span the range of $\mathbf{X}(N+1)$, *i.e.*, any sliding window vector $X_{N\text{-}+L'+i'+j}$ can be expressed as a linear combination of the computed column subspace from $\mathbf{X}(N+1)$.

Since the eigenvectors of the covariance matrix $\mathbf{C}_{SSA}(N+1)$ correspond to the desired column subspace, this is actually a typical rank-two modification of the symmetric eigen-problem, *i.e.*, meanwhile a new data column is appended to the Hankel matrix (*i.e.*, rank-one modification), an old data column is subtracted (*i.e.*, rank-two

72

modification). The above-mentioned PAST algorithm is suitable to be implement to rSSA, because it is able to update in a recursive fashion the dominant eigenvectors of the signal covariance $\mathbf{C}_{SSA}(N+1)$, *i.e.*, the subspace of $\mathbf{X}(N+1)$.

Adaptation of PAST to rSSA

From (5.8), the random vector $z(k)$ can be substituted by the sliding window vector X_k:

$$V\left[\mathbf{W}\left(N+1\right)\right] = \sum_{k=N-L'+i'}^{N+1}\left\|X_k - \mathbf{W}\left(N+1\right)\mathbf{W}^H\left(N+1\right)X_k\right\|^2 \tag{5.31}$$

By introducing the same approximation:

$$\overline{h}'(k) = \mathbf{W}^H(k-1)X_k \tag{5.32}$$

the original cost function is converted into a quadratic criterion:

$$\overline{V}\left[\mathbf{W}\left(N+1\right)\right] = \sum_{k=N-L'+i'}^{N+1}\left\|X_k - \mathbf{W}\left(N+1\right)\overline{h}'(k)\right\|^2 \tag{5.33}$$

This became a typical optimization function in Least Square problems which can be minimized by:

$$\mathbf{W}\left(N+1\right) = \mathbf{U}_1'\left(N+1\right) = \mathbf{C}_{SSA,X\overline{h}'}\left(N+1\right)\mathbf{C}_{SSA,\overline{h}'}^{-1}\left(N+1\right) \tag{5.34}$$

where $\mathbf{C}_{SSA,X\overline{h}'}$ is the covariance matrix formed by the sliding window vector X_k and $\overline{h}'(k)$, and $\mathbf{C}_{SSA,\overline{h}'}$ is the covariance matrix formed by $\overline{h}'(k)$ and $\overline{h}'(k)^T$:

$$\mathbf{C}_{SSA,X\overline{h}'}(N+1) = \mathbf{C}_{SSA,X\overline{h}'}(N) + X_{N+1}\overline{h}_{N+1}'^T - X_{N-L'+i'}\overline{h}_{N-L'+i'}'^T \tag{5.35}$$

$$\mathbf{C}_{SSA,\overline{h}'}(N+1) = \mathbf{C}_{SSA,\overline{h}'}(N) + \overline{h}_{N+1}'\overline{h}_{N+1}'^T - \overline{h}_{N-L'+i'}'\overline{h}_{N-L'+i'}'^T \tag{5.36}$$

When the matrix inversion lemma is applied to (5.34), the well-known RLS algorithm can be easily derived, which is shown in the chart below.

---

1. From an initial SVD the recursive algorithm can be initialized with $\mathbf{U}_1'(N)$, later $\mathbf{C}_{SSA,\bar{h}'}(N)$ and $\mathbf{P}'(N)$ can be computed:

$$\mathbf{C}_{SSA,\bar{h}'}(N) = \left[\mathbf{U}_1'^{T}(N)\mathbf{X}(N)\right]\left[\mathbf{U}_1'^{T}(N)\mathbf{X}(N)\right]^{T} \qquad (5.37a)$$

$$\mathbf{P}'(N) = [\mathbf{C}_{SSA,\bar{h}'}(N)]^{-1} \qquad (5.37b)$$

---

2. Given a new incoming sliding window vector X_{N+1}, $\mathbf{U}_1'^{T}(N+1)$, $\mathbf{P}'(N+1)$ and $\bar{h}'(N+1)$ can be updated using the following algorithm:

Updating:

$$\bar{h}'(N+1)^{*} = \mathbf{U}_1'^{T}(N)X_{N+1} \qquad (5.37c)$$

$$\mathbf{K}'(N+1)^{*} = \frac{\bar{h}'(N+1)^{*T}\mathbf{P}'(N)}{[\mu + \bar{h}'(N+1)^{*T}\mathbf{P}'(N)\bar{h}'(N+1)^{*}]} \qquad (5.37d)$$

$$\mathbf{U}_1'(N+1)^{*} = \mathbf{U}_1'(N) + \left[X_{N+1} - \mathbf{U}_1'(N)\bar{h}'(N+1)^{*}\right]\mathbf{K}'(N+1)^{*} \qquad (5.37e)$$

$$\mathbf{P}'(N+1)^{*} = \left(\frac{1}{\mu}\right)\left[\mathbf{P}'(N) - \mathbf{P}'(N)\bar{h}'(N+1)^{*}\mathbf{K}'(N+1)^{*}\right] \qquad (5.37f)$$

Downdating:

$$\bar{h}'(N+1) = \mathbf{U}_1'^{T}(N+1)^{*}X_{N-L'+i'} \qquad (5.38a)$$

$$\mathbf{K}'(N+1) = \frac{\bar{h}'(N+1)^{T}\mathbf{P}'(N+1)^{*}}{[\mu + \bar{h}'(N+1)^{T}\mathbf{P}'(N+1)^{*}\bar{h}'(N+1)]} \qquad (5.38b)$$

$$\mathbf{U}_1'(N+1) = \mathbf{U}_1'(N+1)^* - [\boldsymbol{X}_{N-L'+i'} - \mathbf{U}_1'(N+1)^* \overline{\boldsymbol{h}}'(N+1)]\mathbf{K}'(N+1) \qquad (5.38c)$$

$$\mathbf{P}'(N+1) = \left(\frac{1}{\mu}\right)\left[\mathbf{P}'(N+1)^* - \mathbf{P}'(N+1)^* \overline{\boldsymbol{h}}'(N+1)\mathbf{K}'(N+1)\right] \qquad (5.38d)$$

The recursive SSA is different than the off-line SSA in the reconstruction step. The recursive SSA is applied here as a preprocessing tool to filter out the undesired measurement noise keeping the system related information, thus, the same "orthogonal projection" concept used to derive PAST can be directly applied for rSSA. After the column subspace $\mathbf{U}_1'(N+1)$ is updated, the "filtered" or "projected" sliding window vector $\tilde{X}_{N+1}$ can be computed by the orthogonal projection:

$$\tilde{X}_{N+1} = \mathbf{U}_1'(N+1)\mathbf{U}_1'(N+1)^T \boldsymbol{X}_{N+1} \qquad (5.39)$$

where $\tilde{X}_{N+1}$ is the reconstructed data vector.

Hence, for each new incoming data, a new sliding vector column X_{N+1} is appended, the column subspace is updated to $\mathbf{U}_1'(N+1)$, and the reconstructed data vector $\tilde{X}_{N+1}$ can be obtained by procedure shown above. Finally the reconstructed data vector $\tilde{X}_{N+1}$ is placed in the corresponding location of the reconstructed Hankel data matrix $\tilde{\mathbf{X}}(N+1)$, then, elements of the same time instant (in the anti-diagonal direction) can be averaged to reconstruct the signal:

$$\tilde{\mathbf{X}}(N+i'-1) = \begin{bmatrix} \tilde{\boldsymbol{y}}_{N-L'+1} & \tilde{\boldsymbol{y}}_{N-L'+2} & \cdots & \tilde{\boldsymbol{y}}_{N-i'+1} & \tilde{\boldsymbol{y}}_{N-i'+2} & \tilde{\boldsymbol{y}}_{N-i'+3} & \cdots & \tilde{\boldsymbol{y}}_N \\ \tilde{\boldsymbol{y}}_{N-L'+2} & \tilde{\boldsymbol{y}}_{N-L'+3} & \cdots & \tilde{\boldsymbol{y}}_{N-i'+2} & \tilde{\boldsymbol{y}}_{N-i'+3} & \tilde{\boldsymbol{y}}_{N-i'+4} & \cdots & \tilde{\boldsymbol{y}}_{N+1} \\ \vdots & \vdots & & \vdots & \vdots & \vdots & & \vdots \\ \tilde{\boldsymbol{y}}_{N-L'+i'} & \tilde{\boldsymbol{y}}_{N-L'+i'+1} & \cdots & \tilde{\boldsymbol{y}}_N & \tilde{\boldsymbol{y}}_{N+1} & \tilde{\boldsymbol{y}}_{N+2} & \cdots & \tilde{\boldsymbol{y}}_{N+i'-1} \end{bmatrix} \qquad (5.40)$$

It is important to emphasize here that the rSSA algorithm explained here may be somehow different than the algorithm used in SSA, more precisely, this is a combined

approach of both SSA and data compression based on the Karhunen-Loéve (KL)
transformation [56], where a sequence of data vectors is coded by their principal
components.

Chapter 6
Simulation study of RSSI-COV and rSSA-SSI-COV

To validate the adaptation of EIV-PAST algorithm to RSSI-COV, and the proposed rSSA solved by PAST, together with its applicability and stability in the on-line tracking of system modal parameters, through a moving window and recursive approach, simulation study was carried out firstly.

Consider a simulated linear 6-DOF system consists in a lumped mass model and a shear building type stiffness matrix, which has the following modal frequencies and damping ratios in its original state:

The system natural frequencies are:

f = [0.9972 , 2.9254 , 4.6600 , 6.0905 , 7.1353 , 7.7556] Hz

Rayleigh damping was assumed for the derivation of damping matrix, the assumed damping ratio for each mode are:

ξ = [0.03 , 0.03 , 0.01 , 0.01 , 0.02, 0.02],

Response is generated using discrete time deterministic state-space model having a spatially white noise as the input, outputs are measured at each DOF. Measurement noise can be added after the system response is obtained. The sampling rate is 200 Hz and the total generated data length is 20000 points, which equals to 100 sec.

6.1 Implementation of the RSSI-COV and rSSA-SSI-COV algorithm

In conducting RSSI method, considering the recursive SVD-updating task carried out by EIV-PAST algorithm updates only the dominant singular vectors, a procedure is proposed to avoid the accumulation of error during the subspace computation:

1. Select a length for the statistic moving window $WL_{statistic}$ which samples the identified modal frequencies along the time axis.

2. Calculate the mean frequency over data sampled by the moving window for each modal frequency.

3. Calculate the Euclidean norm of the standard deviation of each modal frequency, *i.e.*, take the square root over the sum of squares for the computed standard deviations over the moving window of each modal frequency.

4. Repeat 2 and 3 by moving forward the statistic window over a specific frequency data points ($d_{statistic}$).

5. Compare the Euclidean norm of displacement "k" and "$k+1$", and calculate their percentage of difference. If the percentage between the two segments is greater than the specific criteria (*e.g.* 50%), the traditional SVD will be computed at that given time instant and serves as a restart for EIV-PAST.

6. Continues the recursive computation of modal frequencies, the statistic window moves a step forward until the displacement length of the statistic moving window $d_{statistic}$ has been reached, and repeat the steps 2, 3, 4, 5.

The above procedure is summarized in the flow chart shown in **Figure 6-1**.

6.2　Simulation study 1: time invariant 6-DOF system

The simulation study starts with the case where the system is time-invariant. Thus, the most basic requirement to be meet is the sufficient stability to track the modal parameters in a recursive manner, when these latter have not any change.

Noise free

Figure 6-2 shows the recursive tracking results for the response generated by the 6-DOF system subjected to a spatially white noise input excitation, without adding any kind of noise. From now on, the same number of block rows i will be used for block columns, *i.e.*, a square Hankel Covariance matrix. Since this is a simulation example with known DOF, naturally the system order is defined to be 12. Comparing **a)** and **b)**, one can note that by increasing the moving window length L used to form the Hankel Covariance matrix, the stability is better. This matches the assumption for Covariance for which the data length must be theoretically tending to the infinity.

Figure 6-3 shows the result for the tracking of damping ratio. From **a)**, the use of a short moving window (1500 points equals to 7.5 sec) leads to a very unstable damping ratio and wrong trace for the 1st mode. By increasing the window length to 3000 points, although the deviation from correct answers is still large as it always occurs in damping ratio estimates due to its high sensitivity to any perturbation, at least, stable results were achieved. The two largest damping ratios correspond to the 1st and 2nd mode.

Adding noise correlated with output (SSI assumption violated)

Consider the addition of the input acceleration to the measurement as a noise correlated with output, which occurs in acceleration measurements as that discussed in section

2.2.3, the purpose is to test the robustnss of RSSI-COV when its assumptions were violated. In this case, the moving window length is fixed to 2000 points, system order is 12. Frequency tracking results is shown in **Figure 6-4**. The effect of increase number of block rows i is shown by comparing **a)** and **b)**. The 1st mode shown in **a)** was perturbed by noise; the higher the number of block rows i, the better the noise separation, consequently a more stable tracking result was obtained in **b)**.

The recursive tracking of damping ratio is shown in **Figure 6-5** for the same case when the added noise violate the assumptions. If the number of block rows i is insufficient to separate noise from the system information, negative damping appears due to noise perturbation as shown in **Figure 6-5 a)**. Although negative damping was corrected by increasing the number of block rows in **Figure 6-5 b)**, the trace of damping is still unstable and several significant changes occurs in damping tracking meanwhile there is not any variation in the correct damping ratio answer. Given this situation, damping ratio cannot be used as an reliable index of system change or damage.

6.3 Simulation study 2: time varying 6-DOF system with sudden stiffness reduction.

To simulated drastic system change scenarios, sudden stiffness reduction and damping ratio changes were introduced in the 6-DOF system. The loss of stiffness was introduced in the 1st DOF of the simulated shear-building type system, the resulting changes in modal frequency are presented in **Table 6-1**. Comparing with the precision level of SSI shown in section 3.1, the resulting change in the 1st modal frequency become significant (more than 0.1 Hz for the 1st mode) until the stiffness reduction in 1st DOF is more than 50%.

Noise free

Firstly, the RSSI-COV algorithm is applied to trace these sudden drops in modal frequencies without adding noise to the simulated measurement. Result for modal frequencies is shown in **Figure 6-6**. The number of blocks i is 70, system order is 12; the statistic window length $WL_{statistic}$ is 400 frequency points, displacing by every 100 points (as explained in **Figure 6-1**). The restart criterion is 50% of difference between this and the previous standard deviation Euclidean norm. Similar to the results obtained in 6.2, the tracking stability was enhanced by increasing the moving window length. However, as that shown in **Figure 6-7 b)** and **Figure 6-8 b)**, variations in damping ratio cannot be traced correctly, no clear tendency can be observed even increasing the moving window length or system order. Since RSSI algorithm only shows good frequency tracking capability, hereafter the results for damping ratio will be omitted.

Between 7000 and 9000 data points, the 1st mode damping ratio shown in **Figure 6-7 b)** has increased to an abnormal level, which indicates existence of problems in the identification. Until the system order is increased to 16, 2 pairs of SV more than that required theoretically, as that shown in **Figure 6-8 a)** for frequency and **b)** for damping ratio, a more reasonable range for the 1st mode damping ratio is reached (the negative damping ratio corresponds to spurious poles) although it is not accurate at all.

Based on the previous experience adquired in off-line system identification, since the system in no longer time-invariant, more orthogonal components is required to span the system subspace, therefore, if insufficient system order is defined, information loss in the recovery of system matrix **A** will lead to an unstable tracking on the 1st modal frequency or damping ratio. The use of more system order, however, introduces spurious poles in the time-frequency plot.

Figure 6-9 shows the six mode shape identification results for several selected points, which are obtained with a system order of 12. Except mode 1, all the identified mode shapes are almost identical to the correct answer. This phenomena is similar to that we find in modal frequency and damping ratio tracking, the 1st mode seems to be the most affected by any violating any assumption of SSI, because we are trying to use a recursive linear identification algorithm, with a certain moving window length, to identify time-varying systems.

Adding noise correlated with output (SSI assumption violated)

The combine effect of system with sudden changes in frequency and the addition of noise correlated with output is presented in **Figure 6-10**, both violating SSI assumptions. The moving window length is 5000 points for both **a)** and **b)**. With a system order of 12 and 150 block rows in **a)**, bad tracking results were obtained and the 1st mode almost disappeared. The combination of noise and time-varying signal increased the required column subspace to describe the system information, although the system order is 12 theoretically as that shown in **Figure 6-10 b)**: by increasing the system order to 18, the 1st modal frequency can be traced correctly, but again, spurious poles appears in the time-frequency plot.

6.4 Simulation study 3: time-varying 6-DOF system with gradual stiffness reduction

A gradual reduction in the 1st DOF stiffness from point 4001 to point 16000 is introduced in the system matrix to simulate slow varying frequencies. There are totally 20000 points in the simulation example. The system natural frequencies and the corresponding damping ratios from 1 to 4000 points are:

$$f_{\text{initial}} = [0.9972 , 2.9254 , 4.6600 , 6.0905 , 7.1353 , 7.7556] \text{ Hz}$$

$$\xi_{\text{initial}} = [0.03 , 0.03 , 0.01 , 0.01 , 0.02, 0.02]$$

After reaching 16000 points the frequencies and damping ratios become finally:

$$f_{\text{final}} = [0.5380 , 2.2141 , 4.0478 , 5.6599 , 6.9051 , 7.6898] \text{ Hz}$$

$$\xi_{\text{final}} = [0.10 , 0.07 , 0.051 , 0.02 , 0.03, 0.05]$$

Between 4000 and 16000 data point, the natural frequencies and damping ratios are interpolated linearly based on the initial and final state of the modal frequency and damping ratio.

Noise free

Firstly the ability of RSSI-COV to trace slow time-varying frequencies is shown in **Figure 6-11**, **a)** for the case of using 2500 points for moving window and **b)** for 4000 points of moving window. For both cases the number of block rows i is 70, system order is defined as 12. The same as that defined in the previous section, the statistic window length $WL_{\text{statistic}}$ is 400 frequency points, displacing by every 100 points; the restart criterion is 50%. Again, the increase of the moving window length has enhanced the tracking stability. However, similar to that found previously, the 1$^{\text{st}}$ mode seems to be very sensitive and lost the stability in the final points. If the moving window length is increased to 5000 points as shown in **Figure 6-11 c)** keeping the system order as 12, certain stability problems still remains; however, similar to what is done in section 6.3, if the system order is increased to 18 keeping intact the remaining parameters, stable results can be achieved for the final points.

In fact, this outcome has a similar sense than that obtained in the simulation study

of section 3.3, where off-line identification task is carried out for two closely-spaced

frequencies blended with time-varying frequencies: larger the number of block rows i,

the time-varying frequencies will be spanned by more orthogonal vectors after being

decomposed by SVD, thus, higher system order is required to prevent the loss of certain

mode information due to the order consumption in covering the most time-varying

component. The fact is ilustrated in **Figure 6-12**, where the number of block rows has

been incremented from 100 to 130, moving window length fixed to 5000 points, and

different system orders is considered.

Adding noise correlated with output (SSI assumption violated)

Consider the addition of a noise correlated with output, to test the robustnss of

RSSI-COV in the case of slow-varying systems when its assumption were violated.

Firstly, two different number of block rows i is compared, and system order is kept as

12. Frequency tracking results is shown in **Figure 6-13**. The effect of the assumption

violation impacts mostly in the recursive identification of the 1st mode; again, due to the

time-varying characteristic of the system, higher system order is needed for larger

number of block rows i, otherwise, the 1st mode information is not covered. This

explains why the outcome in **Figure 6-13 a)** using fewer block rows is better than **b)**.

Consider the use of the Recursive SSA-SSI-COV algorithm, there are two sets of

parameters to be determined, one for recursive SSA (rSSA): moving window length L'

and number of block rows i'; and another for RSSI-COV: L and i. Regarding to the

selection of number of block rows i and i', 100 block rows is a good choice from

previous simulation experiences, this is actually a tradeoff between computation effort

and accuracy. 5000 points is selected for the moving window length of RSSI-COV,

because the larger the window length, more stable the result. To investigate the

influence of the moving window length L' and the number of principal components to be selected in rSSA step, nine different combinations for model parameters are considered. For these cases, firstly the singular spectrum in rSSA step is shown in **Figure 6-14**. To determine the best choice of number of SV in rSSA step, implementation algorithm shown in section **4.1.3.1** can be applied. The singular spectrum in RSSI-COV step is shown in **Figure 6-15**; they are computed from the first 5000 data points which corresponds to the moving window length of RSSI-COV.

From the 9 combinations shown in **Figure 6-15**, the best choice of model parameters for rSSA seems to be a window length L' of 1000 points and 20 SV, for the reason that this choice leads to the best separation of the 6 pairs of singular values (corresponding to the system order). This can be verified by selecting various cases for comparison as shown in **Table 6-2**, the frequency tracking results is shown in **Figure 6-16**.

Although the 1st modal frequency were miss for the last points, in **Figure 6-16 d)**, if the system order is increased to 16, the final segment stabilizes as shown in **Figure 6-17 a)**. This is due to the time-varying property of the signal and the reason explained above. However, if only RSSI-COV is used, even increasing the system order to 30, this final segment is still a little bit unstable. This is shown in **Figure 6-17 b)**.

After the slow time-varying simulation example is studied, several conclusions about the effect of time-varying system in the model parameters are obtained:

✓ The required number of orthogonal components (*i.e.*, system order to be chosen) to span the system subspace is more than the actual system order, when it comes to the signal processing of time-varying systems.

✓ Although a better noise elimination can be achieved using larger number of block columns i, however, the required number of orthogonal components (*i.e.*, system order to be chosen) to span the system subspace is also greater. If the selected system order is lower than the required, spurious modes appear instead of the correct frequency.

✓ The larger the moving window length L in RSSI-COV step, more stable the tracking results. On the contrary, the shorter is the moving window length L' in rSSA, better the filtering result and, thus, the identification quality.

Chapter 7

Application of recursive SSI algorithms in damage detection and early warning

The RSSI-COV and rSSA-SSI-COV algorithms has been validated through numerical examples, sensitivity study of subspace model parameters and their selection criteria were also conducted in chapter 6. In the following, these two algorithms will be applied to trace modal parameters for several cases: firstly the shaking table test of a 3-story steel structure with instantaneous stiffness reduction, followed by the shaking table experiment of a 2-bay reinforced-concrete frame, both subjected to earthquake ground motions, and finally to the bridge scouring experiment.

7.1 Application: shaking table test of a 3-story steel structure with instantaneous stiffness reduction

A 3-story full-scale steel frame is designed and constructed at the National Center for Research on Earthquake Engineering (NCREE) in Taipei, Taiwan, in 2007/01/17. As shown in **Figure 7-1**, the structure consists of a single bay with a 3m by 2m floor area and 3m tall stories. The structure is constructed using H150x150x7x10 steel I-beam elements with each beam-column joint designed as a bolted connection. To apply additional dead load upon each floor, concrete blocks are fastened to the floor diaphragms until the total mass of each floor is precisely 6,000 kg. The entire structure is constructed upon a large-scale shaking table capable of applying base excitation to the structure. In order to change the stiffness of the story abruptly, an extra stiffener (brace) is installed in the first story as shown in **Figure 7-1,** a lock-up system is designed as a connection between the stiffener and the first floor. The steel rod in the

lock-up system can be released at any time instant to simulate the abrupt degradation of the first story inter-story stiffness.

To measure the output data of the structure, a total of 12 accelerometers are installed, with 4 accelerometers on the top of each floor, and there is a LVDT displacement sensor installed on the lock-up system to detect the release time. Several test cases listed in **Table 7-1** were analyzed in this section by applying RSSI-COV and rSSA-SSI-COV.

7.1.1 White noise base excitation

Firstly off-line identification is carried out to identify the modal parameters when the steel frame is subjected to a white noise base excitation, data of the 12 accelerometers are used simultaneously. Either for the case with added brace (AB) or the case without brace (NB), 15000 points (75 sec) were used to form Toeplitz matrix; the system order is determined to be 20 from the singular spectrum shown in **Figure 7-2 a)**, for the case with added brace, and 26 for the case with brace removed as shown in **b)**. From both singular spectrums, although there are 3 pairs of singular values far from the others, which corresponding to the three dominant translational modes in X direction, the remaining modes need to be identified and serve as the base information for recursive tracking of modal frequencies, thus, not only X-direction translational modes will be excited by the earthquake ground motions. The stabilization diagrams for both cases AB and NB are shown in **Figure 7-3**, only the stable poles are considered and their corresponding modal frequencies and damping ratios are shown in **Table 7-2**. There are 6 stable modes for the case AB and 10 for case NB, their respective mode shapes are shown in **Figure 7-4**, moreover, four additional modes were identified from the NB case as shown in **Figure 7-5**, mostly coupled modes. The mode shapes are

normalized such that the 3rd floor translation amplitude in X-direction is 0.5.

RSSI-COV is applied to trace the modal frequencies for both AB and NB case excited by white noise. Data of all 12 sensors are used simultaneously, the moving window length is 10 seconds (2000 points), a block Hankel Covariance matrix with 100 rows is adopted. For the AB case, results for two different system orders, 6 and 16 respectively, are presented in **Figure 7-6 a)** and **b)**; **Figure 7-6 c)** and **d)** show the outcome for the NB case, for system orders of 6 and 20 respectively. The dotted lines are the frequencies previously identified by off-line method. With a system order of 6, the three translational modes in X direction can be traced for both cases, by increasing the system order, those slightly and not continuously excited modes appear in some time periods, however, a lot of spurious modes also appear in the diagram.

Through the application of RSSI-COV, result shown in the time-frequency plot can be compared with the outcome of off-line identification. Although modes like 1st torsion mode (2.2966 Hz) appears only for a few 10 seconds approximately, as that shown in **Figure 7-6 b)**, it appears as a stable diagram in the use of SSI-COV, the same with the 2nd torsion mode and coupled modes identified in **Figure 7-6 d)**.

7.1.2 El Centro 100 gal

Consider the application of RSSI-COV algorithm to track recursively modal frequencies when the structure is no longer excited by a white noise but by an earthquake. Although the white noise assumption is violated, it can be overcome by increasing the moving window length and the block row number as proved before, besides, is it known that the structure vibrates under its own natural frequency when it is subjected to earthquake ground motion.

Firstly, the recursive identification is applied to the cases when there is no sudden release of the stiffener but the frame is subjected to El Centro earthquake excitation. The same window length of 2000 points and 100 block rows are used for both cases with brace and without brace. Two different choices of system order are considered: firstly, 3 pairs of singular values is selected and later, this is increased to take into account more modes. The outcome is shown in **Figure 7-7**.

With the system order defined as 6, only the first three dominant modes can be extracted. From the plot shown in **Figure 7-7 a)**, the 3rd X-translational modal frequency (5.2736 Hz) has shifted to the 2nd torsion mode (7.3282 Hz), the reason is that the signal power of the 3rd X-translational mode is lower than that of the 2nd torsion mode as that shown in the spectrogram of **Figure 7-8 a)**, constructed with Short-Time Fourier Transform (STFT). Once the system order is increased to 14, both the three translational and torsion modes are identified, however, spurious modes also appear in the diagram. On the other hand, three X-direction translational modes dominates in NB case throughout the time history, this is also verified by the spectrogram shown in **Figure 7-8 b)**. The torsion modes are not well excited in this NB case as that shown in **Figure 7-7 d)**.

Consider now the cases when the brace is suddenly removed at 14.75 and 29.41 seconds. As the brace is removed at 14.75 seconds, the moving window length should be less than 2000 points (10 seconds) to leave a sufficient time length before the release of stiffener. Although a larger moving window length can enhance the tracking stability, it also implies that the algorithm will takes more time to detect system change. To make possible a faster detection of the instantaneous stiffness reduction, a moving window length of 1000 points (5 seconds) is adopted. The number of block rows is 100.

Figure 7-9 shows the result for both RSSI-COV and rSSA-SSI-COV. The moving window length for rSSA is set to be 500 points (2.5 s) with the same number of block rows than RSSI-COV, and 6 principal components are extracted using rSSA. With a system order of 6, the RSSI-COV result for the brace removed at 14.75 seconds is shown in **Figure 7-9 a)**, the change in the three translational modal frequencies in X direction was correctly traced, the unique drawback is that, even using a quite short moving window length, the sudden drop in frequency is delayed about 3 to 4 seconds to be reflected completely in the modal frequency trace. Moreover, the 1st modal frequency lost its stability after 40 seconds. From the spectrogram shown in **Figure 7-10 a)**, the amplitude of the 1st translational mode was decreased after about 39 seconds and hence the 1st torsion mode takes place instead. The application of rSSA algorithm before RSSI-COV has enhanced the tracking stability as shown in **Figure 7-9 b)**, the orthogonal projection performed in rSSA as a signal filter helps to RSSI-COV to extract signal component consistent with those modes has been traced.

From **Figure 7-9 c)** and **d)**, when a higher system order is used, all excited modes are also revealed. There is a high frequency mode (about 16 Hz) appearing just after 14 seconds, which is the stiffener mode comparing with the off-line identification result. The sudden release of the stiffener changes not also the translational modal frequencies in X direction, but torsion modes and coupling modes are also excited by this event although their contribution is much smaller than the dominant modes. This can be understood by comparing the singular spectrum between different time instants as shown in **Figure 7-11**: **a)** at the beginning there are only three modes clearly excited; **b)** once the stiffener is release, not only translational modes but torsion modes and coupling modes appear. It is also interesting to observe what is occurring in the segment from 35 to 45 seconds in **Figure 7-9 d)**, the 3rd mode cannot be traced even with a

higher system order because it is no longer excited as that shown in **Figure 7-10 b)**. This is very clear by comparing **Figure 7-11 c)** with **a)**, there is only one pair above 10^2 in **c)**, meanwhile there are three pairs in **a)** above the quantity. On the other side, **Figure 7-9 e)** and **f)** shows a comparison between RSSI-COV and rSSA-SSI-COV. Although rSSA was able to enhance the tracking stability, the coupled mode at 8.1 Hz appears instead of the 3rd X-translational mode after approximately 40 seconds.

The three translational mode shapes identified from the case where the brace is removed at 14.75 seconds are shown in **Figure 7-12**. These mode shapes are extracted from data point of 10 and 30 seconds, the first with brace and the second without brace. For the another case where the brace is removed at 29.41 seconds, examples of mode shapes are taken from 40 seconds and the comparison with their corresponding mode shapes obtained by offline identification are shown in **Figure 7-13**. The 1st translational mode in X-direction is the same as that identified previously by offline analysis. The coupled X-Y translational mode has some phase difference, also the amplitude in Y-direction is also larger comparing with the offline reference. Torsion modes are similar with the reference, but the 3rd Y-translational mode (8.0540 Hz) obtained by offline identification is now coupled with the 2nd torsion mode, and the frequency is slightly higher: 8.2017 Hz.

As conclusions obtained from El Centro earthquake, although the RSSI-COV is able to track modal parameters and the pre-processing with rSSA can enhance the tracking stability, there are several challenges to face in use of recursive subspace algorithms. Besides the time delay to show up the system change due to the use of a moving window, it is hard to determine the system order, thus, there is an uncertainty about the total number of modes can be excited over time. To leave nothing out, usually

the system order is defined in a way that even for modes with insignificant contribution can be considered, such as coupled modes. The fact leads to several consequences, first is that, as that shown in this case of El Centro earthquake, some modes are excited in some time periods and disappears in another periods, but once the mode disappears the trace goes to another mode or is just converted into a spurious mode, making quite confusing the time-frequency plot.

The second is, simpler models are required for online damage detection. As in this case of the 3-story steel frame with instantaneous stiffness reduction in X-direction, usually the sensors will be placed only in X-direction since the frame is symmetric and its structural dynamics are dominated by the X-direction translational modes. However, when the coupled modes engaged in due to the selection of a higher system order, it is possible to identify more than one modal frequencies for each mode as that occurs in **Figure 7-9 d**), *i.e.*, coupling modes also appear. Since there are only sensors in X-direction, there is no way to distinguish coupled modes from true translational modes.

7.1.3 TCU082 100 gal

Consider another case where the same steel frame is subjected to Chi-Chi earthquake ground motion, data recorded from station TCU082 (N–S direction with a duration of 98 s) were adopted as the input excitation. Since the effects of a three dimensional structure in the recursive identification work has been discussed, the variation in X-translational modal frequencies will be the focus of this example, and only the six accelerometers in X-direction will be used.

For the first case where the stiffener is released at 38.15 seconds, system order is

defined as 6 to trace the first three dominant modes, **Figure 7-14 a)** shows the result for a moving window length of 2000 points (10 seconds) and **b)** shows the improved result when the window length is increased to 3000 points. For the second case where the stiffener is released at 52.07 seconds, the outcome is shown in **Figure 7-15**, **a)** for using RSSI-COV alone with the same system order, window length is 3000 points, 100 block rows, and **b)** for the improved result using rSSA-SSI-COV. Parameters for rSSA are: window length L'= 500 points, i'= 100 rows, subspace order= 14, and the window length for RSSI-COV is L= 2000 points, system order 8, rows i= 100. System order has to be increased to 8 to reveal all information regarding the translational modes in X-direction, and consequently some spurious modes and torsion modes appear.

7.2 Application 2: shaking table test of a 1-story 2-bay RC frame

A 1-story 2-bay RC frame was designed following the ACI 318-05 design code. Dimensions and details of the RC frame can be found in **Figure 7-16.** The instrumentation of the RC frame can be accessed from the **Figure 7-17**. A total of six specimens were constructed with the same design details (denotes as RCF1, RCF2…, RCF6). This RC frame has been previously studied in [31, 32] by signal processing and nonlinear identification approaches to extract the damage feature. In [51] the RC frame is also used to trace the stiffness degradation of equivalent linear time-varying structure and the non-linear hysteretic parameters with stiffness and strength degradations.

The RC frame specimen denoted "RCF6" is used to prove the frequency tracking capability of RSSI-COV. A series of shaking table tests with increasing intensity of input excitation were applied on the specimen RCF6 to create different damage levels. Chi-Chi earthquake ground motion data from station TCU082 (N–S direction with a

duration of 98 s) was adopted as an input excitation to this frame. Based on the recorded maximum inter-story drift, it is shown that a different level of damaged was induced in each specimen. White noise excitation (with a low level peak amplitude defined as 30 gal) was also conducted in between each strong excitation to simulate the normal ambient vibration measurements before and after each earthquake. Block diagram shown in **Figure 7-18** summarizes the excitation sequence of the test specimen on the shaking table, and the corresponding peak amplitude. A total of 97.4 s of acceleration response data were collected from the ambient vibration excitation, with a sampling rate of 200 Hz. The 800 gal* test data was not recorded.

Since this is a 1-story frame excited horizontally and in the same plane of the frame, only three accelerometers: A1, A4 and A7 are used for identification. The frame can be simplified to be a SDOF system, for which is assumed that an equivalent linear time-varying system is able to describe the lateral strength degradation. RSSI-COV is the algorithm used to trace the modal frequencies.

The model parameter of RSSI-COV is firstly chosen as follows: the moving window length is 5000 points (equivalent to 25 seconds) for more stability, number of blocks i is 200, the system order is determined to be 2 because a SDOF equivalent time-varying linear system is assumed. The statistic window length $WL_{statistic}$ is 400 frequency points, displacing by every 100 points (as explained in **Figure 6-1**). The restart criterion is 50% of difference between this and the previous Euclidean norm of standard deviation. The time-frequency plot for the series of earthquake TCU082 scaled to different PGA is shown in **Figure 7-19**, recursive identification of the interspersed 30 gal white noise excitation is also shown in **Figure 7-20**.

In the first case, the frame is subjected to TCU082 earthquake with a PGA of 600

gal. Before 30 seconds where the excitation is very small, RSSI-COV cannot identify correctly the undamaged state frequency, which is about 5.7 Hz as that determined by WN1. The first damage point occurs immediately after the 30 seconds, as that indicated in [32], and the identified frequency dropped to 3.9 Hz. The second point correspond to 37.66 seconds where the peak acceleration occurs. Due to the use of a moving window of 25 seconds, at this second damage the decay in frequency starts at 38.27 seconds with 3.62 Hz and ends at 40.82 seconds with 3.08 Hz. Although a larger moving window allows a more stable tracking capability, it takes more time to reflect the system change. After the shaking of this 600 gal earthquake, the lowest frequency reached during the shaking is about 2.9 Hz, which is also consistent with that identified from 30 gal white noise excitation (WN2), which is 3.0 Hz.

The lowest frequency reached at the second test of 1000 gal TCU082 is 2.27 Hz, however, the frequency determined by WN4 is about 2.6 Hz. This may be explained by the fact that, after 1000 gal earthquake, the concrete has been severely cracked, and the lateral stiffness is highly reduced; however, at the final 10 seconds of this test where the excitation level is very small (it is about 0.02 g, *i.e.*, 20 gal), the frequency increases to 2.4 Hz in the final segment of 1000 gal earthquake. The same phenomenon is observed for all cases: 3.6 Hz for the 1st case with peak amplitude of 600 gal, and for the remaining cases the frequency oscillates between 2.2 to 2.5 Hz in the final segment. These results are actually quite similar to that identified from white noise excitation (30 gal) which ranges between 2.4 and 2.6 Hz, from WN3 to WN8.

The discrepancy in the identified frequencies between strong motion and ambient vibrations can be explained by the fact that, the strength degradation of RC frame is mainly due to the concrete crack. However, the open-off of the cracks does not occur if

the excitation level is small, *i.e.*, the lateral stiffness is much larger when the vibration is small, therefore, higher natural frequency will be reached for the RC frame under ambient excitations.

Unlike the modal frequencies identified from the 3-story steel frame in section 7.1 which is almost totally constant, the natural frequencies identified from 30 gal white noise excitation for the RC frame shown in **Figure 7-20**, oscillates between 5.66 Hz and 5.78 Hz even in the undamaged state, *i.e.*, the RC frame does not behave linearly and the signal is slightly time-varying.

From experience gathered in the simulation example of section 6, more orthogonal components than the theoretical system order is required to span the information of a time-varying system, *i.e.*, the system order should be defined larger than 2. To avoid excessive spurious poles in the plot, a good choice would be the first 4 singular values from the singular spectrum shown in **Figure 7-21**, because they represent the 99.6% of total singular value powers. The frequency trace for RCF6 specimen is summarized in **Figure 7-22**. The moving window length is reduced to 3000 points (equivalent to 15 seconds), and consequently the trace is not as stable as it is when the window length is 5000 points, but one can expect that it can reflect the system change more quickly. The number of blocks rows *i* is 100.

The use of a system order of 4 has covered the segment before 30 seconds which is incorrrect when a system order of 2 is used. As that shown in **Figure 7-23**, signal before 24 seconds are probably a mix of measurement noise and structural response to ambient vibrations, but it were cut by the resolution of the measurements. Although the natural frequency was able to be identified from data of the first 24 seconds, this may not be reliable considering the vibration level is less than 1 gal and the resolution of the

measurement. From **Figure 7-22 a)**, the identified frequency corresponding to the undamaged state oscillates between 5.5 and 5.75 Hz (between 28 and 29.6 seconds), which is quite consistent with that identified from WN1. After the first damage point, the identified behavior is the same as that described previously.

Novelty Index

The Novelty Index (NI) is calculated by using the first set of the test data (from WN1 excitation) as a reference to develop the system matrix (**A**, **C**) and noise covariances (**Q**, **R**), following the procedure described in section 2.4. Based on the developed system matrix, the Kalman filter estimation was used to predict the responses for other test cases based on the procedure shown in **Appendix C**.

The Kalman filter prediction time history at the undamaged state (WN1) is shown in **Figure 7-24**. Three sensors: 1, 4, 7 are used and a system order of 8 is defined. Although the theoretical order for a SDOF system is 2, extra components is added to cover the nonlinear and noise components, making sure that the prediction is good at the undamaged state. After 600 gal earthquake shaking, the frame was damaged and the predicted time history of WN2 is shown in **Figure 7-25**. The prediction error become larger than the undamaged state.

Figure 7-26 shows the change of NI for both Euclidean norm as Mahalanobis norm among different test cases. A larger index was observed for test cases subjected to severe excitation. **Table 7-3** shows the results of outlier analysis (both Euclidean norm and Mahalanobis norm) from the damage detection of a 1-story 2-bay RC frame subject to a series of white noise excitations. The parameter α is set as 2, this corresponds to an interval of 95.5% confidence for a real normal distribution. The change of the identified

dominant frequency from the test specimen with respect to the estimated NI is shown in **Figure 7-27**.

It is concluded that the RSSI-COV method can provide a technique for continuous monitoring of a structure by using either earthquake or ambient vibration measurement. Although white noise excitation is assumed for the RSSI model, it is able to overcome this assumption violation by increasing the subspace dimension (number of block rows) which allows a better signal decomposition, but a higher system order is required to cover the system information. Drawback is the spurious poles that appear in the time-frequency plot due to the assumption violation.

On the another side, the novelty index analysis based on the Kalman filter prediction error can provide the possibility of getting early warning of structural damage before severe damage occurs by using output-only measurements.

7.3 Application 3: bridge pier scouring experiment

Consider a four span bridge with its steel decks simply supported on three cylindrical piers as shown in **Figure 7-28 a)**. The piers are buried with 30 cm of depth and confined by coarse sand. The goal of the experiment is to monitor the state of the bridge under continuous scouring, to extract its vibrating features allowing early warning of the pier settlement or failure in the foundation of the bridge, and to locate damage through an output-only signal processing approach.

The experiment was conducted in Hydraulic Research Institute of Water Resources Agency, Ministry of Economic Affairs, located at Nanshijiao (經濟部水利署南勢角水工試驗所), Taipei, Taiwan. Several tests take place as shown in **Table 7-4**. In order to create a local damage scenario, a brick wall was used to address the flow and to reduce

the stream width, as consequence of the increase in flow rate, the scour rate and depth will be also increased. From experimental observation, the failure mechanism was pier settlement caused by base hollowing. **Figure 7-28 c)** shows the final state of the bridge, pier three settled and is the one that suffers most from the scour, followed by pier two but this latter has not settled. Due to the stream width reduction, pier 1 almost does not feel the scour effects at all.

In order to measure the horizontal vibrations in the transverse direction of the bridge, excited by the impact of water flow on the pier, a total of twelve VSE-15D velocity sensors (Tokyo Sokushin Corporation) were installed uniformly along the center line of the deck. Configuration of the bridge and sensor location is shown in **Figure 7-28 a)**. A laser displacement-meter was also installed in January 24 and March 29, 2011, to monitor the settlement occurred in pier 3. In the last test conducted in March 29, twelve AS-2000 accelerometers are used instead. **Table 7-5** shows the sensors specifications.

7.3.1 Bridge pier imminent settlement indicator: modal frequency drop

7.3.1.1   Test conducted in 2011/01/19 with full measurements

To analyze vibration data of the experimental bridge under continuous scour, firstly the modal frequencies will be extracted along time to identify damage. The rSSA-SSI-COV algorithm will be the main tool to carry out this job, but also the RSSI-COV algorithm is applied for comparison purpose.

The control parameter of the model is shown in **Table 7-6**. The determination of the subspace order for rSSA and the system order for RSSI-COV follows the same procedures of SSA-SSI-COV shown in section 4.1.3.1: the singular spectrum is

analyzed in RSSI-COV step using 5000 points of the signal regenerated with rSSA, for which the subspace order (number of SV) also must to be determined. 3000 points correspond to the moving window length for rSSA: L', and 5000 is the length L for RSSI-COV. The number of SV chosen from rSSA which leads to the emergence of a jump in the singular spectrum of RSSI-COV will be the best choice for the rSSA subspace order. Location of the jump also indicates the system order. However, this only gives an estimate for the required system order, because as the scour depth increases, boundary conditiosn and consequently the dynamic behavior changes; similar to that observed in section 7.1(3-story steel frame), the required system order is different for different time periods. On the other side, for the case where RSSI-COV is applied alone, the parameters were referenced to that chosen for rSSA-SSI-COV but with higher block rows to separate system information from noise perturbation.

The initial 5000 data points were used for the order determination, when the bridge is excited only by ambient vibrations. Several singular spectrums is shown in **Figure 7-29**, when there are only 15 singular values selected in rSSA, the jump become very clear and it is located between 18 to 22 SV at the singular spectrum of RSSI-COV. The number of singular values in rSSA and the system order for RSSI-COV must be chosen towards the upper limit, *i.e.*, the first appearance of the jump, trying to make sure that all information is covered despite the spurious or noise contaminated poles, therefore, 25 SV were selected from rSSA and the system order is determined to be 20.

The identified modal frequencies are plotted in **Figure 7-30 a)** for RSSI-COV and **b)** for rSSA-SSI-COV. The frequency poles were plotted every 0.25 seconds. Although the spurious modes are scattered, the evolution of the modal frequencies is clear. It is evident the advantage of rSSA-SSI-COV over RSSI-COV, since the second algorithm

could not track the 2nd modal frequency with the same system order and even with much higher number of block rows.

To further clarify the frequency tracking results, besides that the poles with negative and more than 50% of damping ratio were discarded, the stable system poles can be discriminated from the spurious poles using the same technique used to construct the offline stability diagram. The procedure is to compare poles between two successive time instants. A pole will be marked as frequency stable if the percentage of difference between two time instants is less than the specified criterion. Furthermore, from the frequency stable poles, the same procedure can then be applied to damping ratios and mode shapes with their respective criterions. The time-frequency plot after applying stability criterion is shown in **Figure 7-31**.

Interesting phenomena can be observed in the time-frequency plot shown in **Figure 7-31**. The 1st modal frequencies of the bridge under ambient vibration is almost 2 Hz higher than that obtained under the water flow excitation, the same with the 2nd modal frequency. This indicates the dynamic characteristic of the bridge under ambient excitation is different than when it is excited by an applied loading. After 485 seconds, both the 1st and the 2nd modal frequency decrease rapidly up to 2000 seconds, because at this first time period, the surface sand was taken by the stream rapidly. Hereafter, up to approximately 7200 seconds corresponds to a period of "stationary scouring", the modal frequencies decrease very slowly and by a almost constant rate. The fact can be verified by the scour depth taken by the video camera installed inside the pier, shown in **Figure 7-32**. The initial depth corresponds to the depth at which the pier is buried. The scour depth increases very fast in pier 3, however, below 7.5 cm is beyond the reach of the camera. But from the scour profile of pier 2, it is evident that after 1000 seconds, the

scour rate is almost constant.

After 7200 seconds, there is a sudden drop both in the 1st as the 2nd modal frequency. The 2nd mode drops from 17 Hz to 12 Hz, and the 1st from 7.8 Hz to 7.2 Hz approximately. Up to about 8000 seconds, another frequency drop occurs, and now the 2nd mode decreases from 12 Hz to 10 Hz, and the 1st mode from 7.2 Hz to 6.3 Hz approximately. Observing the "zoom in" shown in **Figure 7-31 b)**, a very long period wave appears just after 8000 seconds; from experimental observation, this long period signal is induced by the bridge settlement, but before this event, there is nothing abnormal in the signal except that this has overstep the measure range after about 7200 seconds. The sudden frequency drop is an indicator of imminent pier settlement 800 seconds before its occurrence.

The reason of this evident modal frequency drop especially in the 2nd mode can be explained as the consequence of the change in the dynamic characteristics of the bridge. There are possible two reasons about this sudden frequency drop: (1) once the scour reaches at the bottom of the pier which is simply supported because the sand confinements were all removed, the loss of the stiffness provided by the sand along the bottom area makes the pier very unstable and, causes a sharp drop of the 2nd modal frequency which is more sensible. (2) The another possibility is the mode coupling effect in a three dimensional structure. Similar to that observed in section 7.1, due to the coupling modes, different frequencies is possible for only one mode if a three dimensional structure is simplified to a plane structure, *i.e.*, they will have a similar mode shape in the considered plane but with different frequencies. In the scouring experiment, only the vibration parallel to the stream flow is measured, thus, when the scour reaches bottom area of the pier, the coupling modes may take place due to the

change in dynamic behavior instead of the original modes,.

However, since the signal oversteps the measure range, more tests is required to check above statement and make sure that the frequency drop before the settlement is not occasional or due to other unknown factors. Moreover, to check that the occurrence of the long period signal corresponding to the first settlement, a KEYENCE LK-2000 Laser displacement sensor is installed above pier 3 in the test conducted in January 24, 2011.

7.3.1.2   *Test conducted in 2011/01/24 with full measurements*

In this test there are only 9 sensors from No. 1 to No. 9 are available. The order determination for rSSA-SSI-COV model is shown in **Figure 7-33** , **a)** shows the singular spectrum in rSSA step, and the remaining figures are made from the SVD in RSSI-COV step, using the 5000 points contained in the moving window. From the examples shown in **Figure 7-33**, the choice of 20 SV leads to a very clear jump, however, considering that the system changes over time, the rSSA subspace order is chosen towards the upper limit and defined as 35, *i.e.*, case c) in **Figure 7-33**, and the system order is selected at the jump, which is 34. The model parameter is shown in **Table 7-7**.

The evolution of the modal frequencies is shown in **Figure 7-34**. The displacement sensor is also installed to measure the settlement at pier 3. The frequency evolution pattern is similar to what has been discussed: the water arrivals and impacts the piers at about 205 seconds, after that the modal frequencies decrease rapidly up to about 1000 seconds, and hereafter is the stationary scour stage and the frequency decrease rate become almost constant. The first sudden frequency drop is detected at about 6000

seconds, the drop is not as large as that occurs in the previous test: the 2nd mode decreases from about 13.3 Hz to 12.8 Hz, the drop in 1st modal frequency is not clear due to the scatter in the data. This sudden drop occurred 2000 seconds before the 1st settlement which happened at 8030 seconds approximately, and can be served as the feature indicating imminent bridge settlement. Once the settlement occurs, the decrease in 2nd modal frequency is significant: from 12.8 Hz to about 11.7 Hz, and many coupled modes appear. After the first settlement the data become quite sparse especially for the 1st mode, but arriving to 11000 seconds, there is a sudden increase in modal frequencies. From experimental observation, steel decks which are originally simply supported on the top of pier and without contact each other, get stuck after several settlements, this explains the sudden increase in modal frequencies.

On the other hand, it is proved in **Figure 7-34 b)** that the settlement is always accomplished by the appearance of a long period signal in the velocity measurement.

7.3.1.3 Test conducted in 2011/01/26 with full measurements

Although with the Laser displacement sensor installed in the test conducted in 2011/01/24, the relationship between settlement and long frequency signal is verified, there are only data of 9 sensors available. Therefore, another test was carried out in 2011/01/26, the model parameter is shown in **Table 7-8**; the singular spectrums used to determined the system order is shown in **Figure 7-35**. Unlike previous cases, the subspace order for rSSA and the system order for this test is reduced to the best choice. **Figure 7-36** Shows the time-frequency plot of the modal frequencies.

The same pattern one can found in **Figure 7-36**, the water arrivals at about 30 seconds, the decrease in the natural frequency of the bridge in the first 500 seconds is

very fast because the surface sands were whisked away by the stream and the scour depth increments rapidly; after 500 seconds, the scour rate was slowed down to the "stationary" stage during the subsequent 5000 seconds, until a sharp drop of 2nd modal frequency occurs at approximately 5500 seconds, which warns of an imminent settlement. This latter event occurs in pier 3, evidently a long period signal appears at the first time around 5820 seconds in the 9th sensor measurement indicating pier settlement, which is shown in **Figure 7-36 b)**. After several bridge settlements, and again, decks originally simply supported on the top of pier without contact each other get stuck, this explains why a sudden increase in modal frequencies after approximately 8000 seconds.

7.3.1.4 Test conducted in 2011/03/29 with full measurements

The velocity sensors are very sensitive and high quality expensive sensors made specially to measure ambient vibrations, otherwise, accelerometers are commonly used sensors for vibration-based system identification with more affordable prices. Therefore, another test was conducted in 2011/03/29 applying both RSSI-COV and rSSA-SSI-COV algorithm to the acceleration measurements. Data measured by the twelve sensors are used simultaneously. The acceleration data are filtered in field by an analogous band-pass filter having its plateau zone on the Frequency Response Function between 0.02 Hz and 50 Hz.

It is difficult to select a suitable system order directly by RSSI-COV, hence, firstly the singular spectrums from the combined approach rSSA-SSI-COV are considered as that shown in **Figure 7-37**. The same as what has been done in previous tests, the subspace order in rSSA which cause the appearance of a jump in the singular spectrum of RSSI-COV step leads to the better choice for the system order. **Figure 7-37 a)** shows

the singular spectrum constructed with rSSA; from **Figure 7-37 b)** to **f)** which corresponds to singular spectrum constructed in RSSI-COV, the jump begins to appear with 45 SV chosen from rSSA, which is shown in **Figure 7-37 c)**, and the jump is located at 44 SV. Hereafter, the jump gets more clear while less SV is chosen. To be conservative and trying to reveal all identifiable modes, the order shown in **c)** is chosen, the model parameters for rSSA-SSI-COV is shown in **Table 7-9**.

Figure 7-38 shows a comparison between the outcome of RSSI-COV and rSSA-SSI-COV after applying the same stability criteria used before. Evidently the addition of rSSA before RSSI-COV can enhance the tracking capability and stability in addition to the function to determine the system order. The pattern shown in the time-frequency plot is quite the same as that shown before: the water arrivals at about 860 seconds, from now on the modal frequencies slowly decrease until the occurrence of the first settlement at 5057 seconds.

A close picture was taken to the traces between 4500 and 5500 seconds and it is shown in **Figure 7-39**. The 4th mode appears at about 4650 seconds and decreases rapidly until about 4950 seconds, moment at which the 1st and 2nd mode frequency trace (the poles with frequency and damping ratio stables) are almost completely lost. This indicates that there is a very unstable dynamic behaviour before the 1st settlement which occurs at 5057 seconds, this together with the appearance and fast decrement of the 4th mode constitutes a good indicator of imminent bridge settlement. During the time period with successive settlements between 5057 and about 6000 seconds, the traced modal frequencies are also very dispersed and the reduction in 3rd modal frequency is evident. However, after 6000 seconds the modal frequencies slowly increase because the decks are getting stuck each other.

Furthermore, this close look to the frequency traces shown in **Figure 7-39** allows to see that, actually, there are about two frequency traces for 3rd mode, three traces for 2nd mode and about six traces for 1st mode very close one to another. Besides the factor of three dimensional mode coupling effect, these closely-spaced frequencies indicates the time varying characteristic of the bridge natural frequencies.

7.3.2 Damage location indicator: mode shape slope ratio

Mode shapes have been widely used to figure out the damage location throughout its curvature in many researches. The node which suffers from stiffness loss has usually larger curvature than the other nodes. The mode shape is a relative quantity which can be scaled arbitrary, however, the mode shape curvature is not independent of the scaling criteria and consequently, the identification of damage location depends on how one scale the mode shape. Taking into account this fact, the concept of mode shape curvature can be modified to a quantity which is independent of scaling, and here the definition of mode shape slope ratio is introduced.

Curvature is the rate of change of the mode shape slope, to cancel out arbitrary scaling, ratio between consecutive slopes can be used instead of the rate of change of the mode shape slope. Moreover, sign of the curvature indicates the concavity. For mode shapes identified from field data, sign changes introduced in the concavity due to imperfections in the shape could make difficult the identification of damage location. To avoid all these inconveniences, the mode shape slope ratio can be defined as follows:

$$
\begin{cases}
\text{If } m_i/m_{i+1} > 0 \text{ and } m_i > m_{i+1} \longrightarrow \text{ slope ratio}(i) = m_i/m_{i+1} \\
\text{If } m_i/m_{i+1} > 0 \text{ and } m_i < m_{i+1} \longrightarrow \text{ slope ratio}(i) = m_{i+1}/m_i \\
\text{If } m_i/m_{i+1} < 0 \qquad\qquad\quad \longrightarrow \text{ slope ratio}(i) = \{\text{slope ratio}(i) + \text{slope ratio}(i+1)\}/2
\end{cases}
\tag{7.1}
$$

where m_i is the slope of the ith discrete segment of the spline interpolated mode shape. By defining the slope ratio this way, the sign problem can be avoided, and the resultant slope ratio will only reflect how large is the slope change in a given point. At the peak point of the mode shape where the slope sign changes, the 3rd criterion applies and it is just taking an average of the adjacent slope ratios. Finally, to avoid the a disproportionate increment in slope ratio comparing to the others, when slope in the divisor is near zero, a base 10 logarithm can be applied to the slope ratio. For the implementation, the computed mode shapes can be smoothed by curve fitting and interpolated with a spline function, which is sampled at 52 points to obtain 50 slope ratios along the bridge.

7.3.2.1 Mode shape slope ratio for test conducted in 2011/01/19

Figure 7-40 shows examples for the identified 1st modes shape from the test in 2011/01/19 for two different time instants. **Figure 7-41** shows the same but for the 2nd mode shape.

From what is shown in **Figure 7-40** and **Figure 7-41**, there are two identified mode shapes for both 1st mode and 2nd mode. The 1st modal frequencies are separated by about 2.5 Hz one to another, and by 3 to 4 Hz for the 2nd modal frequencies. Hence, although apparently there are three trace of frequencies revealing in the time-frequency plot shown in **Figure 7-31**, where the second trace is not very clear, however, both the 2nd and 3rd trace corresponds to the 2nd mode. From the experience learned from section 7.1, a possible explanation of this phenomenon is the mode coupling, because the bridge is simplified to a plane model for which only horizontal vibration is measured.

Comparing **Figure 7-40 a)** and **b)** to **Figure 7-40 c)**; also comparing **Figure 7-41 a)** and **b)** to **Figure 7-41 c)** and **d)**, there is no significant difference by visual observation, and the result with or without smoothing is similar. The 1st mode shape slope ratio is shown in **Figure 7-42 a)** for the smoothed shape and **b)** for the shape only interpolated by a spline function.

The automatic discrimination of the mode shapes is based on the fact that, for this experimental bridge, the complex mode shape poles shown in **Figure 7-40** and **Figure 7-41** are almost a straight line either 1st or the 2nd mode, *i.e.*, the amplitude of the poles can be treated as normal modes by only adding a plus o minus sign according to its phase. The 1st mode has non zero crossings and the 2nd mode has only one zero crossing. The correlation coefficient **R** between the real part and imaginary part is another useful criteria to filter out spurious poles. The defined **R** criterion for different tests is shown in **Table 7-10**.

From **Figure 7-42**, for both **a)** and **b)**, the zone with higher slope ratio become wider after 1000 seconds, indicating that the system has been changed. Initially the peak is located at the center of the bridge which is expected for a 1st mode shape; while the scouring depth increments, the peak moves toward 300 cm, specially between 7200 and 8000 seconds as that shown in **Figure 7-42 a)**, moments corresponding to imminent pier settlement and, precisely the pier 3 is located at 325 cm.

The 2nd mode slope ratio is shown in **Figure 7-43 a)** for the smoothed shape and **b)** for the shape only interpolated by a spline function. Two peaks exist in the 2nd mode shape as expected. Although the 2nd peak is located at 325 cm (pier 3 location), but it does not change at all along the time history, otherwise, it is the first peak located at 200 cm which has a drastic movement toward 100 cm at about 7200 seconds, time instant at

which the 2nd modal frequency suddenly drops. Therefore, the 2nd mode shape is not appropriate to identify the damage location in the bridge, but the drastic change of the 1st peak position is also an indicator of imminent pier settlement.

7.3.2.2 *Mode shape slope ratio for test conducted in 2011/01/26*

Figure 7-44 shows examples of 1st and 2nd identified mode shape from different time instants. In this case the difference is evident. However, the measurement of sensor No. 12 seems to have some problem because it has consistently a phase difference with all the remaining sensors. This inconvenience is the reason of a peak slope ratio appearing at about 400 cm to 430 cm, shown in **Figure 7-45 b)** and **Figure 7-46 b)**, where the mode shape is not smoothed.

From the smoothed mode shape shown in **Figure 7-45 a)**, it is clear that the 1st mode slope ratio is a good indicator of the damage location. In the undamaged state, the peak is low and located at the center as it is normal for 1st mode shape; as scour occurs, the peak amplitude increases and moves rapidly to the region between 300 and 350 cm of the bridge from left to right, where is precisely the pier three location. After 7000 seconds, again, the peak moves to the region between 200 and 250 cm, where is the location of the pier two. This is because the decks on the pier three got stuck and stiffness increased, as a consequence of the fact, the peak of the slope ratio moves to pier 2 at which the scour continues.

In the other side, observing **Figure 7-46 a)**, there are two peaks appearing in the slope ratio for the 2nd mode which are reasonable considering nature of the 2nd mode shape. Although a peak falls in the same region between 300 and 350 cm, there is no criterion to distinguish where the damage is located from the two peaks, besides that the

first peak (on the top of the figure) seems to be more sensible to the scour state. However, the same as that occurred for the 2nd modal frequency, the 2nd mode shape ratio can serve for the early warning purpose since position of the first peak changes suddenly just before the 1st settlement occurs.

7.3.2.3 *Mode shape slope ratio for test conducted in 2011/03/29*

The mode shape slope ratio results for the test conducted in 2011/03/29 are similar to that obtained in the two previous cases. Although three modes were identified, only the 1st mode shape slope ratio serves for the identification of damage location. **Figure 7-47** shows the outcome for the 1st mode, the 2nd mode and the 3rd mode are shown in **Figure 7-48** and **Figure 7-49** respectively.

7.3.3 Novelty Index

The Novelty Index analysis can be also applied to the scouring experiment. The test conducted in 2011/01/26 is selected for the purpose. The system matrix (**A**,**C**) and noise covariance (**Q**,**R**) can be computed following the procedure described in section 2.4. The model parameters are: data window of 6000 points, 110 block rows and the system matrix order is defined as 20. Based on the developed system matrix, the Kalman filter estimation was used to predict the responses for the vibration time history of all sensors.

Unlike the case of RCF6 mentioned in section 7.2 for which there are available 8 white noise test and the statistics was made for every white noise data sequence; for the bridge scouring experiment, a moving window of 2000 points (10 seconds) is adopted to compute the error norm statistics and to perform the outlier analysis, and it moves by every 2000 points, the same as the window length.

Figure 7-50 shows the results of outlier analysis (both Euclidean norm and Mahalanobis norm). The parameter α is set as 2.5 which corresponds to an interval of 99% confidence for a real normal distribution. However, 90 seconds after the scouring began, both Euclidean norm and Mahalanobis norm outliers have reached to almost 100% and 80% respectively. Probably the very fast change in boundary condition of the bridge in the first minutes has introduced large prediction errors. Although outlier analysis cannot be applied, evolution of the statistics like the error norm mean and standard deviation can be checked. **Figure 7-51** shows the result for the evolution of error mean and **Figure 7-52** shows that for the error standard deviation, for both Euclidean norm and Mahalanobis norm.

From **Figure 7-51 b)** and **Figure 7-52 b)**, it is found that Mahalanobis norm is also a good indicator of inminent bridge settlement because both the error mean and standard deviation were suddenly raised at about 5500 seconds. After the occurrence of the 1st settlement at 5820 seconds approximately, both the error standard deviation as error mean went down again to the original level. After about 7500 seconds both quantities was suddenly reduced to the level at the beginning of the scouring test, this is because after several settlements the decks are getting stuck, with the increase of the horizontal stiffness the prediction error was reduced.

The novelty analysis also can be made for every sensor separately to detect damage location. The outlier analysis does not apply here because it reaches to the top at the beginning as that occurs in **Figure 7-50**. The error mean and standard deviation per sensor are shown in **Figure 7-53** and **Figure 7-54** respectively. It is clear from these figures that both the error RMS mean and standard deviation of sensors 9 and 10 are much larger than the other sensors, followed by sensors 7 and 8. Since sensors 9 and 10

113

are the two sensors next to the pier 3, which suffers from settlement; and sensor 7 and 8 are installed on the deck supported by pier 2 and 3, a quite deep the scour has also been reached at pier 2, hence, one can conclude that the novelty analysis done for each sensor separately is in fact an effective way to locate damage location.

Chapter 8
Conclusions

8.1 Research conclusions

The changes of features in a structural system may due to the change of environmental loading pattern, the nonlinear inelastic response of structure or structural damage when subjected to severe external loading. The detection of the change of features or damage in large structural system, such as buildings and bridges, can improve safety and reduce maintenance costs. Therefore, feature extract and damage detection from vibration structures are the goals of SHM.

Development of off-line identification procedure is discussed in the first part this thesis, with the aim of finding accurate and true modal parameters, a stabilization diagram is implemented by plotting the identified poles against the data matrix order, where the system order is fixed. In the sensitivity analysis, both the covariance driven as the data driven Stochastic Subspace System Identification techniques are proved to be robust and stable even the model assumptions were violated: (1) In the case of nonlinear signals, an equivalent linear model can be realized. (2) When there are extra noise added to the signal even when the noise is correlated with output, modal frequencies along with the mode shapes can be accurately identified by increasing the order of projection or covariance matrix. (3) Signals of a time-varying system will be decomposed in more and more "equivalent linear frequencies" as one goes up in the stabilization diagram and the poles will not stabilize with increase in the number of block rows. (4) The estimates of damping ratio are very sensitive to noise and the identification results are not reliable. (5) The closely-spaced frequencies blended with noise can be accurately identified with the help of the new developed SSA-SSI-COV identification algorithm, which is applied

to the identification of Canton Tower, a benchmark problem for SHM of high-rise slender structures. Thus, the capacity of SSI-based algorithm is demonstrated. Through the off-line analysis on the field response data of Canton Tower, the following conclusions are drawn:

1. The difficulty in using SSI-DATA to identify these frequencies may be explained based on the conclusions obtained from previous simulation studies which indicate that closely-spaced frequencies are difficult to be identified when the measurements are noisy and generally only one equivalent frequency can be identified. Although finally SSI-COV could distinguish these close frequencies, giant Toeplitz matrix size was required which is actually excessively time and memory demanding.

2. The use of SSA as a pre-processing tool for SSI-COV enhances greatly the early emergence of a stable diagram for the identifiable modes and allows finding the best choice of system order. In the case of using 95 SV from SSA, a clear jump appears in the singular spectrum obtained in SSI-COV which indicates the best system order, and most of all modes are stabilizes starting from about the 25th row or even earlier. On the contrary, by using SSI-COV alone the stability starts approximately after 100 to 125 rows.

3. SSA as preprocessing technique cannot be used in conjunction with SSI-DATA, worse result in stability than using SSI-DATA alone was obtained. The signal regeneration by SSA has negative effects in the orthogonal projection carried out in SSI-DATA, which is, in fact, the best least square fit of the future measurements in terms of the past measurements.

4. The advantage of SSA over the low-pass filter is proved in this study. The use of SSA leads to an earlier emergence of a stable diagram, *i.e.*, accurate answers can be realized

with lower matrix order (number of block rows).

5. Preprocessing raw data with decimation is always necessary in system identification, which is able to reduce the computation effort and leads to an accurate and fast convergence of the identified modal parameters.

In the second part of this research, the on-line system parameter estimation technique from output-only measurements is developed through Covariance driven Recursive Stochastic Subspace identification (RSSI-COV) moving window approach. To make possible the SVD-updating task, Extended Instrumental Variable version of Projection Approximation Subspace Tracking algorithm (EIV-PAST) was adapted for the purpose. Furthermore, the recursive Singular Spectrum Analysis (rSSA) algorithm is proposed through the introduction of PAST algorithm, and then, the recursive rSSA-SSI-COV method is complete.

Both RSSI-COV and rSSA-SSI-COV are validated through numerical simulation study of time-varying dynamic system. Several conclusions were obtained from the simulation study: (1) The tracking stability increases with the window length of RSSI-COV, but this latter does not increase the computation time. This is an advantage of RSSI-COV over RSSI-DATA. However, larger is the window length, more the time delay to detect system change. (2) From the experience learned in numerical study, the window length for rSSA should be much smaller than that used for RSSI-COV, recommended value is about half of the window length of RSSI-COV. (3) The required system order for time-varying systems is higher than the theoretical value, because signals of a time-varying system demand more orthonormal vectors to span the system information. The higher the number of block rows (subspace dimension), *i.e.*, better decomposition is achieved, however, the larger the system order demand. This latter is

117

even more evident when the noise is engaged in. (4) In the presence of a noise which violated the SSI assumption, huge system order is required for RSSI-COV to track recursively the modal parameters. The preprocessing with rSSA enhanced the tracking stability and allows tracking the time-varying modal information with less system order.

Through the application of recursive analysis on several laboratory tests, the online tracking capability and robustness of RSSI-COV and rSSA-SSI-COV are demonstrated. Moreover, various conclusions can be obtained from the experimental application regarding to SHM and damage detection:

1. The model reduction of a three dimensional structure to, *e.g.*, a plane structure, it is possible to find more than one frequency for a single mode (with a very similar mode shape) due to the mode coupling effect in three dimensions although the structure is symmetric. System change is not the only reason for the variation in the modal frequency, it is also possible the frequency shifting due to mode coupling when the external loading pattern changes or caused by the same system change. The second reason is observed in the experiment of 3-story steel frame with instantaneous stiffness reduction.

2. To avoid confusion between system change and modal coupling, higher system order is required. Moreover, the presence of non-linearity and time-varying frequencies such as the bridge under constant scour demands a lot orthonormal vector, *i.e.*, system order to span the system information. The procedure described in SSA-SSI-COV can be effectively applied to rSSA-SSI-COV during the undamaged state and an initial estimate of the system order is offered. The system order must be chosen toward the upper limit keeping a margin for when the system has changed and when the non-linearity and time-varying pattern become strong.

3. The goal of early warning to imminent bridge pier settlement is achieved. A sudden drop in higher modal frequencies is always present at all bridge scour tests. The decrement in frequency is even more significant after the occurrence of the first settlement, and the frequency poles are very sparse at this stage. The accuracy and robustness offered by rSSA-SSI-COV seems to be the key to obtain evidences of imminent bridge settlement. The accuracy and stability are important issues because the changes in modal frequencies are usually small even the structure has been damaged.

4. The peak value of the first mode shape slope ratio is a good indicator of the damage location. Although the higher modes are difficult to locate damage because more than one peak exists, together with the higher modal frequencies these mode shape slope ratios present sudden changes in peak position when the bridge is subjected to imminent settlement. All this evidences indicate that the dynamic behavior of bridge is completely different when the sand confinement is completely removed due to scouring and the settlement is about to occur.

5. Besides the change in modal parameters, the novelty index through Kalman filter prediction error also provides a useful statistical index of damage, the prediction error by every sensor can also indicate the damage location, making possible the damage detection and early warning.

8.2 Recommendations for future work

The long-term goal of the research in SHM is the application of the system identification and damage detection methods to the real scale structures, which in fact are much more complex, and in addition to the environmental factors, both the automatization of the identification process for continuous monitoring, as seeking for

reliable criterias and indexes to translate the system identification outcome into a safety or warning message are challenges to be overcome. Therefore, further researches and experiences with large scale structures are needed.

The computation speed is another difficult to be overcome in the online application. In the bridge scouring experiment, all 12 sensors were required in the application of rSSA-SSI-COV to realize accurately the modal frequencies and mode shapes, however, using a modern computer and in terms of the selected rSSA-SSI-COV parameters, the computation consumed about 10 times more than the required timing for online application. Although with reduced number of sensors and reducing the number of block rows (less accuracy) the timing requirement can be satisfied, the tracking result for modal frequencies is more scattered and is not as clear as that obtained with full measurements; furthermore, it is impossible to recover a good mode shape if only a few points are available, and thus, damage location cannot be identified. A feasible solution to increase the computation speed is through the developement of parallel computation algorithms which can exploit the full computation potential of the microcontroller of each sensing unit.

Although the system damage and location can be identified correctly in this study, there is still a lack in this research about damage quantification and the estimation of the remaining service life. Since SSI-based algorithms are able to accurately identify the modal parameters, a possible approach is through the finite element model updating of the mass, dampin and stiffness matrix, therefore the damage can be quantified and the remaining service life can be assessed.

References

[1] Abdelghani M., Basseville M. and Benveniste A. "*In-operation damage monitoring and diagnostics of vibrating structures, with applications to offshore structures and rotating machinery*". Proceedings of IMAC 15, Orlando FL,USA, 1815~182,1997.

[2] Abdelghani M., Goursat M., Biolchini T., Hermans L.and Van Der Auweraer H. "*Performance of output-only identification algorithms for modal analysis of aircraft structures*". Proceedings of IMAC XVII : 17th international modal analysis conference. Kissimmee FL, 8-11 February 1999.

[3] Alonso, F.J., Del Castillo J.M., and Pintado P. "*Application of singular spectrum analysis to the smoothing of raw kinematic signals*". Journal of Biomechanics, 2005. 38(5): p. 1085-1092.

[4] Asmussen, J.C. and Brincker R. "*Statistical Theory of the vector random decrement technique*". Journal of Sound and vibration (1999) 226(2), 329-344.

[5] Basseville M., Benveniste A., Goursat M. "*Output-Only Subspace-Based Structural Identification: From Theory to Industrial Testing Practice*". Journal of Dynamic Systems, Measurement, and Control, Vol. 123, December, 2001.

[6] Bassville M., Benveniste A., Goursat M. and Mevel L. "*In-flight vibration monitoring of aeronautical structures*". IEEE Control System Magazine, October 2007, 27-41.

[7] Basseville M. et al. "*In situ damage monitoring in vibration mechanics: diagnostics and predictive maintenance*". Mechanical systems and signal processing (1993) 7(5), 401~423.

[8] Bendat J. S., Palo P. A., Coppolino R. N. "*A general identification technique for nonlinear differential equations of motion*". Probabilistic Engineering Mechanics 7: 43-61, 1992.

[9] Bodeux J.B. and Golinval J.C. "*Modal identification and damage detection using the data-driven stochastic subspace and ARMAv methods*". Mechanical Systems and Signal Processing (2003) 17(1), 83–89

[10] Caicedo, Juan Martin; Dyke, Shirley J.; Johnson, Erik A. "*Natural Excitation Technique and Eigensystem Realization Algorithm for Phase I of the IASC-ASCE Benchmark Problem: Simulated Data*". Journal of Engineering Mechanics, ASCE, pp. 49-60, January, 2004.

[11] Chang, Peter C.; Alison, Flatau and Liu, S. C.. "*Review Paper: Health Monitoring of Civil Infrastructure*". Structural Health Monitoring 2003 2: 257.

[12] Chang, C. C., and Li, Z. "*Recursive Stochastic Subspace Identification for Structural Parameter Estimation*". SPIE Proceedings Vol. 7292 729235-9. 2009.

[13] De Cock K., Mercère G., De Moor B. "*Recursive subspace identification for in-flight modal analysis of airplanes*". Proceedings of the International Conference on Noise and Vibration Engineering (ISMA 2006), Leuven, Belgium, Sept. 2006, pp. 1563-1577.

[14] Doebling, Scott; Farrar, Charles and Prime, Michael. "*A summary review of vibration-based damage identification methods*". Shock and Vibration Digest, 30(2), 91–105, 1998.

[15] Ewins, D.J. "*Modal Testing: Theory and Practice*". Research Studies Press Ltd., Letchworth, Hertfordshire, UK, 1984.

[16] Farrar, Charles R.; Doebling, S. W. and Nix, David A. "*Vibration-based structural damage identification*". Phil. Trans. R. Soc. Lond. A 2001 359, 131-149 doi: 10.1098/ rsta. 2000.0717

[17] Goethals, I.; Mevel, L.; Benveniste, A.; and De Moor, B. "*Recursive output only subspace identification for in-flight flutter monitoring*". Proc. of the 22nd International Modal Analysis Conference, Dearborn, Michigan, 2004.

[18] Golub, Gene H.; Van Loan, Charles F. "*Matrix computations*". Johns Hopkins University Press, 1996.

[19] Gustafsson, T. "*Recursive system identification using instrumental variable subspace tracking*". Proc. of the 11th IFAC Symposium on System Identification, Fukuoka, Japan, 1997.

[20] Gustafsson T. "*Instrumental Variable Subspace Tracking Using Projection Approximation*". IEEE transactions on signal processing, Vol. 46, No. 3, March 1998.

[21] Guyader A. and Mevel L., "*Covariance driven subspace methods: Input/output vs. output-only*". Proc. Int. Modal Anal. Conf., Orlando, FL, Feb. 2003, Paper no. 136.

[22] Hart, Gary C. and Wong, Kevin. "*Structural Dynamics for Structural Engineers*". John Wiley&Sons, Inc. 2000.

[23] James, G. H.; Carne, T. G.; Lauffer, J. P.; and Nord, A. R. "*Modal testing using natural excitation*". Proc., 10th Int. Modal Analysis Conference, San Diego, 1992.

[24] Juang, J.N. "*Applied system identification*". Englewood Cliffs, NJ, USA: Prentice Hall, 1994.

[25] Juang, J.N. and Pappa R.S. "*Eigensystem realization algorithm for modal parameter identification and model reduction*". Journal of Guidance, Control, and Dynamics. Vol. 8, no. 5, pp. 620-627. 1985

[26] Juang J.N., Cooper J.E., Wright J.R. "*An eigensystem realization algorithm using data correlations (ERA/DC) for modal parameter identification*". Journal of Guidance Control and Dynamics (1987) Volume: 3, Pages: 620-627.

[27] Larimore, W. E. "*The Optimality of Canonical Variate Identification by Example*". Proc. of SYSID, 4-6 July, Copenhagen, Denmark, 2, 151-156, 1994.

[28] Lin, Ping; Zhang, Nanxiong; and Ni, Bin. "*On-line Modal Parameter Monitoring of Bridges Exploiting Multi-core Capacity by Recursive Stochastic Subspace Identification Method*". 2008 American Control Conference, Seattle, Washington, USA, June 11-13, 2008. Page 632 – 637.

[29] Ljung, Lennart. "*System Identification: Theory for the User*". Second edition, Prentice Hall, Upper Saddle River, NJ, USA, 1999.

[30] Loh, C.H. and Weng, J.H. "*Damage Detection Using Stochastic Subspace Identification with Partial Measurements*". Proc. of the 7th international workshop on structural health monitoring, Stanford, California, 2009.

[31] Loh, C.H.; Chao, S.H.; Weng, J.H.; and Liao, W.I. "*Identification of Damage in Reinforced Concrete Structures from Different Levels of Earthquake Excitations*". Proc. of 12th International Conference on Fracture, Ottawa, Canada, 2009.

[32] Loh; C.H.; Mao, C.H.; Chao, S.H.; Weng, J.H. "*System identification and damage evaluation of degrading hysteresis of reinforced concrete frames*". Earthquake Engng Struct. Dyn. 2011; 40:623–640 Published online 25 August 2010 in Wiley Online Library (wileyonlinelibrary.com). DOI: 10.1002/eqe.1051

[33] Ku, Chiu Jen; Cermak, Jack Edward; Chou, Li-Shu. "*Random decrement based method for modal parameter identification of a dynamic system using acceleration responses*". Journal of Wind Engineering and Industrial Aerodynamics 95 (2007) 389–410.

[34] Mercère, G., Lecoeuche, S., and Lovera, M. "*Recursive subspace identification based on instrumental variable unconstrained quadratic optimization*". International J. of Adaptive Control and Signal Processing, 18, 771-797, 2004.

[35] Ni, Y. Q.; Xia, Y.; Liao, W. Y.; Ko, J. M.. "*Technology innovation in developing the structural health monitoring system for Guangzhou New TV Tower*". Journal of Structural Control and Health Monitoring, 2009; 16: 73-98.

[36] Peeters, Bart and De Roeck, Guido, "*Reference-based stochastic subspace identification for output-only modal analysis*". Mechanical Systems and Signal Processing 13(6) 855-878, 1999.

[37] Peeters, Bart. "*System Identification and Damage Detection in Civil Engineering*". Ph.D. Dissertation, Katholieke Universiteit, Leuven, December 2000.

[38] Peeters, Bart and De Roeck, Guido, "*Stochastic system identification for operational modal analysis: a review*". J. Dyn. Syst. Meas. Control 123, 2001, 659-666.

[39] Pridham, Brad A. and Wilson, John C. "*Identification of base-excited structures using output-only parameter estimation*". Earthquake Engng. Struct. Dyn. 33: 133-155, 2004.

[40] Qin, Q.; Li, H.B. and Qian, L.Z. "*Modal identification of Tsing Ma Bridge by using improved eigensystem realization algorithm*". Journal of Sound and vibration (2001) 247(2), 325-341.

[41] Reynders, Edwin et al. "*Uncertainty bounds on modal parameters obtained from stochastic subspace identification*". Mechanical Systems and Signal Processing 22, 948-969, 2008.

[42] Smith, GA; Robinson, AJ. "*A comparison between the EM and subspace identification algorithms for time-invariant linear dynamical systems*". November7, 2000. Cambridge University.

[43] Söderström, Torsten and Stoica, Petre. "*System identification*". Prentice-Hall International, 1989.

[44] Sohn H., Farrar, C.R., Hemez F.M., Shunk D.D., Stinemates D.W., Nadler B.R. "*A review of structural health monitoring literature: 1996–2001*". Los Alamos National Laboratory report No. LA-13976-MS. Los Alamos, New Mexico; 2004.

[45] Trefethen, Lloyd N. and Bau, David. "*Numerical linear algebra*". Society for Industrial and Applied Mathematics, 1997.

[46] Van Overschee, P. and De Moor, B. "*N4SID: Subspace Algorithms for the Identification of Combined Deterministic-Stochastic Systems*". Automatica, 30(1), 75-93, 1994.

[47] Van Overschee, P. and De Moor, B. "*Subspace Identification for Linear Systems: Theory - Implementation - Applications*". Kluwer Academic Publishers, Dordrecht, The Netherlands, 1996.

[48] Verhaegen, M. and Dewilde, P. "*Subspace model identification, Part Ⅰ: The output-error state space model identification class of algorithms*". International J. of Control, 56, 1187-1210, 1992.

[49] Weng, J.H.; Loh, C.H.; Lynch, J.P.; Lu, K.C.; Linn, P.Y.; Wang, Y. "*Output-Only Modal Identification of a Cable-Stayed Bridge Using Wireless Monitoring Systems*". J. of Engineering Structure, 30 (2), 2008, 1802-1830.

[50] Weng, J.H. "*Application of Subspace Identification in System Identification and Structural Damage Detection*". Ph.D. Dissertation, National Taiwan University, Taiwan, June 2010.

[51] Wu, Ai-Lun; Yang, J.N and Loh, C.H. "*Detection of damages in nonlinear reinforced concrete frames*". Proc. SPIE 7981, 79812O (2011); doi:10.1117/12.877203. San Diego, California.

[52] Yu, Dan-Jiang and Ren, Wei-Xin. "*EMD-based stochastic subspace identification of structures from operational vibration measurements*". Engineering Structures Volume 27, Issue 12, October 2005, Pages 1741-1751.

[53] Zhang, Y.; Zhang, Z.; Xu, X.; Hua, H. "*Modal parameter identification using response data only*". Journal of Sound and Vibration 282: 367-380, 2005.

[54] Welch, Peter D. "*The Use of Fast Fourier Transform for the Estimation of Power Spectra: A Method Based on Time Averaging Over Short, Modified Periodograms*". IEEE Transactions on Audio Electroacoustics, Volume AU-15 (June 1967), pp. 70–73.

[55] Ren, Wei-Xin and Zong, Zhou-Hong. "*Output-only modal parameter identification of civil engineering structures*". Structural Engineering and Mechanics, Vol. 17, No. 3-4 (2004)

[56] Yang, Bin. "*Projection Approximation Subspace Tracking*". IEEE transactions on signal processing, Vol. 43, No. I, January 1995.

[57] Chung, L.L. "*Course note on structural control (II)*". National Taiwan University, Civil Engineering department. Structure Division. 2010.

[58] Loh, C.H.; Weng, J.H.; Liu, Y.C.; Lin, P.Y. and Huang, S.K. "*Structural damage diagnosis based on on-line recursive stochastic subspace identification*". Smart Mater. Struct. 20 (2011) 055004 (10pp).

[59] Giraldo, Diego F.; Song, Wei; Dyke, Shirley J.; and Caicedo, Juan M.. "*Modal Identification through Ambient Vibration: Comparative Study*". J. Engrg. Mech. 135, 759 (2009).

[60] Jazwinski, A.H. "*Stochastic processes and filtering theory*". Academic Press, Inc, New York, 1970.

[61] Andersen, P. "*Identification of civil engineering structures using ARMA models.*" Ph.D. dissertation, Univ. of Aalborg, Aalborg, Denmark, 1997.

[62] Yan, Ai-Min; De Boe, Pascal and Golinval, Jean-Claude. "*Structural Damage Diagnosis by Kalman Model Based on Stochastic Subspace Identification*". Structural Health Monitoring, June 2004, vol. 3 no. 2 103-119.

[63] A Benchmark Problem on Structural Health Monitoring of High-Rise Slender Structures. Phase I: Field vibration measurement and model updating. "*Description of the measurement*". http://www.cse.polyu.edu.hk/benchmark/index.htm

[64] A Benchmark Problem on Structural Health Monitoring of High-Rise Slender Structures. Phase I: Field vibration measurement and model updating. "*Description of the FE model and model reduction*". http://www.cse.polyu.edu.hk/benchmark/index.htm

[65] Golyandina, Nina; Nekrutkin, Vladimir; Zhigljavsky, Anatoly. "*Analysis of time series structure: SSA and related techniques*". Boca Raton, Fla. : Chapman & Hall/CRC, c2001

[66] Xin J., Tsuji H., Sano A. "*Optimal sampling interval for system identification based on decimation and interpolation*". IEE Proc.-Control Theory Appl., Vol. 142, No. I , January I995.

[67] Sinha N.K., Puthenpura S. "*Choice of the sampling interval for the identification of continuous-time systems from samples of input/output data*". IEE Proc. Vol. 132, Pt. D, No. 6, November 1985.

[68] Middleton, R.H., and Goodwin, G.C. "*Digital estimation and control*". Prentice-Hall, 1990.

Appendix A: Frequency Domain Decomposition (FDD)

The Frequency Domain Decomposition can be considered as an SVD-enhanced power sepctrum, and it applies when it is the case of multiple measurements. The procedure starts from estimating the power spectrum density matrix, which is formed applying Discrete Fourier Transform (DFT) to the Covariance matrix shown in (2.22), for time lag k ranging theoretically from minus infinity to infinity:

$$\mathbf{S}_y\left(e^{j\omega\Delta t}\right) = \sum_{k=-\infty}^{\infty} \mathbf{R}_i e^{-j\omega k\Delta t} \tag{A.1}$$

where $\mathbf{S}_y \in \Re^{l\times l}$ is the spectrum matrix. Having in mind that only finite data length N is available, only estimates of the spectrum can be calculated. There is a more straight-forward way to compute the spectrum estimated called modified Welch's periodogram [54], which begins by calculating the DFT of the weighted measured signal:

$$\mathbf{Y}_i\left(e^{j\omega\Delta t}\right) = \sum_{k=0}^{n-1} \mathbf{w}_k \mathbf{y}_k e^{-j\omega k\Delta t} \tag{A.2}$$

where $\mathbf{w}_k$ is a window function to avoid leakage. n is a segment of the total data length N. If n is a power of 2, DFT can be efficiently computed using FFT at the discrete frequencies:

$$\omega_\rho = \frac{\rho}{n}\frac{2\pi}{\Delta t} \quad , \quad \rho = 0, 1, 2, ..., n\text{-}1$$

The spectrum estimate is a product between the obtained DFT and its Hermitian transpose denoted as the superscript ^{H}, scaled by the squared norm of the window function, but averaging over all available samples of DFTs, *i.e.*, periodogram:

$$\hat{\mathbf{S}}_y\left(e^{j\omega_\rho \Delta t}\right) = \frac{1}{\tilde{p}} \sum_{i=1}^{\tilde{p}} \left(\frac{1}{\sum_{k=0}^{n-1}|\mathbf{w}_k|^2} \right) \mathbf{Y}_i\left(e^{j\omega_\rho \Delta t}\right) \mathbf{Y}_i^H\left(e^{j\omega_\rho \Delta t}\right)$$ (A.3)

where $\tilde{p}$ is the number of available samples of DFT from the total data of length N. Overlap is permitted in the sampling and, if higher frequency resolution is required, the sampled segment can be zero-padded.

Finally, SVD is applied to the spectrum matrix (which is a complex valued matrix) for each discrete frequency ω_ρ. The set of major singular values can be plotted against frequency and a singular spectrum in frequency domain will be obtained. The advantage of using FDD over the traditional power spectrum is that, information of multiple sensors can be gathered and combined in only one outcome, especially if it is the case of closely-spaced frequencies, its effects will be reflected in the singular values, *e.g.*, if there are two close frequencies, weight of the second singular value will become closer to the first one.

Appendix B: Prediction Error Method through Stochastic Subspace Identification (PEM/SSI)

The objective of this appendix section is to show the similarity that exists between the system realization algorithm based on autoregressive (AR) model, solved through prediction error method/least square (PEM/LS), and SSI-DATA. This enables one to modify the traditional least square PEM to a subspace approach.

Prediction error methods PEMs are very common and widely used system identification methods. The main idea is to identify a system of linear equations in the sense that: based on past inputs and outputs, can predict any output. For the special case of multivariate output-only measurements, these models are known as autoregressive with moving average vector ARMAv [59].

In the output only system identification, the traditional PEM is carried out using a two-stage least squares approach. The autoregressive AR model can be written as:

$$\hat{\boldsymbol{y}}_k = -\mathbf{A}_1 \boldsymbol{y}_{k-1} - \mathbf{A}_2 \boldsymbol{y}_{k-2} - ... - \mathbf{A}_i \boldsymbol{y}_{k-i} \tag{B.1}$$

where the matrices $\mathbf{A}_k \in \mathfrak{R}^{l \times l}$ are the multivariate AR matrix coefficients; $\boldsymbol{y}_k$ is the measurement vector.

The first step is the fitting of the autoregressive AR model to the measurements using least square:

$$\begin{bmatrix} \boldsymbol{y}_{i+1}^T \\ \boldsymbol{y}_{i+2}^T \\ \vdots \\ \boldsymbol{y}_{i+j}^T \end{bmatrix} = \begin{bmatrix} \boldsymbol{y}_i^T & \boldsymbol{y}_{i-1}^T & \cdots & \boldsymbol{y}_1^T \\ \boldsymbol{y}_{i+1}^T & \boldsymbol{y}_i^T & \cdots & \boldsymbol{y}_2^T \\ \vdots & \vdots & & \vdots \\ \boldsymbol{y}_{i+j-1}^T & \boldsymbol{y}_{i+j-2}^T & \cdots & \boldsymbol{y}_j^T \end{bmatrix} \begin{bmatrix} -\mathbf{A}_1^T \\ -\mathbf{A}_2^T \\ \vdots \\ -\mathbf{A}_i^T \end{bmatrix} + \begin{bmatrix} \boldsymbol{\varepsilon}_{i+1}^T \\ \boldsymbol{\varepsilon}_{i+2}^T \\ \vdots \\ \boldsymbol{\varepsilon}_{i+j}^T \end{bmatrix} \Rightarrow \begin{bmatrix} \boldsymbol{\varepsilon}_{i+1}^T \\ \boldsymbol{\varepsilon}_{i+2}^T \\ \vdots \\ \boldsymbol{\varepsilon}_{i+j}^T \end{bmatrix} = \begin{bmatrix} \boldsymbol{y}_{i+1}^T \\ \boldsymbol{y}_{i+2}^T \\ \vdots \\ \boldsymbol{y}_{i+j}^T \end{bmatrix} - \begin{bmatrix} \hat{\boldsymbol{y}}_{i+1}^T \\ \hat{\boldsymbol{y}}_{i+2}^T \\ \vdots \\ \hat{\boldsymbol{y}}_{i+j}^T \end{bmatrix} \tag{B.2}$$

similar to the number of block rows in SSI, i is the order of the AR model, j is the

available data length for least square.

The error sequence obtained from least square fitting can be used as pseudo-inputs of the system and therefore, a pseudo-ARX model (AR model with exogenous input) can be built and again, fitted with least square:

$$\hat{\boldsymbol{y}}_k = -\mathbf{A}_1 \boldsymbol{y}_{k-1} - \mathbf{A}_2 \boldsymbol{y}_{k-2} - ... - \mathbf{A}_i \boldsymbol{y}_{k-i} + \mathbf{C}_1 \boldsymbol{\varepsilon}_{k-1} + \mathbf{C}_2 \boldsymbol{\varepsilon}_{k-2} + ... + \mathbf{C}_{ic} \boldsymbol{\varepsilon}_{k-ic}$$

$$\begin{bmatrix} \boldsymbol{y}_{2i+1}^T \\ \boldsymbol{y}_{2i+2}^T \\ \vdots \\ \boldsymbol{y}_{2i+j}^T \end{bmatrix} = \left[\begin{array}{cccc|cccc} \boldsymbol{y}_{2i}^T & \boldsymbol{y}_{2i-1}^T & \cdots & \boldsymbol{y}_{i+1}^T & \boldsymbol{\varepsilon}_{2i}^T & \boldsymbol{\varepsilon}_{2i-1}^T & \cdots & \boldsymbol{\varepsilon}_{2i-ic+1}^T \\ \boldsymbol{y}_{2i+1}^T & \boldsymbol{y}_{2i}^T & \cdots & \boldsymbol{y}_{i+2}^T & \boldsymbol{\varepsilon}_{2i+1}^T & \boldsymbol{\varepsilon}_{2i}^T & \cdots & \boldsymbol{\varepsilon}_{2i-ic+2}^T \\ \vdots & \vdots & & \vdots & \vdots & \vdots & & \vdots \\ \boldsymbol{y}_{2i+j-1}^T & \boldsymbol{y}_{2i+j-2}^T & \cdots & \boldsymbol{y}_{i+j}^T & \boldsymbol{\varepsilon}_{2i+j-1}^T & \boldsymbol{\varepsilon}_{2i+j-2}^T & \cdots & \boldsymbol{\varepsilon}_{2i-ic+j}^T \end{array} \right] \begin{bmatrix} -\mathbf{A}_1^T \\ -\mathbf{A}_2^T \\ \vdots \\ -\mathbf{A}_i^T \\ \mathbf{C}_1^T \\ \mathbf{C}_2^T \\ \vdots \\ \mathbf{C}_{ic}^T \end{bmatrix} + error \quad (B.3)$$

where ic is the order selected for the pseudo-inputs and $\mathbf{C}_k \in \Re^{l \times l}$ are the pseudo-input matrix coefficients. The AR model coefficient matrices $\mathbf{A}_k$ are, therefore, arranged and associated with the state-space model as that is done in the conventional state-space realization algorithm [61]. This two step algorithm is also knwon as the AR-ARX method. However, our target is to compare the PEM/LS algorithm with the orthogonal projection used in SSI-DATA, to later, be able to apply the SSI procedure to PEM.

Actually, the equation (B.2) can be rewritten as a simple least square problem in the notation of SSI:

$$\mathbf{Y}_{f/1,1}^T = \mathbf{Y}_{p/1,i}^T \, \boldsymbol{\alpha}_{\mathbf{A}} + error \quad (B.4)$$

where $\mathbf{Y}_{f/1,1}^T$ is the transpose of the 1$^{\text{st}}$ row of the future output measurement shown in (2.26) and $\mathbf{Y}_{p/1,i}^T$ is the transpose if the past output measurements from row 1 to row i.

131

$\boldsymbol{\alpha}_A$ is the matrix containing the AR model coefficient matrices $\mathbf{A}_k$.

The well-known least square solution for $\boldsymbol{\alpha}_A$ and, $\hat{\mathbf{Y}}_{f/1,1}^T$, the best estimate of

$\mathbf{Y}_{f/1,1}^T$ is:

$$\boldsymbol{\alpha}_A = \left(\left(\mathbf{Y}_{p/1,i}^T\right)^T \mathbf{Y}_{p/1,i}^T\right)^{-1}\left(\mathbf{Y}_{p/1,i}^T\right)^T \mathbf{Y}_{f/1,1}^T = \left(\mathbf{Y}_{p/1,i}\mathbf{Y}_{p/1,i}^T\right)^{-1}\mathbf{Y}_{p/1,i}\mathbf{Y}_{f/1,1}^T \tag{B.5a}$$

$$\hat{\mathbf{Y}}_{f/1,1}^T = \mathbf{Y}_{p/1,i}^T\left(\mathbf{Y}_{p/1,i}\mathbf{Y}_{p/1,i}^T\right)^{-1}\mathbf{Y}_{p/1,i}\mathbf{Y}_{f/1,1}^T \tag{B.5b}$$

$$\hat{\mathbf{Y}}_{f/1,1} = \mathbf{Y}_{f/1,1}\mathbf{Y}_{p/1,i}^T\left(\mathbf{Y}_{p/1,i}\mathbf{Y}_{p/1,i}^T\right)^{-1}\mathbf{Y}_{p/1,i} \tag{B.5c}$$

where (B.5c) is simply the transpose of (B.5b), and one can realize that (B.5c) is almost the same expression that (2.34), the only difference is that (2.34) gets at once the best estimate for whole future measurement $\mathbf{Y}_{f/1,i}$ while only one block row is obtained by (B.5c).

Therefore, the projection matrix obtained in (2.38) can be interpreted as, in fact, the best estimate of the future output in terms of the past outputs in a least square sence, *i.e.*, orthogonal projection of the future data in the past data. Therefore, PEM and SSI-DATA can be combined and stated at the following:

First, obtain the projection matrix, *i.e.*, the best estimates of the future data From (2.37) and (2.38). Then, the error matrix can be obtained by computing the difference between the estimate data matrix and the original data matrix:

$$\bar{\mathbf{e}} = \mathbf{Y}_f - \mathbf{P}_i = \begin{bmatrix} y_{i+1} & y_{i+2} & \cdots & y_{i+j} \\ y_{i+2} & y_{i+3} & \cdots & y_{i+j+1} \\ \vdots & \vdots & & \vdots \\ y_{2i} & y_{2i+1} & \cdots & y_{2i+j-1} \end{bmatrix} - \begin{bmatrix} \hat{y}_{i+1} & \hat{y}_{i+2} & \cdots & \hat{y}_{i+j} \\ \hat{y}_{i+2} & \hat{y}_{i+3} & \cdots & \hat{y}_{i+j+1} \\ \vdots & \vdots & & \vdots \\ \hat{y}_{2i} & \hat{y}_{2i+1} & \cdots & \hat{y}_{2i+j-1} \end{bmatrix} = \begin{bmatrix} \varepsilon_{i+1} & \varepsilon_{i+2} & \cdots & \varepsilon_{i+j} \\ \varepsilon_{i+2} & \varepsilon_{i+3} & \cdots & \varepsilon_{i+j+1} \\ \vdots & \vdots & & \vdots \\ \varepsilon_{2i} & \varepsilon_{2i+1} & \cdots & \varepsilon_{2i+j-1} \end{bmatrix} \tag{B.6}$$

After this point, the same elements of the error matrix can be grouped and

averaged along its antidiagonal as that is done for SSA (section 2.7) and considered as pseudo-inputs. In a similar way than the projection for SI using input-output data [47], and using the LQ decomposition formulated before, the Hankel data matrix can be now re-arranged by inserting the corresponding pseudo-input matrix:

$$\mathbf{H}' \equiv \begin{bmatrix} y_{i+1} & y_{i+2} & \cdots & y_{i+j'} \\ y_{i+2} & y_{i+3} & \cdots & y_{i+j'+1} \\ \vdots & \vdots & & \vdots \\ y_{2i} & y_{2i+1} & \cdots & y_{2i+j'-1} \\ \hline \varepsilon_{2i-ic+1} & \varepsilon_{2i-ic+2} & \cdots & \varepsilon_{2i-ic+j'} \\ \varepsilon_{2i-ic+2} & \varepsilon_{2i-ic+3} & \cdots & \varepsilon_{2i-ic+j'+1} \\ \vdots & \vdots & & \vdots \\ \varepsilon_{2i} & \varepsilon_{2i+1} & \cdots & \varepsilon_{2i+j'-1} \\ \hline y_{2i+1} & y_{2i+2} & \cdots & y_{2i+j'} \\ y_{2i+2} & y_{2i+3} & \cdots & y_{2i+j'+1} \\ \vdots & \vdots & & \vdots \\ y_{3i} & y_{3i+1} & \cdots & y_{3i+j'-1} \end{bmatrix} = \begin{bmatrix} \mathbf{Y}'_p \\ \hline \mathbf{E}_p \\ \hline \mathbf{Y}'_f \end{bmatrix} \tag{B.7}$$

where ic is the order selected for the pseudo-inputs, and since the first i data points were used in the least square fitting, for this second stage the data begins at point $i+1$, j' is used for the row length instead of j, since length of this latter is no longer the same.

A new projection matrix can be obtained by performing a similar LQ decomposition to (B.5):

$$\mathbf{H}' = \begin{matrix} li \\ l \times ic \\ li \end{matrix} \begin{matrix} \overset{li}{\overbrace{}} & \overset{l \times ic}{\overbrace{}} & \overset{li}{\overbrace{}} & \overset{j'}{\overbrace{}} \\ \begin{pmatrix} \mathbf{L}'_{11} & \mathbf{0} & \mathbf{0} \\ \mathbf{L}'_{21} & \mathbf{L}'_{22} & \mathbf{0} \\ \mathbf{L}'_{31} & \mathbf{L}'_{32} & \mathbf{L}'_{33} \end{pmatrix} \begin{pmatrix} \mathbf{Q}'^T_1 \\ \mathbf{Q}'^T_2 \\ \mathbf{Q}'^T_3 \end{pmatrix} \end{matrix} = \mathbf{L}'\mathbf{Q}' \tag{B.8}$$

$$\mathbf{P}' = \mathbf{Y}'_f \Big/ \begin{bmatrix} \mathbf{Y}'_p \\ \mathbf{E}_p \end{bmatrix} = \mathbf{O}'\hat{\mathbf{X}}'_i = \begin{pmatrix} \mathbf{L}'_{31} & \mathbf{L}'_{32} \end{pmatrix} \begin{pmatrix} \mathbf{Q}'^T_1 \\ \mathbf{Q}'^T_2 \end{pmatrix} \in \Re^{li \times j'} \tag{B.9}$$

Thereafter, the SVD can be applied to $\mathbf{O}' = \begin{pmatrix} \mathbf{L}'_{31} & \mathbf{L}'_{32} \end{pmatrix}$ to determine the system order, and to separate the system subspace (non-zero singular values) from the noise subspace (vanishing singular values), finally the system matrices ($\mathbf{A}$,$\mathbf{C}$) can be determined as presented before in the section 2.3.

In fact, the LQ decomposition of the Hankel matrix shown in (B.7) is the transpose version of the least square problem shown in (B.3):

$$
\begin{bmatrix}
\mathbf{y}_{2i+1}^T & \mathbf{y}_{2i+2}^T & \cdots & \mathbf{y}_{3i}^T \\
\mathbf{y}_{2i+2}^T & \mathbf{y}_{2i+3}^T & \cdots & \mathbf{y}_{3i+1}^T \\
\vdots & \vdots & & \vdots \\
\mathbf{y}_{2i+j'}^T & \mathbf{y}_{2i+j'+1}^T & \cdots & \mathbf{y}_{3i+j'-1}^T
\end{bmatrix}
=
\left[
\begin{array}{cccc|cccc}
\mathbf{y}_{2i}^T & \mathbf{y}_{2i-1}^T & \cdots & \mathbf{y}_{i+1}^T & \boldsymbol{\varepsilon}_{2i}^T & \boldsymbol{\varepsilon}_{2i-1}^T & \cdots & \boldsymbol{\varepsilon}_{2i-ic+1}^T \\
\mathbf{y}_{2i+1}^T & \mathbf{y}_{2i}^T & \cdots & \mathbf{y}_{i+2}^T & \boldsymbol{\varepsilon}_{2i+1}^T & \boldsymbol{\varepsilon}_{2i}^T & \cdots & \boldsymbol{\varepsilon}_{2i-ic+2}^T \\
\vdots & \vdots & & \vdots & \vdots & \vdots & & \vdots \\
\mathbf{y}_{2i+j'-1}^T & \mathbf{y}_{2i+j'-2}^T & \cdots & \mathbf{y}_{i+j'}^T & \boldsymbol{\varepsilon}_{2i+j'-1}^T & \boldsymbol{\varepsilon}_{2i+j'-2}^T & \cdots & \boldsymbol{\varepsilon}_{2i-ic+j'}^T
\end{array}
\right]
\begin{bmatrix}
-\mathbf{A}_{11}^T & -\mathbf{A}_{12}^T & \cdots & -\mathbf{A}_{1i}^T \\
-\mathbf{A}_{21}^T & -\mathbf{A}_{22}^T & \cdots & -\mathbf{A}_{2i}^T \\
\vdots & \vdots & & \vdots \\
-\mathbf{A}_{i1}^T & -\mathbf{A}_{i2}^T & \cdots & -\mathbf{A}_{ii}^T \\
\hline
\mathbf{C}_{11}^T & \mathbf{C}_{12}^T & \cdots & \mathbf{C}_{1i}^T \\
\mathbf{C}_{21}^T & \mathbf{C}_{22}^T & \cdots & \mathbf{C}_{2i}^T \\
\vdots & \vdots & & \vdots \\
\mathbf{C}_{ic1}^T & \mathbf{C}_{ic2}^T & \cdots & \mathbf{C}_{ii}^T
\end{bmatrix}
+ error
\quad (B.10)
$$

where the block column vector containing the system information in (B.2) $\boldsymbol{\alpha}_{\mathbf{A}}$ now become a matrix of i block columns. However, this latter mentioned matrices are not our interest, what is desired is the best estimate of the future data $\mathbf{Y}'_f$ in terms of the past data $\mathbf{Y}'_p$ and pseudo-input $\mathbf{E}_p$, $i.e.$, $\mathbf{Y}'_f / \begin{bmatrix} \mathbf{Y}'_p \\ \mathbf{E}_p \end{bmatrix}$: orthogonal projection matrix of $\mathbf{Y}'_f$ in the row space spanned by $\mathbf{Y}'_p$ and $\mathbf{E}_p$.

So far, the comparison between SSI-DATA and PEM/SSI is complete, and in simple words, PEM/SSI is actually a 2-step-projection SSI-DATA algorithm, since the orthogonal projection is done twice. The performance of this algorithm is tested and discussed in Chapter 3, where simulation study is carried out.

Appendix C: Novelty index through Kalman-Filter-based prediction error

If a structure is subject to damage, the system matrix **A** will be changed, therefore, if the system information is stored at the undamaged state and used for prediction of the structure response, it is expected that, as the damage is accentuated, the prediction will deviate in a higher degree from the measured response. Statistics made from this prediction error serve as useful indexes for damage detection [62]. Discrete-time Kalman filter with unknown inputs is the instrument used to perform this prediction error task.

To make the Kalman Filter more adaptive, the version of Kalman Filter shown in chapter 3 of [60] is used, which consiste of 2 states: prediction state and updating state. Formulas to be implemented are shown below, detail derivation of each statement can be find in [60].

Firstly assume an initial system state $\hat{x}$ (*0/0*) and prediction error covariance **P**(*0/0*) and later, using the system matrices (**A**,**C**) and the stochastic noise covariances (**Q**,**R**) computed by SSI-DATA algorithm shown in section 2.5, the Kalman filter algorithm can be implemented as follows:

(1) Given the state $\hat{x}$ (*k/k*) and **P**(*k/k*), compute the predicted state:

$$\hat{x}(k+1/k) = \mathbf{A}\hat{x}(k/k) \tag{C.1}$$

where (*k+1/k*) means the predicted state at *k+1* step from step *k*.

(2) Compute the predicted error covariance matrix:

$$\mathbf{P}(k+1/k) = \mathbf{A}\mathbf{P}(k/k)\mathbf{A}^T + \mathbf{Q} \tag{C.2}$$

(3) Compute the Kalman gain matrix:

$$\mathbf{K}(k+1) = \mathbf{P}(k+1/k)\mathbf{C}^T \left[\mathbf{C}\mathbf{P}(k+1/k)\mathbf{C}^T + \mathbf{R}\right]^{-1} \tag{C.3}$$

(4) Compute the updated system state from the measurement $y(k+1)$

$$\hat{\boldsymbol{x}}(k+1/k+1) = \hat{\boldsymbol{x}}(k+1/k) + \mathbf{K}(k+1)[\boldsymbol{y}(k+1) - \mathbf{C}\hat{\boldsymbol{x}}(k+1/k)] \tag{C.4}$$

where $(k+1/k+1)$ means the updated state at $k+1$ step from measurement at $k+1$.

(5) Compute the updated error covariance matrix:

$$\mathbf{P}(k+1/k+1) = [\mathbf{I} - \mathbf{K}(k+1)\mathbf{C}]\mathbf{P}(k+1/k)[\mathbf{I} - \mathbf{K}(k+1)\mathbf{C}]^T + \mathbf{K}(k+1)\mathbf{R}\mathbf{K}^T(k+1) \tag{C.5}$$

(6) set $k = k+1$ and return to step (1).

This 2-state Kalman filter differs from the Forward Innovation model [62], because the Kalman Gain of this latter is constant and it is obtained by solving Riccatti equation. However, the 2-state Kalman Gain is updated at each state by the prediction error covariance.

The prediction error can be computed at the predicted state as:

$$\boldsymbol{e}(k+1/k+1) = \boldsymbol{y}(k+1) - \mathbf{C}\hat{\boldsymbol{x}}(k+1/k) \tag{C.6}$$

since $\hat{\boldsymbol{x}}(k+1/k)$ is determined only by the system matrix $\mathbf{A}$, degree of change in the system will be reflected directly in the computed prediction error. The advantage of the use of the 2-state Kalman filter is that, the update state will correct this deviation at every step, which could be very large when the system was severely changed.

Several statistical indexes can be defined based on the computed prediction error

sequence. The Novelty Index (*NI*) [62] is defined as the Euclidean norm of the multivariate error vector:

$$NI_k^E = \left\| \boldsymbol{e}_k \right\| \tag{C.7}$$

or as the Mahalanobis norm:

$$NI_k^M = \sqrt{\boldsymbol{e}_k^T \boldsymbol{\Sigma}_k^{-1} \boldsymbol{e}_k} \tag{C.8}$$

where $\boldsymbol{\Sigma}_k = \mathbf{y}\mathbf{y}^T / N$ is the sample covariance marix, *N* is the number of sample points contained in the sequence, and **y** is the multivariate measurement sequence. In online applications, a moving window with a given length can be used to sample a sequence from the online prediction error and later, statistics can be calculated from the norm sequence being considered.

Moreover, an outlier analysis can be done from the norm sequences. The mean $\bar{\theta}'$ and standard deviation $\bar{\sigma}'$ can be calculated from the undamaged state:

$$\bar{\theta}' = \frac{1}{N_l} \sum_{k=1}^{N_l} NI'_k \quad \text{and} \quad \bar{\sigma}' = \sqrt{\frac{1}{N_l} \sum_{k=1}^{N_l} \left(NI'_k - \bar{\theta}' \right)^2} \tag{C.9}$$

where the prime sign indicates undamaged state. An upper control limit can be defined as a horizontal line:

$$UCL = \bar{\theta}' + \alpha\bar{\sigma}' \tag{C.10}$$

If the coefficient α is chosen as 3, this corresponds to an interval of 99.7% confidence for a real normal distribution. The outlier analysis is then performed by counting how many times the prediction error norms (in % of total samples) are passing over the upper limit, in the given windowed sequence. Additionally, the ratio of the

137

mean values and standard variations of *NI*, between damaged and reference states respectively, can also be used as damage indicators.

A similar strategy can be applied to each sensor individually and (C.7) become a simple Root-Mean-Square of the error sequence. Then, (C.9) and (C.10) can be applied to the sampled data of each sensor individually; comparison between the outcome of each sensor allows to find the damage location, since is expected that the damage occurs in the place where is larger the prediction error.

Table 2-1   Comparison of identification results of SSI-COV

	Excitation level and number of rows*	Frequency						Damping					
		1	2	3	4	5	6	1	2	3	4	5	6
True answer	---	**1.0107**	**2.2795**	**3.9280**	**5.4433**	**7.5773**	**8.2290**	**0.0351**	**0.0299**	**0.0101**	**0.0088**	**0.0105**	**0.0058**
velocity measurements (noise free data)													
Square Toeplitz matrix	50 dB, 2~10 rows	1.0131	2.2554	3.9181	5.4500	7.5837	8.2146	0.0424	0.0282	0.0106	0.0111	0.0110	0.0060
	50 dB, 2~30 rows	1.0143	2.2538	3.9190	5.4515	7.5830	8.2149	0.0467	0.0301	0.0100	0.0110	0.0111	0.0059
	50 dB, 2~100 rows	1.0039	2.2666	3.9175	5.4522	7.5902	8.2216	0.0321	0.0255	0.0105	0.0115	0.0090	0.0072
Rectangular Toeplitz matrix	50 dB, 2~70 rows	1.0033	2.2575	3.9184	5.4527	7.5823	8.2167	0.0320	0.0260	0.0108	0.0112	0.0108	0.0061
	50 dB, 2~100 rows	1.0121	2.2637	3.9240	5.4565	7.5767	8.2427	0.0406	0.0297	0.0091	0.0125	0.0081	0.0078
	50 dB, 2~150 rows	1.0046	2.2646	3.9178	5.4526	7.5865	8.2198	0.0324	0.0253	0.0106	0.0115	0.0098	0.0068
Acceleration measurements (noisy data)													
Square Toeplitz matrix	0 dB, 5~100 rows	1.0058	2.2659	3.9321	5.4659	7.5751	8.2349	0.0607	0.0270	0.0087	0.0066	0.0094	0.0096
	10 dB, 5~100 rows	1.0158	2.2657	3.9229	5.4553	7.5808	8.2430	0.0321	0.0306	0.0093	0.0118	0.0075	0.0087
	50 dB, 5~125 rows	1.0010	2.2686	3.9162	5.4510	7.5896	8.2250	0.0328	0.0234	0.0105	0.0117	0.0083	0.0074
Rectangular Toeplitz matrix	0 dB, 10~100 rows	0.6522	2.3028	3.9342	5.4737	7.5775	8.2389	1.0000	0.0744	0.0111	0.0080	0.0082	0.0086
	0 dB, 20~100 rows	1.0274	2.2637	3.9311	5.4768	7.5787	8.2394	0.3001	0.0374	0.0113	0.0080	0.0082	0.0085
	0 dB, 30~100 rows	1.0019	2.2634	3.9298	5.4778	7.5799	8.2402	0.0815	0.0348	0.0112	0.0080	0.0082	0.0086
	0 dB, 50~100 rows	1.0039	2.2657	3.9319	5.4648	7.5746	8.2353	0.0688	0.0276	0.0087	0.0067	0.0094	0.0096
	10 dB, 50~150 rows	1.0174	2.2653	3.9232	5.4558	7.5805	8.2418	0.0417	0.0300	0.0093	0.0119	0.0075	0.0086
	50 dB, 2~300 rows	---**	---**	3.9639	5.4806	7.5969	8.2275	---**	---**	0.1506	0.0484	0.0161	0.0085
	50 dB, 10~200 rows	---**	2.2791	3.9178	5.4520	7.5874	8.2228	---**	0.0385	0.0108	0.0117	0.0090	0.0071
	50 dB, 20~150 rows	1.0349	2.2646	3.9177	5.4521	7.5861	8.2214	0.0267	0.1205	0.0106	0.0115	0.0095	0.0068
	50 dB, 30~150 rows	1.0063	2.2649	3.9177	5.4520	7.5864	8.2219	0.0576	0.0253	0.0106	0.0115	0.0093	0.0069
	50 dB, 50~150 rows	0.9975	2.2651	3.9172	5.4522	7.5876	8.2230	0.0407	0.0240	0.0107	0.0115	0.0090	0.0071

* Number of rows for square Toeplitz matrix, means the number of block rows and columns from the beginning to the end of the stabilization diagram. But for rectangular Toeplitz matrix the first value is the number of block columns which is fixed, and the second value is the maximum block rows reached in the stabilization diagram. The solutions are picked from the last row of the diagram.

** The empty spaces means not identified parameters.

Table 3-1 Comparison of the identified frequencies of the 6 DOF simulation example

	Algorithm	Frequency						Error (%)					
		1	2	3	4	5	6	1	2	3	4	5	6
True answer	---	**1.0107**	**2.2795**	**3.9280**	**5.4433**	**7.5773**	**8.2290**						
Added 50% white noise	SSI-COV	0.9806	2.2619	3.9329	5.4764	7.5804	8.2441	2.98	0.77	0.13	0.61	0.04	0.18
	SSI-DATA	0.9865	2.2623	3.9328	5.4763	7.5780	8.2419	2.40	0.76	0.12	0.61	0.01	0.16
	PEM/SSI	0.9898	2.2716	3.9315	5.4771	7.5789	8.2431	2.07	0.35	0.09	0.62	0.02	0.17
Added 100% white noise	SSI-COV	0.9846	2.2581	3.9315	5.4778	7.5806	8.2393	2.59	0.94	0.09	0.63	0.04	0.13
	SSI-DATA	0.9795	2.2557	3.9322	5.4770	7.5795	8.2445	3.09	1.04	0.11	0.62	0.03	0.19
	PEM/SSI	0.9878	2.2476	3.9351	5.4814	7.5827	8.2491	2.26	1.40	0.18	0.70	0.07	0.24
Added 200% white noise	SSI-COV	0.9807	2.2662	3.9342	5.4716	7.5752	8.2332	2.97	0.58	0.16	0.52	0.03	0.05
	SSI-DATA	0.9747	2.2499	3.9314	5.4846	7.5693	8.2504	3.57	1.30	0.09	0.76	0.11	0.26
	PEM/SSI	0.9841	2.2656	3.9296	5.4838	7.5830	8.2422	2.63	0.61	0.04	0.74	0.08	0.16

Table 3-2 Comparison of the identified damping ratios of the 6 DOF simulation example

	Algorithm	Damping						Error (%)					
		1	2	3	4	5	6	1	2	3	4	5	6
True answer	---	**0.0351**	**0.0299**	**0.0101**	**0.0088**	**0.0105**	**0.0058**						
Added 50% white noise	SSI-COV	0.0643	0.0296	0.0105	0.0085	0.0074	0.0086	83.07	0.81	3.50	3.22	29.70	47.55
	SSI-DATA	0.0598	0.0302	0.0105	0.0077	0.0067	0.0075	70.21	1.08	4.25	12.08	36.43	29.23
	PEM/SSI	0.0574	0.0272	0.0092	0.0079	0.0061	0.0074	63.41	8.89	9.20	9.83	41.77	27.19
Added 100% white noise	SSI-COV	0.0659	0.0312	0.0090	0.0081	0.0063	0.0085	87.63	4.34	10.65	7.32	40.04	46.20
	SSI-DATA	0.0714	0.0293	0.0097	0.0072	0.0068	0.0083	103.28	1.84	3.59	17.50	35.44	43.96
	PEM/SSI	0.0520	0.0283	0.0085	0.0059	0.0069	0.0071	47.98	5.21	15.95	33.22	34.51	23.22
Added 200% white noise	SSI-COV	0.0669	0.0338	0.0117	0.0099	0.0072	0.0068	90.48	13.31	16.15	13.29	31.85	17.16
	SSI-DATA	0.0551	0.0249	0.0128	0.0095	0.0079	0.0073	56.89	16.75	26.97	8.48	24.78	25.29
	PEM/SSI	0.0449	0.0260	0.0093	0.0078	0.0065	0.0074	27.87	12.99	7.84	10.52	37.89	27.81

Table 3-3 Different set of frequency and k_3 values used in the modeling

Natural frequency	Duffing parameter k_3
0.1 Hz	-0.26 k = -0.10264
1 Hz	-80 k = -3158.2734
10 Hz	-7300 k = -28819244.85

*mass was assumed unitary, therefore the required stiffness k can be derived.

Table 3-4 Comparison of identification results for nonlinear signals

		Frequency		Damping	
		50 rows	200 rows	50 rows	200 rows
0.1 Hz, k_3 : -0.26k	SSI-COV	0.0960	0.0960	0.095	0.091
	SSI-DATA	0.0955	0.0964	0.071	0.080
1 Hz, k3 : -80k	SSI-COV	0.9642	0.9608	0.010	0.017
	SSI-DATA	0.9624	0.9598	0.018	0.014
10 Hz, k3 : -7300k	SSI-COV	9.8719	9.8812	0.010	0.009
	SSI-DATA	9.9054	9.8879	0.011	0.009

* SSI-COV uses 10000 points for correlation, SSI-DATA uses 10000 columns for Hankel matrix. System order is defined as 2. Rows are increased from 2 to 200 rows.

Table 3-5 Comparing identification results of two close frequencies with signal generated by ambient vibrations

		Frequency		**Damping ratio**	
	Correct answer	0.3432	0.3681	0.01	0.04
	Noise free				
SSI-DATA	10000 columns, 5 to 100 rows, system order 4	0.3450	0.3669	0.023	0.027
SSI-COV	10000 points covariance, 5 to 100 rows, system order 4	0.3437	0.3668	0.025	0.023
	Noisy				
SSI-DATA	10000 columns, 5 to 150 rows, system order 4	0.3429	0.3682	0.017	0.035
SSI-COV	10000 points covariance, 5 to 150 rows, system order 4	0.3425	0.3673	0.020	0.037
SSA-SSI-COV	16 SV, 3500 points covariance, 2 to 100 rows, system order 4	0.3454	0.3603	0.009	0.007
SSA-SSI-COV	14 SV, 3500 points covariance, 2 to 100 rows, system order 4	0.3456	0.3606	0.006	0.007
SSA-SSI-COV	8 SV, 3500 points covariance, 2 to 100 rows, system order 4	0.3466	0.3656	0.011	0.010
SSA-SSI-COV	4 SV, 3500 points covariance, 2 to 100 rows, system order 4	0.3420	0.3647	-0.001	-0.005
SSA-SSI-COV	8 SV, 3500 points covariance, 2 to 100 rows, system order 8	0.3483	0.3640	-0.003	-0.008
SSA-SSI-COV	14 SV, 3500 points covariance, 2 to 100 rows, system order 8	0.3447	0.3657	0.009	-0.005

Table 4-1 Comparison of the identified modal parameters of Canton Tower

FEM Mode number			Wind	Wind	1	2	3	4	5	6	7
FEM Mode		Frequency	--	--	**0.1100**	**0.1590**	**0.3470**	**0.3680**	**0.4000**	**0.4610**	**0.4850**
SSI-COV	18000 points,	Frequency	0.0404	0.0409	0.0902	0.1392	0.3652	0.4243	0.4752	0.5060	0.5223
Order 90	300 rows	Damping	0.2885	1.0000	0.0693	0.0135	-0.0004	-0.0008	0.0018	0.0018	0.0000
SSI-DATA	8000 columns,	Frequency	0.0110	0.0339		0.1377	0.3655	0.4402	0.4774	0.5193	
Order 90	280 rows	Damping	1.0000	0.0727		0.0080	-0.0015	0.0048	-0.0002	-0.0017	
SSA-SSI-COV	15000 points	Frequency	0.0345	0.0465	0.0958	0.1391	0.3648	0.4232	0.4756	0.5063	0.5226
136SV, order 120	170 rows	Damping	0.2368	0.1978	0.0700	0.0106	0.0024	0.0056	0.0006	0.0024	-0.0008
SSA-SSI-COV	15000 points	Frequency	0.0376	0.0572		0.1388	0.3644	0.4238	0.4757	0.5063	0.5226
95SV, order 90	140 rows	Damping	0.2412	0.3991		0.0122	0.0042	0.0039	0.0006	0.0031	-0.0008

FEM Mode number			8	9	10	11	12	13	14	15
FEM Mode		Frequency	**0.7380**	**0.9020**	**0.9970**	**1.0380**	**1.1220**	**1.2440**	**1.5030**	**1.7260**
SSI-COV	18000 points,	Frequency	0.7982	0.9649	1.1507	1.2031	1.2525	1.3891	1.6401	1.9463
Order 90	300 rows	Damping	0.0041	0.0013	0.0002	0.0058	0.0022	0.0036	0.0022	0.0053
SSI-DATA	8000 columns,	Frequency	0.7977	0.9654	1.1794	1.2281		1.3848	1.6397	1.9428
Order 90	280 rows	Damping	0.0009	-0.0004	0.0017	0.0010		0.0008	0.0003	0.0014
SSA-SSI-COV	15000 points	Frequency	0.7986	0.9652	1.1509	1.1932	1.2518	1.3899	1.6407	1.9445
136SV, order 120	170 rows	Damping	0.0020	0.0006	0.0006	0.0008	0.0013	0.0018	0.0010	0.0026
SSA-SSI-COV	15000 points	Frequency	0.7986	0.9653	1.1512		1.2517	1.3899	1.6407	1.9446
95SV, order 90	140 rows	Damping	0.0022	0.0008	0.0007		0.0015	0.0020	0.0012	0.0031

Note: rows are block rows. 18000 points and 15000 points are the data length to perform covariance.

Table 4-2 Comparison of the identified modal parameters of Canton Tower for different sampling rates

FEM Mode number			Wind	Wind	1	2	3	4	5	6	7
FEM Mode		Frequency	--	--	**0.1100**	**0.1590**	**0.3470**	**0.3680**	**0.4000**	**0.4610**	**0.4850**
SSI-COV	18000 points,	Frequency	0.0404	0.0409	0.0902	0.1392	0.3652	0.4243	0.4752	0.5060	0.5223
Order 90	300 rows	Damping	0.2885	1.0000	0.0693	0.0135	-0.0004	-0.0008	0.0018	0.0018	0.0000
Sampling rate: 25 Hz	9721 points,	Frequency	0.0397	0.0407	0.0899	0.1391	0.3659	0.4250	0.4755	0.5057	0.5222
SSI-COV Order 90	140 rows	Damping	0.3034	0.6891	0.2008	0.0133	-0.0020	-0.0014	0.0026	0.0028	0.0001
Sampling rate: 10 Hz	3721 points	Frequency	0.0363	0.0452	0.0924	0.1384	0.3658	0.4242	0.4750	0.5059	0.5222
SSI-COV Order 90	140 rows	Damping	0.4674	0.1504	0.0195	0.0085	0.0020	0.0013	0.0016	0.0019	0.0002
Sampling rate: 5 Hz	1721 points	Frequency	There are 6 identified		0.0929	0.1383	0.3657	0.4240	0.4746	0.5061	0.5223
SSI-COV Order 62	140 rows	Damping	frequencies in this range		0.0143	0.0057	0.0023	0.0011	0.0021	0.0016	0.0003

FEM Mode number			8	9	10	11	12	13	14	15	
FEM Mode		Frequency	**0.7380**	**0.9020**	**0.9970**	**1.0380**	**1.1220**	**1.2440**	**1.5030**	**1.7260**	
SSI-COV	18000 points,	Frequency	0.7982	0.9649	1.1507	1.2031	1.2525	1.3891	1.6401	1.9463	
Order 90	300 rows	Damping	0.0041	0.0013	0.0002	0.0058	0.0022	0.0036	0.0022	0.0053	
Sampling rate: 25 Hz	9721 points,	Frequency	0.7983	0.9646	1.1504	1.1940	1.2525	1.3877	1.6400	1.9464	
SSI-COV Order 90	140 rows	Damping	0.0040	0.0013	0.0003	0.0033	0.0022	0.0036	0.0023	0.0053	
Sampling rate: 10 Hz	3721 points	Frequency	0.7984	0.9649	1.1505	1.1909	1.2515	1.3890	1.6398	1.9483	
SSI-COV Order 90	140 rows	Damping	0.0036	0.0018	0.0003	0.0016	0.0023	0.0028	0.0026	0.0066	
Sampling rate: 5 Hz	1721 points	Frequency	0.7987	0.9650	1.1504	1.1917	1.2513	1.3888	1.6361	1.9346	
SSI-COV Order 62	140 rows	Damping	0.0023	0.0021	0.0003	0.0018	0.0017	0.0021	0.0019	0.0012	

Table 6-1   Sudden reduction of modal frequencies due to loss of stiffness

Points	Remaining stiffness in 1st DOF	Frequency						Damping ratio					
		1	2	3	4	5	6	1	2	3	4	5	6
1 ~ 4000	100 %	0.997	2.925	4.660	6.091	7.135	7.756	0.03	0.03	0.01	0.01	0.02	0.02
4001 ~ 7000	95 %	0.991	2.908	4.635	6.064	7.116	7.749	0.04	0.04	0.02	0.02	0.03	0.03
7001 ~ 10000	85 %	0.977	2.868	4.581	6.010	7.079	7.736	0.05	0.04	0.02	0.02	0.03	0.02
10001 ~ 13000	75 %	0.959	2.822	4.521	5.956	7.046	7.727	0.055	0.04	0.02	0.05	0.03	0.01
13001 ~ 16000	50 %	0.893	2.663	4.348	5.827	6.979	7.708	0.08	0.06	0.01	0.07	0.05	0.02
16001 ~ 20000	25 %	0.748	2.416	4.159	5.716	6.929	7.696	0.1	0.05	0.04	0.03	0.02	0.07

Table 6-2   Parameters for rSSA and RSSI-COV

Recursive Singular Spectrum Analysis (rSSA)			
	Block rows i'	Moving window length L'	SV
Case 1	100	4000	30
Case 2	100	2000	30
Case 3	100	1000	30
Case 4	100	1000	20
Recursive Covariance-driven Stochastic Subspace Identification (RSSI-COV)			
	Block rows i	Moving window length L	System order
For all case	100	5000	12

Table 7-1 Shaking table test analyzed by RSSI-COV and rSSA-SSI-COV

No.	Ground excitation	PGA	Stiffness before	Stiffness after	Release time	Data length
1	White Noise	100 gal	Remove brace	Remove brace	--	97.39 sec
2	White Noise	100 gal	Added brace	Added brace	--	97.39 sec
3	El Centro	100 gal	Added brace	Added brace	--	46.08 sec
4	El Centro	100 gal	Remove brace	Remove brace	--	46.08 sec
5	El Centro	100 gal	Added brace	Remove brace	14.75 sec	46.08 sec
6	El Centro	100 gal	Added brace	Remove brace	29.41 sec	46.08 sec
7	TCU082	100 gal	Added brace	Remove brace	38.15 sec	97.39 sec
8	TCU082	100 gal	Added brace	Remove brace	52.07 sec	97.39 sec

Table 7-2 Identified modal frequencies and damping ratios for case AB and NB from white noise excitation

Added brace			No brace		
Mode	Frequency (Hz)	Damping ratio	Mode	Frequency (Hz)	Damping ratio
1st X-translational	1.2356	0.0412	1st X-translational	1.0625	0.0621
1st torsion	2.2885	0.0034	1st torsion	2.2966	0.0033
2nd X-translational	3.6544	0.0044	2nd X-translational	3.1672	0.0004
3rd X-translational	5.2736	0.0078	3rd X-translational	4.9745	0.0076
2nd torsion	7.3282	0.00035	2nd torsion	7.2833	0.0035
3rd torsion	12.5522	0.00094	3rd torsion	12.5511	0.0014
			1st XY-translational	1.4096	-0.0025
			Coupled X-3rd Y-2nd translational	4.7274	0.0631
			3rd Y-translational	8.0540	0.0017
			Local mode	16.2471	-0.0031

Table 7-3 Outlier analysis from the damage detection of a 1-story 2-bay RC frame

subject to a series of white noise excitations

Outliers	WN1	WN2	WN3	WN4	WN5	WN6	WN7	WN8
Mahalanobis norm (%)	4.245	18.963	35.267	41.658	40.888	22.680	31.935	34.328
Euclidean norm (%)	3.383	7.752	16.976	16.833	18.008	9.097	13.337	17.839

Table 7-4 Bridge scour test schedule and arrangement

No.	Date	Sensors	Note
1	2011/01/19	12 velocity sensors	Signal oversteps the measurement range
2	2011/01/24	12 velocity sensors and displacement sensor at pier 3	Only velocity sensors 1~9 available
3	2011/01/26	12 velocity sensors	
4	2011/03/29	12 accelerometers, 4 velocity sensors at center of decks, and displacement meter at pier 3	

Table 7-5 Specification of VSE-15D velocity sensor AS-2000 accelerometer

	VSE-15D velocity sensor	AS-2000 accelerometer
Max. measuring range	± 0.1 m/s	± 2000 gal
Frequency range	0.2 to 0.7 Hz	DC ~ 100 Hz
Sensitivity	1000V/m/s	5mV/gal

Table 7-6 rSSA-SSI-COV and RSSI-COV model parameter for 2011/01/19 test

Parameter	rSSA-SSI-COV		RSSI-COV used alone
	rSSA	RSSI-COV	
Window length	L' = 3000 points	L = 5000 points	L = 5000 points
Block rows	i' = 100	i = 80	i = 110
Order	First 25singular values	First 20 singular values	First 20 singular values

Table 7-7 rSSA-SSI-COV model parameter for 2011/01/24 test

Parameter	rSSA-SSI-COV	
	rSSA	RSSI-COV
Window length	L' = 2000 points	L = 5000 points
Block rows	i' = 100	i = 80
Order	First 35singular values	First 34 singular values

Table 7-8 rSSA-SSI-COV and RSSI-COV model parameter for 2011/01/26 test

Parameter	rSSA-SSI-COV	
	rSSA	RSSI-COV
Window length	L' = 3000 points	L = 5000 points
Block rows	i' = 100	i = 80
Order	First 25singular values	First 24 singular values

Table 7-9 rSSA-SSI-COV and RSSI-COV model parameter for 2011/03/29 test

Parameter	rSSA-SSI-COV		RSSI-COV used alone
	rSSA	RSSI-COV	
Window length	L' = 3000 points	L = 5000 points	L = 5000 points
Block rows	i' = 100	i = 80	i = 100
Order	First 45 singular values	First 44 singular values	First 46 singular values

Table 7-10 Selected correlation coefficient **R** for mode discrimination

	2011/01/19	2011/01/26	2011/03/29
1st mode shape	R > 0.99	R > 0.98	R > 0.98
2nd mode shape	R > 0.97	R > 0.95	R > 0.92
3rd mode shape	Not identified	Not identified	R > 0.90 and R > 0.70
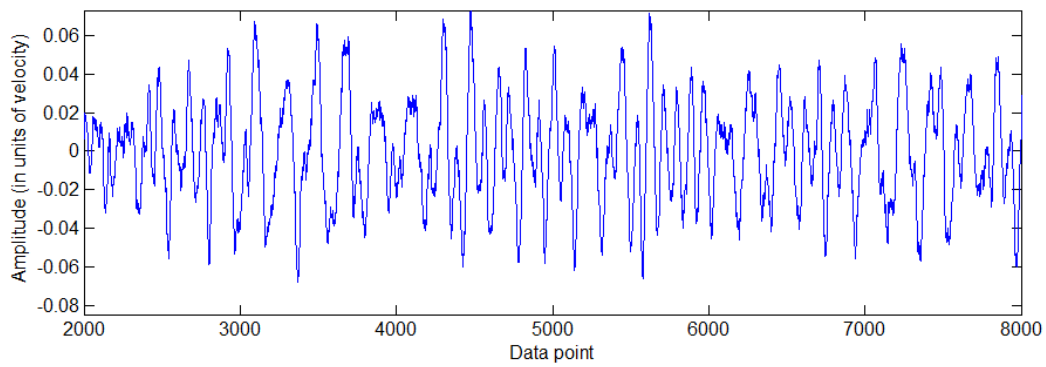
Figure 2-1 Simulated velocity response at 6th DOF, system subjected to white noise excitation.
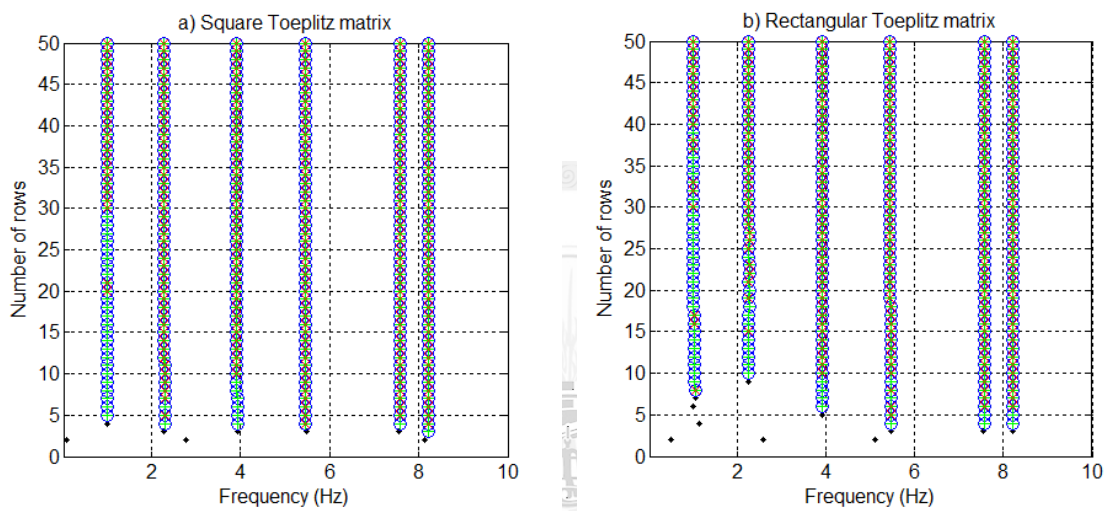
Figure 2-2 Comparison between the 2nd and 3rd version of stabilization diagram.
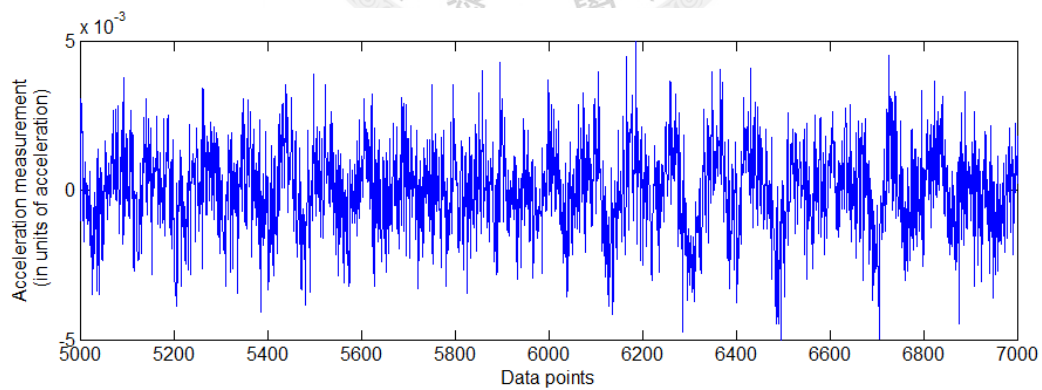
Figure 2-3 Simulated acceleration measurement at 6th DOF. The direct transmitted external acceleration serves as the measurement noise. A trend can be observed within the randomness caused by the $\mathbf{D}u_k$ term.

146
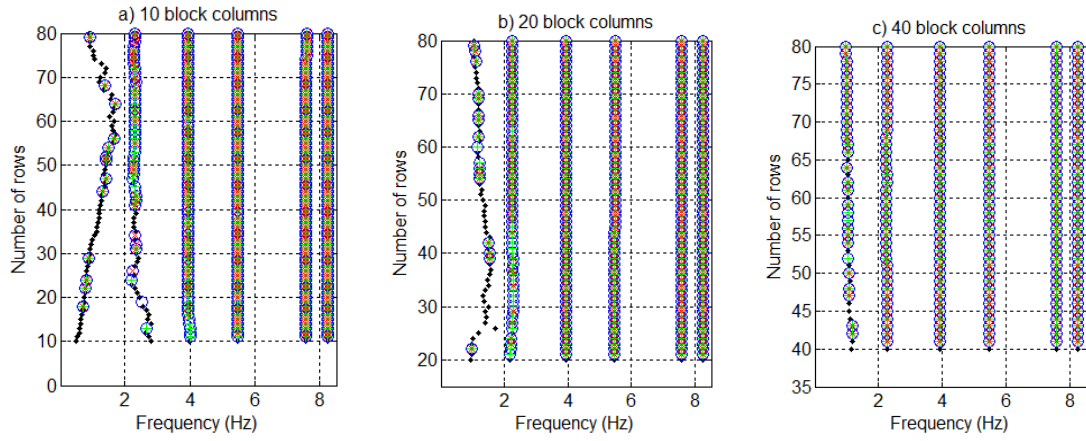
Figure 2-4 Effects of noise and insufficient Toeplitz matrix columns in the use of rectangular Toeplitz matrix.
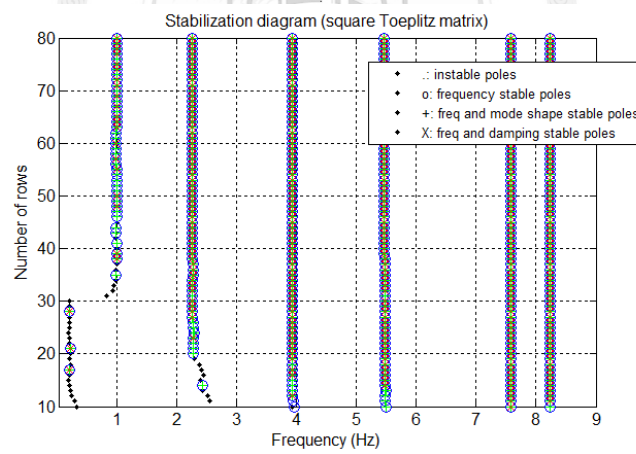
Figure 2-5 Effects of noise in the stabilization diagram by square Toeplitz matrix.
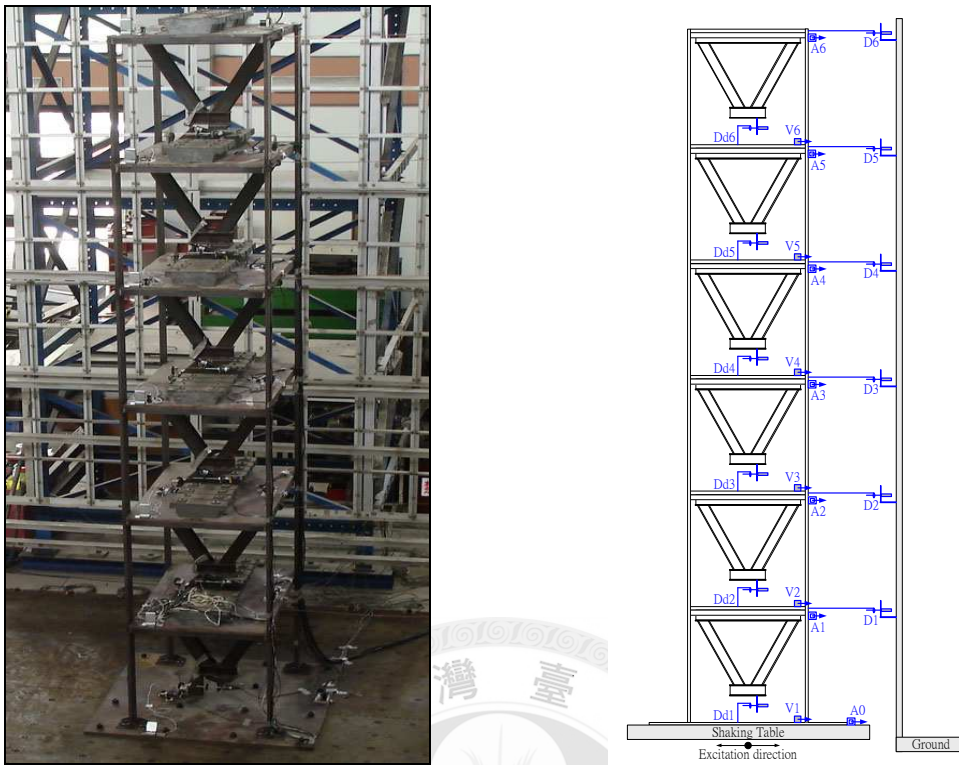
Figure 2-6 Photo of the 6-story structure and its instrumentation. AX are the accelerometers.
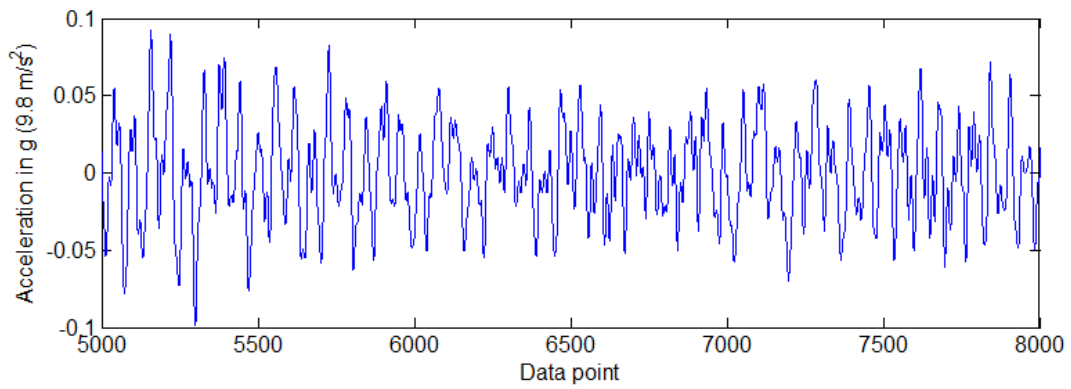
Figure 2-7   Plot of part of the acceleration response measured at 6th floor.

148
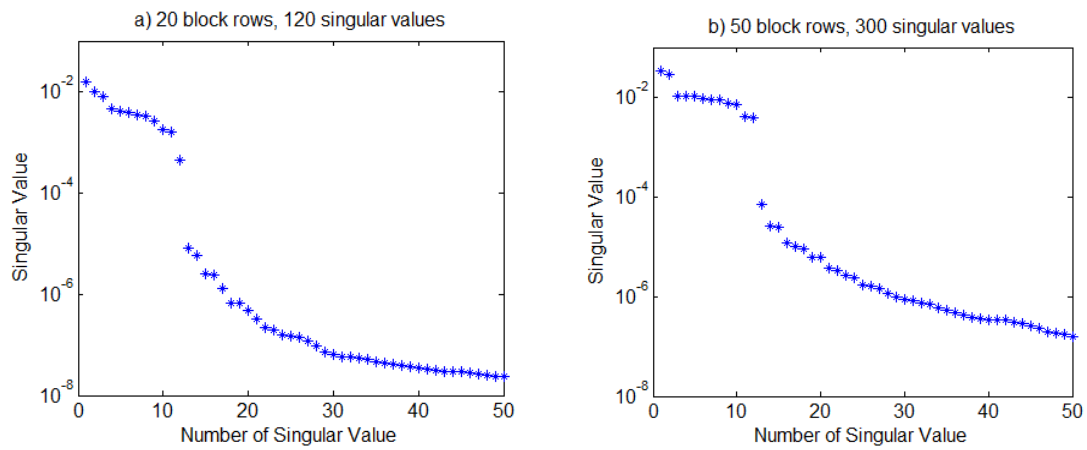
Figure 2-8 Singular values determined from SVD of square Toeplitz matrix. As the matrix size increases, the gap between the first 12 and the rest become more clear.
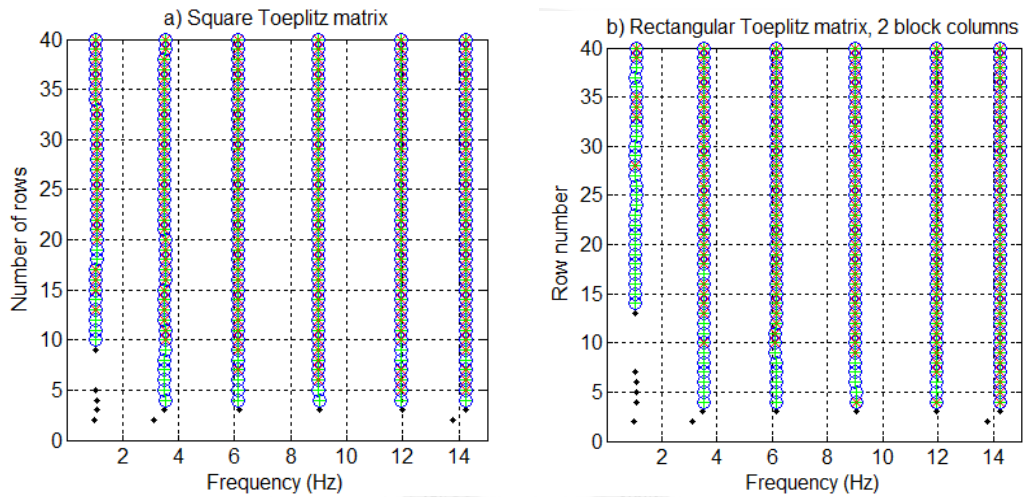
Figure 2-9 Stabilization diagram made using a) square Toeplitz matrix and, b) rectangular Toeplitz matrix.
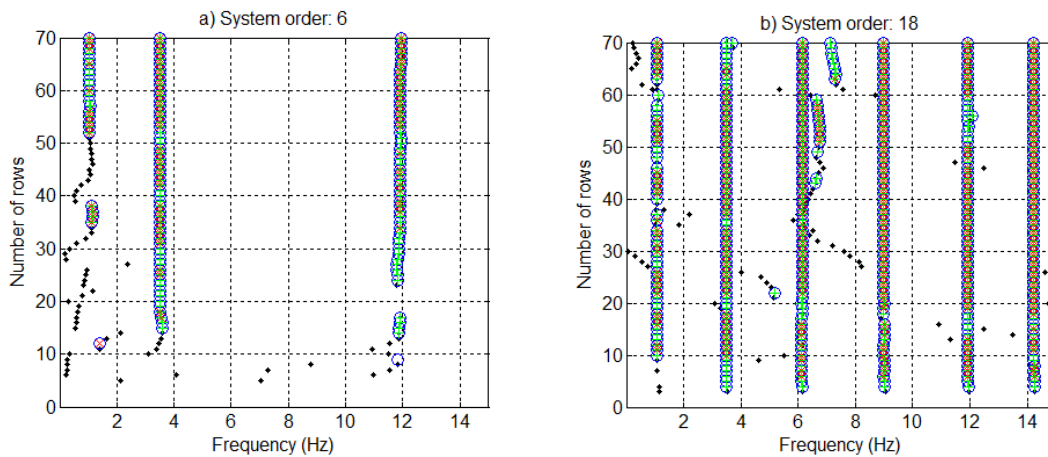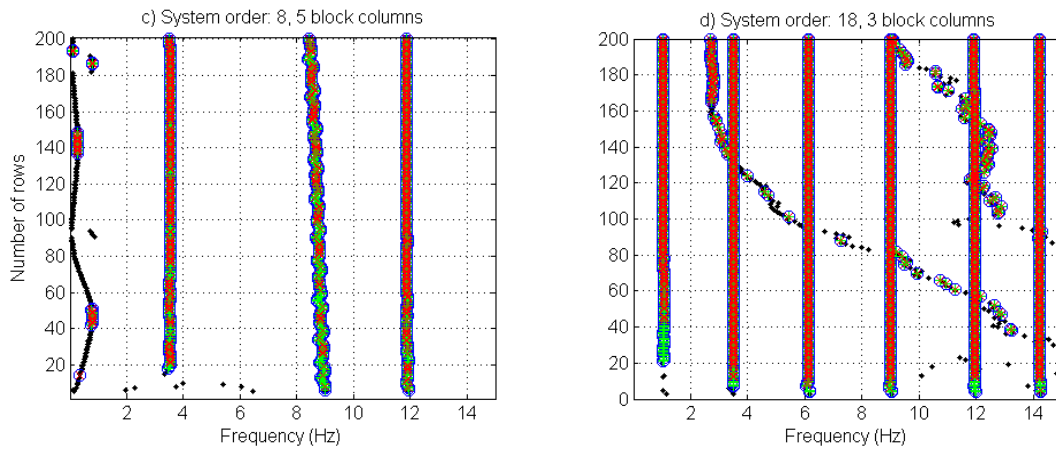
Figure 2-10   Square Toeplitz matrix: a) Underestimation, b) Overestimation of the system order.

Rectangular Toeplitz matrix: c) Underestimation, d) Overestimation of the system order.
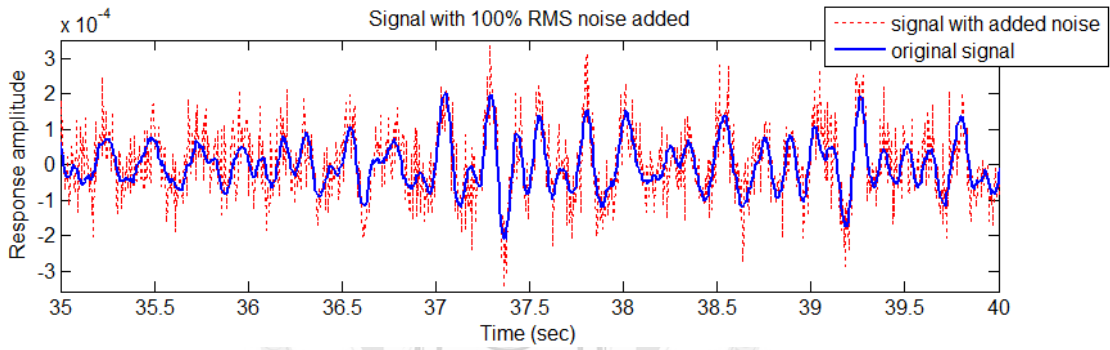
Figure 3-1   Measurement of 6th DOF with added 100% white noise.
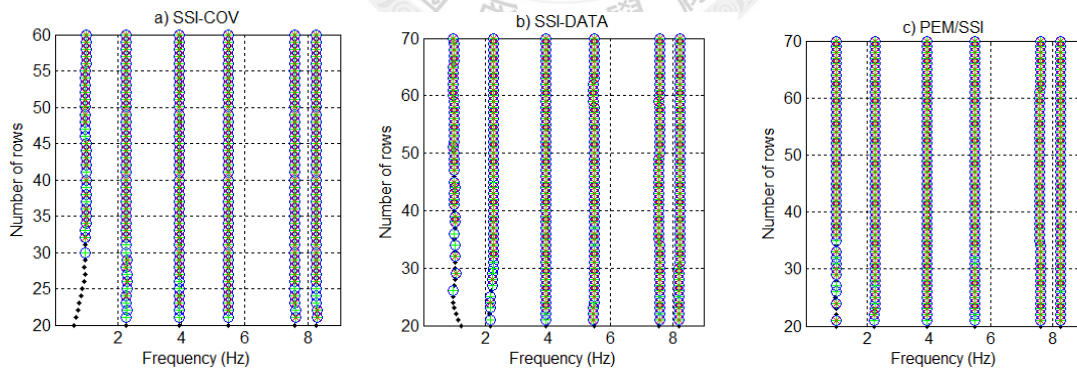
Figure 3-2   Stabilization diagram for added 100% white noise.
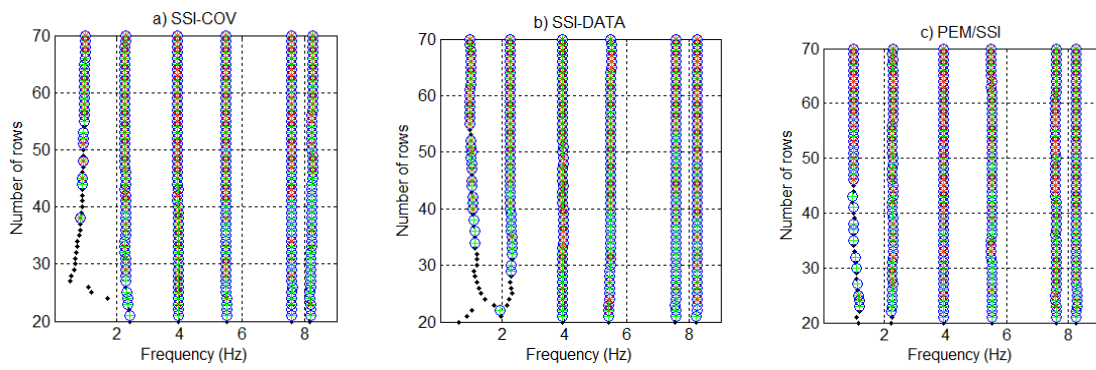
Figure 3-3   Stabilization diagram for added 200% white noise.
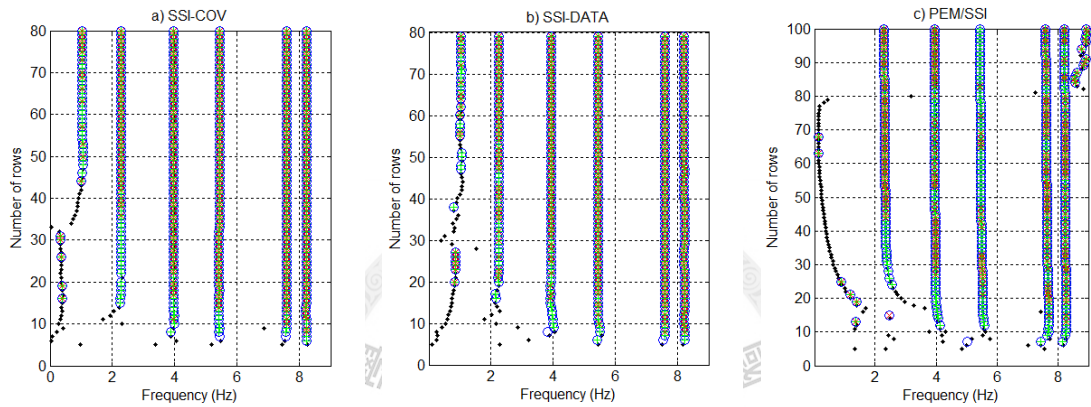
Figure 3-4   Stabilization diagram for added noise correlated with output.
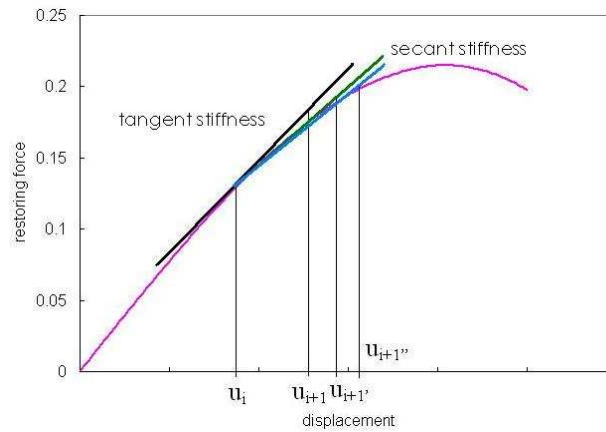
Figure 3-5   Iterative procedure to find the secant stiffness and next- step displacement.
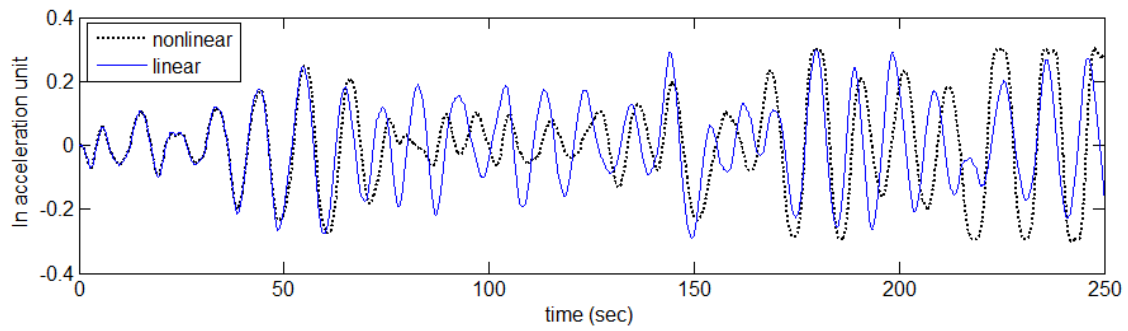
Figure 3-6　comparison between linear and nonlinear acceleration response. Frequency: 0.1 Hz. k_3 : -0.26k.
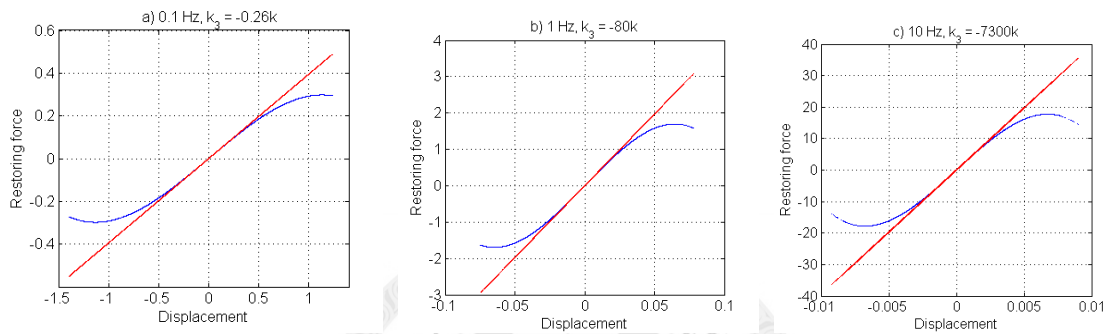
Figure 3-7 Comparison between nonlinear and linear restoring force.
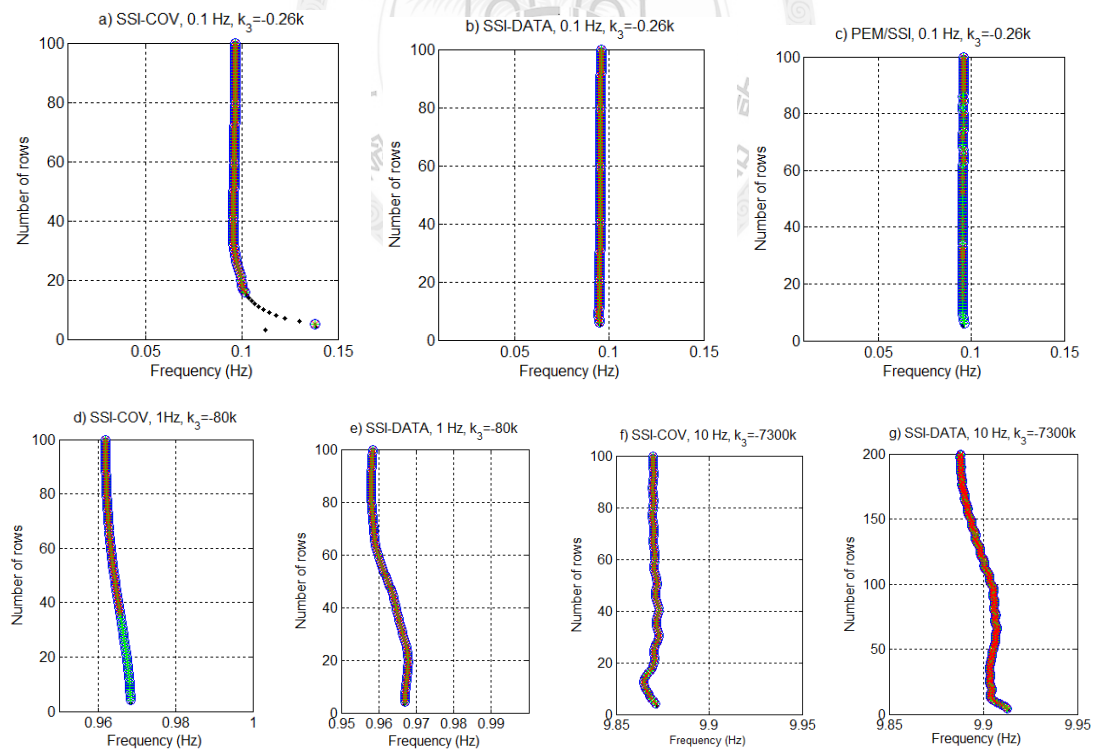
Figure 3-8　Stabilization diagram for 0.1 Hz, k_3 : -0.26k. a) SSI-COV, b) SSI-DATA, c) PEM/SSI.

For 1 Hz, k_3 : -80k. d) SSI-COV. e) SSI-DATA. For 10 Hz, k_3 : -7300k. f) SSI-COV. g) SSI-DATA.
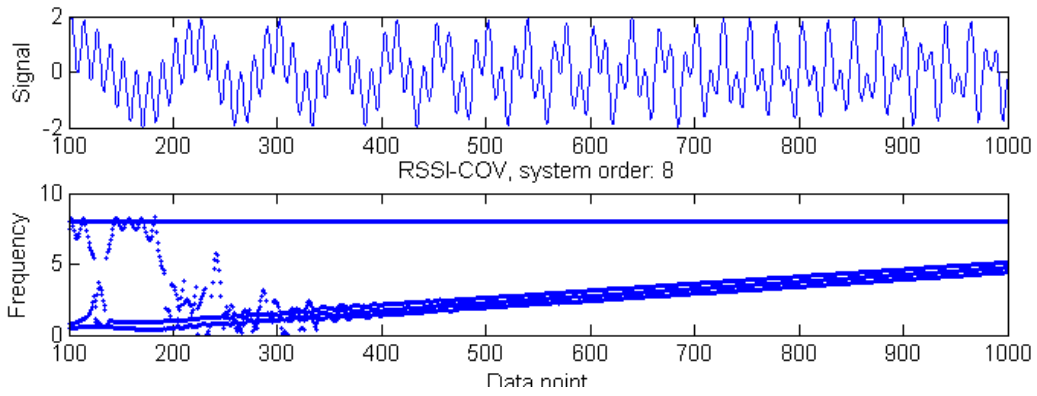
Figure 3-9 Generate signal with two closely-spaced frequency and a time-varying frequency.
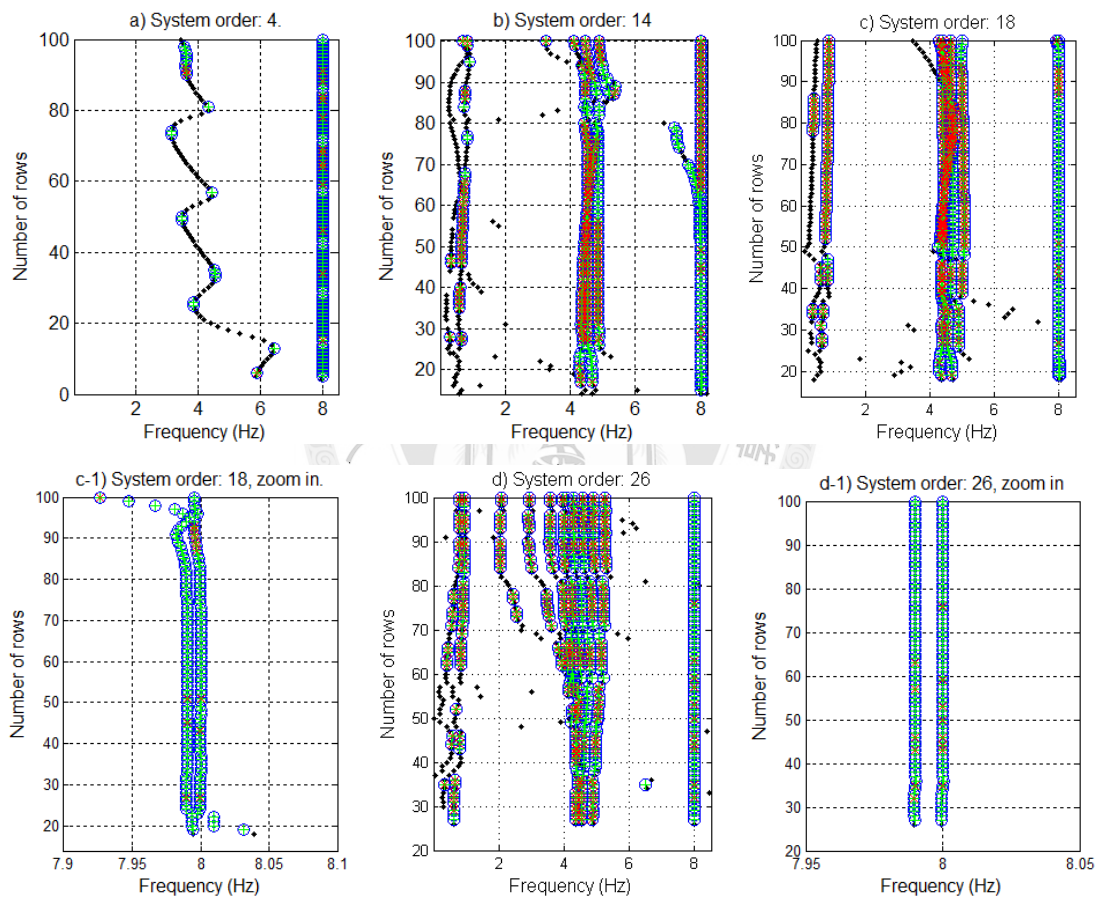
Figure 3-10 Stabilization diagram built with SSI-COV for different system orders.
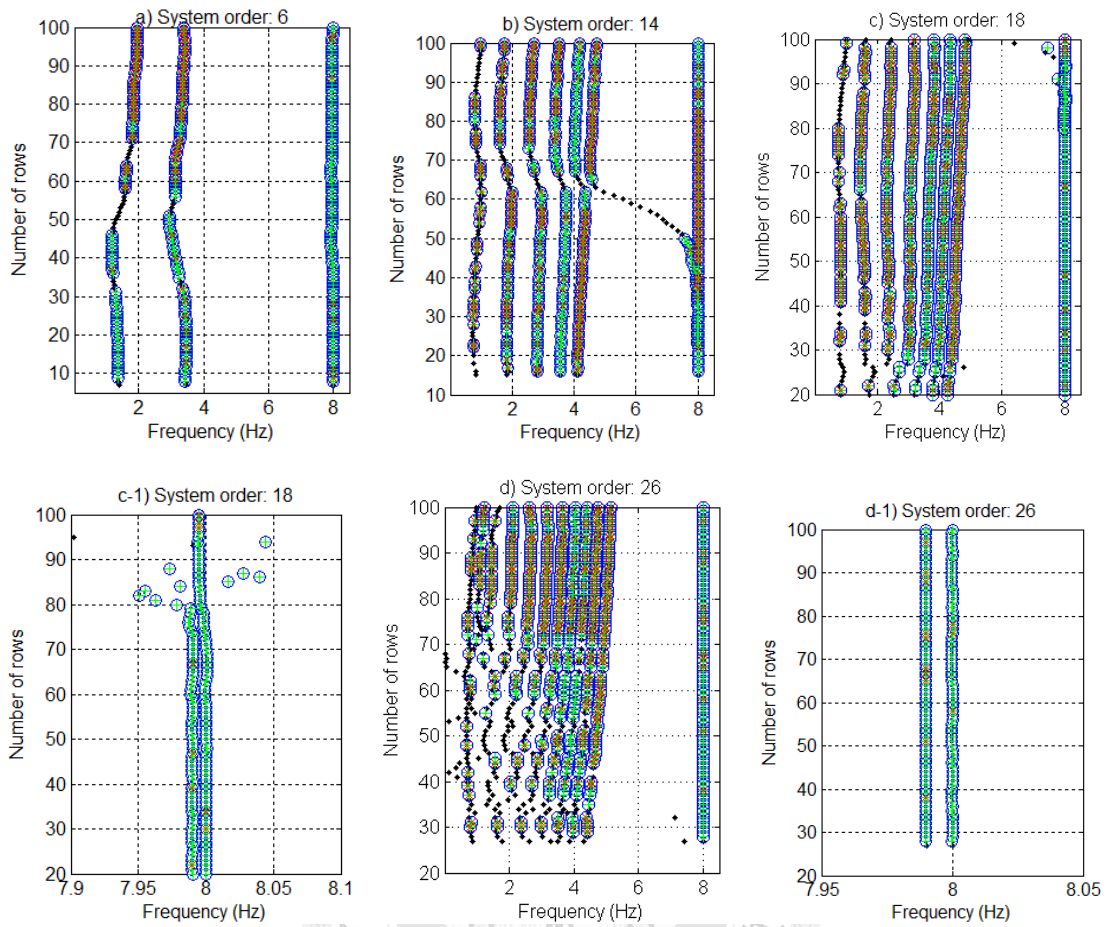
Figure 3-11   Stabilization constructed with SSI-DATA with different system orders.
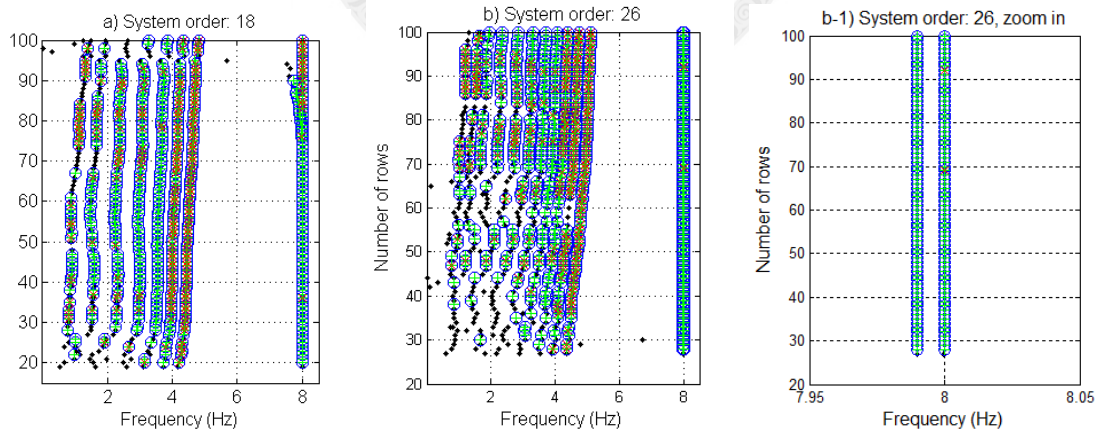
Figure 3-12   Stabilization constructed with PEM/SSI with different system orders.
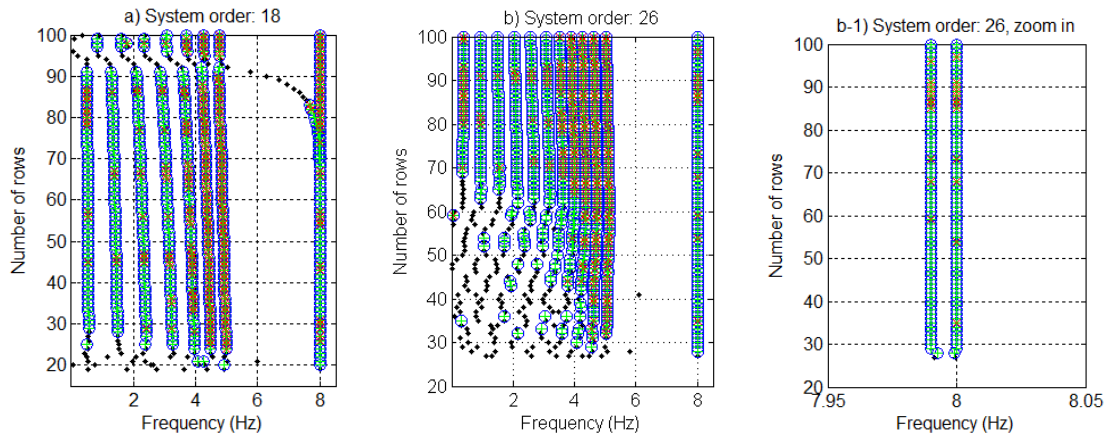
Figure 3-13 Stabilization diagram obtained by applying directly SVD to Hankel data matrix for different system orders.
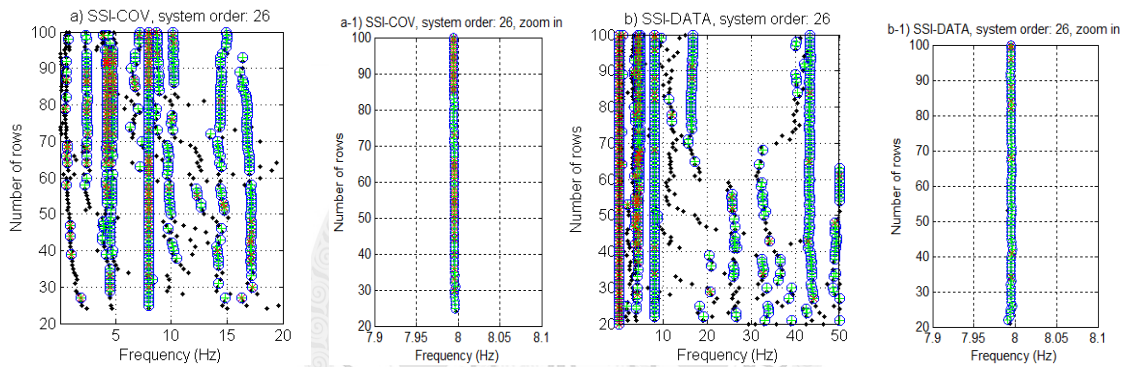
Figure 3-14 Stabilization diagram for signal with 5% noise added.
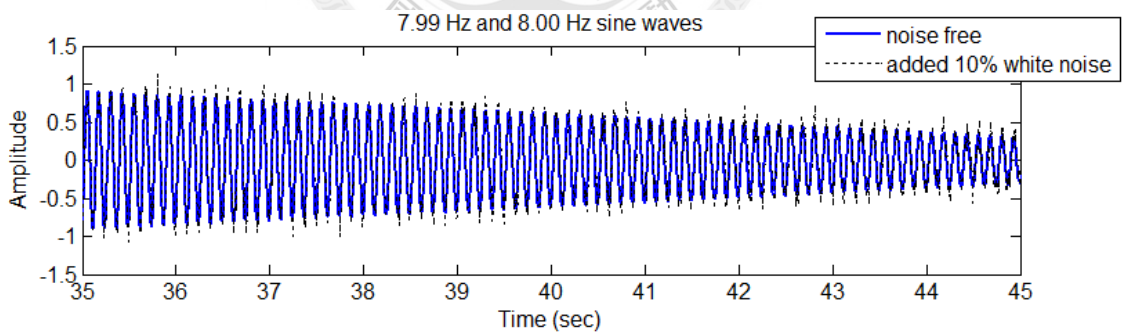
Figure 3-15 7.99 Hz and 8.00 Hz sine wave with added 10% noise.

155
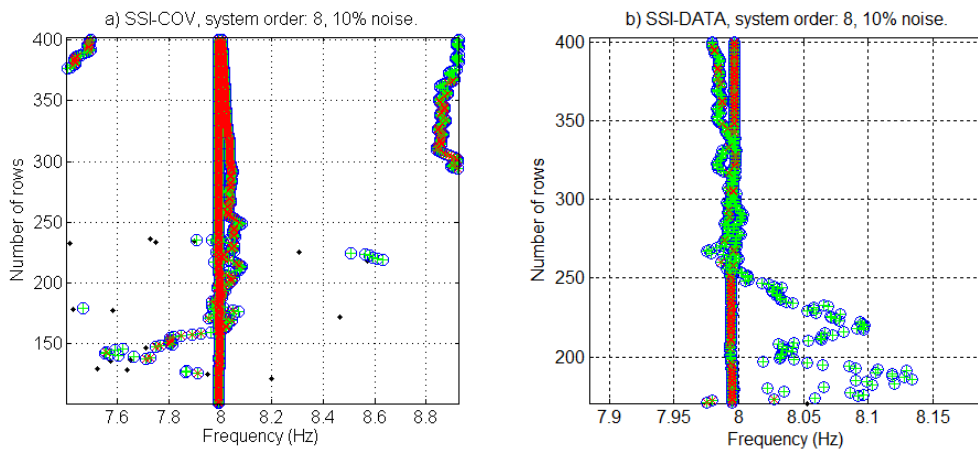
Figure 3-16   Stabilization diagram for signal with added 10% noise, 7.99 Hz and 8.00 Hz.
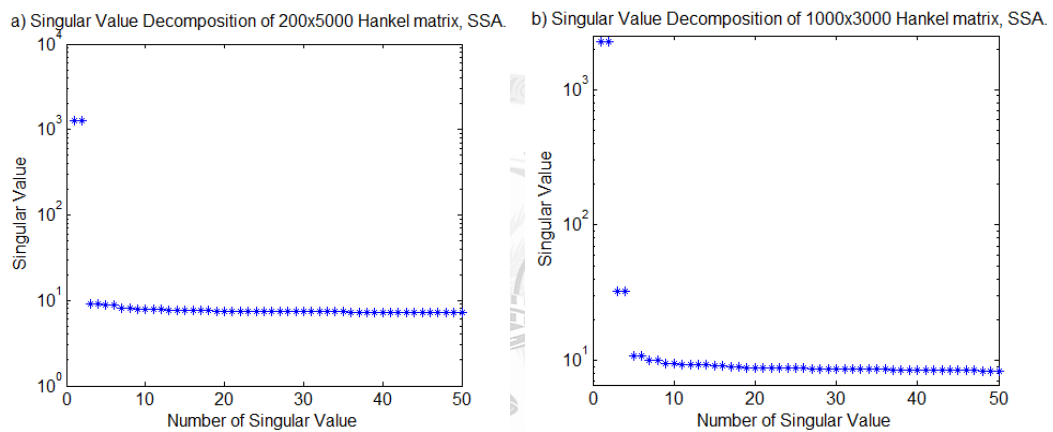
Figure 3-17   Variation of singular values with different dimensions of Hankel matrix.
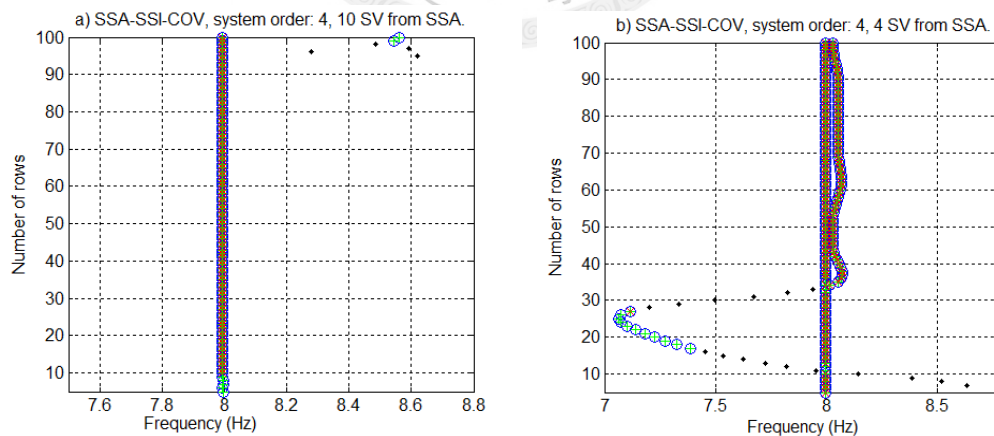
Figure 3-18   Stabilization diagram constructed using SSA-SSI-COV with a) 10 Singular values from 200x5000 Hankel matrix, and b) 4 Singular values from 1000x3000 Hankel matrix, SSA.
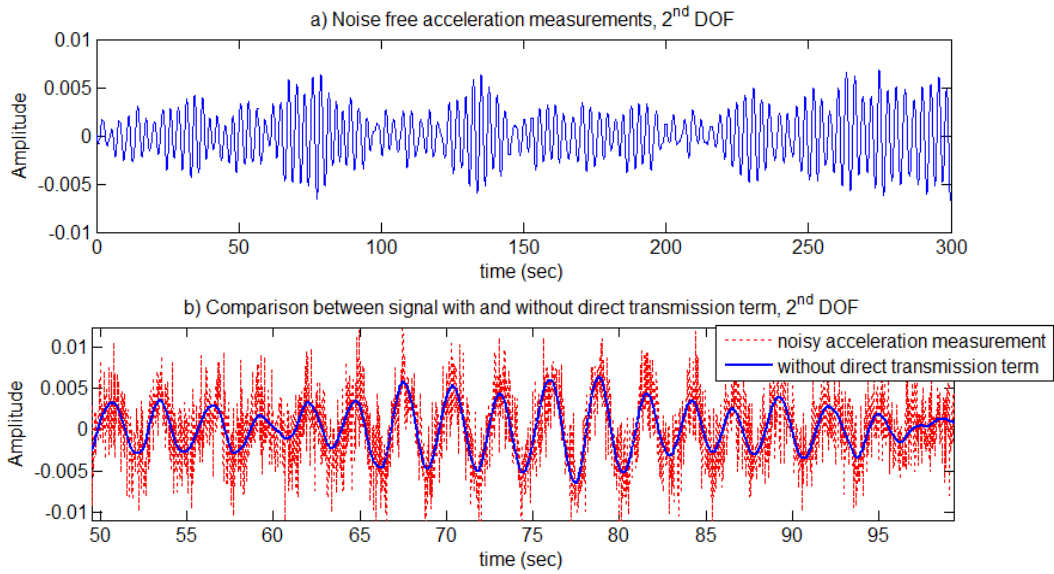
Figure 3-19   Simulated system response. a) Noise free acceleration measurements,

b) with direct transmission of input acceleration.
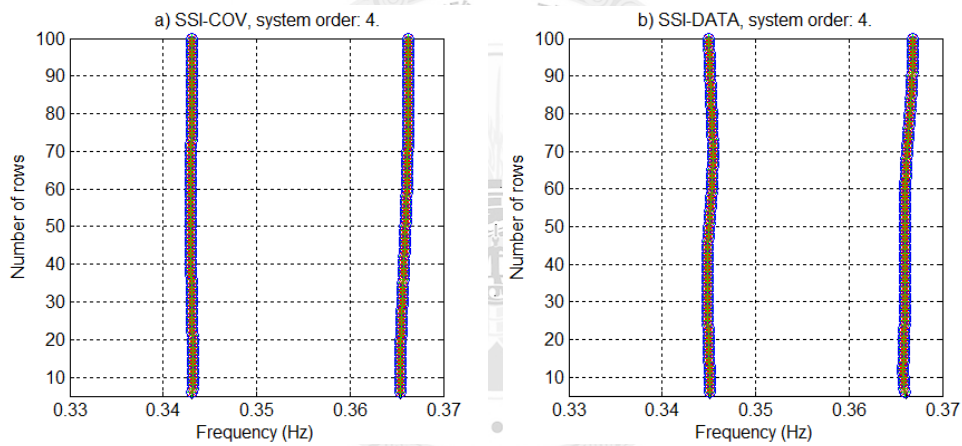
Figure 3-20   Stabilization diagram built using a) SSI-COV and b) SSI-DATA,

10000 columns is used in SSI-DATA and 10000 points were used in covariance for SSI-COV.
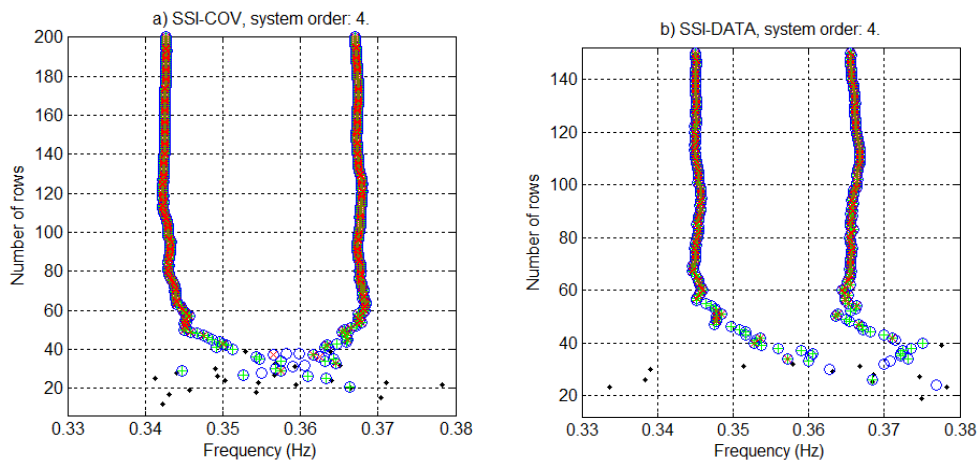
Figure 3-21   Stabilization diagram for noisy acceleration measurements, a) SSI-COV and b) SSI-DATA. 10000

columns is used in SSI-DATA and 10000 points were used in covariance for SSI-COV.
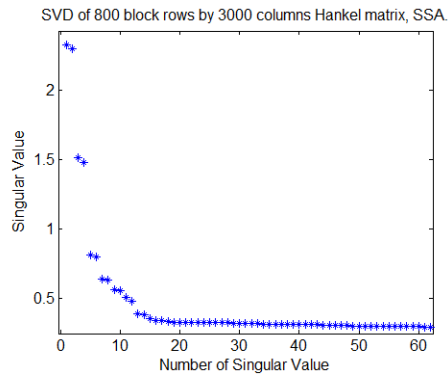
Figure 3-22 Variation of singular values in a 800 block rows by 3000 columns Hankel matrix, applying SSA.
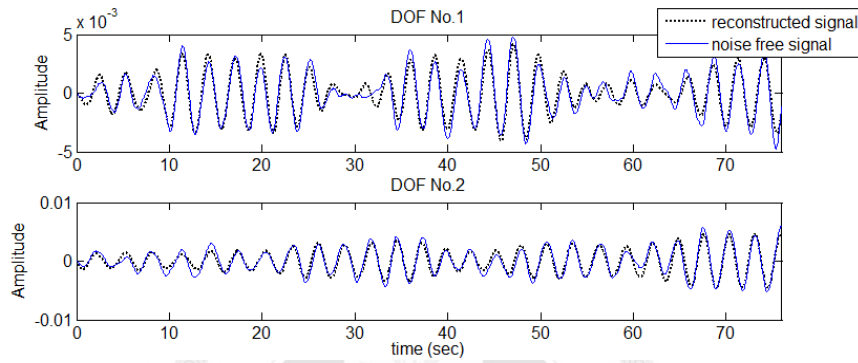
Figure 3-23 Comparison of the reconstructed signal with the noise free acceleration measurements, 8 Singular Values chosen from SSA.
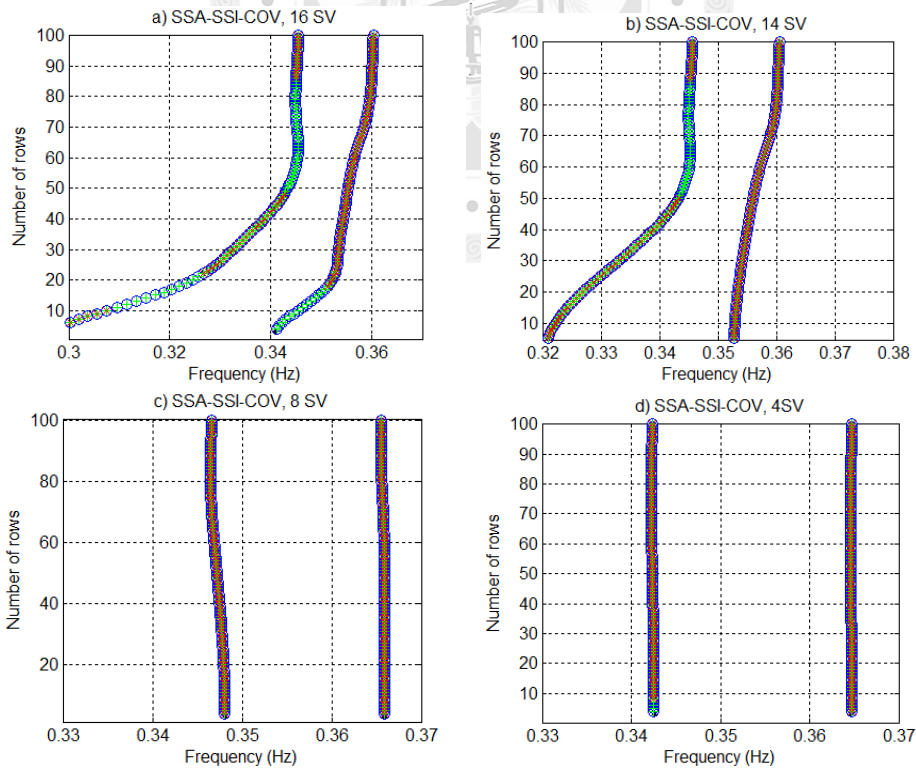
Figure 3-24 Stabilization diagram built with SSI-COV for different singular values extracted from SSA, system order fixed to 4.

158
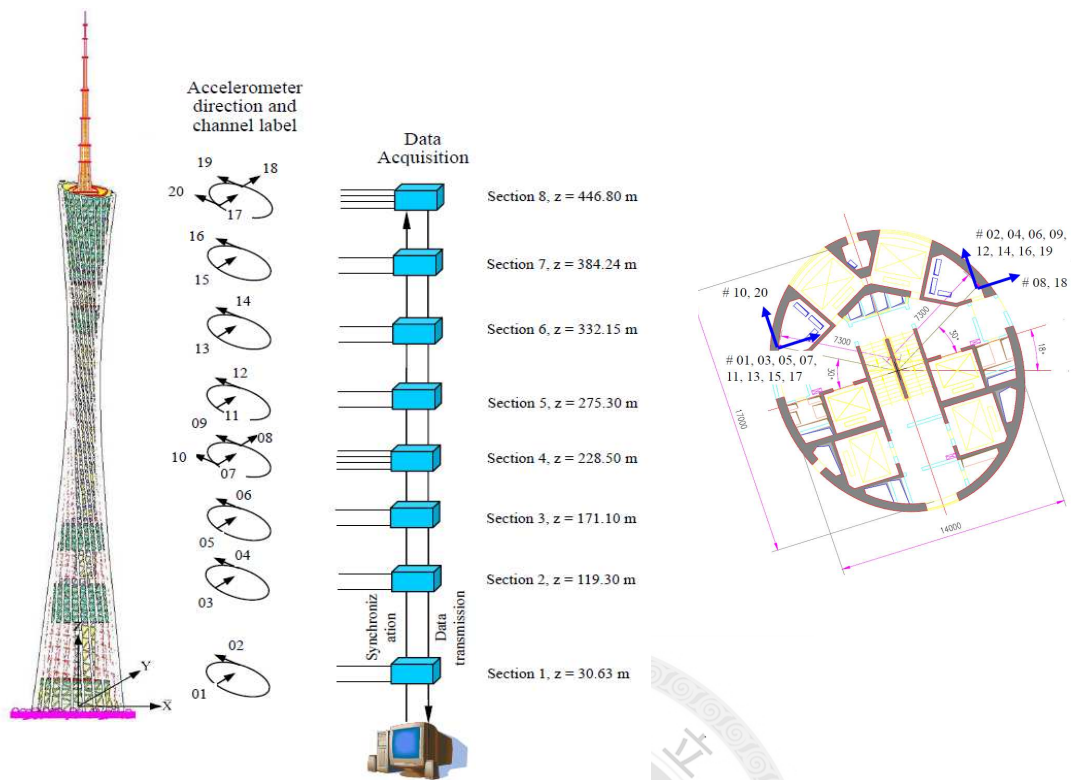
Figure 4-1　Locations of accelerometers in the Canton Tower. A floor section shows the position of accelerometers.
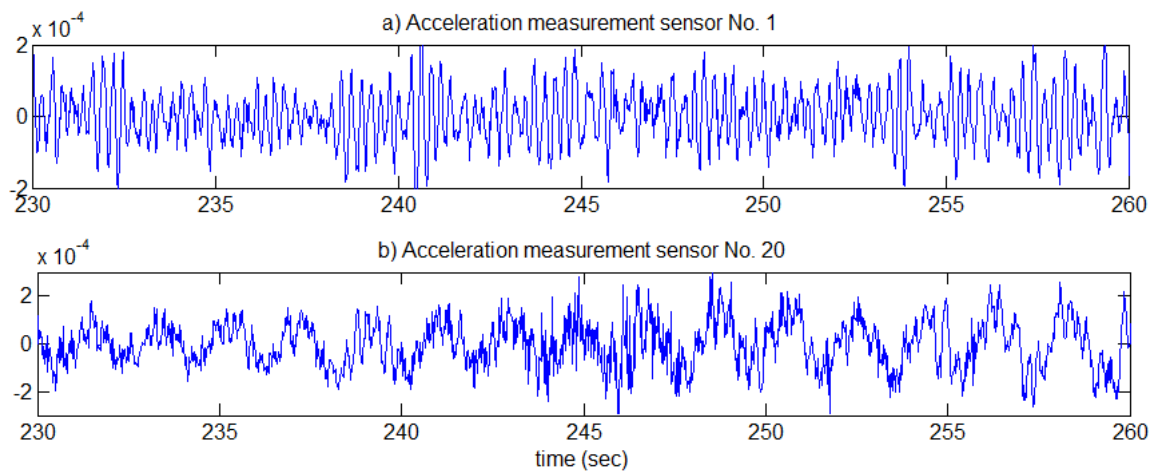
Figure 4-2　Acceleration measurements at the first minutes of the record for a) 1st sensor and b) 20th sensor.
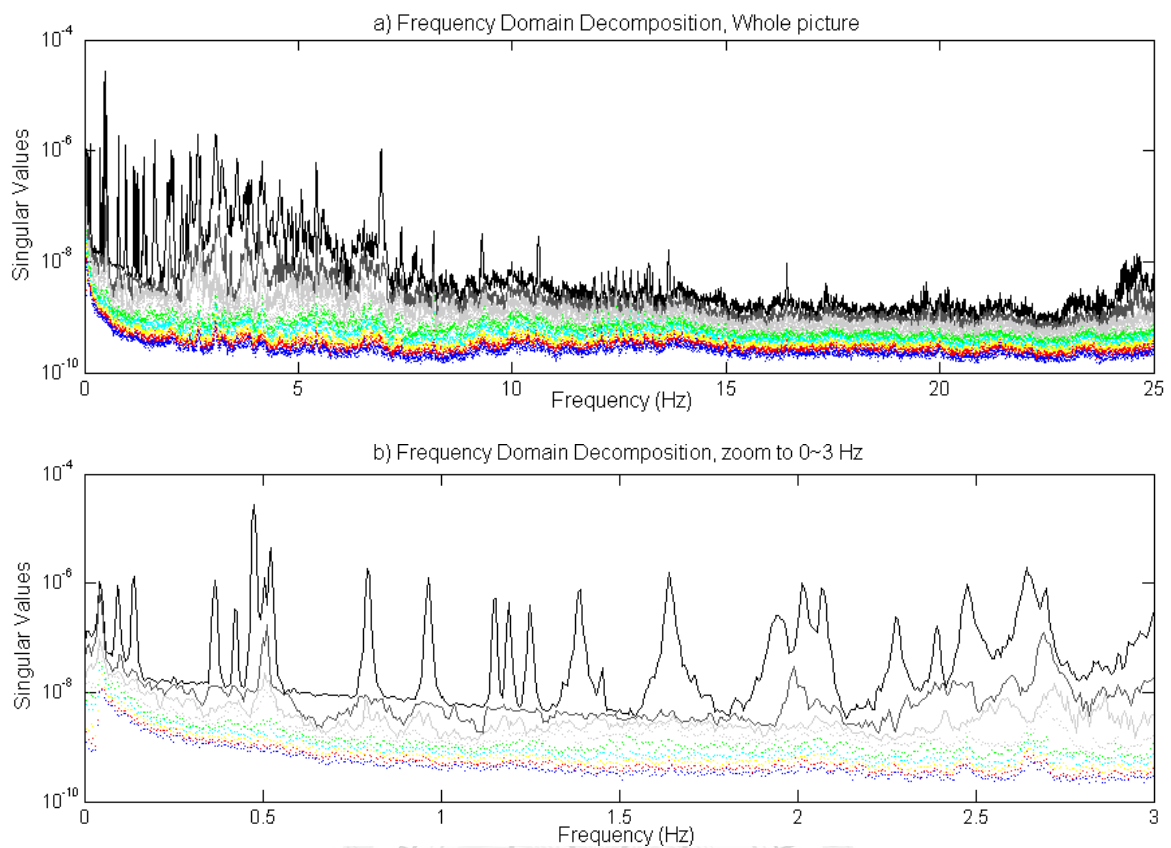
Figure 4-3 Plot of Frequency Domain Decomposition of GNTVT acceleration data,

a) whole picture, b) from 0 to 3 Hz.
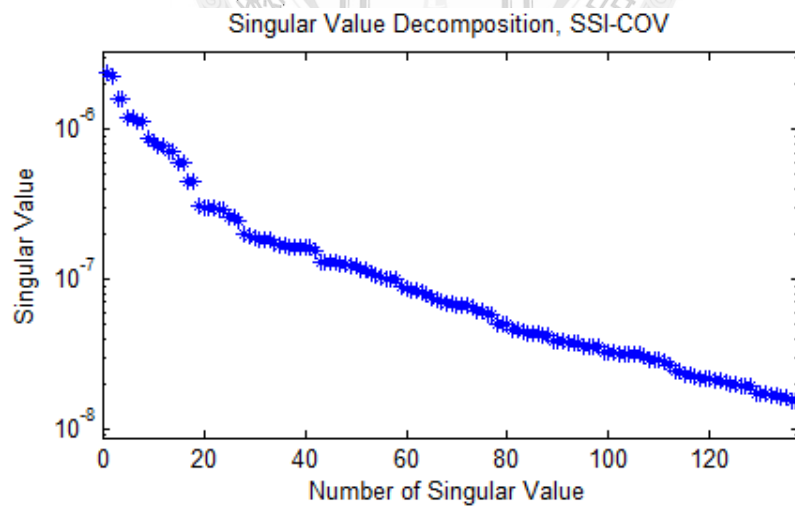
Figure 4-4 Singular Value Decomposition to the square Toeplitz matrix of 300 block rows.

160
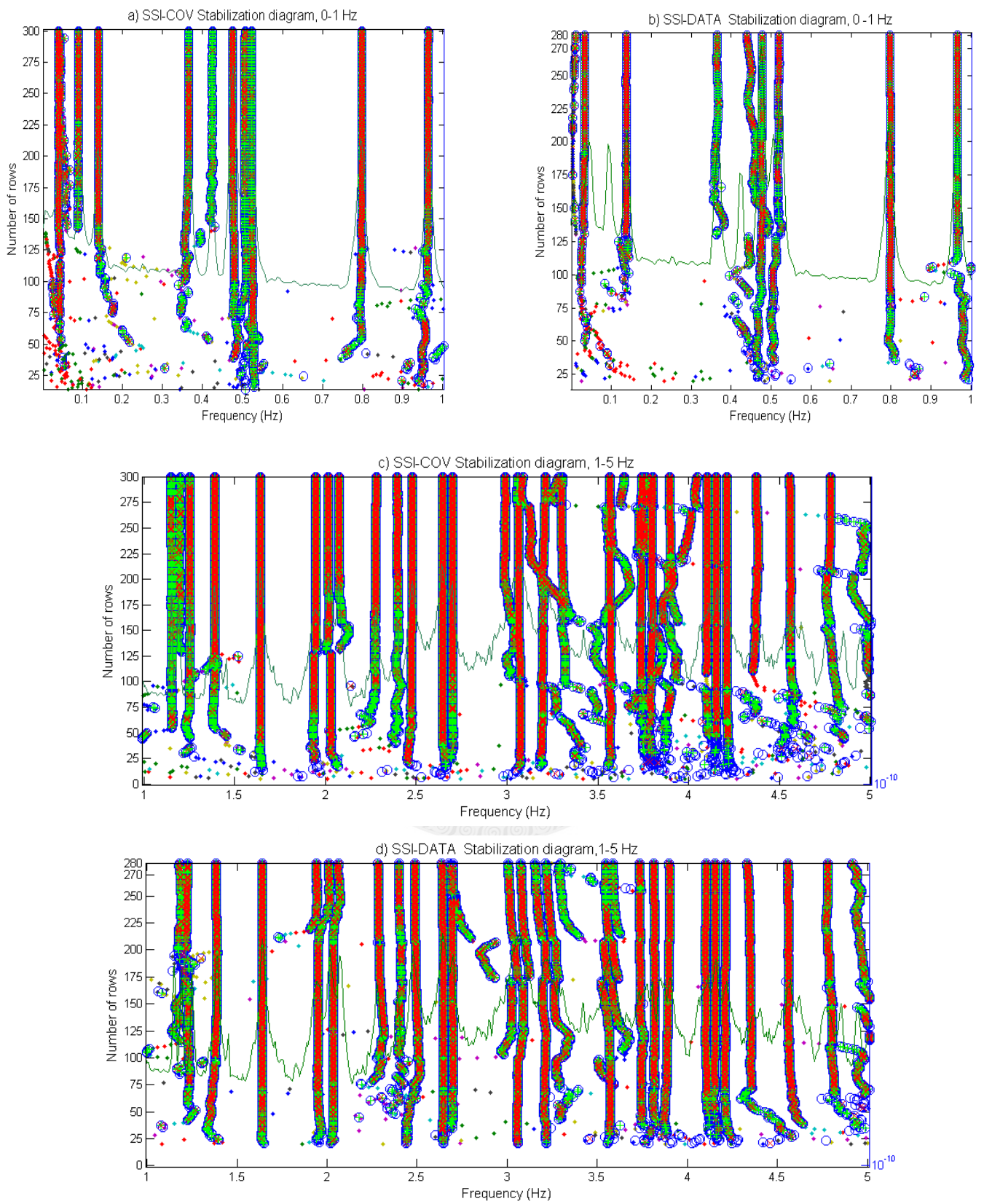
Figure 4-5 Stabilization diagram constructed by SSI-COV and SSI-DATA.

161
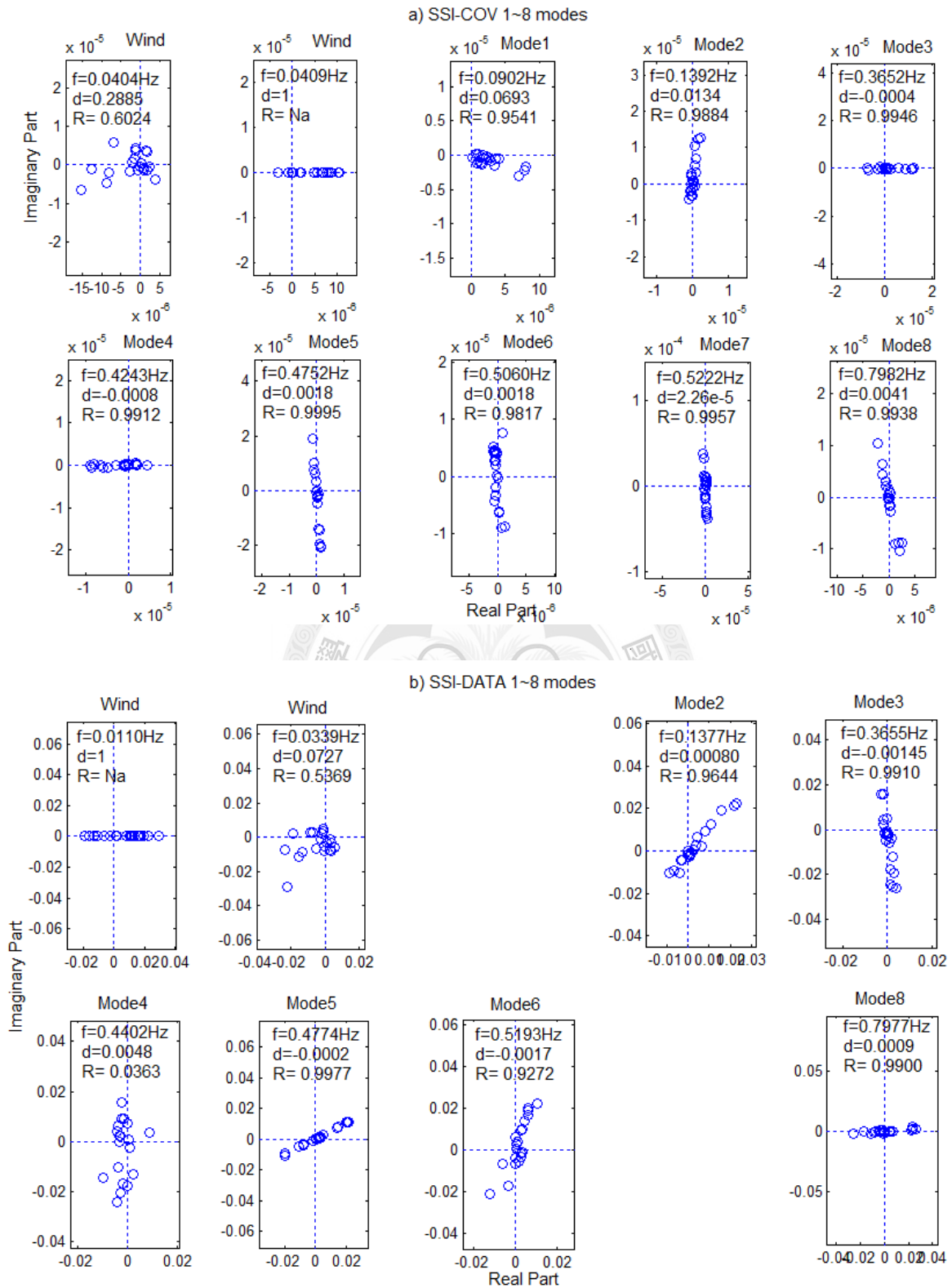
Figure 4-6 Comparing identified frequencies, damping ratios and complex mode shapes from mode 1 to 8, identified by SSI-COV and SSI-DATA.
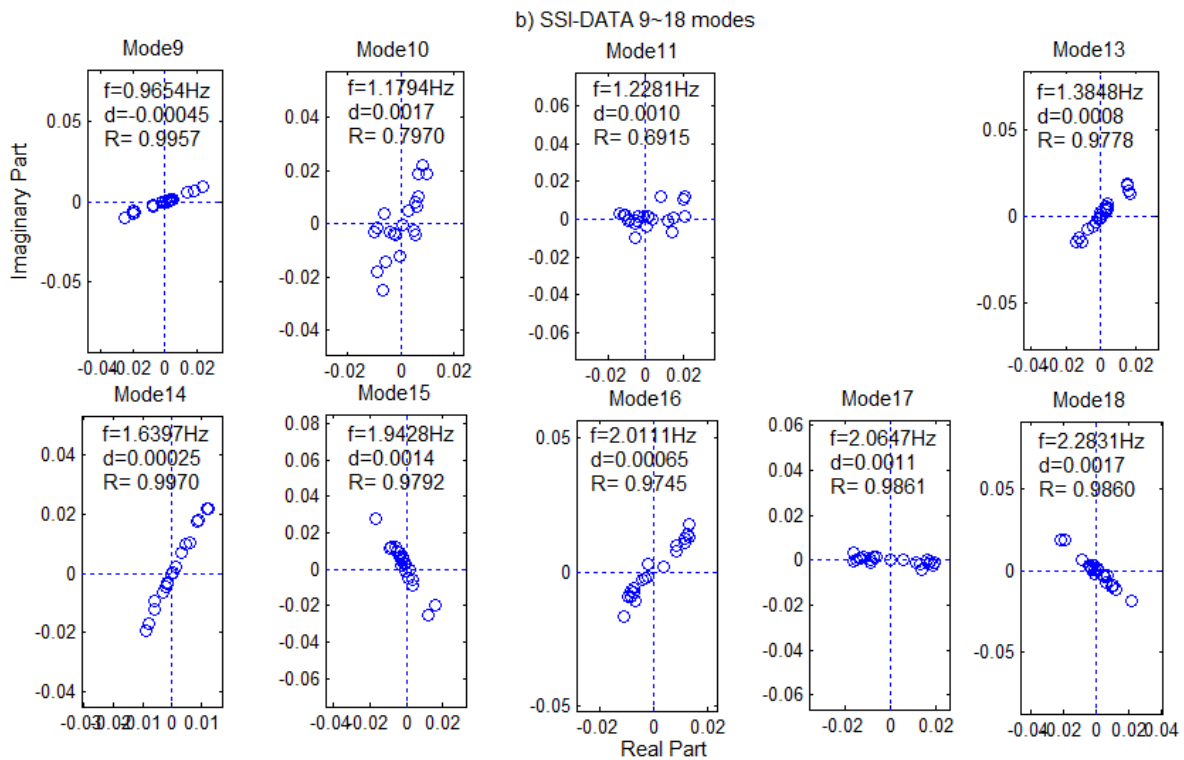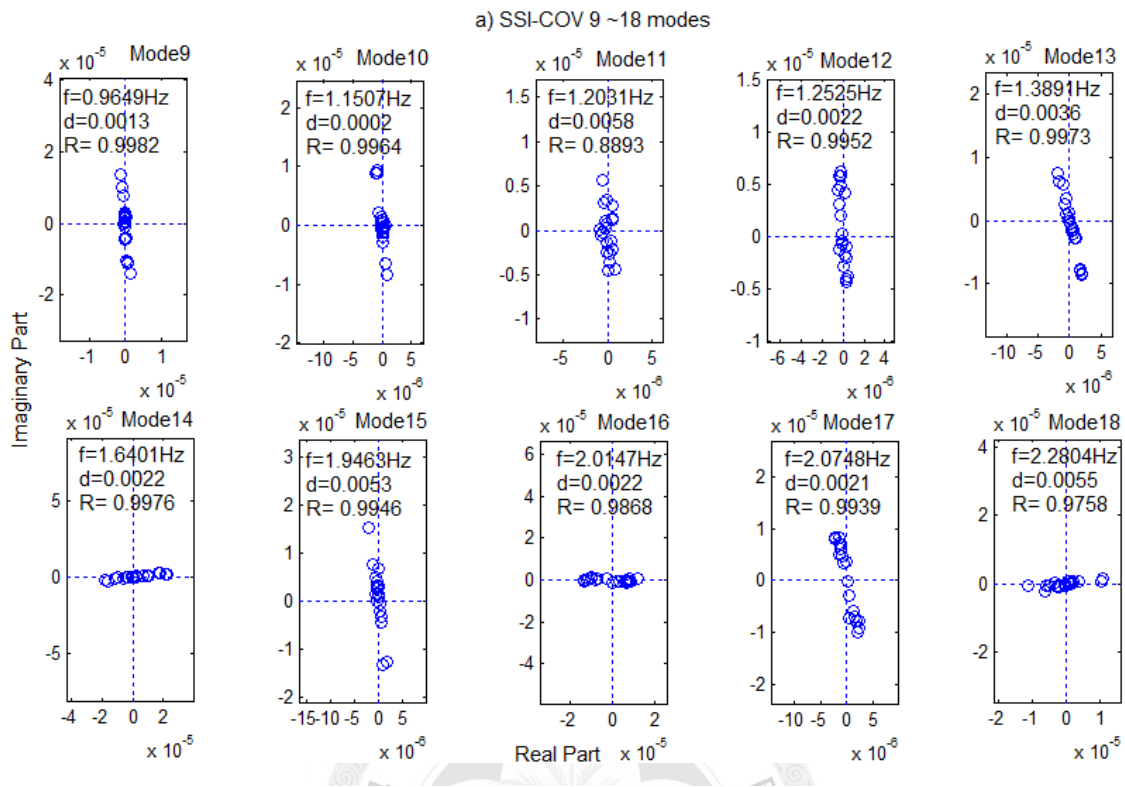
Figure 4-7 Comparing identified frequencies, damping ratios and complex mode shapes from mode 9 to 18, identified by SSI-COV and SSI-DATA.
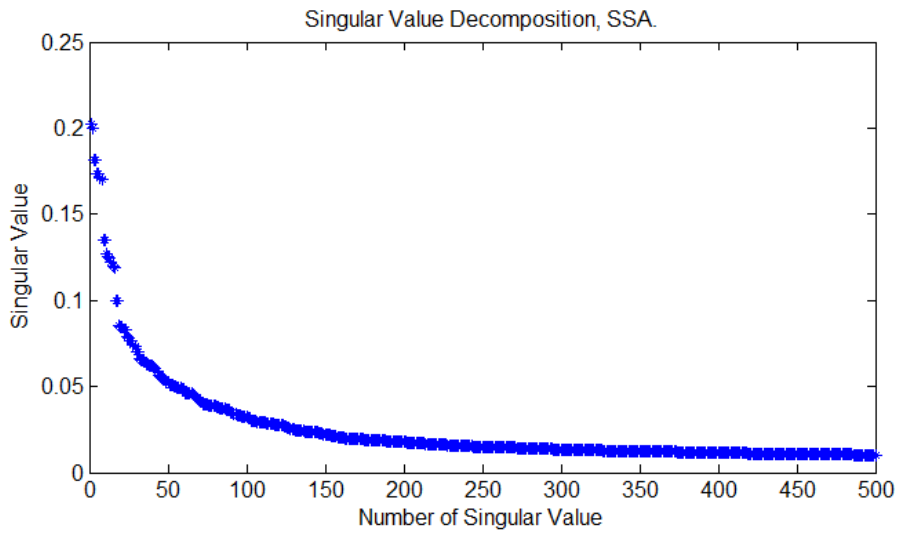
Figure 4-8 Singular value decomposition of Hankel matrix with 340 block rows and 15000 columns.
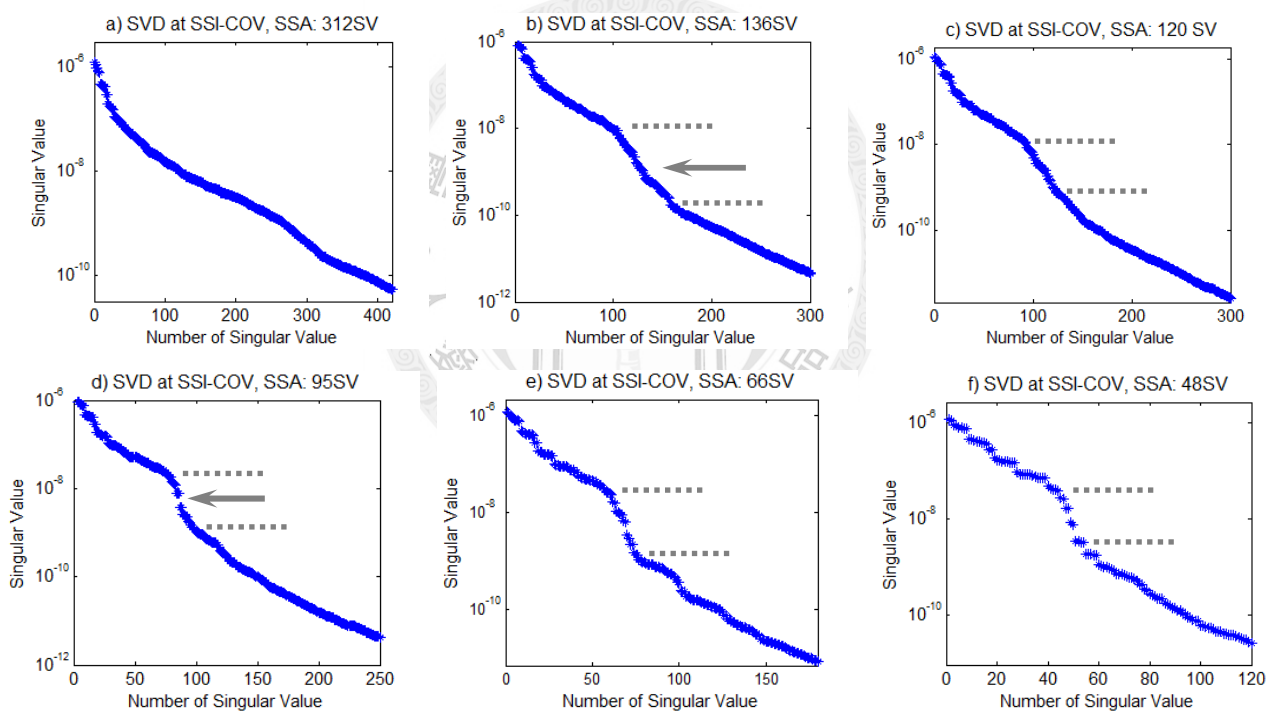
Figure 4-9 Plot the distribution of SV from SSI-COV analysis, data from:

a) 312 SV in SSA, b) 134SV in SSA, c) 120 SV in SSA, d) 95 SV in SSA, e) 66 SV in SSA, f) 48 SV in SSA.
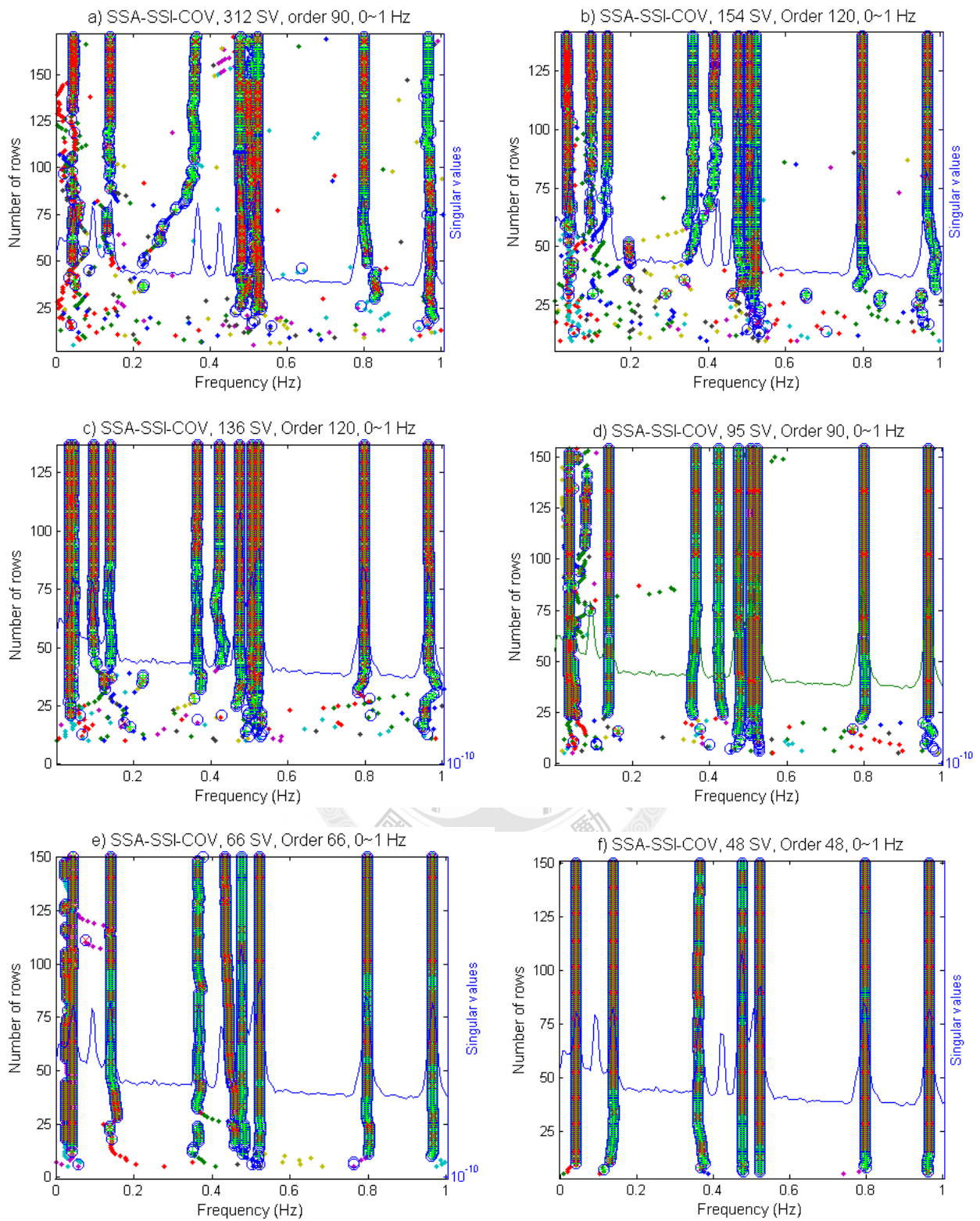
Figure 4-10 Comparison of stability diagram made with SSA-SSI-COV, 0~1 Hz.
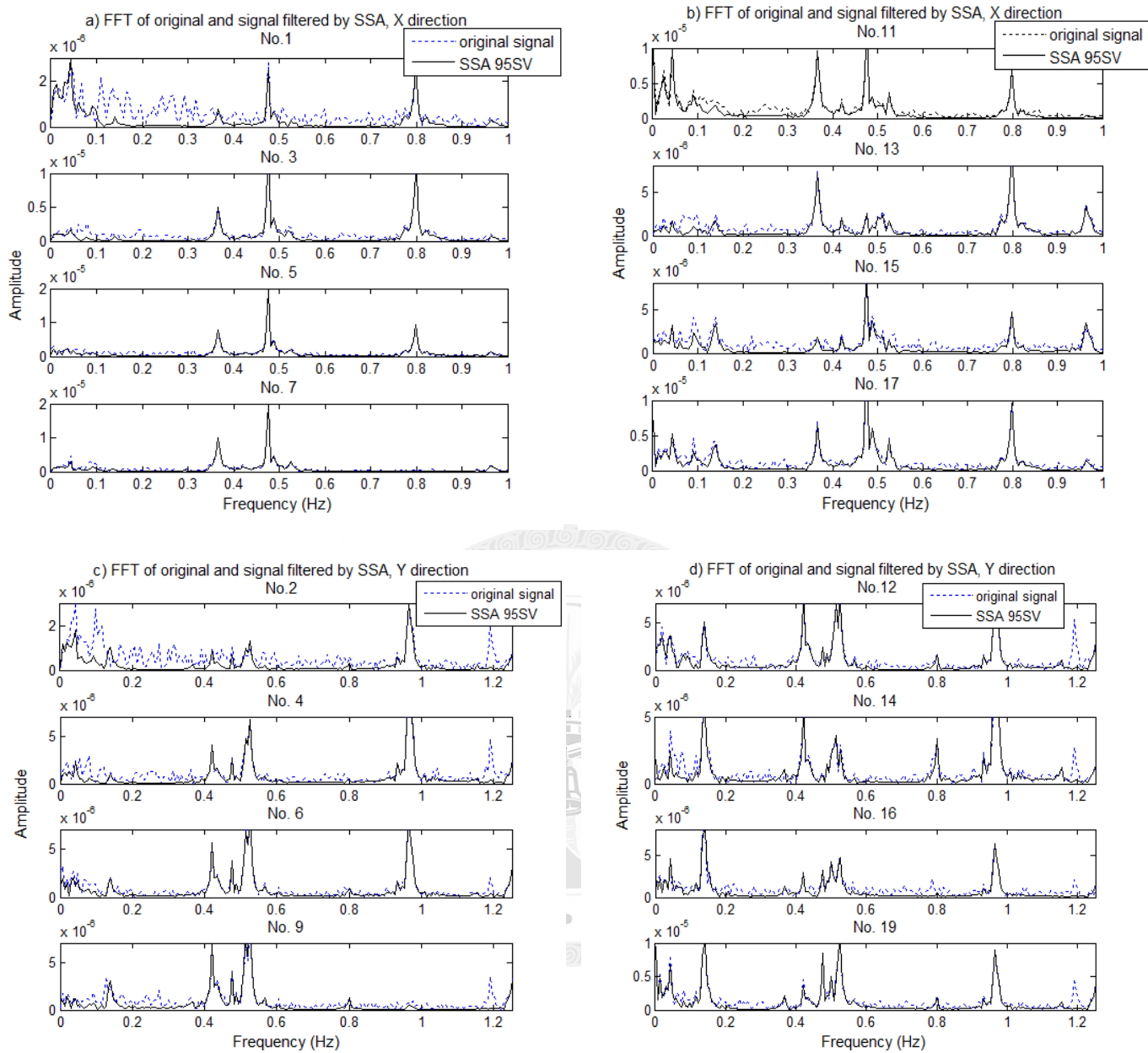
Figure 4-11　Fourier Spectrum of the reconstructed signal with SSA 95 SV.
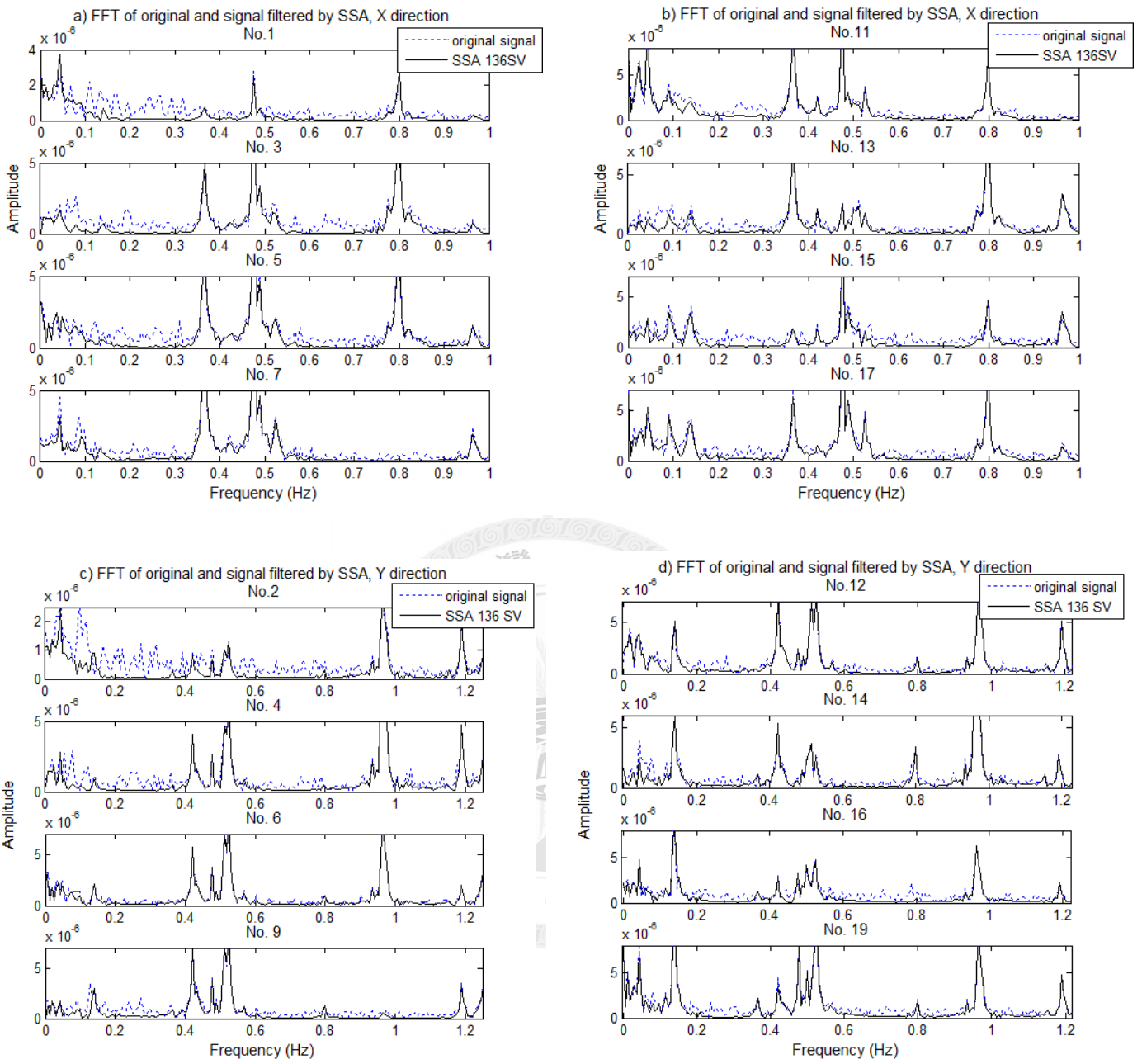
Figure 4-12   Fourier Spectrum of the reconstructed signal with SSA 136 SV.
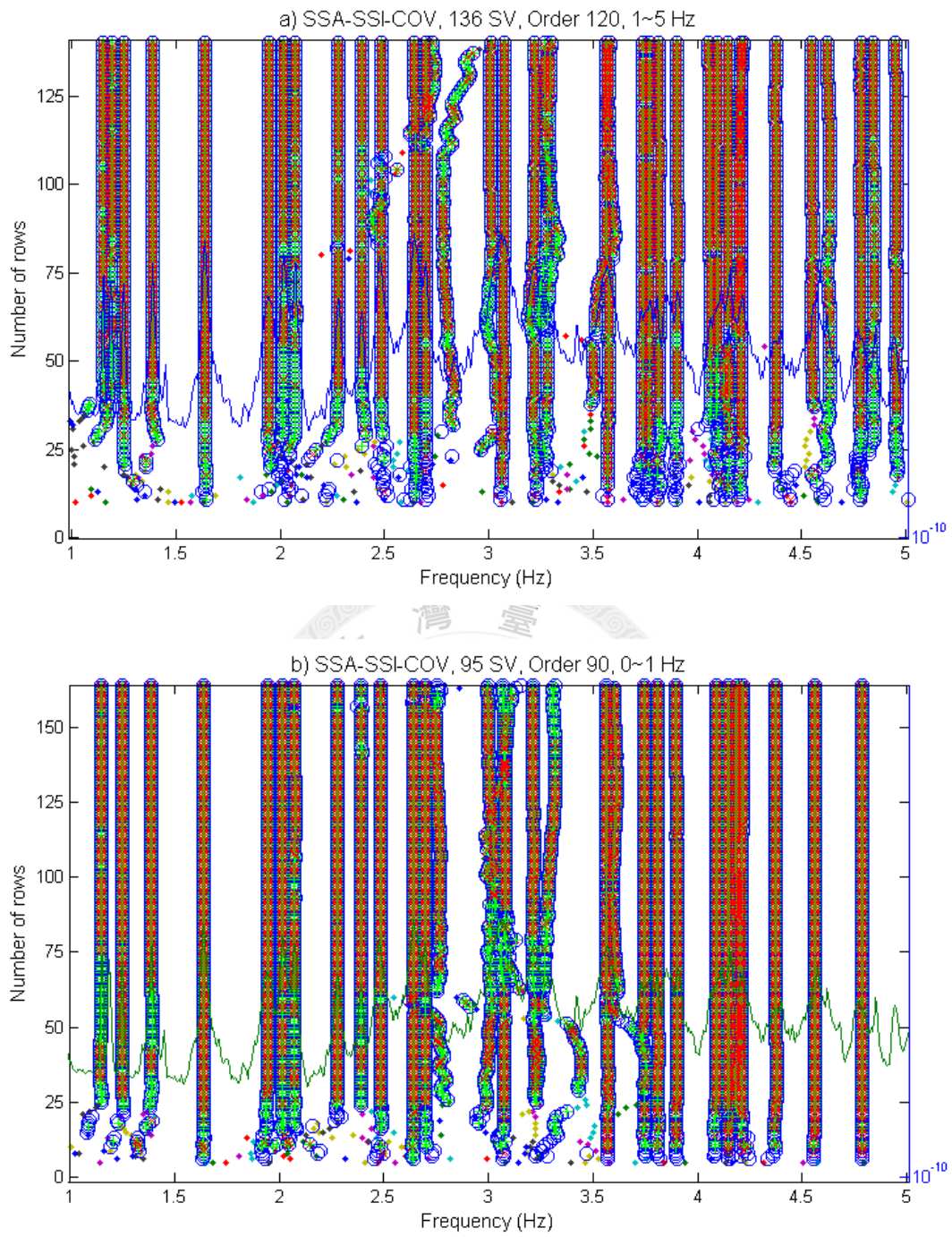
Figure 4-13   Comparison of stability diagram made with SSA-SSI-COV, a) 136 SV and b) 95 SV, 1~5 Hz.
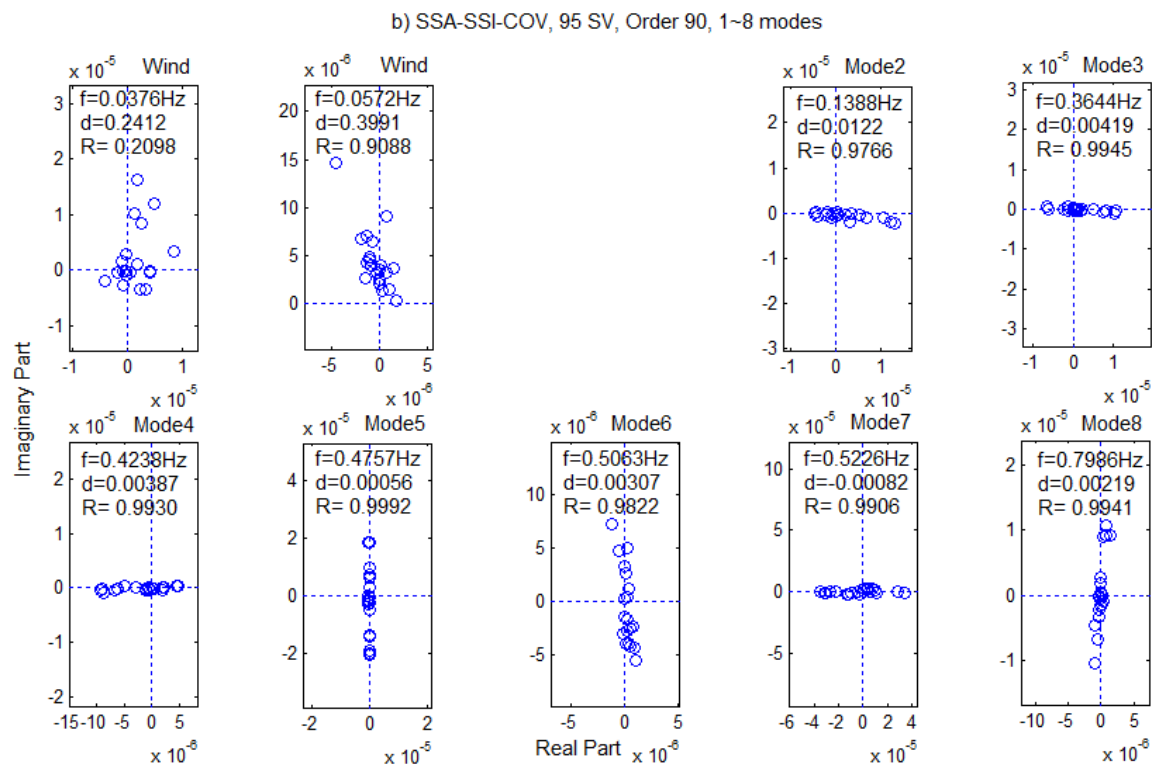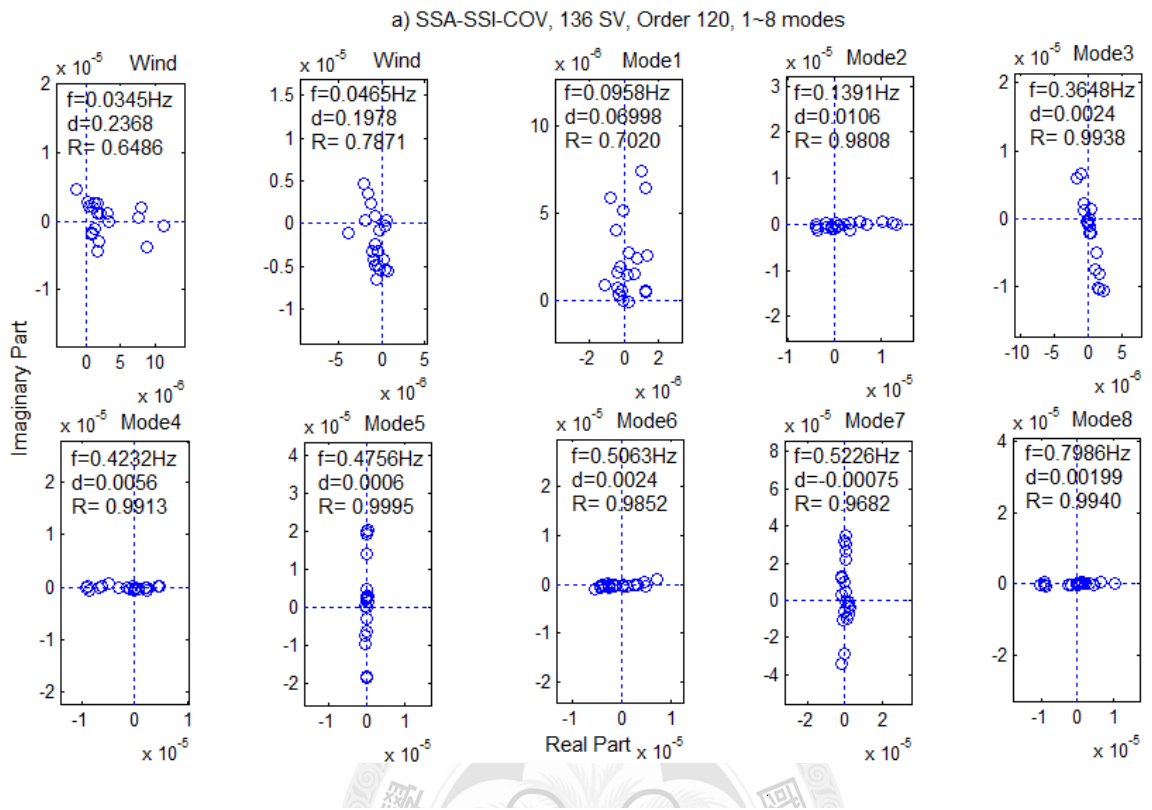
Figure 4-14 Comparing identified frequencies, damping ratios and complex mode shapes from mode 1 to 8, identified by SSA-SSI-COV using a) 136 SV and b) 95 SV.
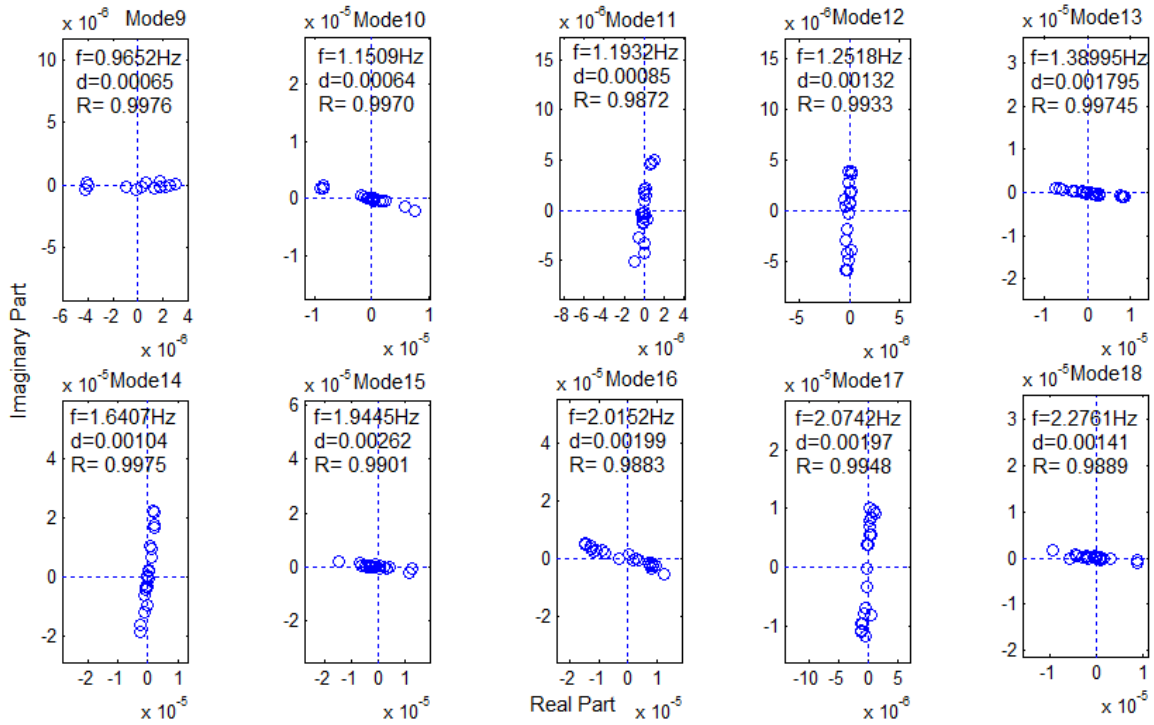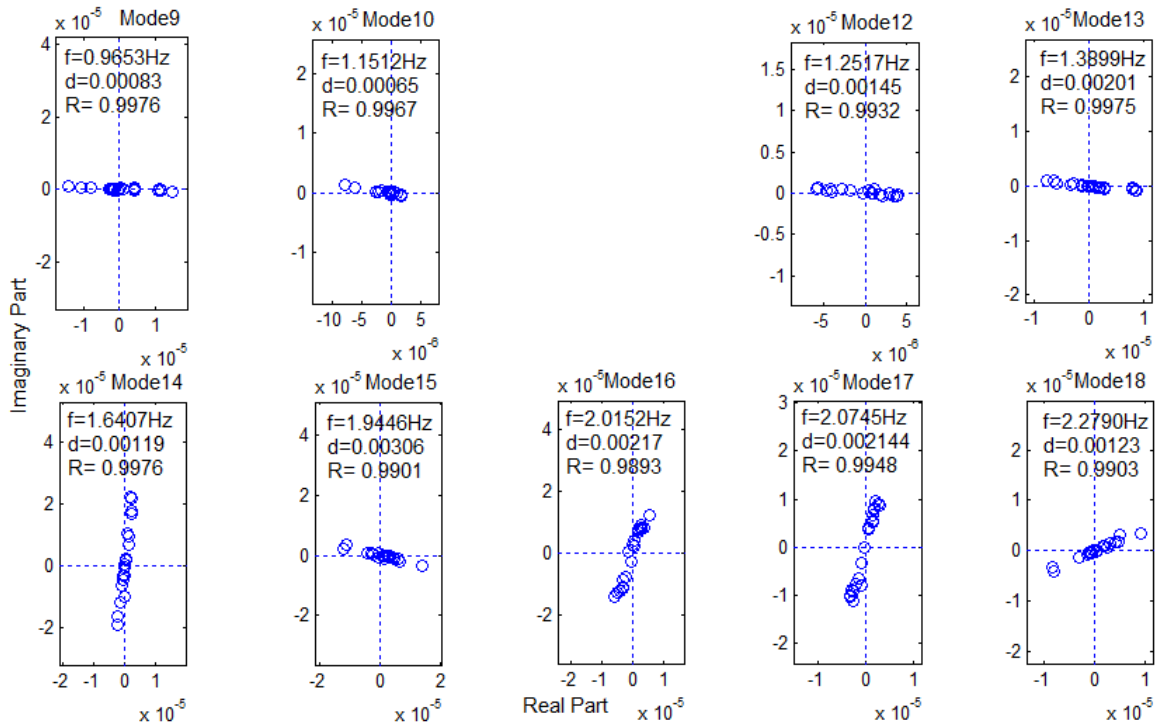
Figure 4-15 Comparing identified frequencies, damping ratios and complex mode shapes from mode 9 to 18, identified by SSA-SSI-COV using a) 136 SV and b) 95 SV.
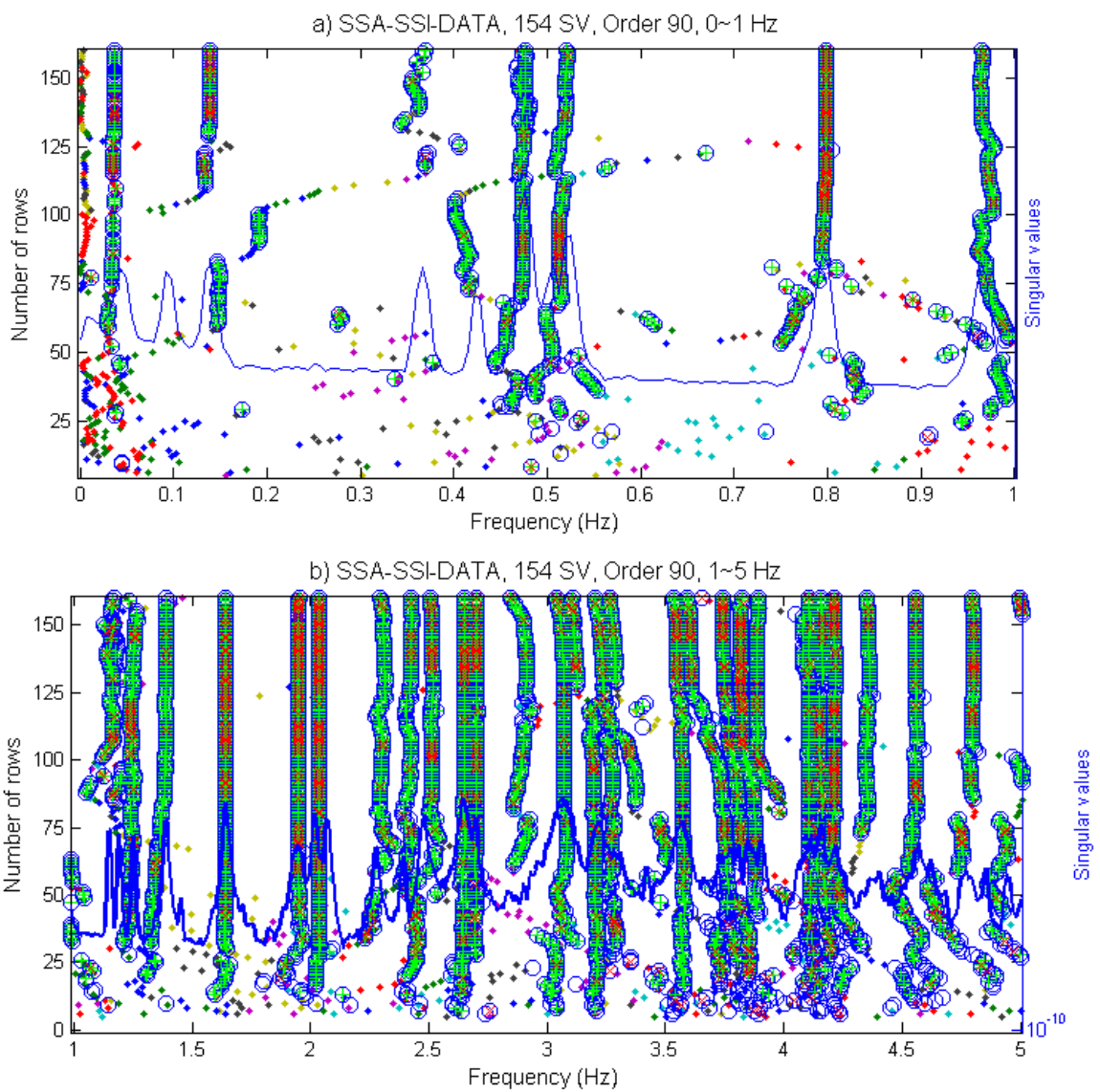
Figure 4-16   Stabilization diagram constructed by SSA-SSI-Data using 154 SV, Order 90 a) 0~1 Hz, b) 1~5 Hz.
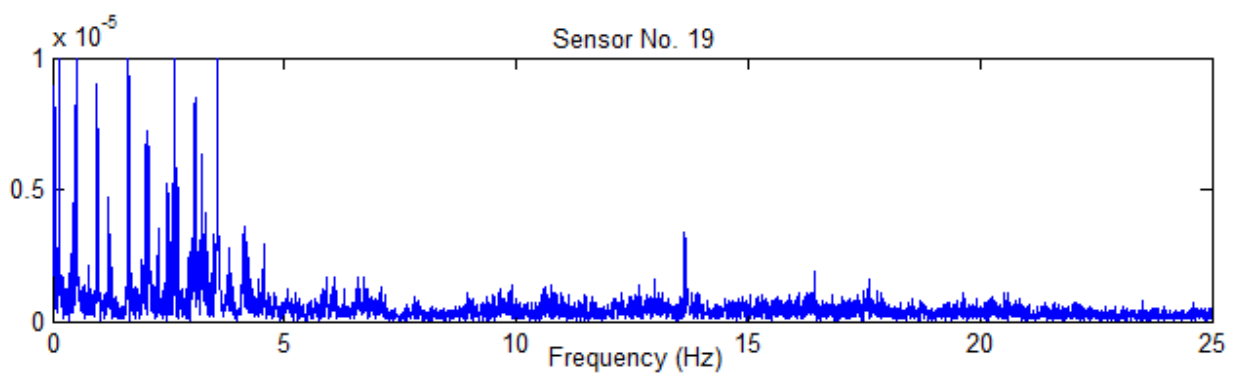
Figure 4-17   Fourier Spectrum of acceleration measurement at sensor No. 19.

171
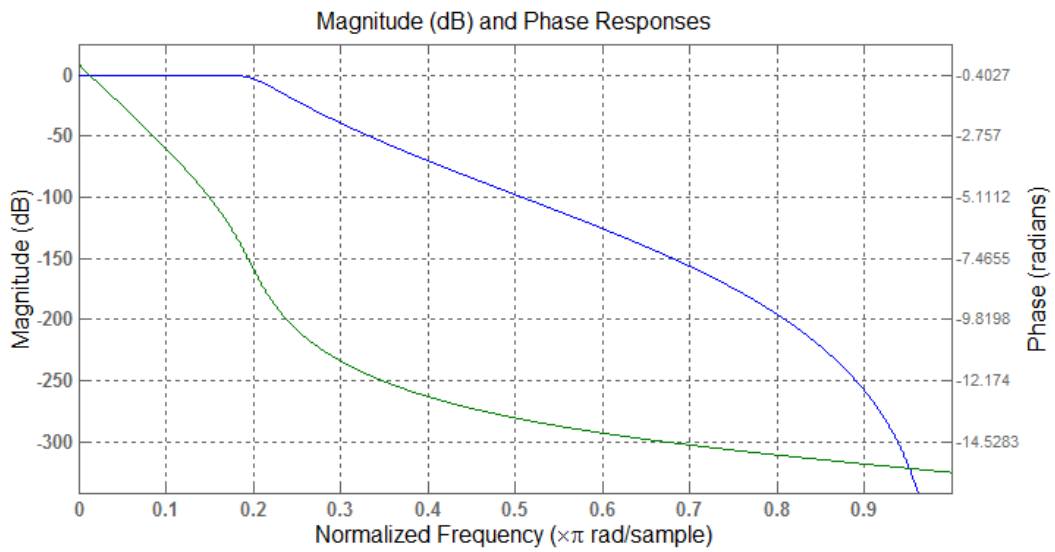
Figure 4-18   Frequency response function of Butterworth filter. Order: 10, cutoff frequency: 5 Hz.
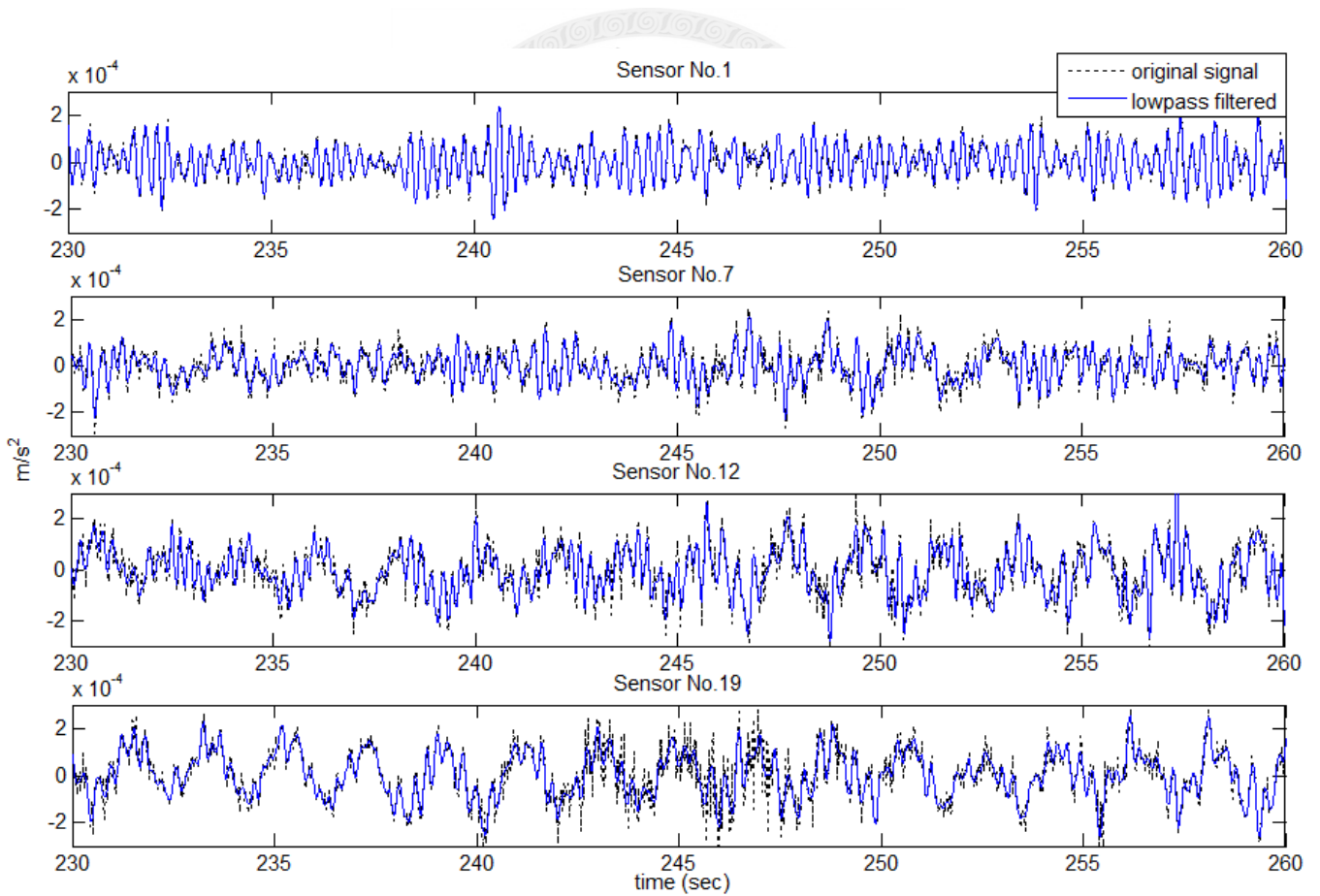
Figure 4-19   Comparison of the low-pass filtered signal with original signal for various sensors.

172
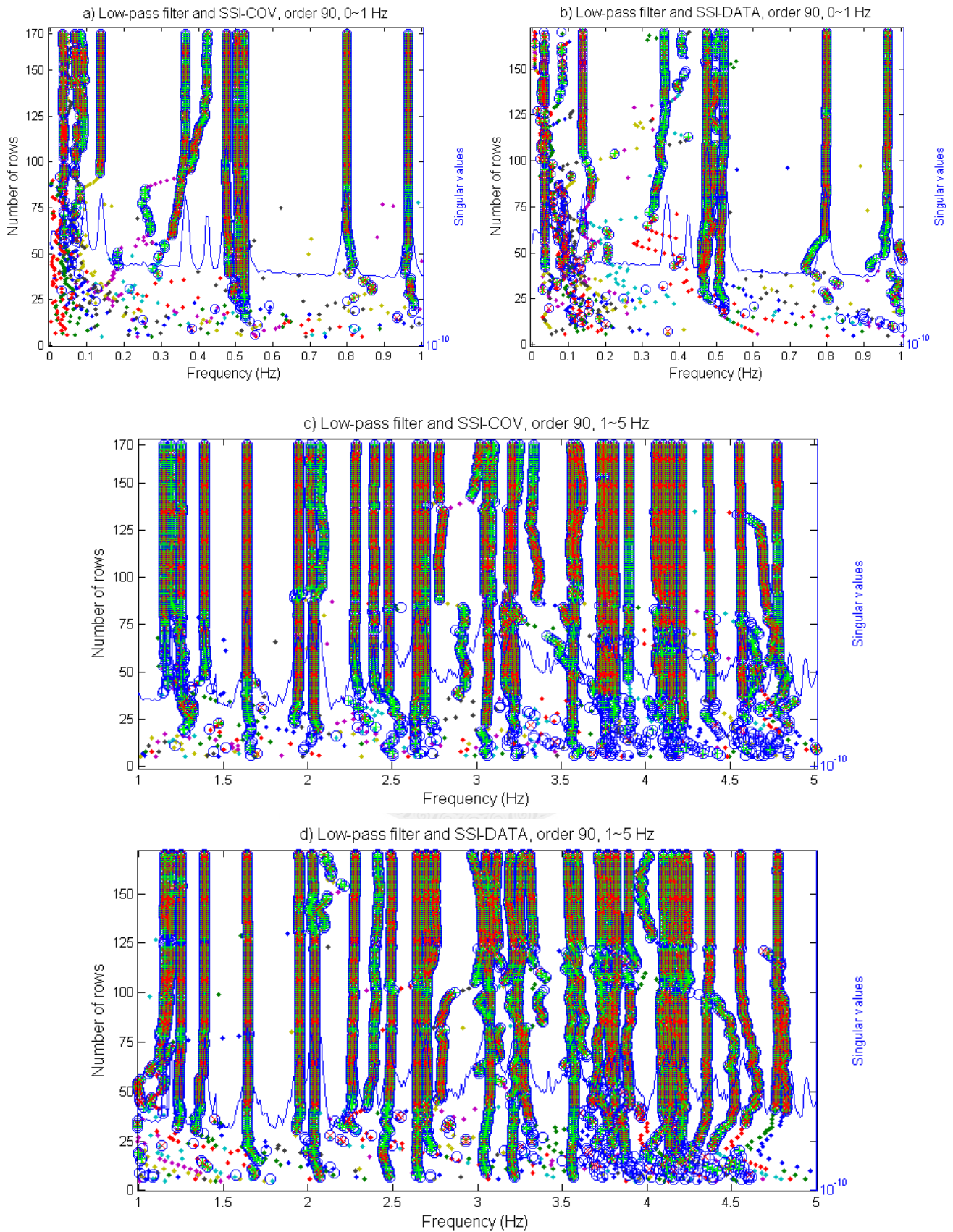
Figure 4-20 Comparison between stabilization diagram constructed with SSI-COV for

a) 0~1Hz, c) 1~5 Hz, and with SSI-DATA for b) 0~1 Hz, d) 1~5 Hz.

173
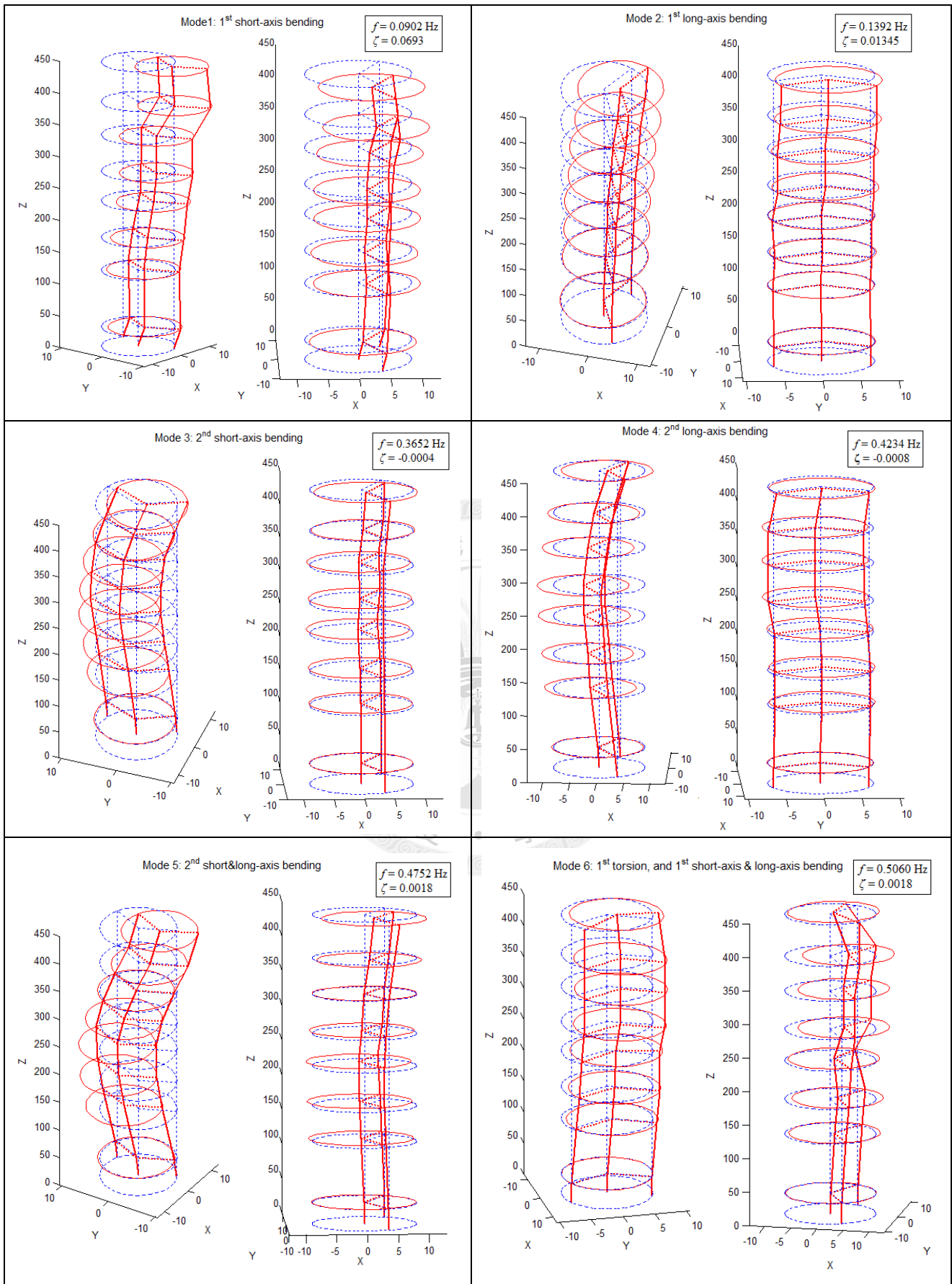
Figure 4-21 Examples of identified mode shapes with SSI-COV, mode 1~6.

174
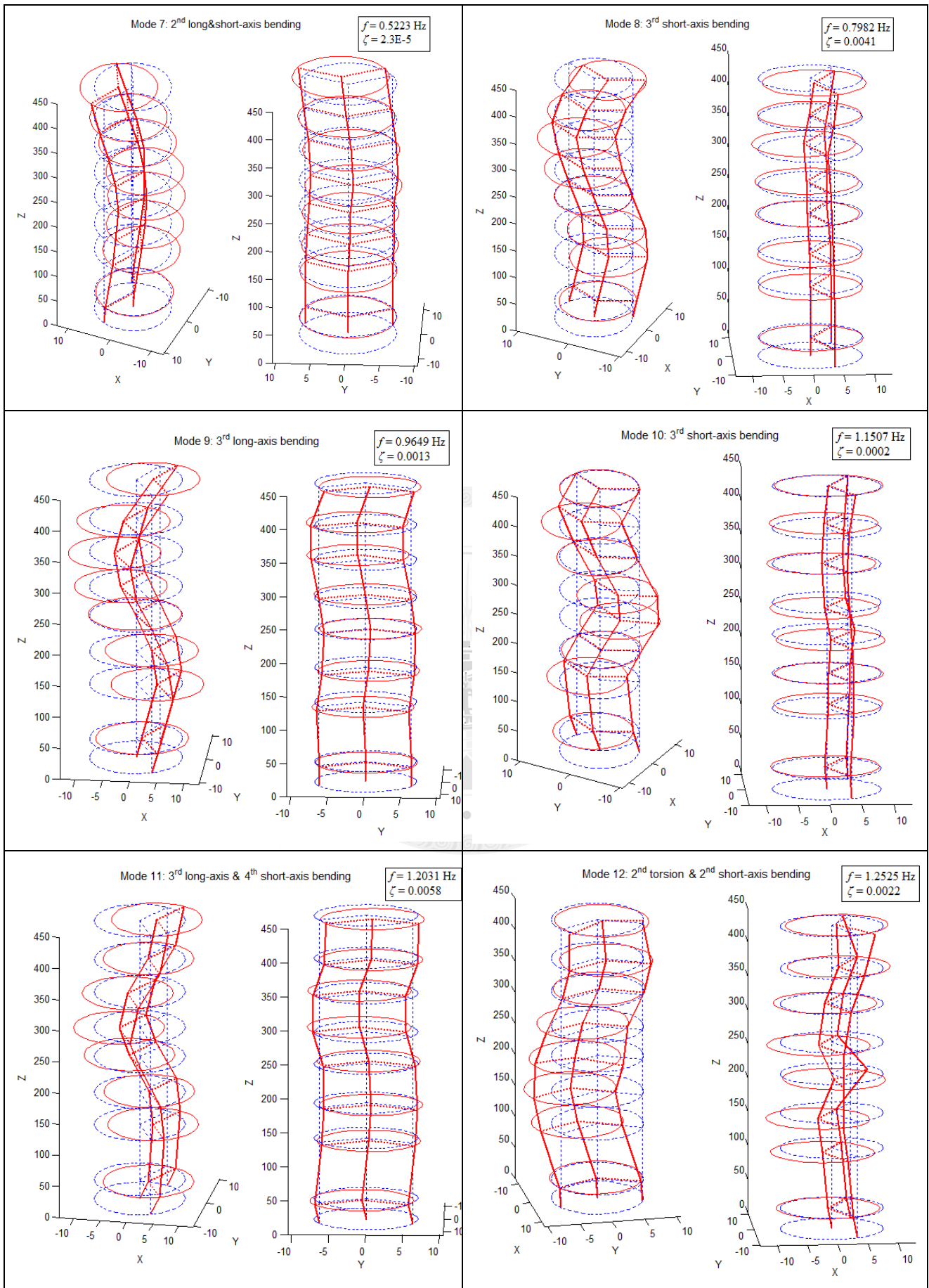
Figure 4-22 Examples of identified mode shapes with SSI-COV, mode 7~12.

175
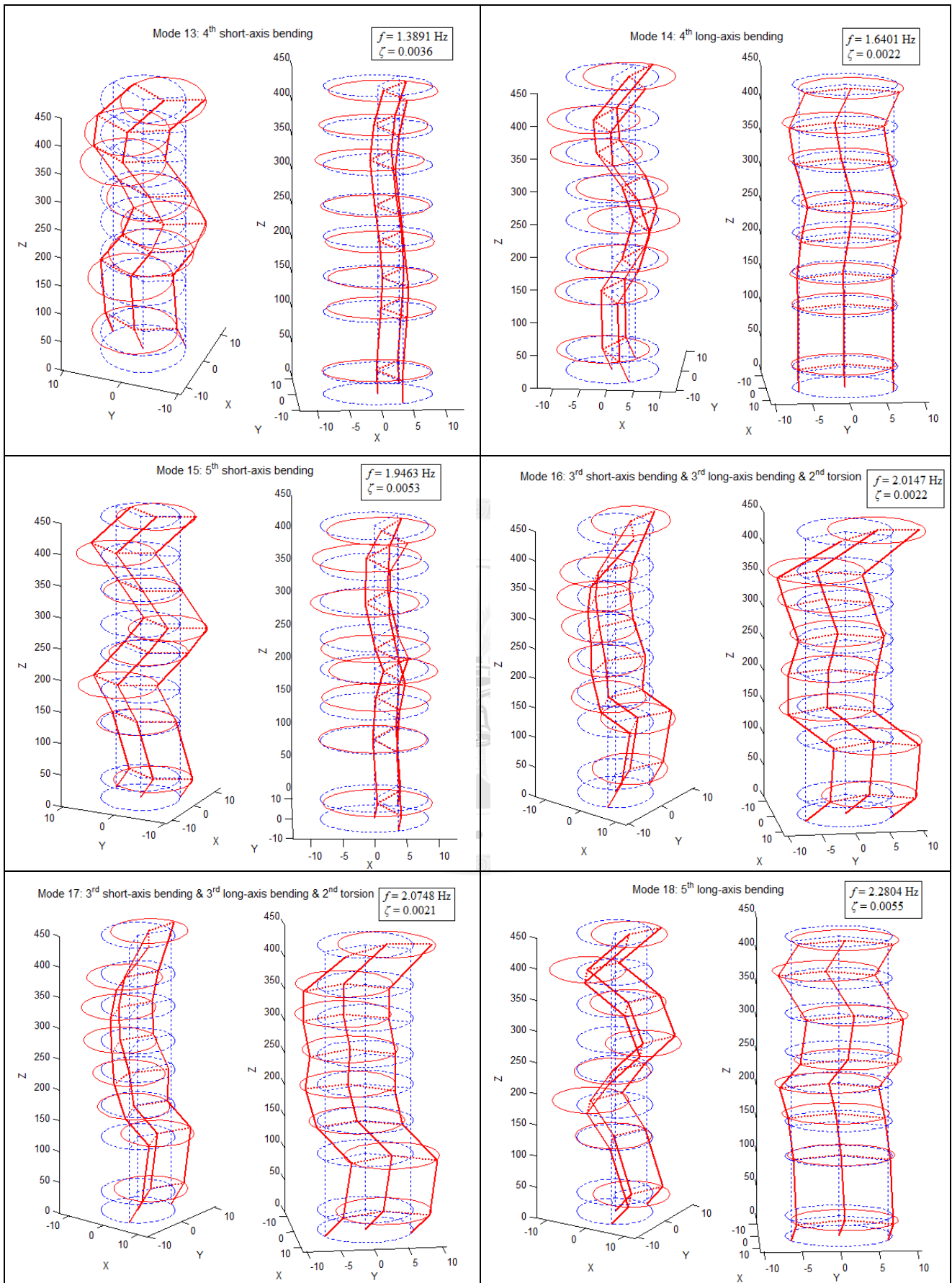
Figure 4-23 Examples of identified mode shapes with SSI-COV, mode 13~18.
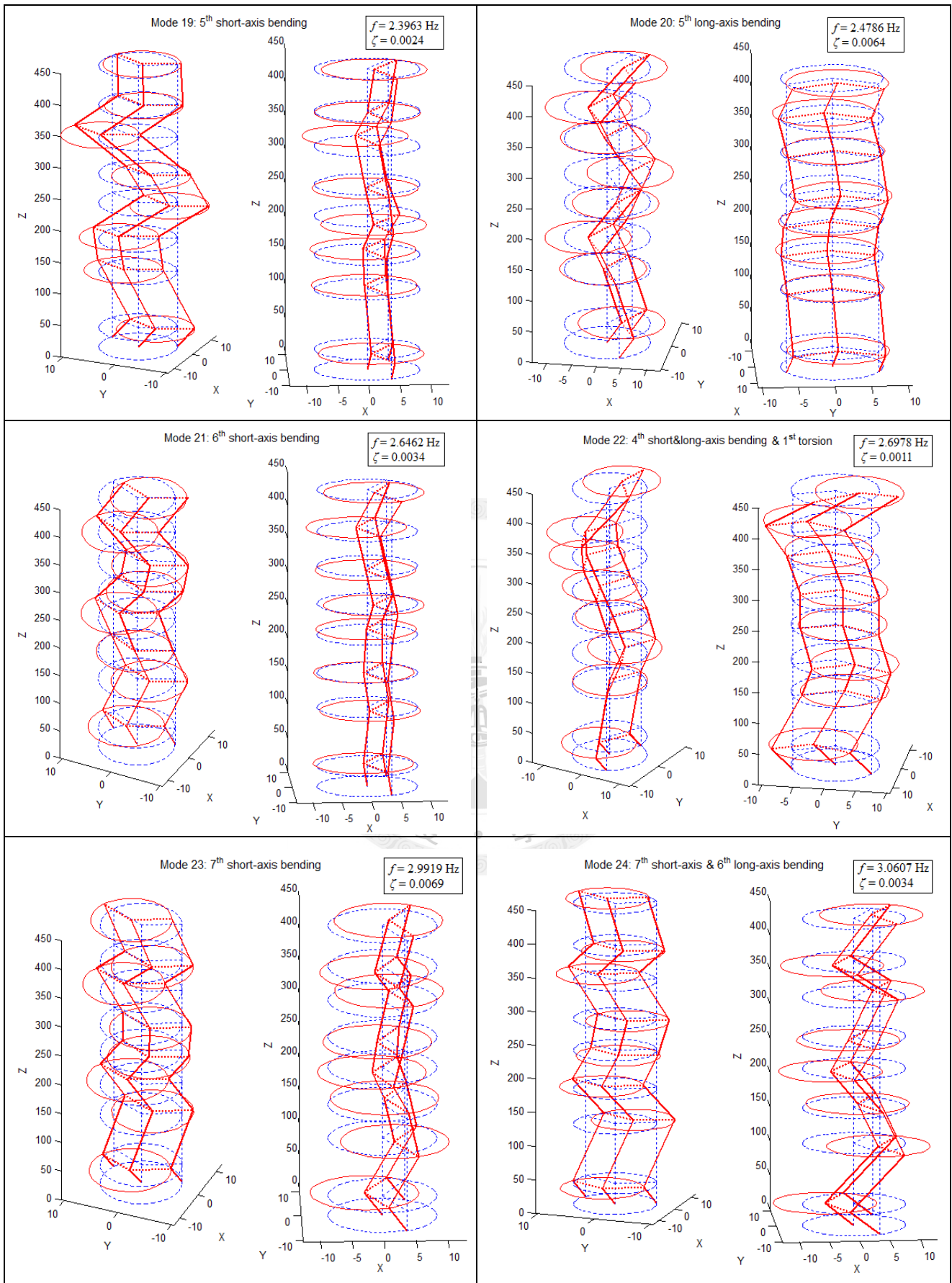
Figure 4-24 Examples of identified mode shapes with SSI-COV, mode 19~24.

177
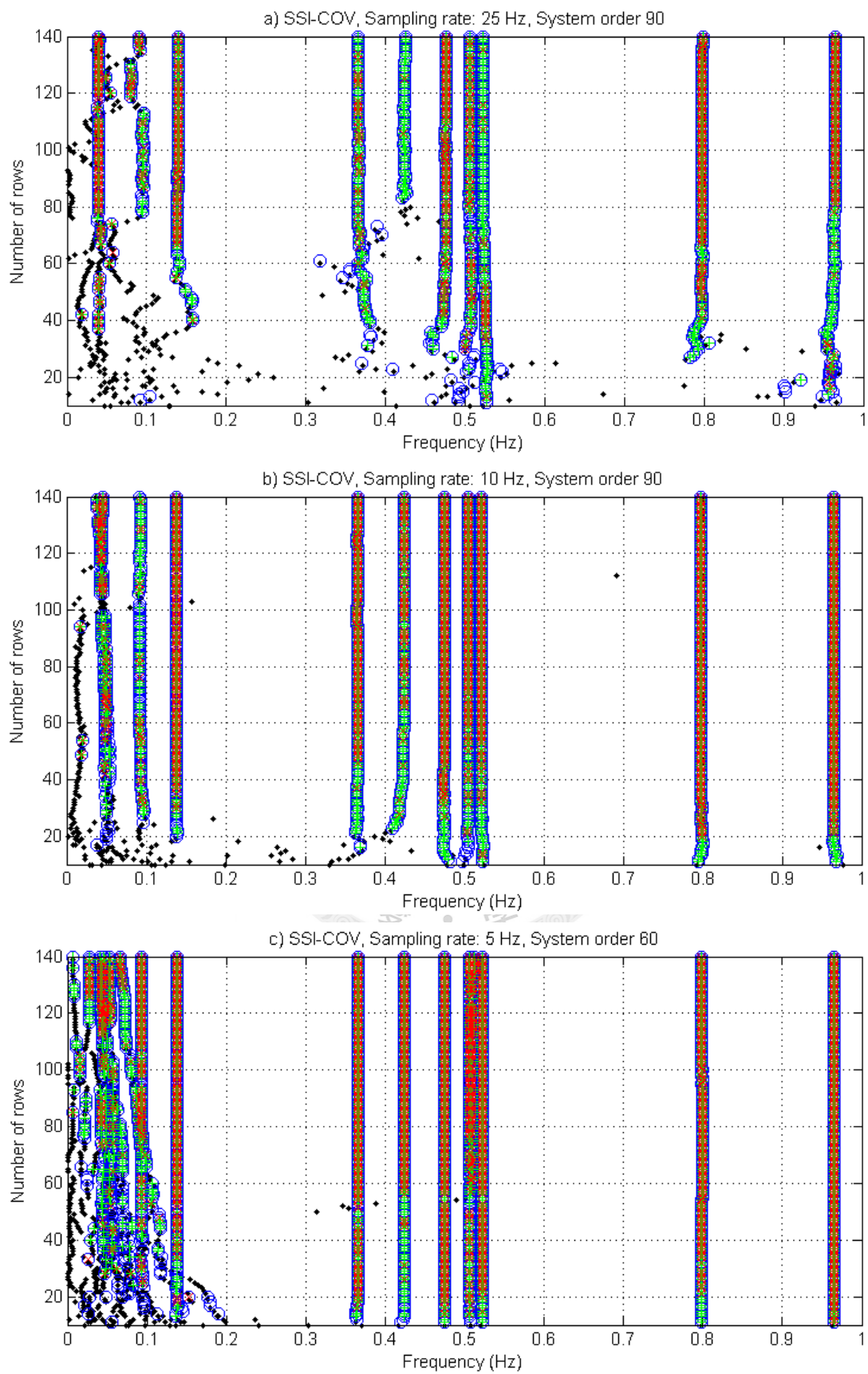
Figure 4-25 Comparison of stabilization diagram for 0~1 Hz, signal downsampled to different rates.

178
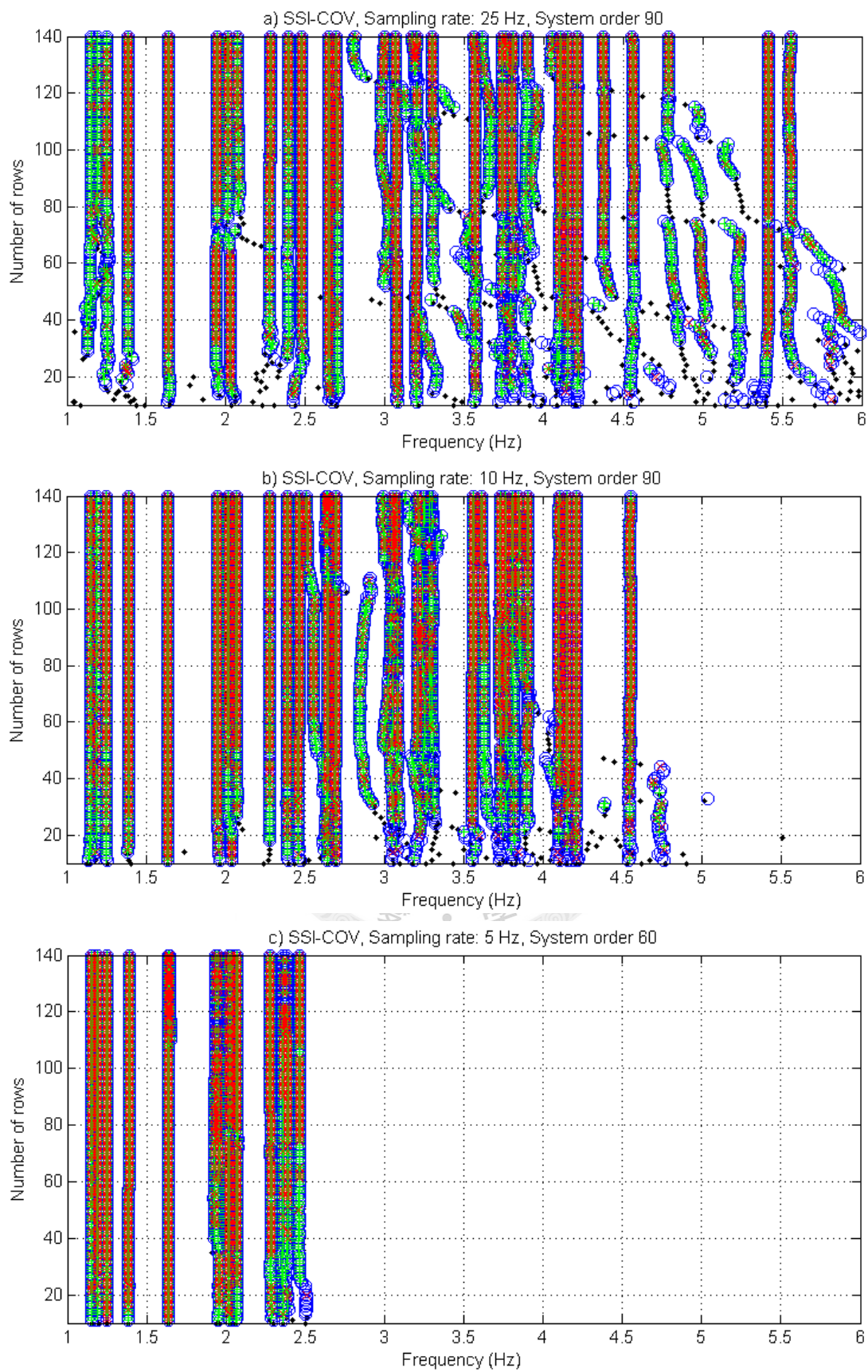
Figure 4-26 Comparison of stabilization diagram for 1~6 Hz, signal downsampled to different rates.

179
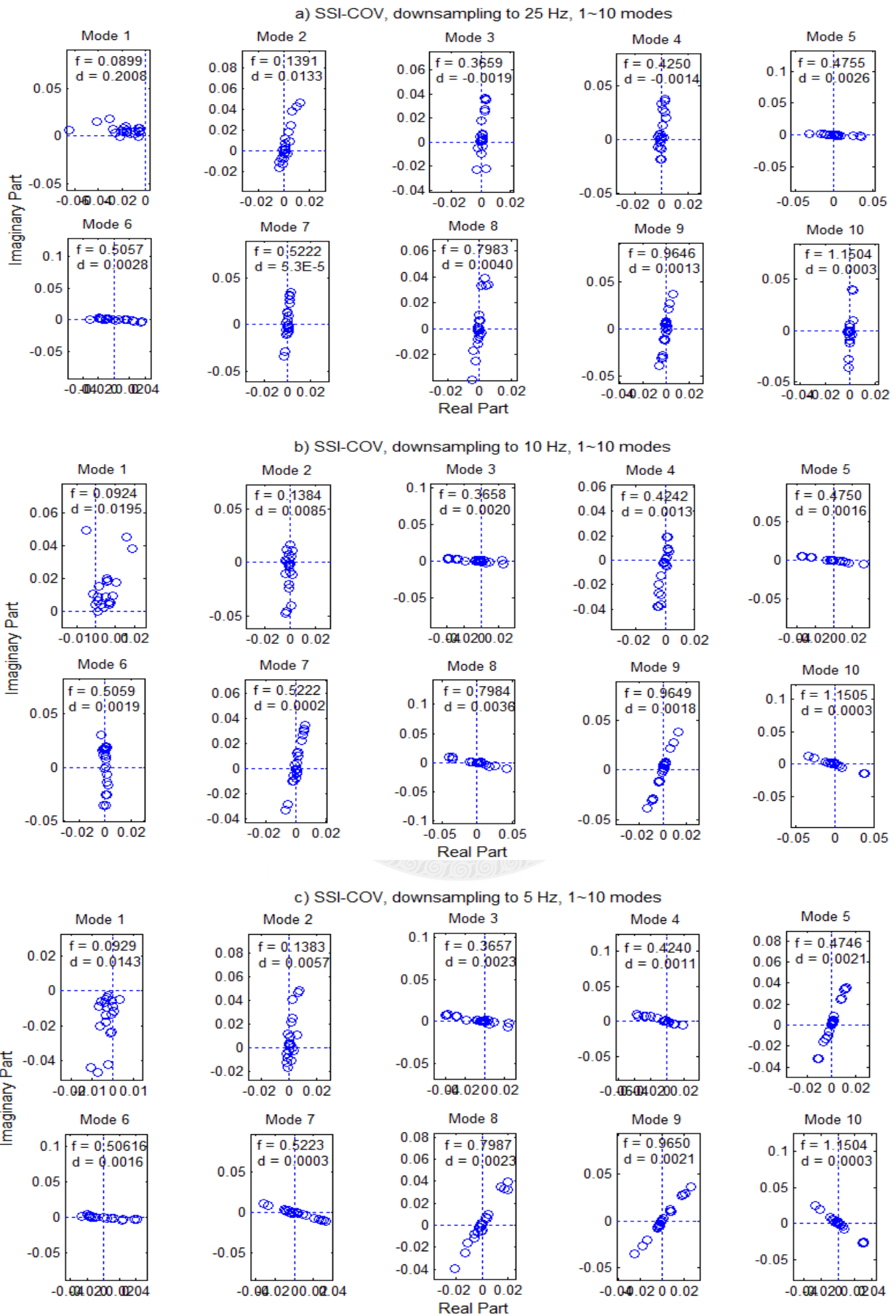
Figure 4-27 Comparison of complex mode shapes for the first 10 modes, signal downsampled to different rates.
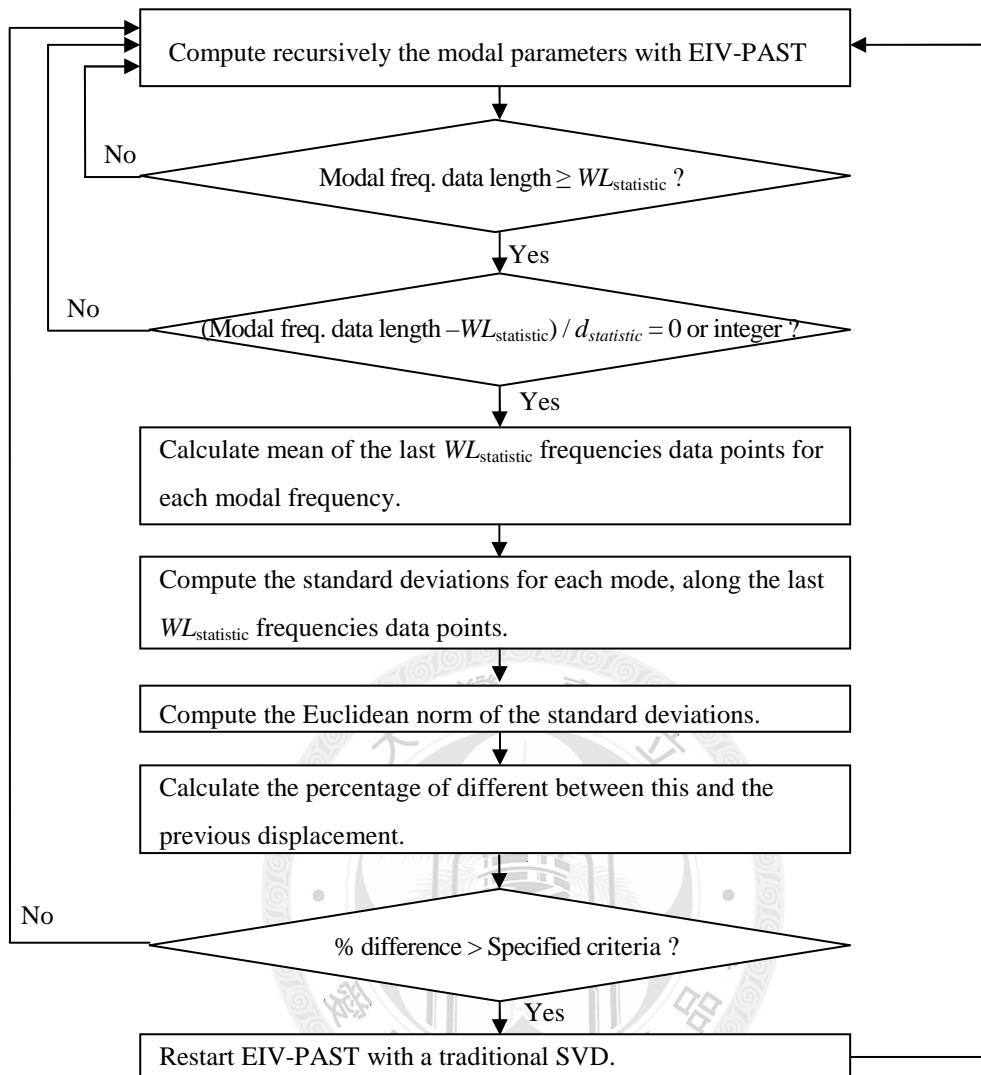
Figure 6-1 Flow chart of the implementation of RSSI-COV.
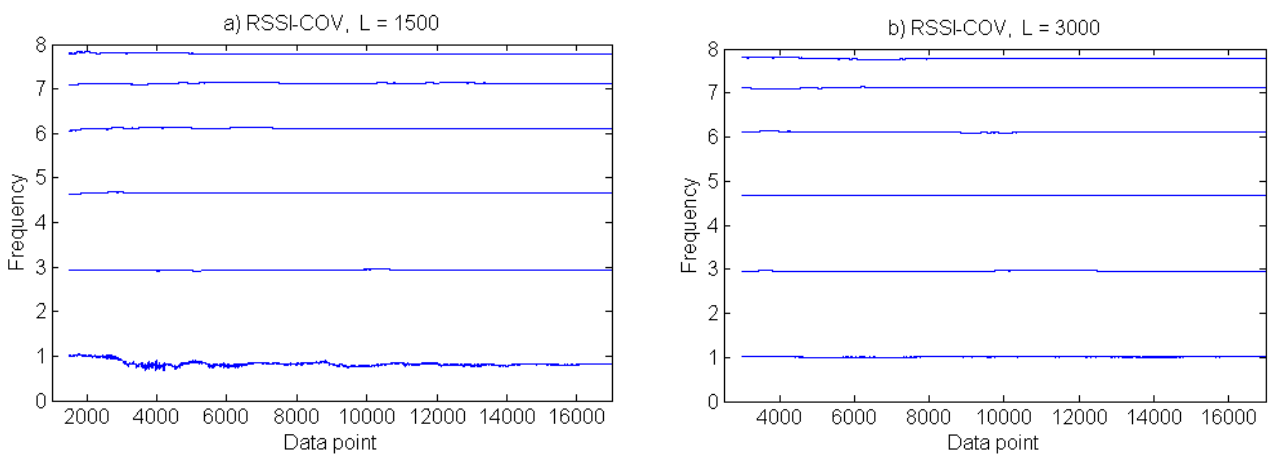
Figure 6-2 Frequency tracking by RSSI-COV for time-invariant system.

a) moving window length = 1500 points. b) moving window length = 3000 points.
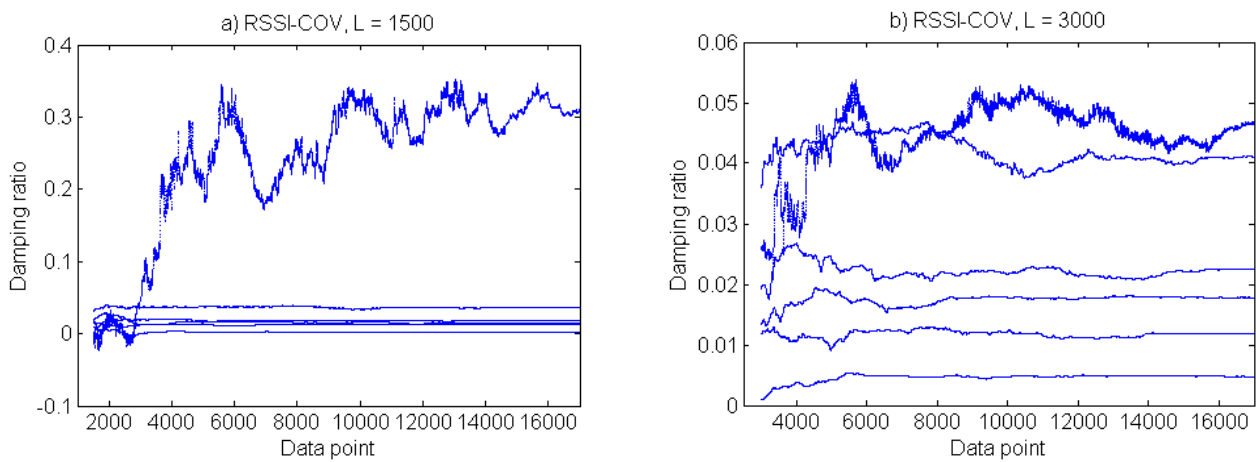
Figure 6-3   Damping ratio tracking by RSSI-COV for time-invariant system.

a) moving window length = 1500 points. b) moving window length = 3000 points.
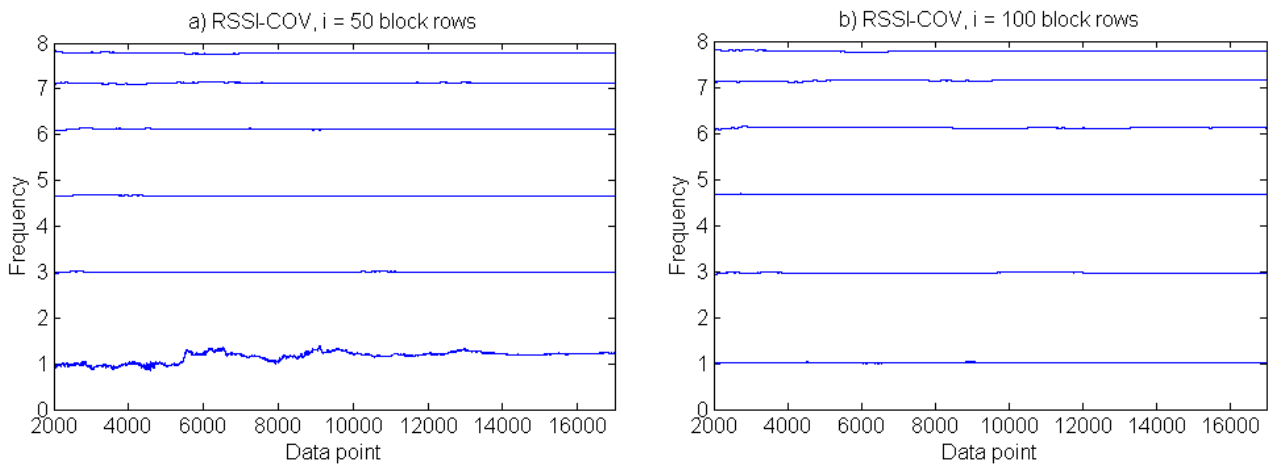
Figure 6-4   Frequency tracking by RSSI-COV for time-invariant system, adding noise correlated with output.

a) number of block rows $i = 50$. b) $i = 100$ block rows.
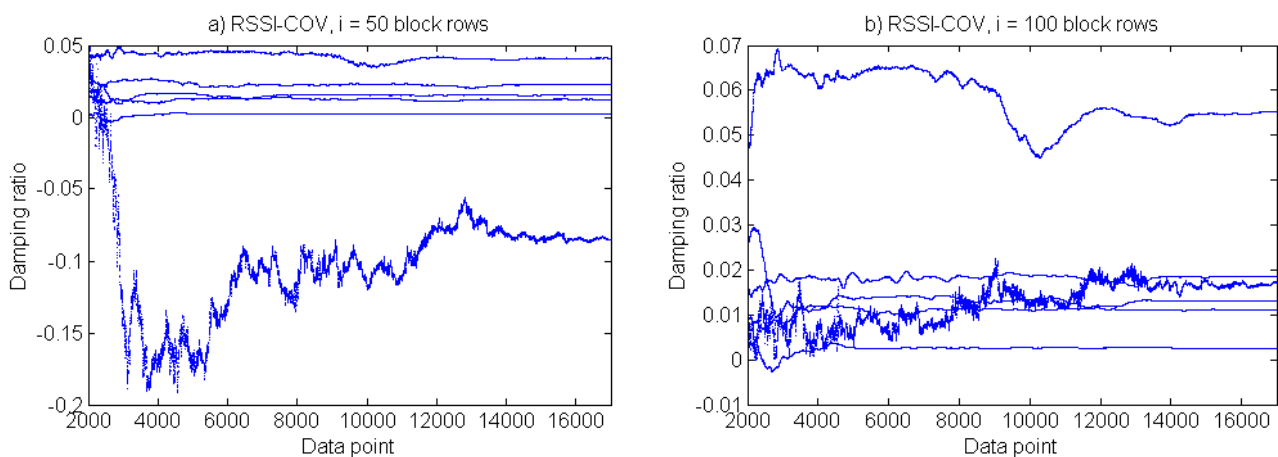
Figure 6-5   Damping ratio tracking by RSSI-COV for time-invariant system, adding noise correlated with output.

a) number of block rows $i = 50$. b) $i = 100$ block rows.

182
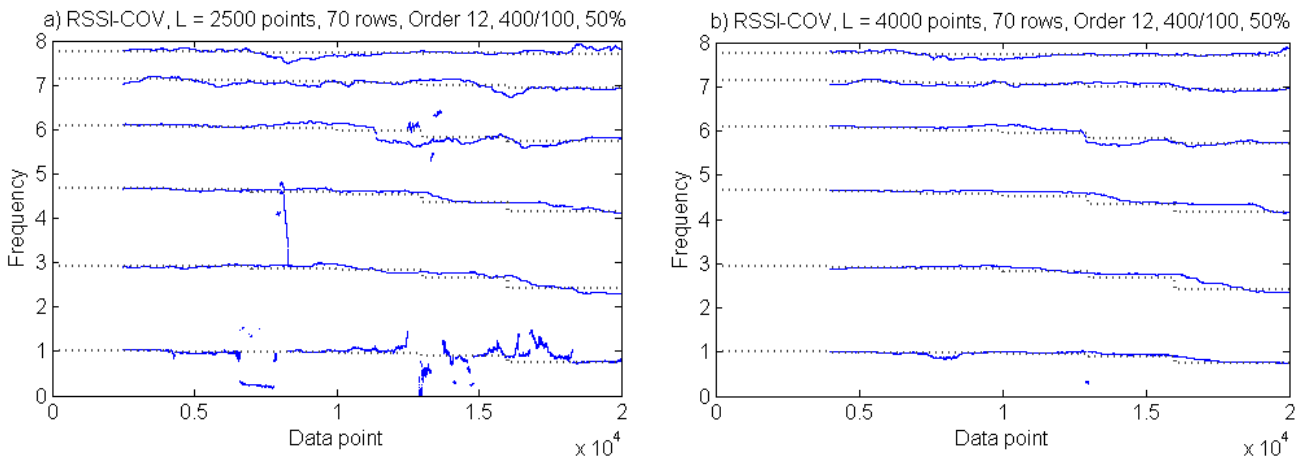
Figure 6-6 Frequency tracking by RSSI-COV for a 6-DOF system with sudden stiffness reduction. a) moving window length $L = 2500$ points. b) $L = 4000$ points.
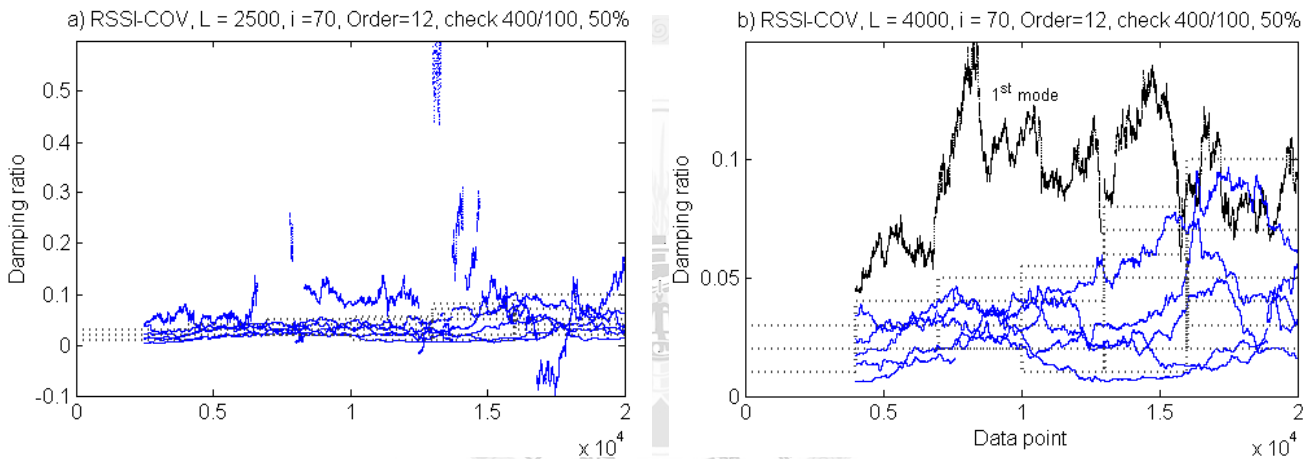
Figure 6-7 Damping ratio tracking by RSSI-COV for a 6-DOF system with sudden stiffness reduction. a) moving window length $L = 2500$ points. b) $L = 4000$ points.
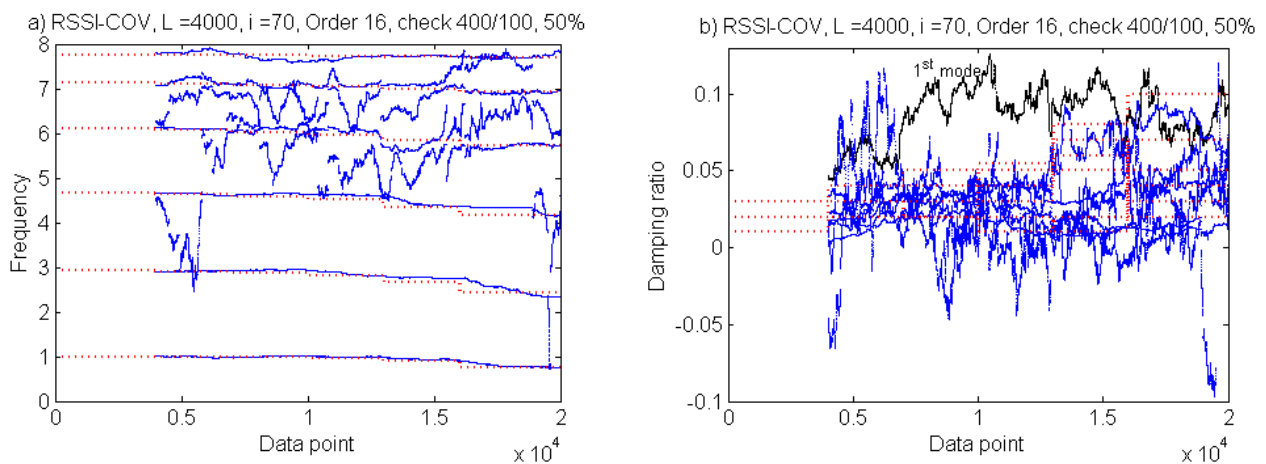
Figure 6-8 a) Modal frequency, and b) damping ratio tracking by RSSI-COV for a 6-DOF system with sudden stiffness reduction. System order: 16.
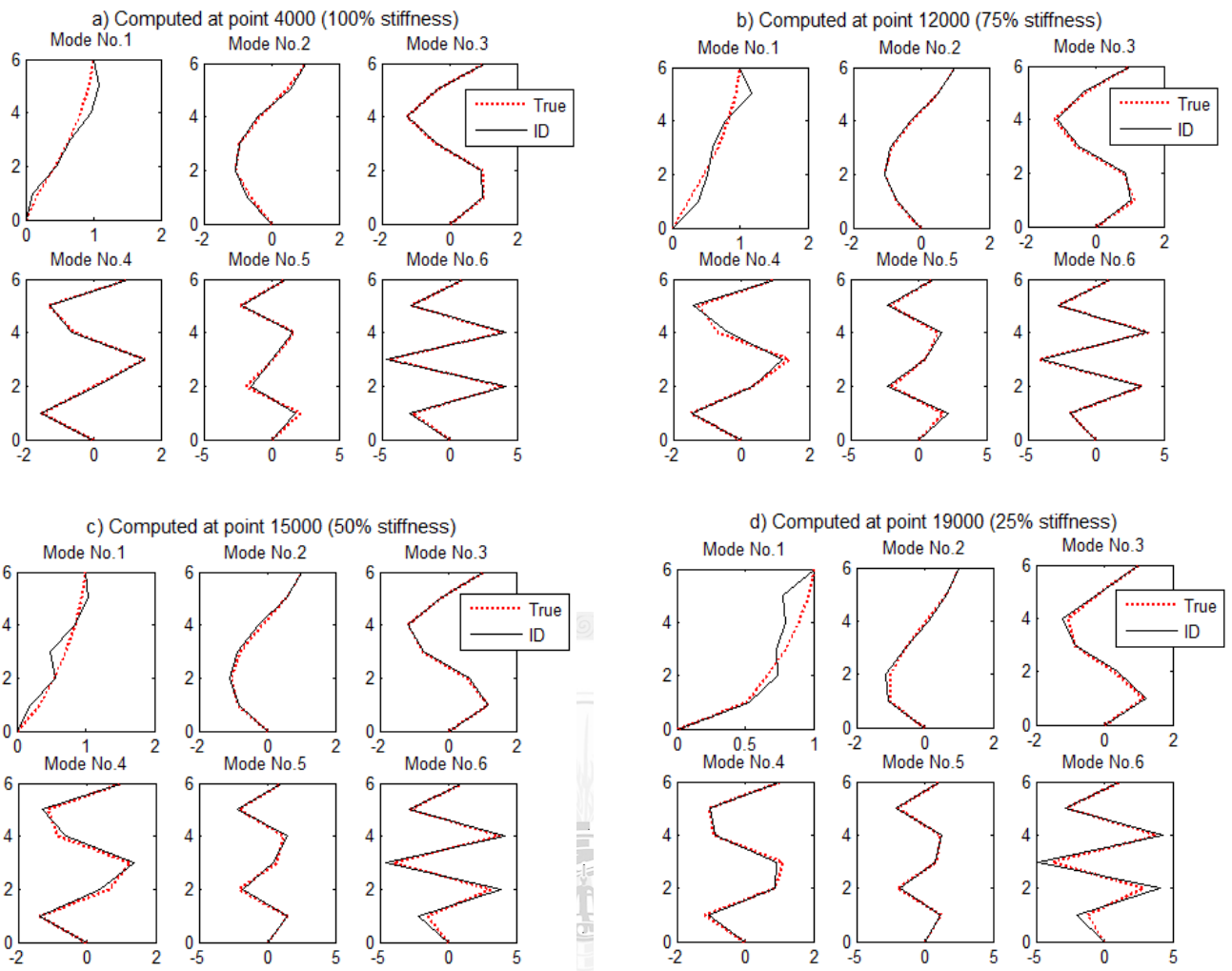
Figure 6-9 Examples of mode shapes computed by RSSI-COV for a 6-DOF system with sudden stiffness reduction.

a) at point 4000 (100% stiffness), b) at point 12000 (75% stiffness),

c) at point 15000 (50% stiffness), d) at point 19000 (25% stiffness).
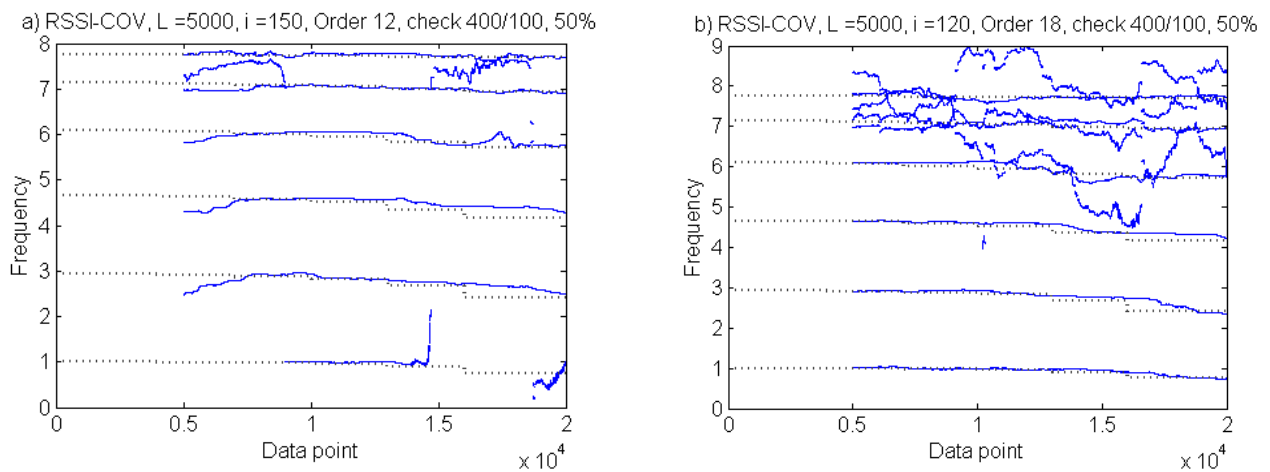
Figure 6-10 Frequency tracking by RSSI-COV for addtion of a noise correlated with output.

a) Order 12, 150 number of block rows *i*. b) *i*=120, Order 18.
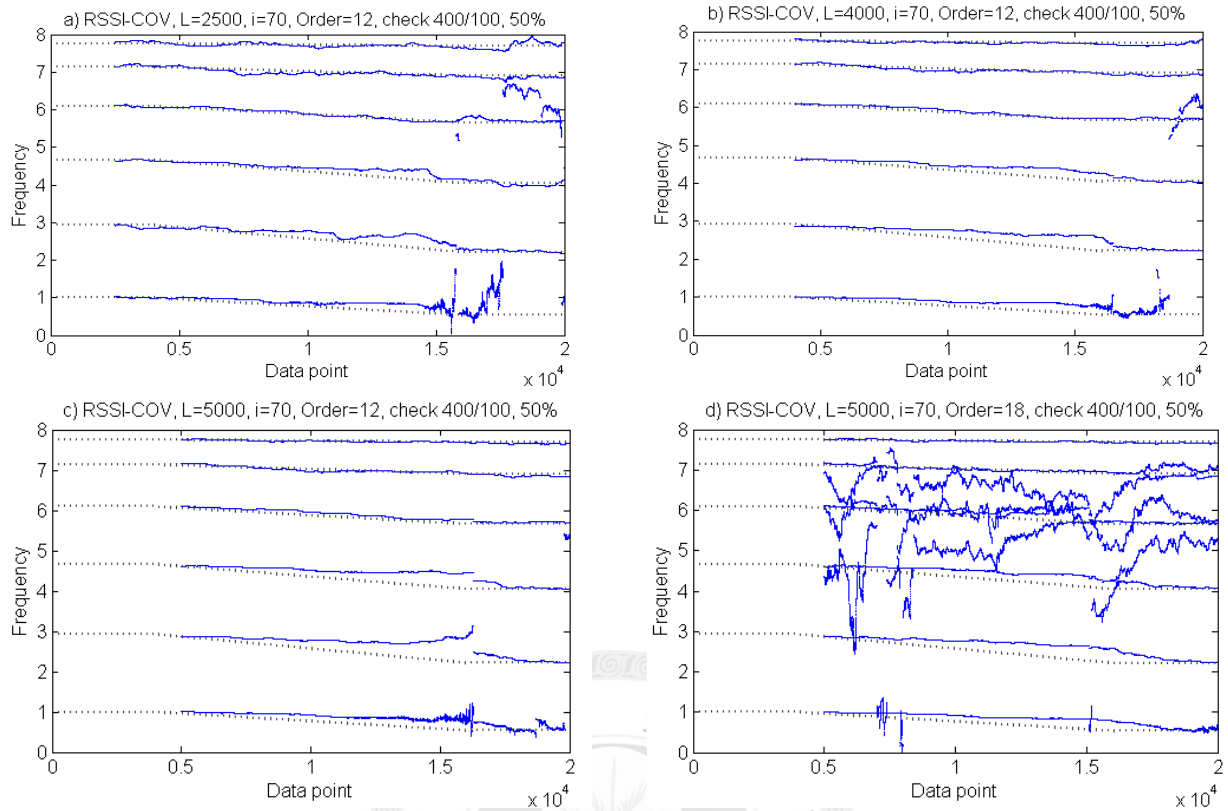
Figure 6-11 Frequency tracking by RSSI-COV for a 6-DOF system with slow stiffness reduction. Noise free. a) moving window length L = 2500 points. b) L = 4000 points. c) L = 5000 points, Order = 12. d) L = 5000 points, Order = 18.
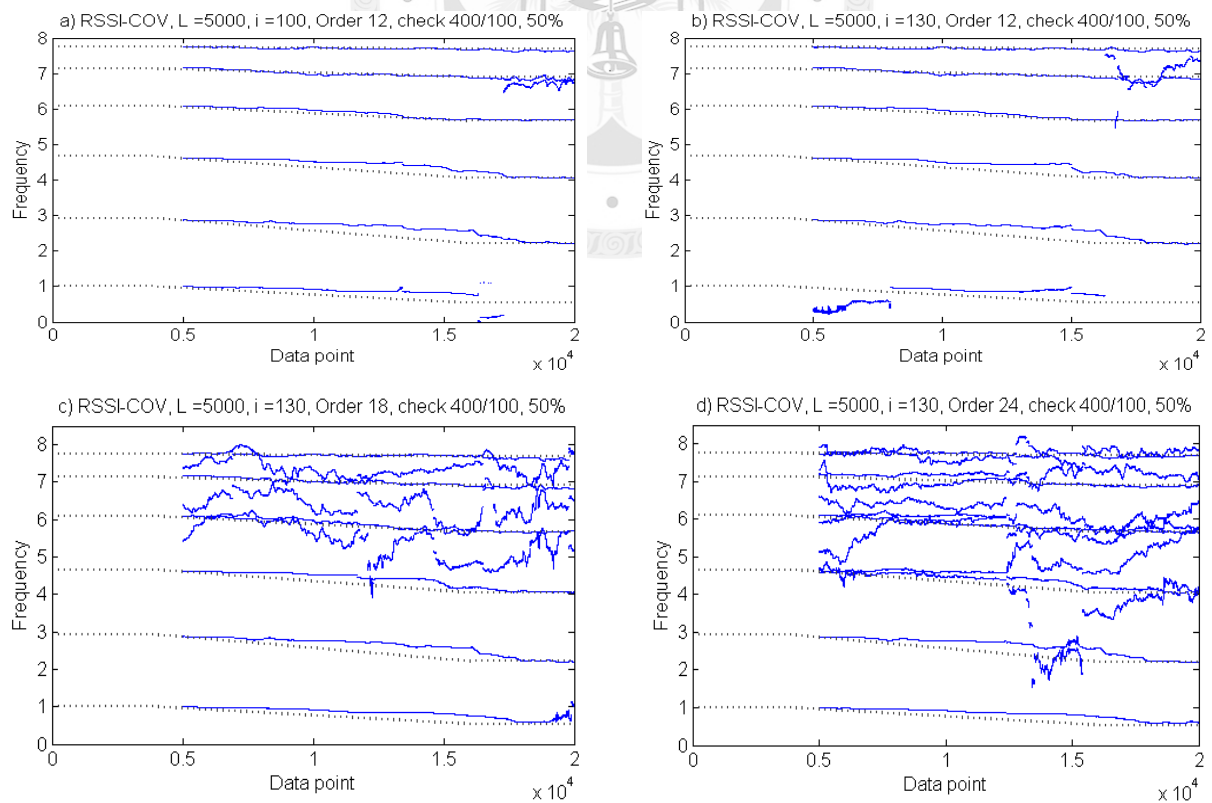
Figure 6-12 Frequency tracking by RSSI-COV considering the time-varying effect. a) number of block rows i = 100, Order 12, b) i = 130, Order 12, c) i = 130, Order 18, d) i = 130, Order = 24.
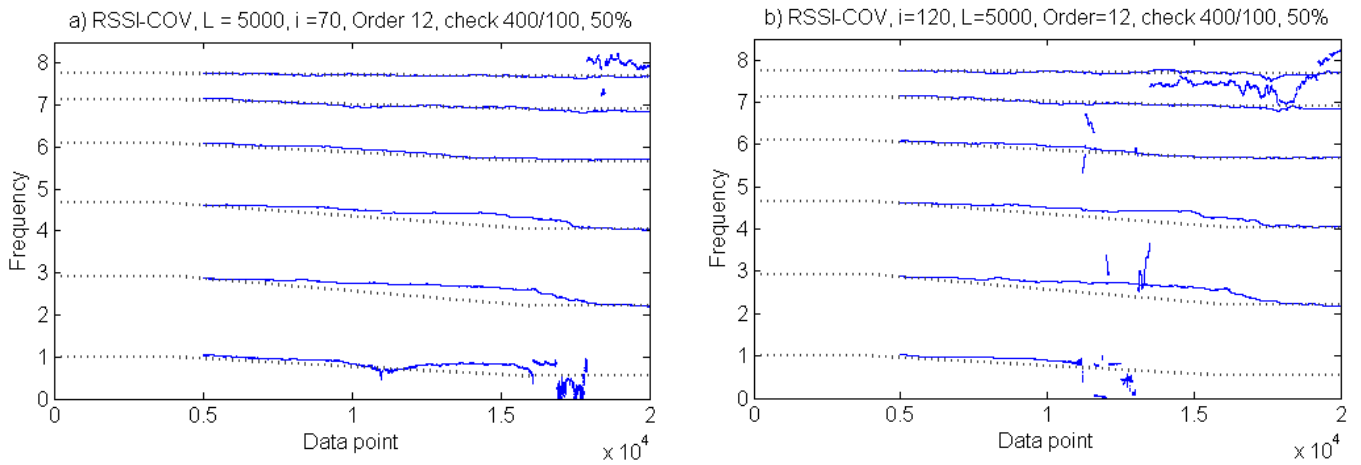
Figure 6-13 Frequency tracking by RSSI-COV for a 6-DOF system with slow stiffness reduction. Noise correlated with output. a) i = 70, b) *i* = 120.
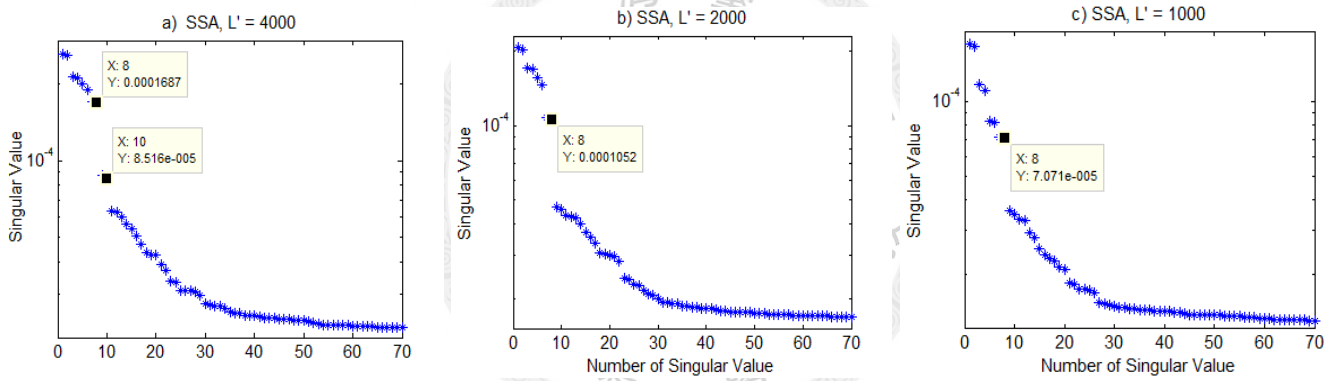
Figure 6-14 Singular spectrum in rSSA step.

186
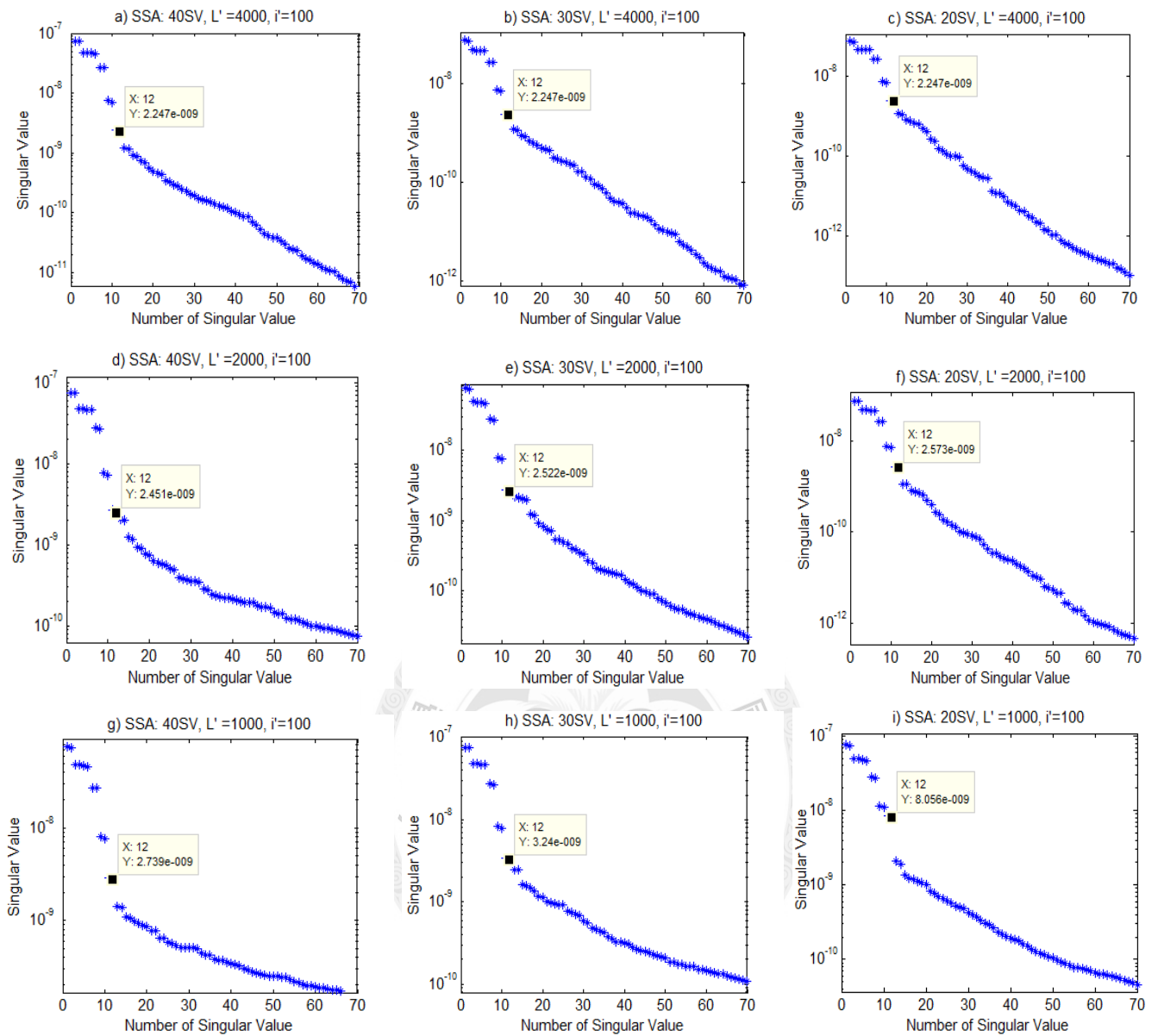
Figure 6-15   Singular spectrum in SSI-COV step, for different combinations of the number of SV in rSSA step and the moving window length *L'*.
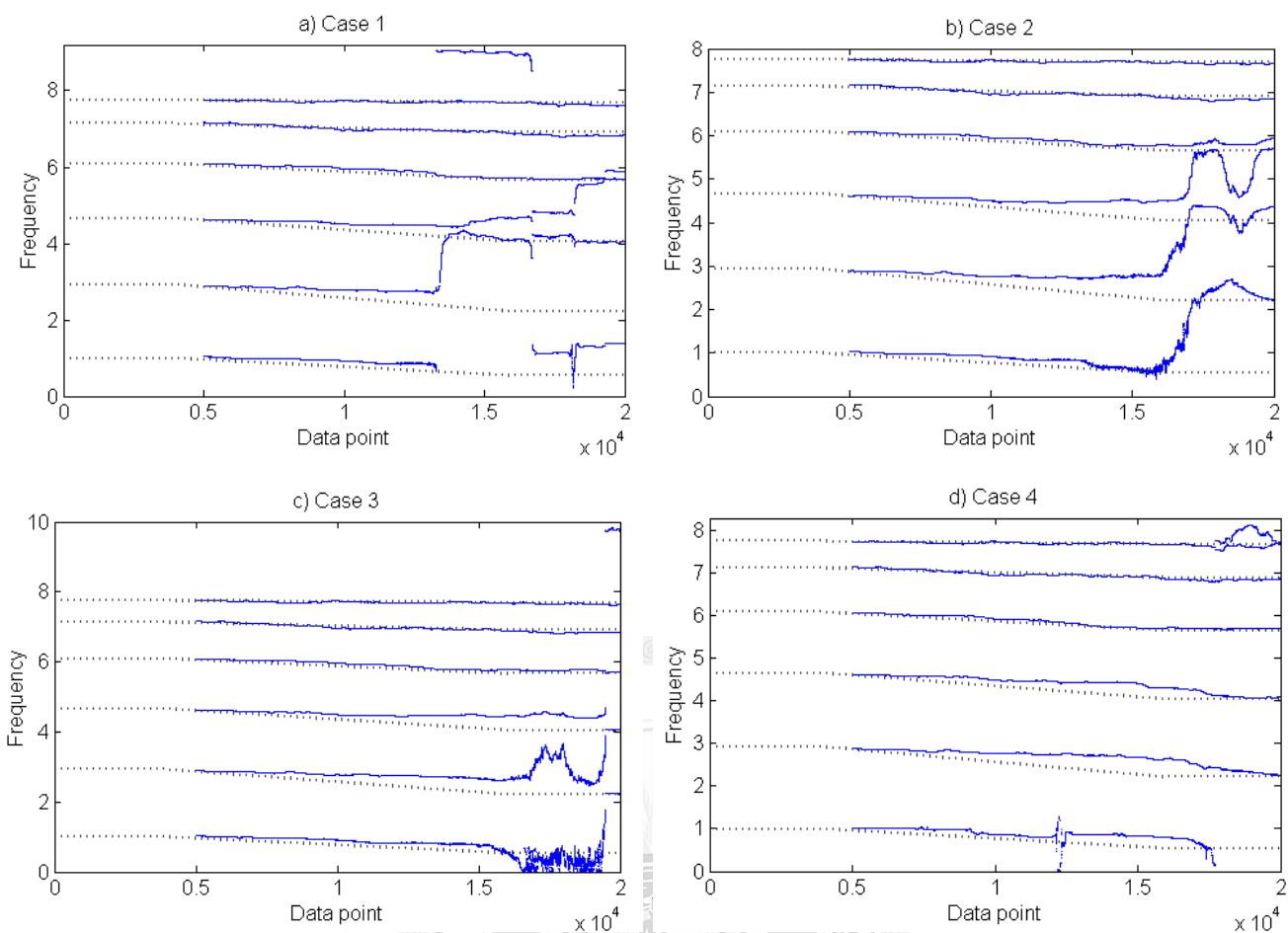
Figure 6-16   Frequency tracking by rSSA-SSI-COV. Noise correlated with output. Comparison of the 4 cases.
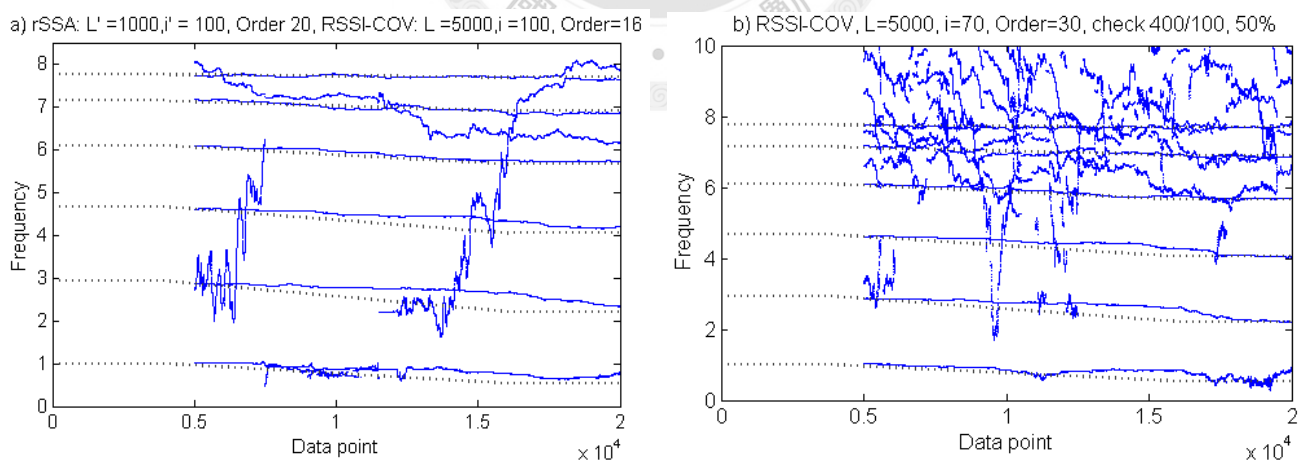
Figure 6-17   Compring the recursive frequency tracking by a) rSSA-SSI-COV, system order 16 and

b) RSSI-COV, order 30.
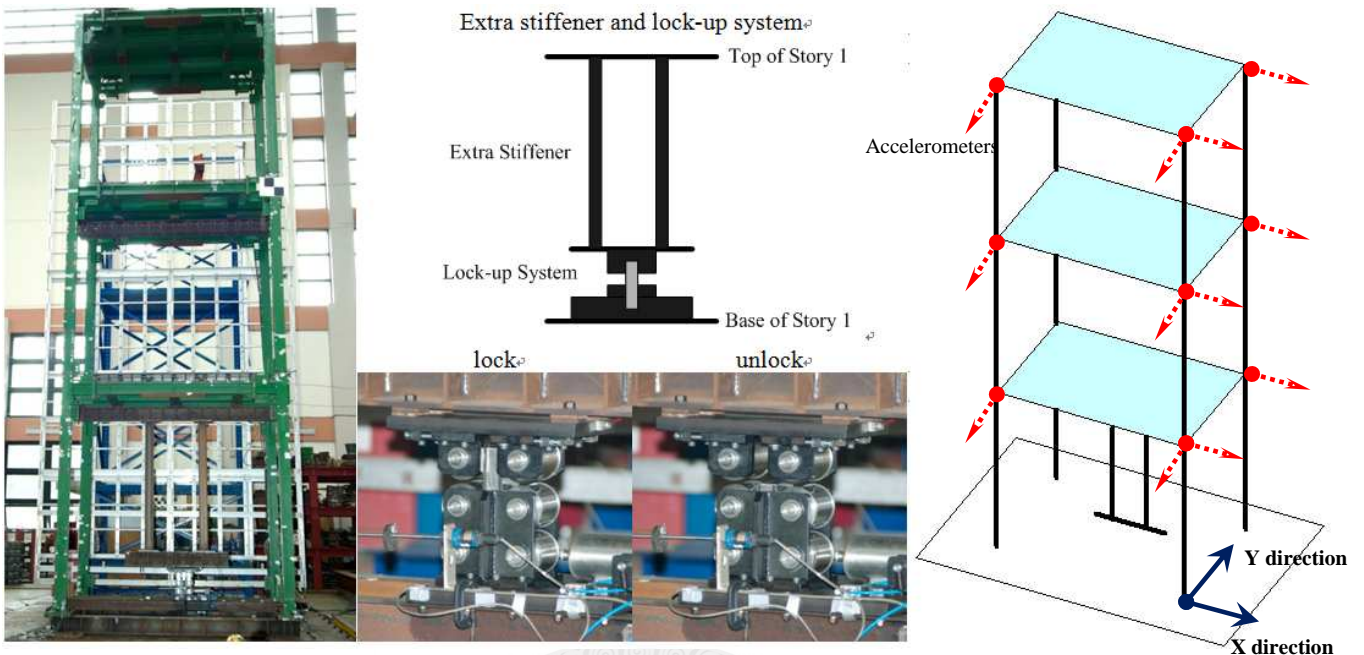
188

Figure 7-1 3-story steel frame with extra stiffener and lock-up system in the 1st story.

Figure 7-1 3-story steel frame with extra stiffener and lock-up system in the 1st story.
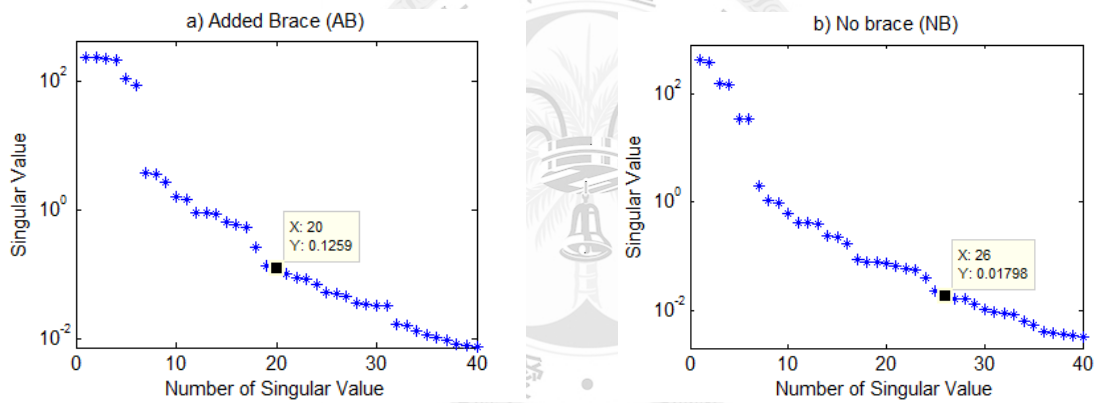
Figure 7-2 Singular spectrum obtained by SSI-COV.
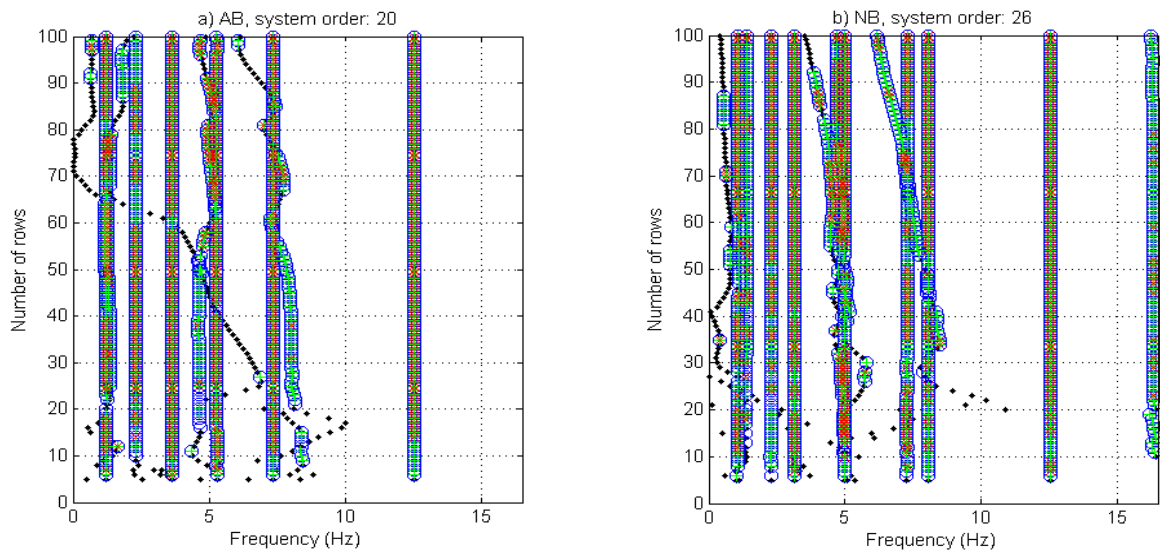
Figure 7-3 Stabilization diagram for pole discrimination.
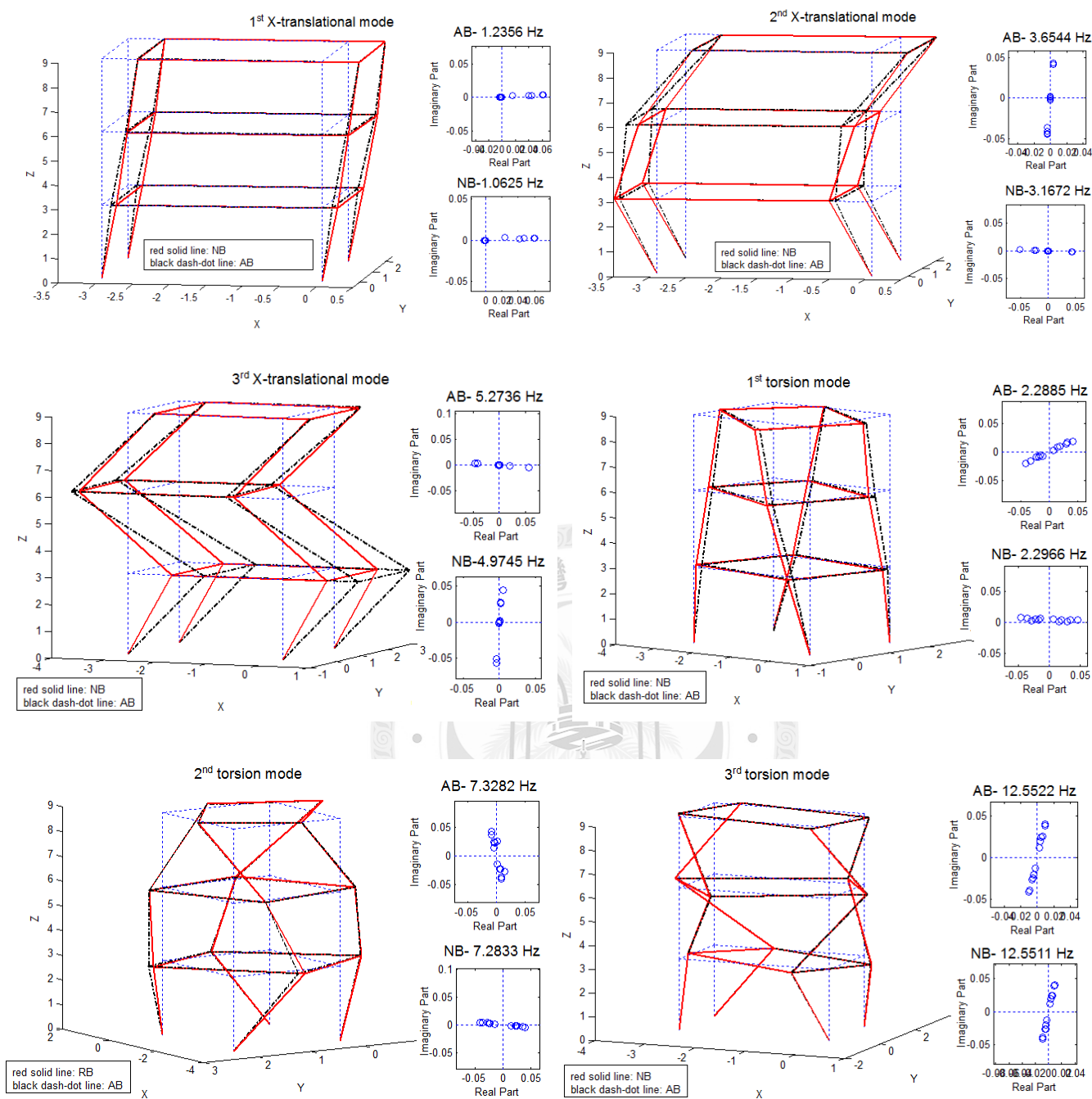
Figure 7-4 Three dimensional mode shapes before and after removing the brace.
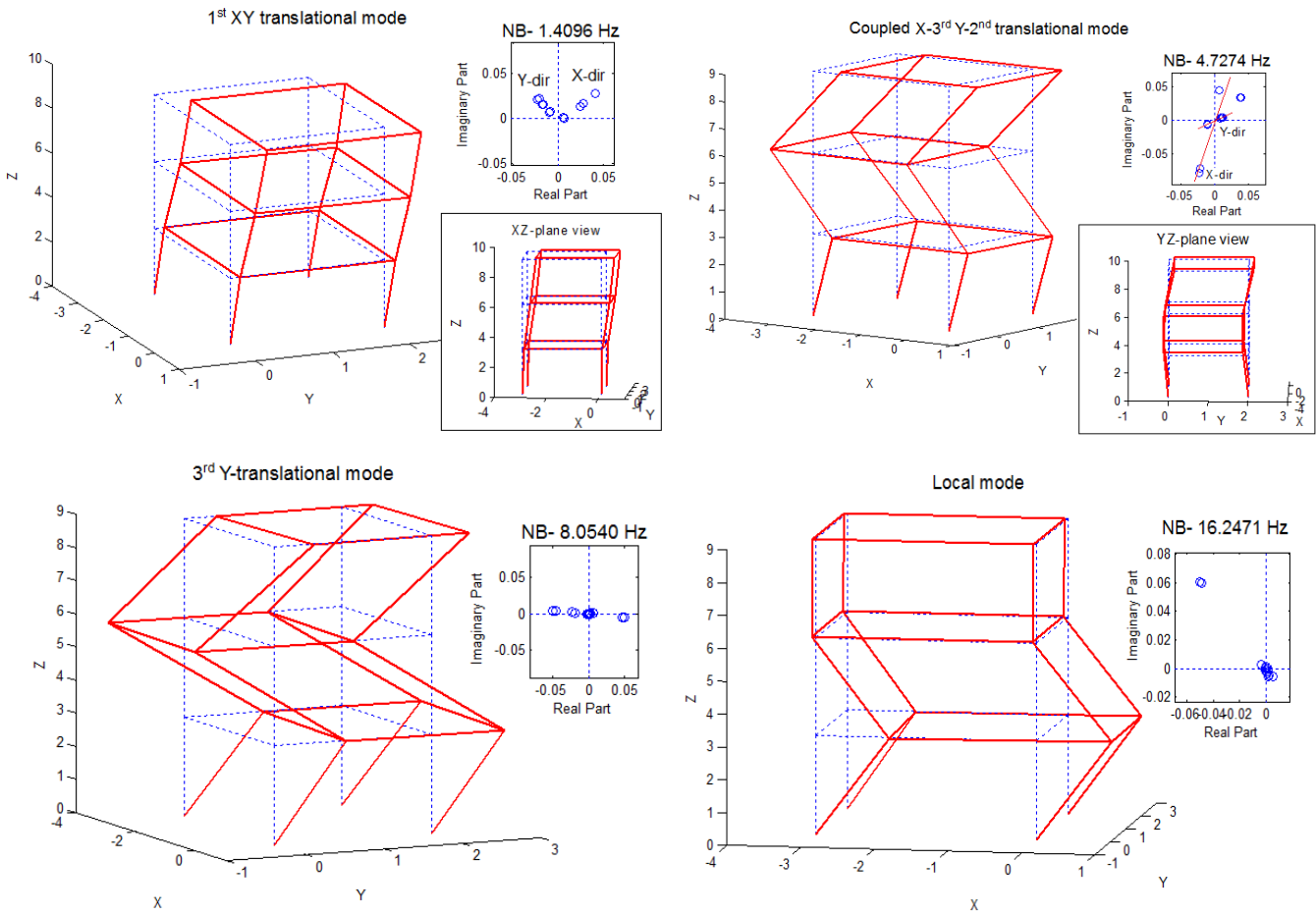
Figure 7-5   Additionally identified three dimensional mode shapes after removing the brace.
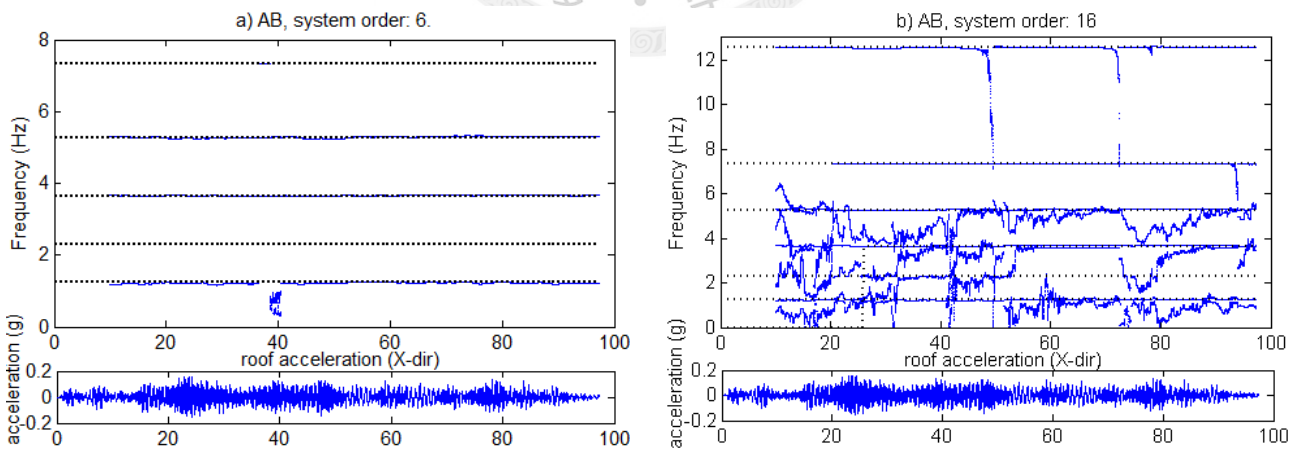
Figure 7-6   Recursive identification of modal frequencies for white noise excitation, a) AB order 6, b) AB order 16.
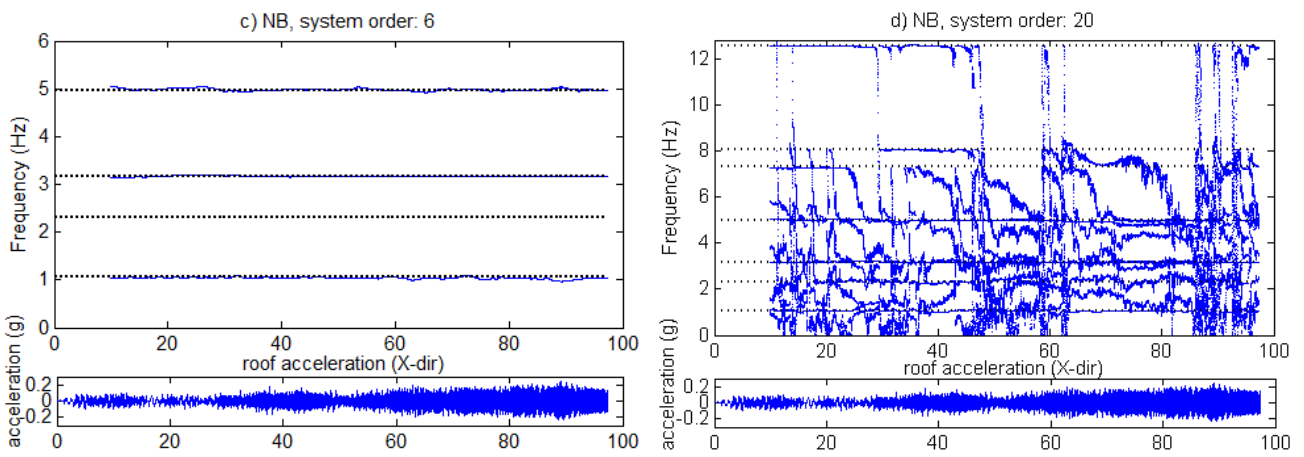
Figure 7-6   Recursive identification of modal frequencies for white noise excitation, c) NB order 6, d) NB order 20.
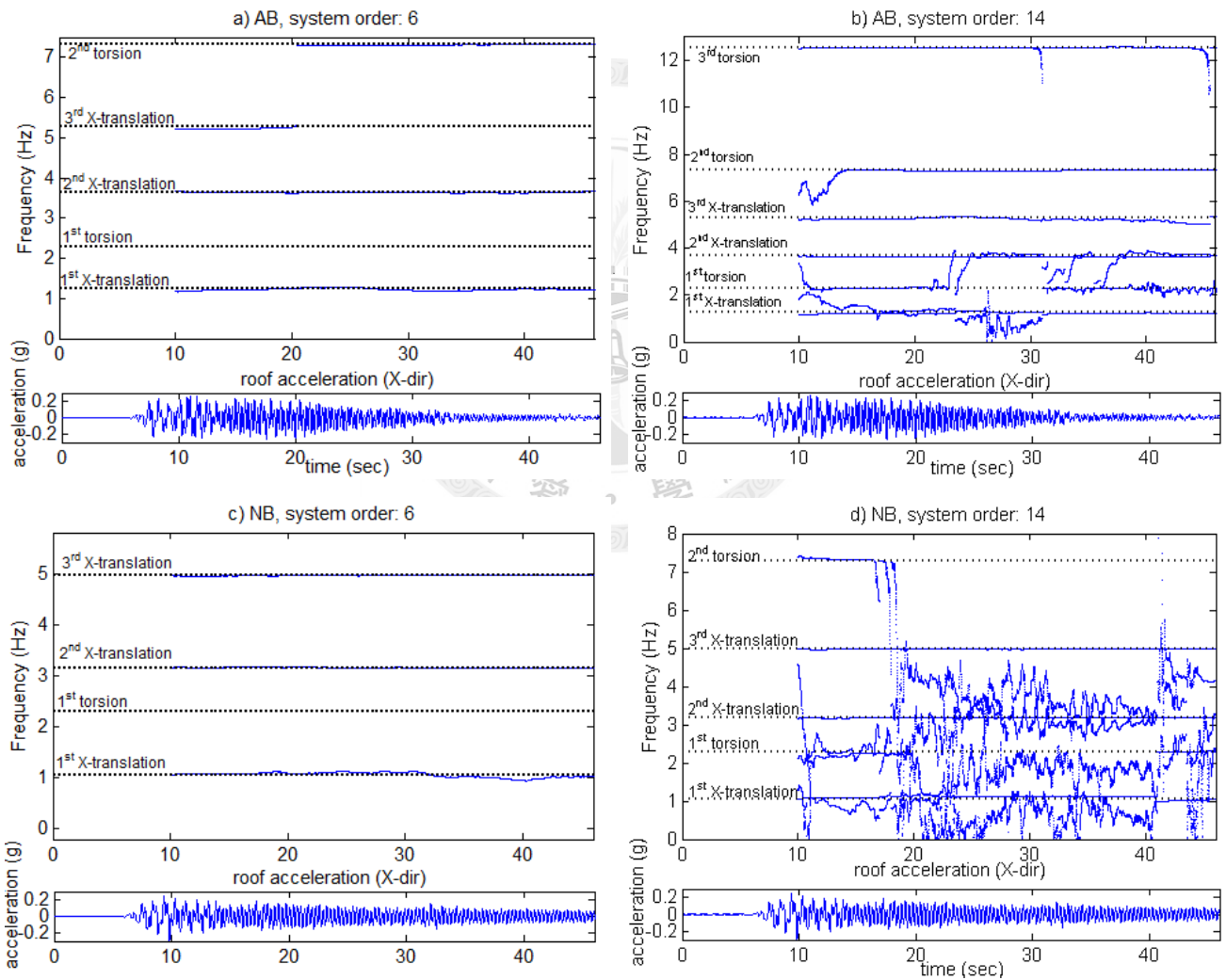
Figure 7-7   Recursive identification of modal frequencies for El Centro earthquake,

with no instantaneous stiffener release.
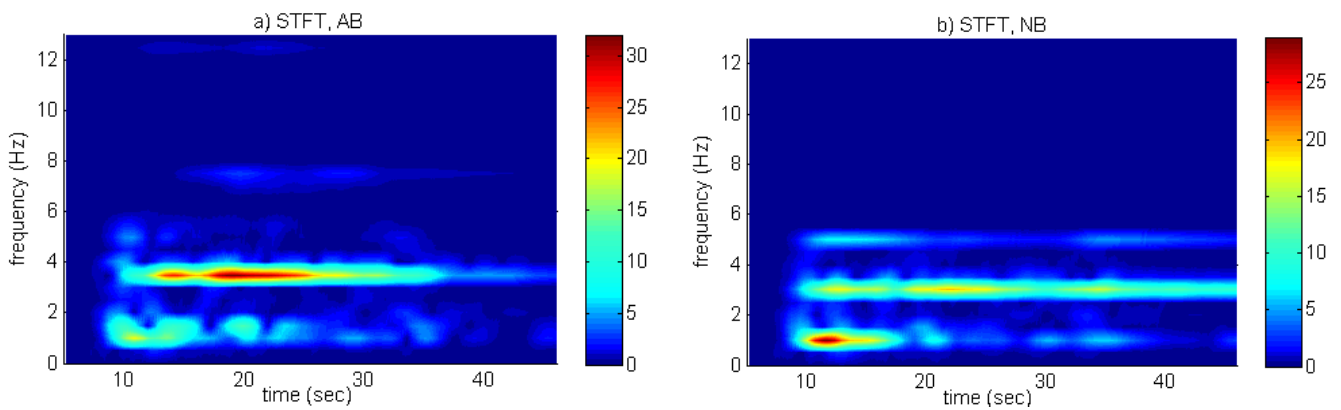
Figure 7-8 Short Time Fourier Transform for steel frame subjected to El Centro earthquake, with no instantaneous stiffener release.
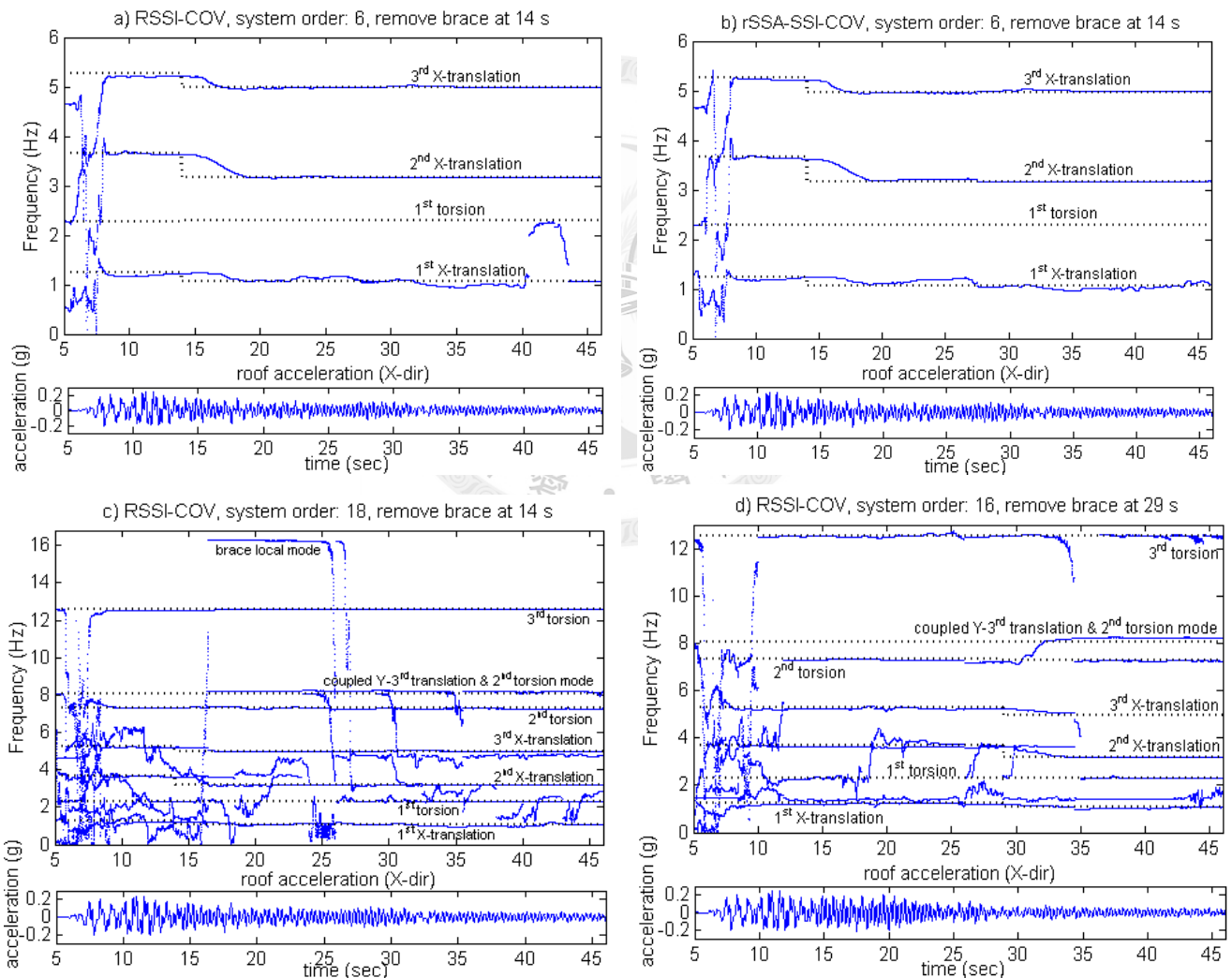
Figure 7-9 Recursive identification of modal frequencies for El Centro earthquake.

Siffener released at 14 and 29 seconds.
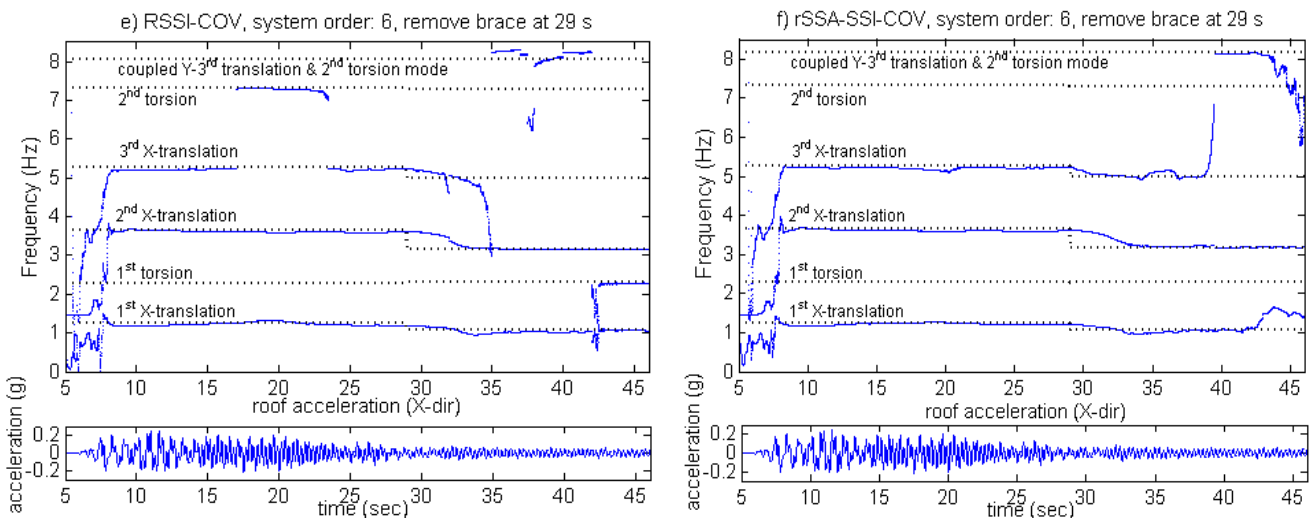
Figure 7-9 Recursive identification of modal frequencies for El Centro earthquake.

Siffener released at 14 and 29 seconds.
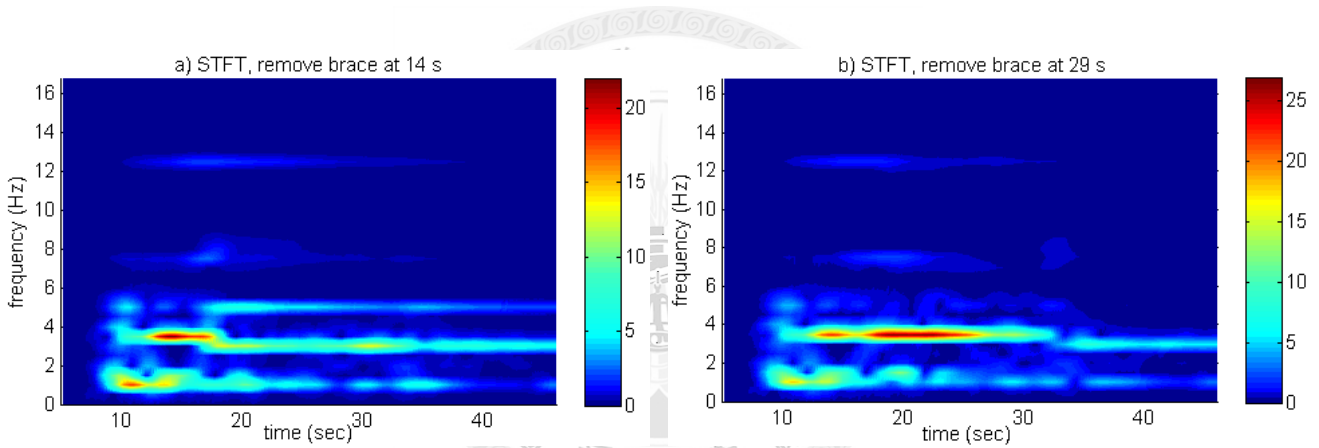
Figure 7-10 Short Time Fourier Transform for steel frame subjected to for El Centro earthquake, instantaneous stiffener release at 14 s and 29 s.
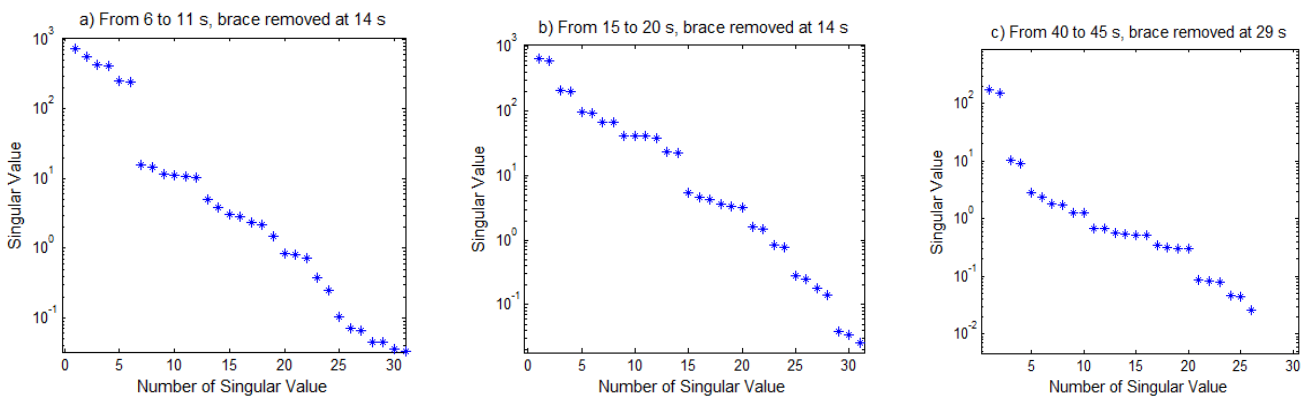
Figure 7-11 Singular spectrum for different time segments.
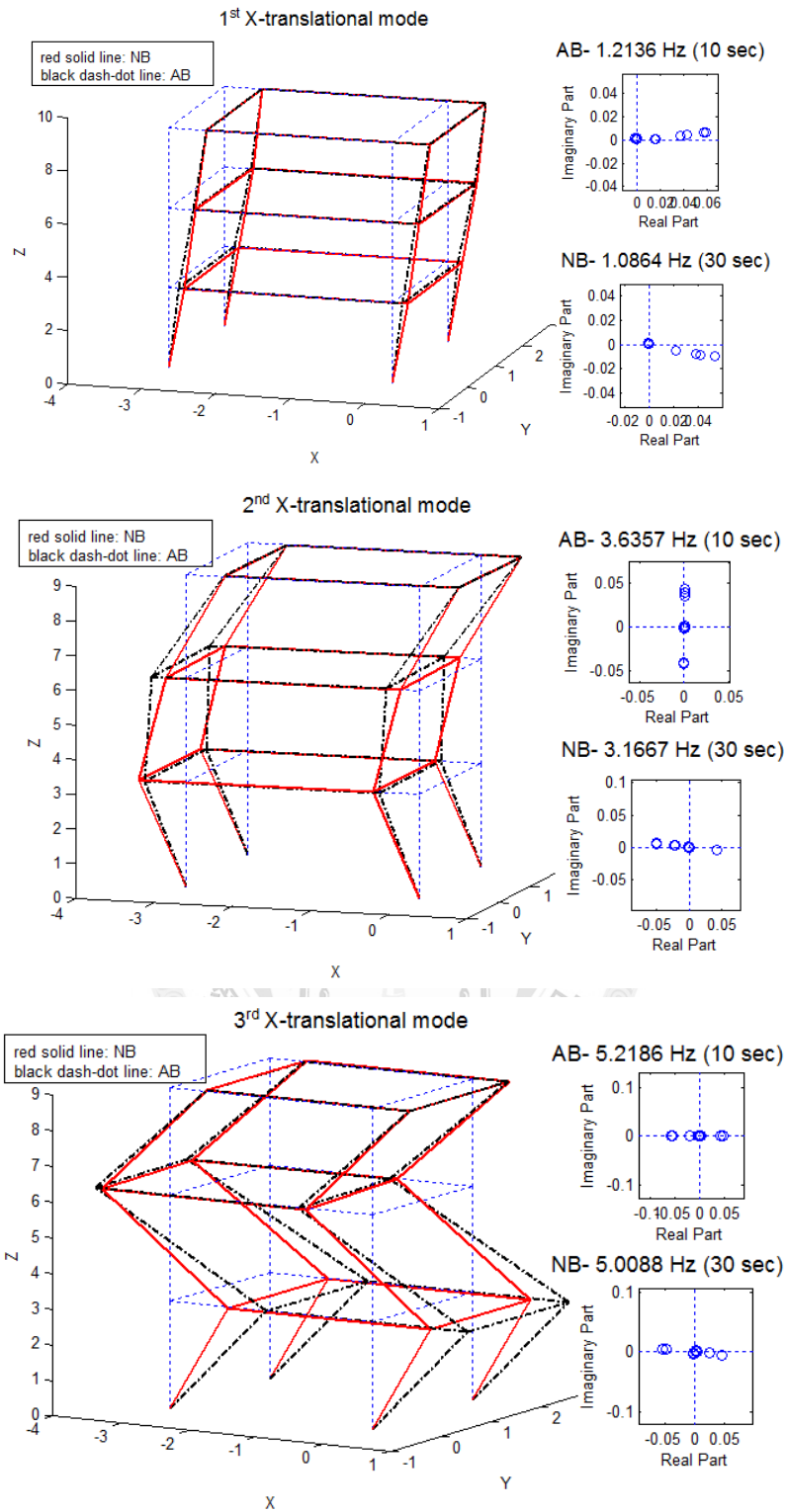
Figure 7-12 Three dimensional mode shapes identified with system order equals to 6, case where the brace is removed at 14 seconds.
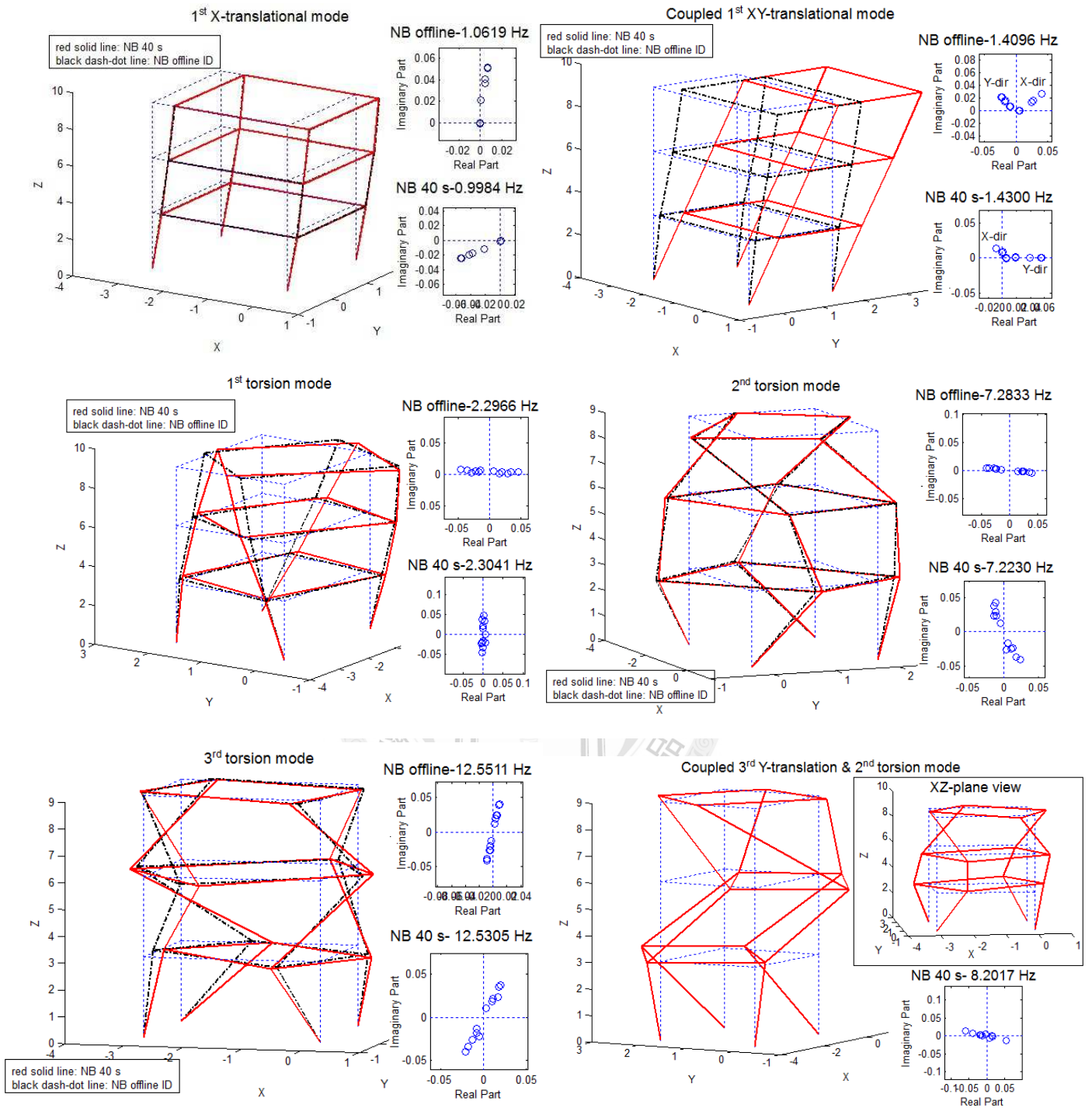
Figure 7-13 Three dimensional torsion and coupled mode shapes identified with system order 16, case where the brace is removed at 29 seconds, comparing with the corresponding offline identified modes.
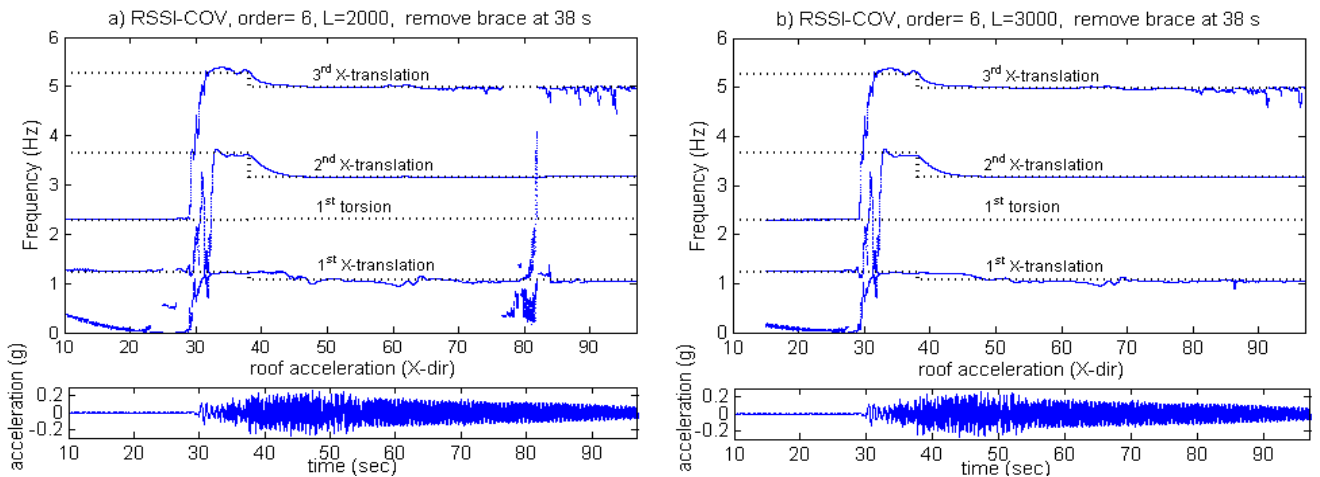
Figure 7-14 Recursive identification of modal frequencies for TCU082 earthquake. Siffener released at 38 seconds.
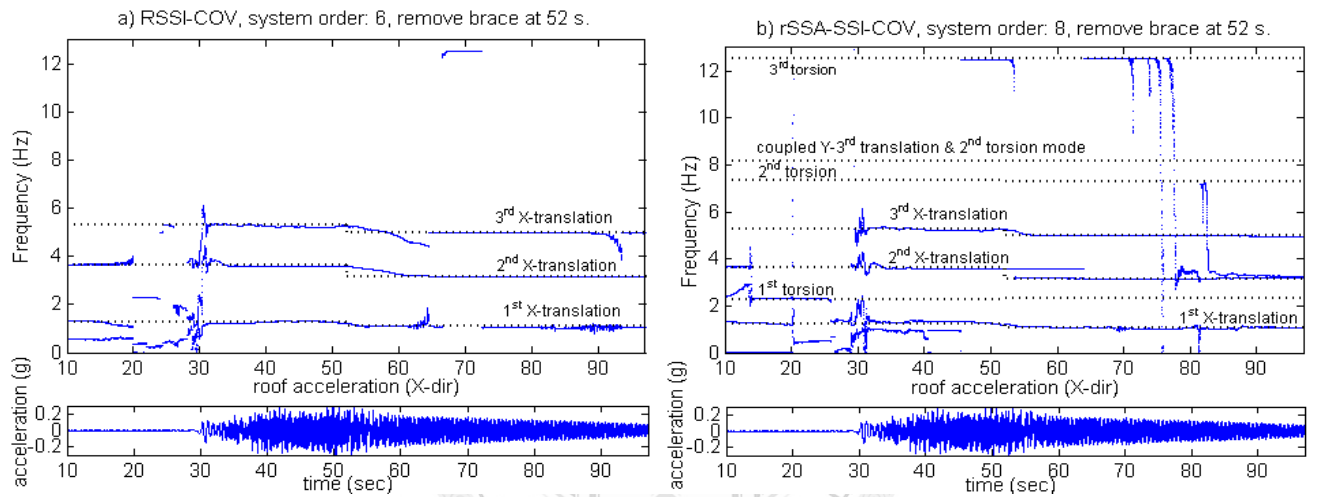
Figure 7-15 Recursive identification of modal frequencies for TCU082 earthquake. Siffener released at 52 seconds.
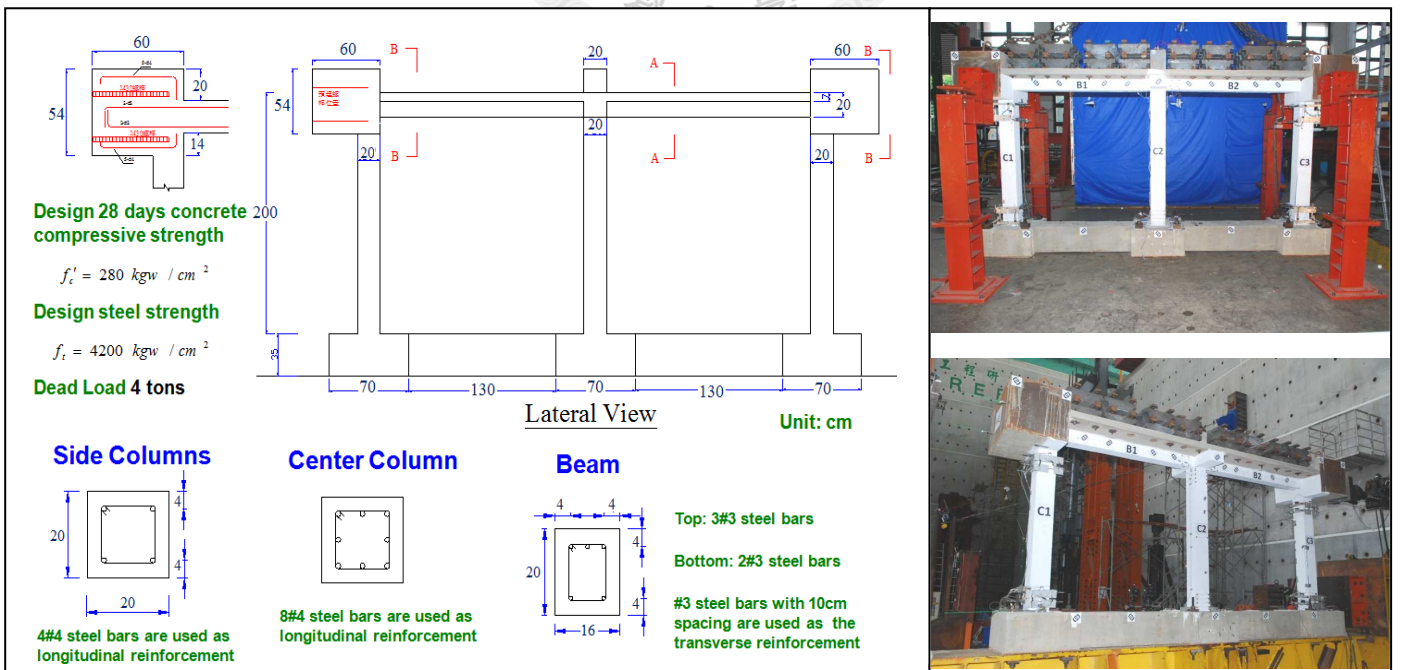
Figure 7-16 Dimensions and the design detail of 1-story 2-bay RC frame.

197
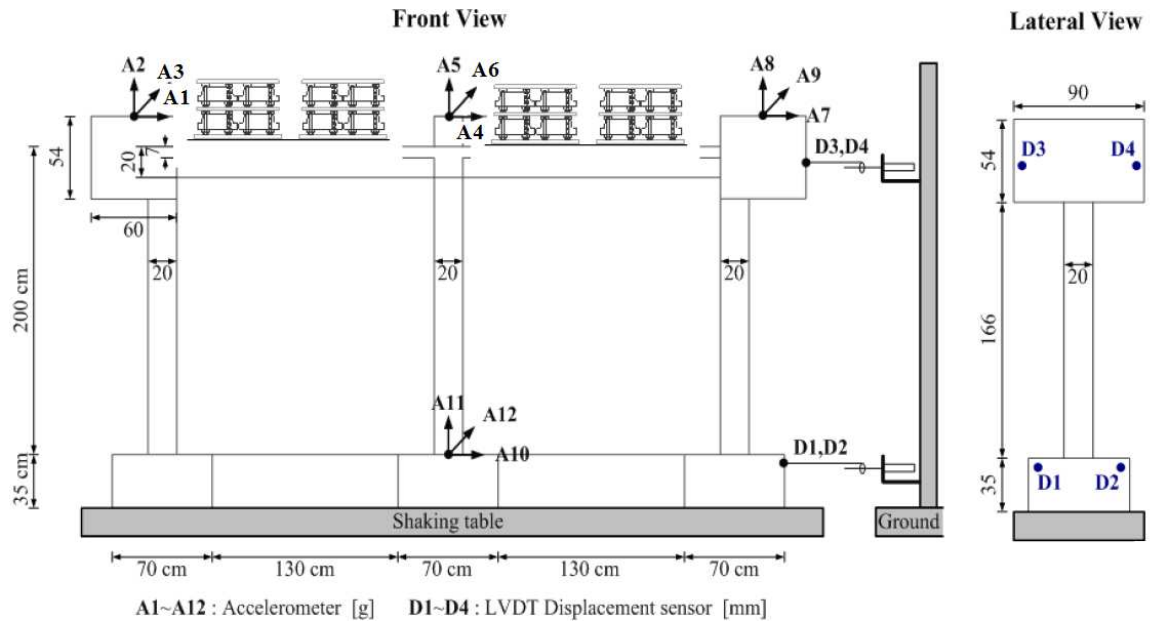
Figure 7-17 Installation and instrumentation of the RC frame.
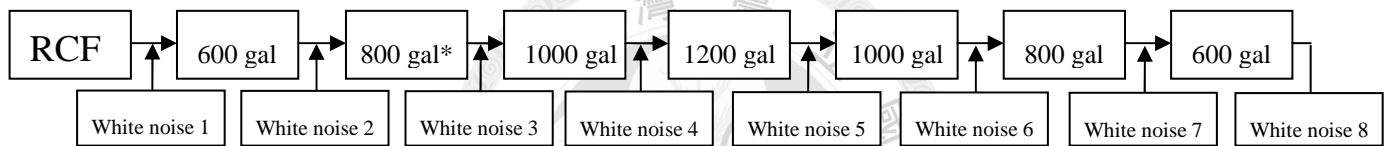
Figure 7-18 Arrangement of the series RCF6 shaking table test.
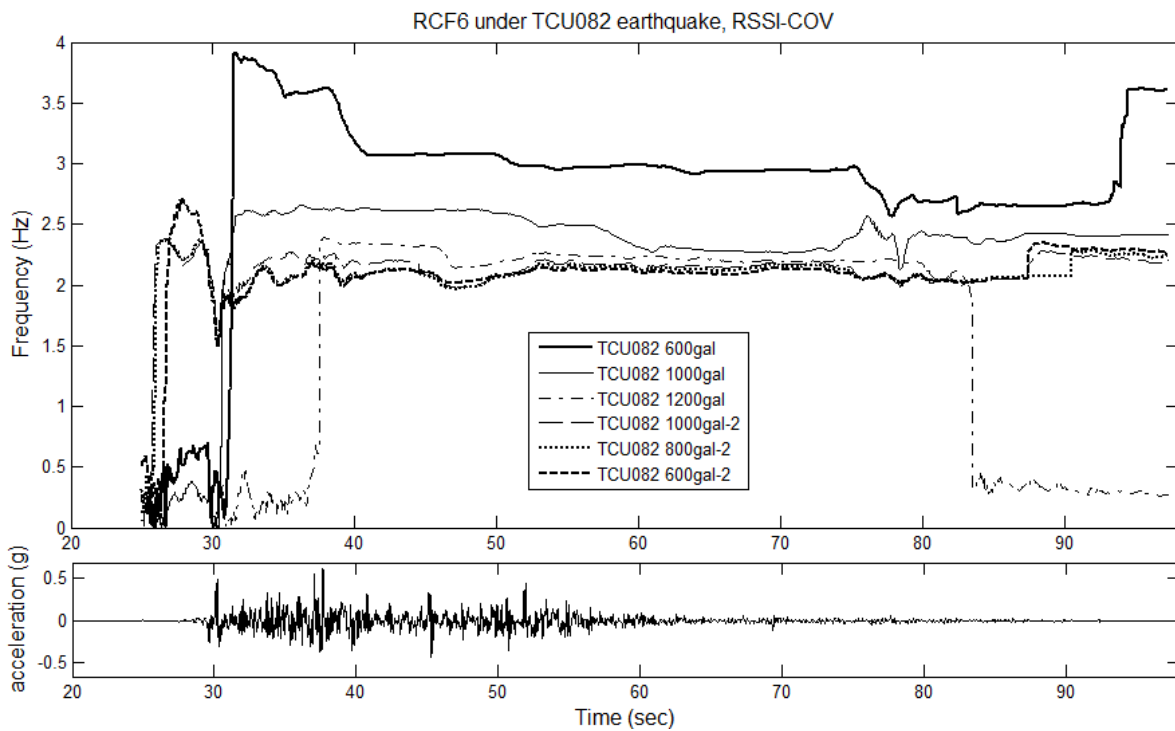
Figure 7-19 Frequency traced by RSSI-COV for the RCF6 frame subjected to series of TCU082 earthquake.
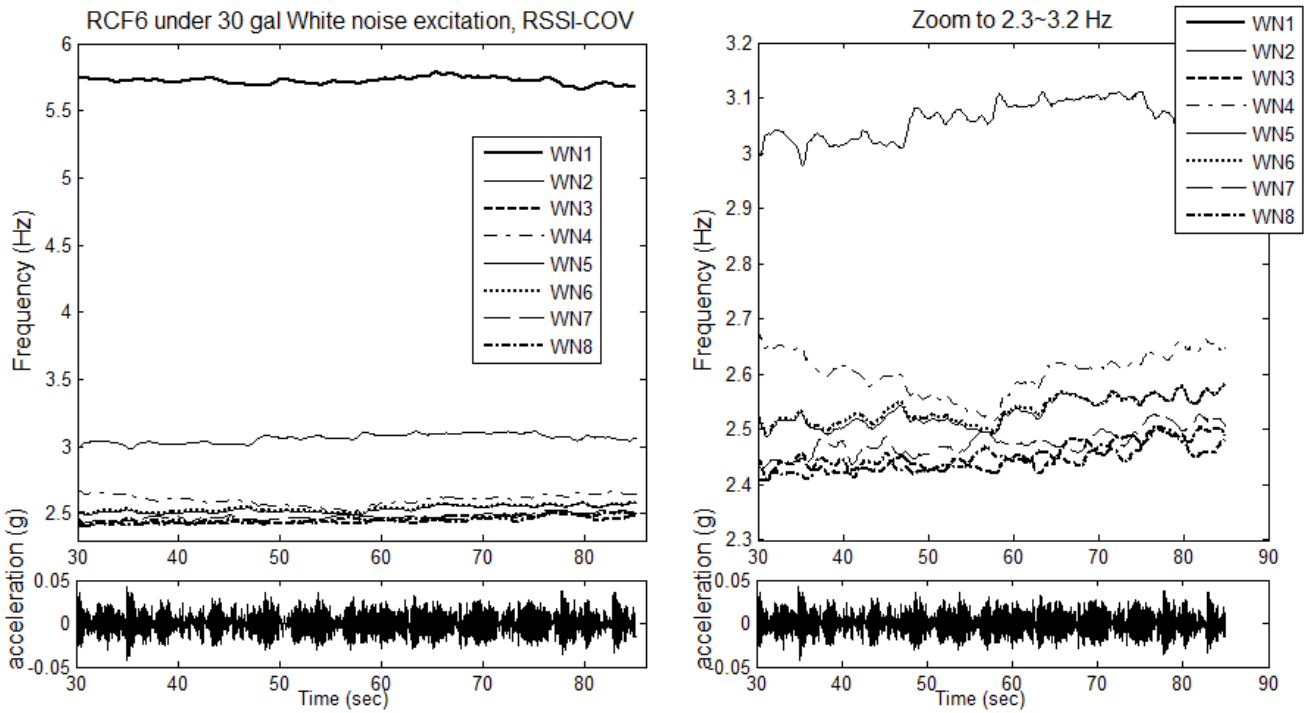
Figure 7-20 Frequency traced by RSSI-COV for the RCF6 frame subjected to 30 gal white noise excitation at different damage state.
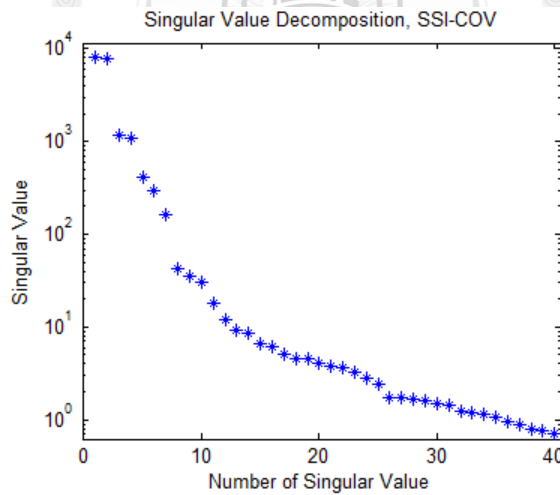
Figure 7-21 Singular spectrum obtained from the data points between 25 and 40 seconds.
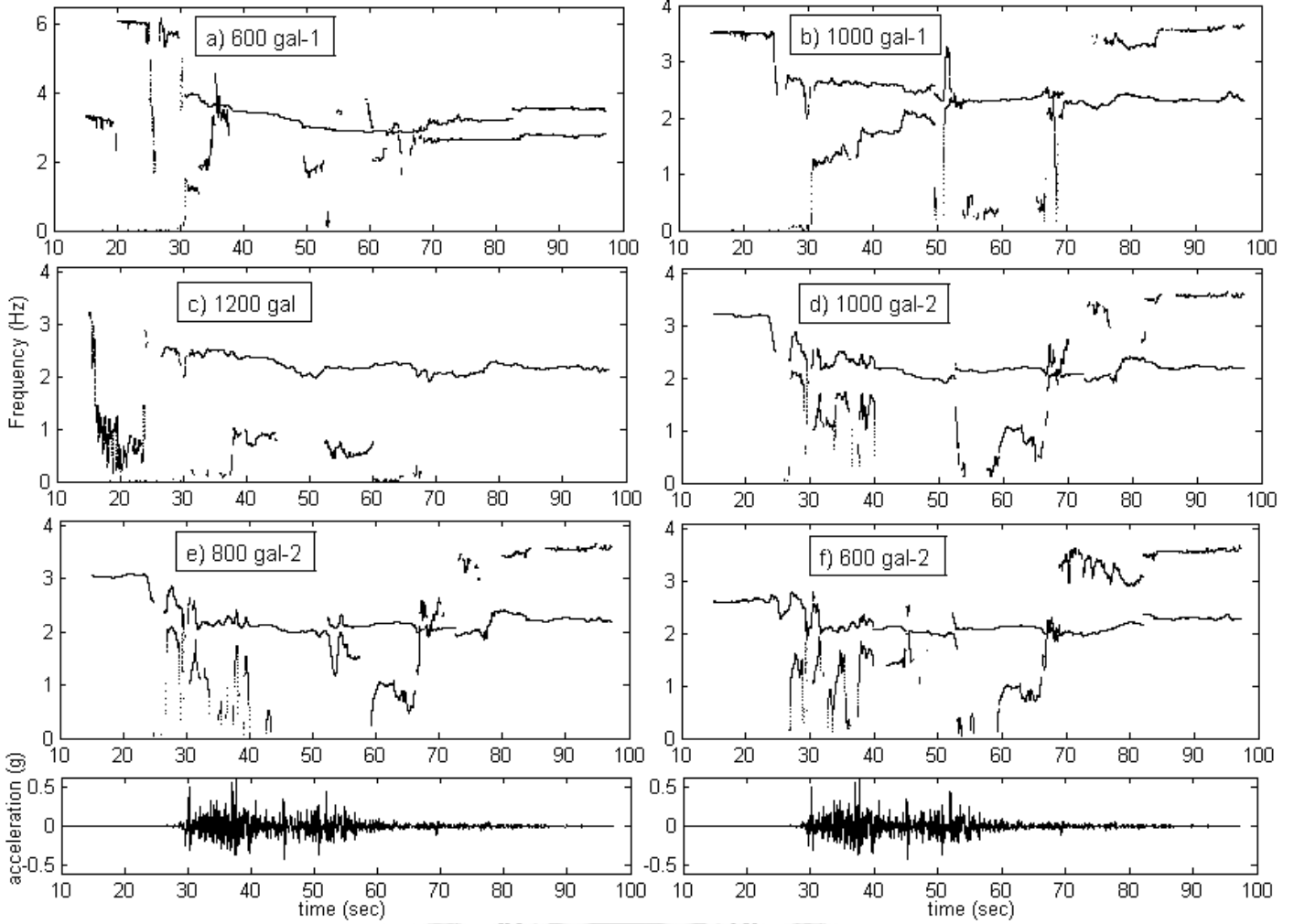
Figure 7-22   Frequency traced by RSSI-COV for the RCF6 frame subjected to series of TCU082 earthquake. System order increased to 4.
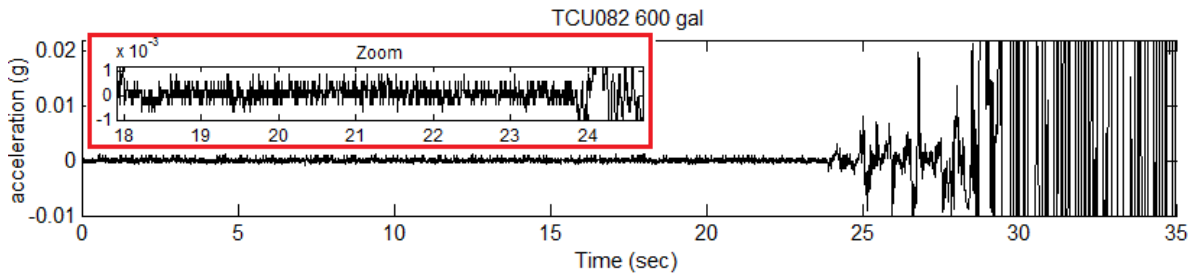
Figure 7-23   The first 35 seconds of 600 gal TCU082 earthquake.
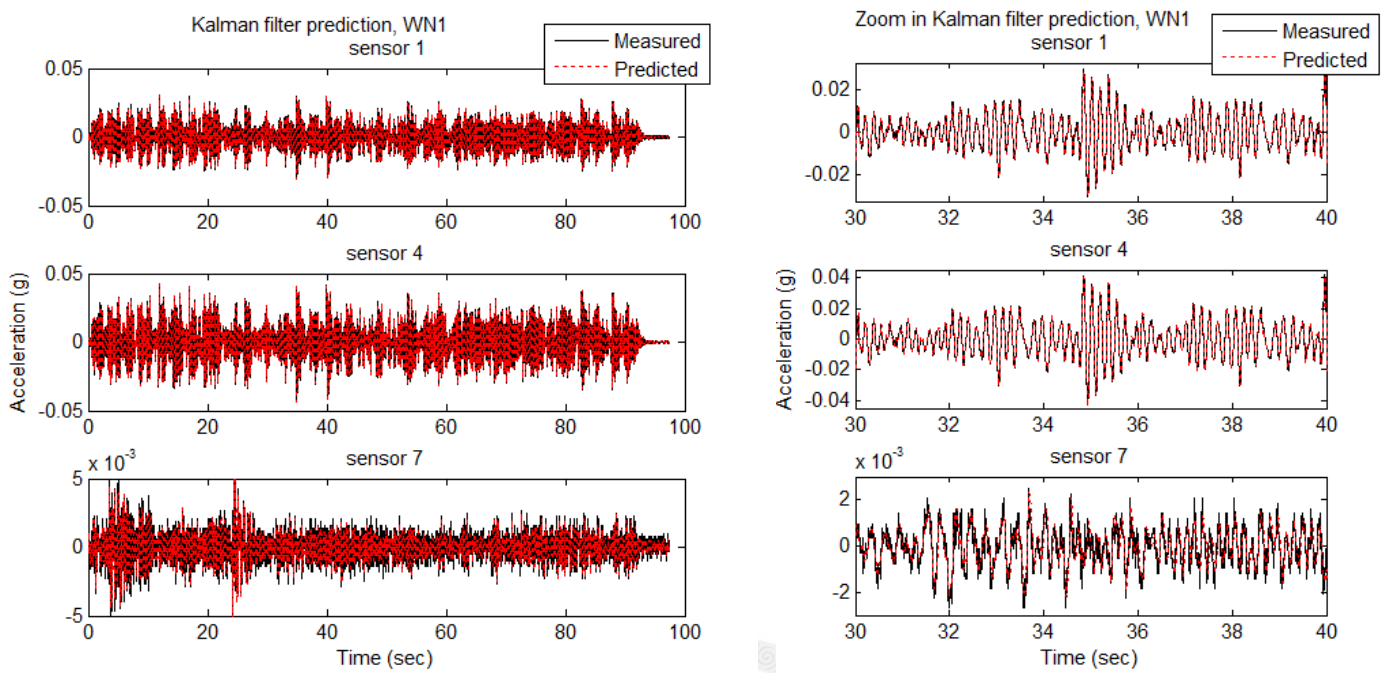
Figure 7-24   Kalman filter prediction of the structure response under WN1 excitation.
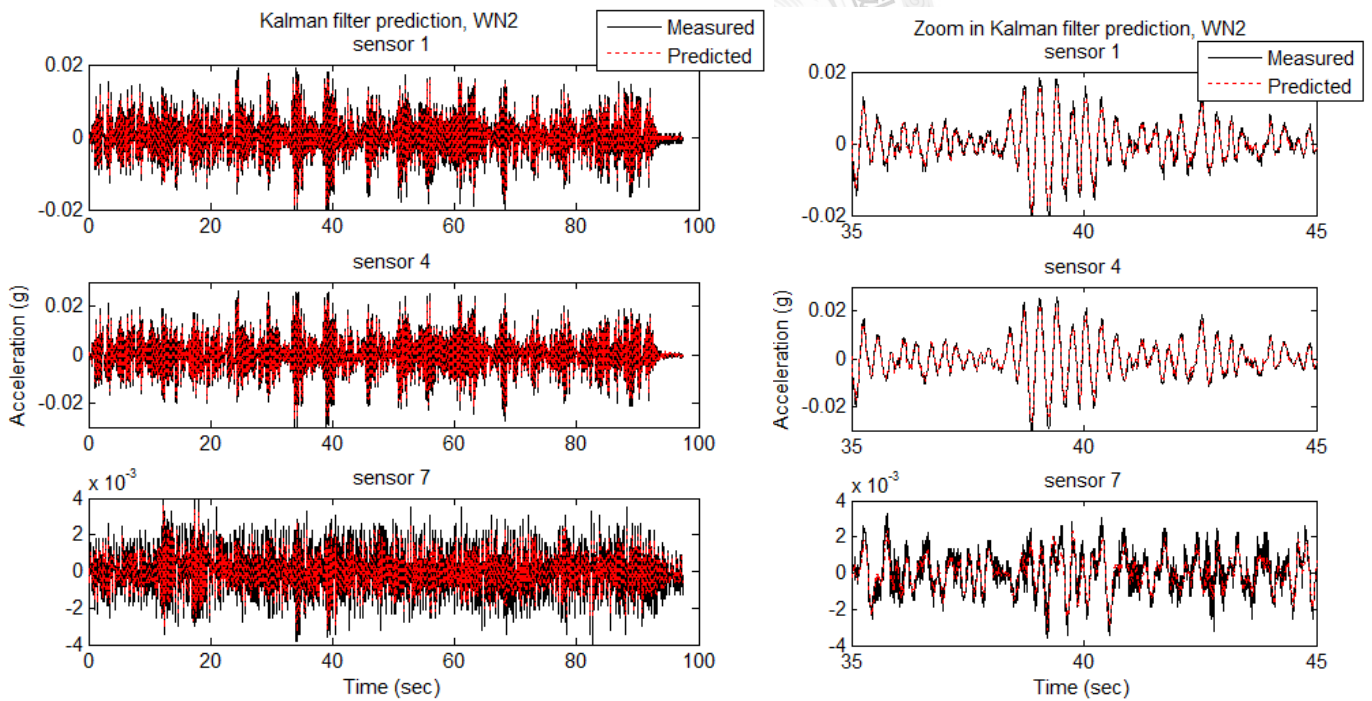
Figure 7-25   Kalman filter prediction of the structure response under WN2 excitation.
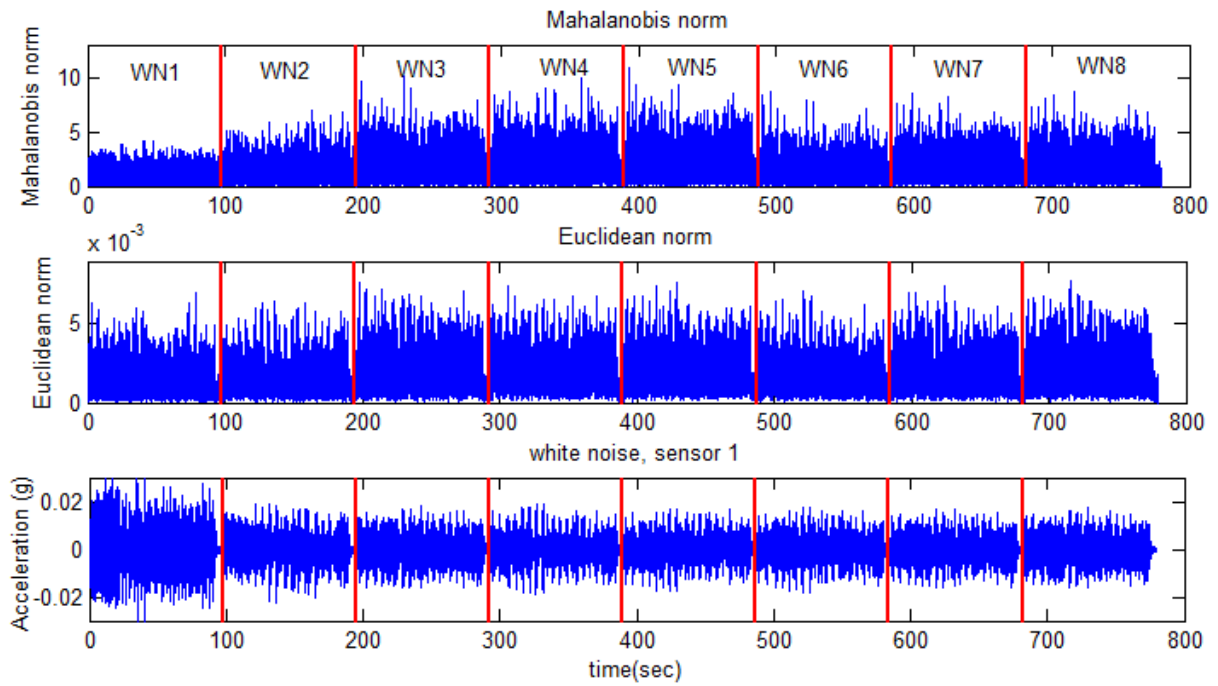
Figure 7-26 Mahalanobis and Euclidean norm of the Kalman filter prediction error.
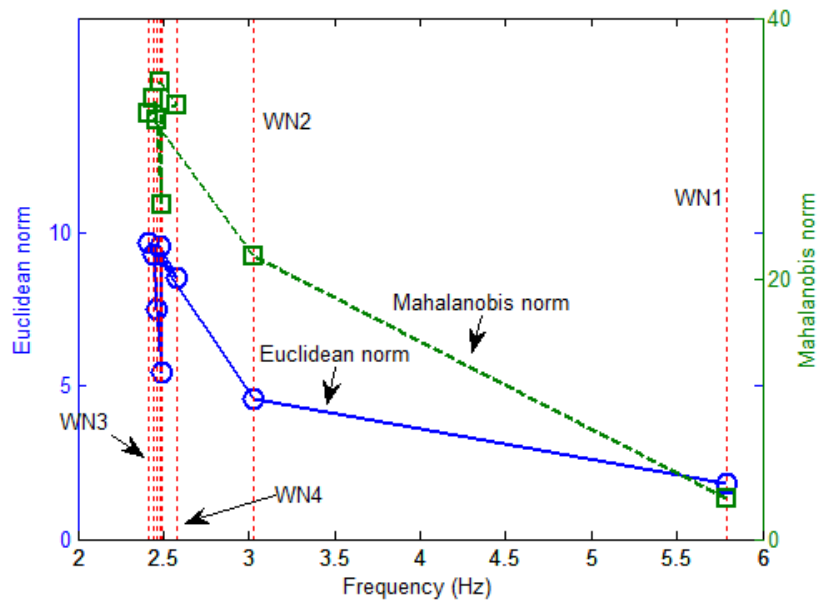
Figure 7-27 The relationship between outlier analysis (Mahalanobis norm and Euclidean norm) with respect to the identified system natural frequency.
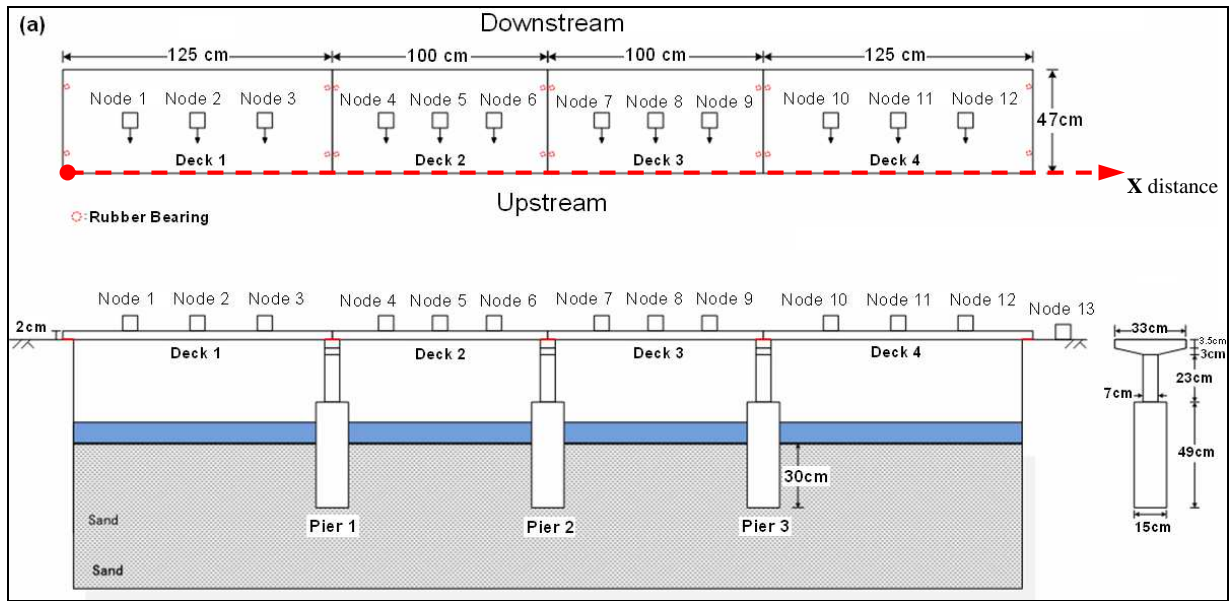
Figure 7-28 (a) Bridge configuration and sensors location (b) Field setup of the bridge

(c) After concluded the scouring experiment
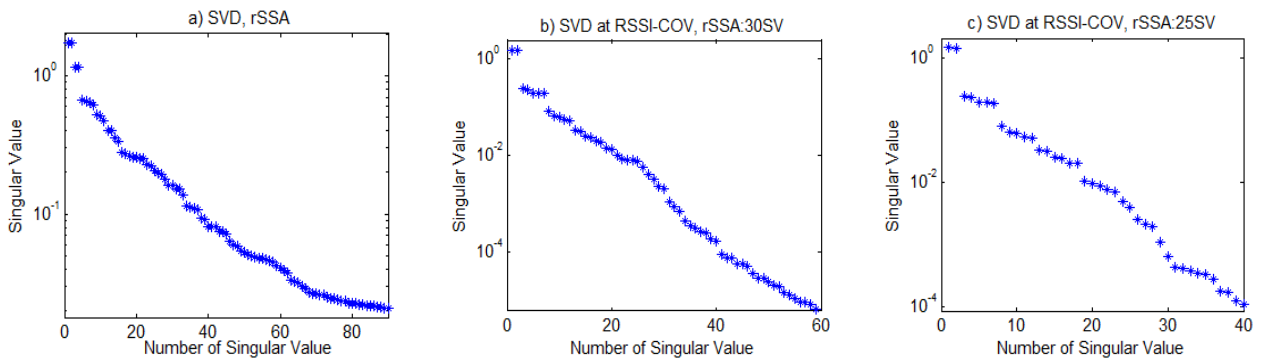
Figure 7-29 Singular spectrum for different choices of singular values in rSSA.
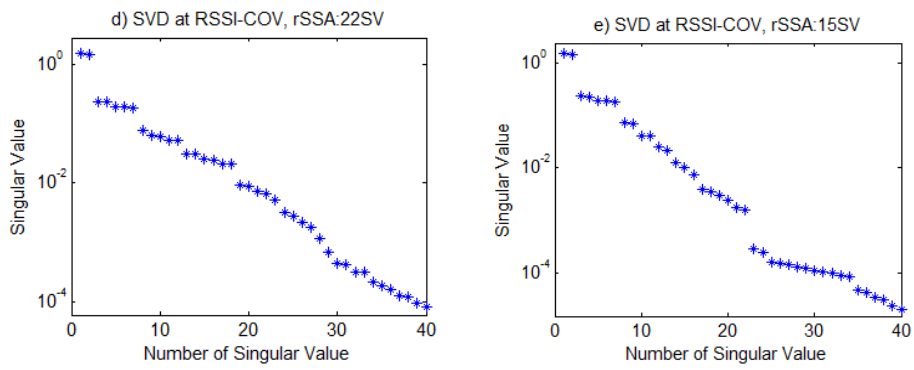
Figure 7-29 Singular spectrum for different choices of singular values in rSSA.
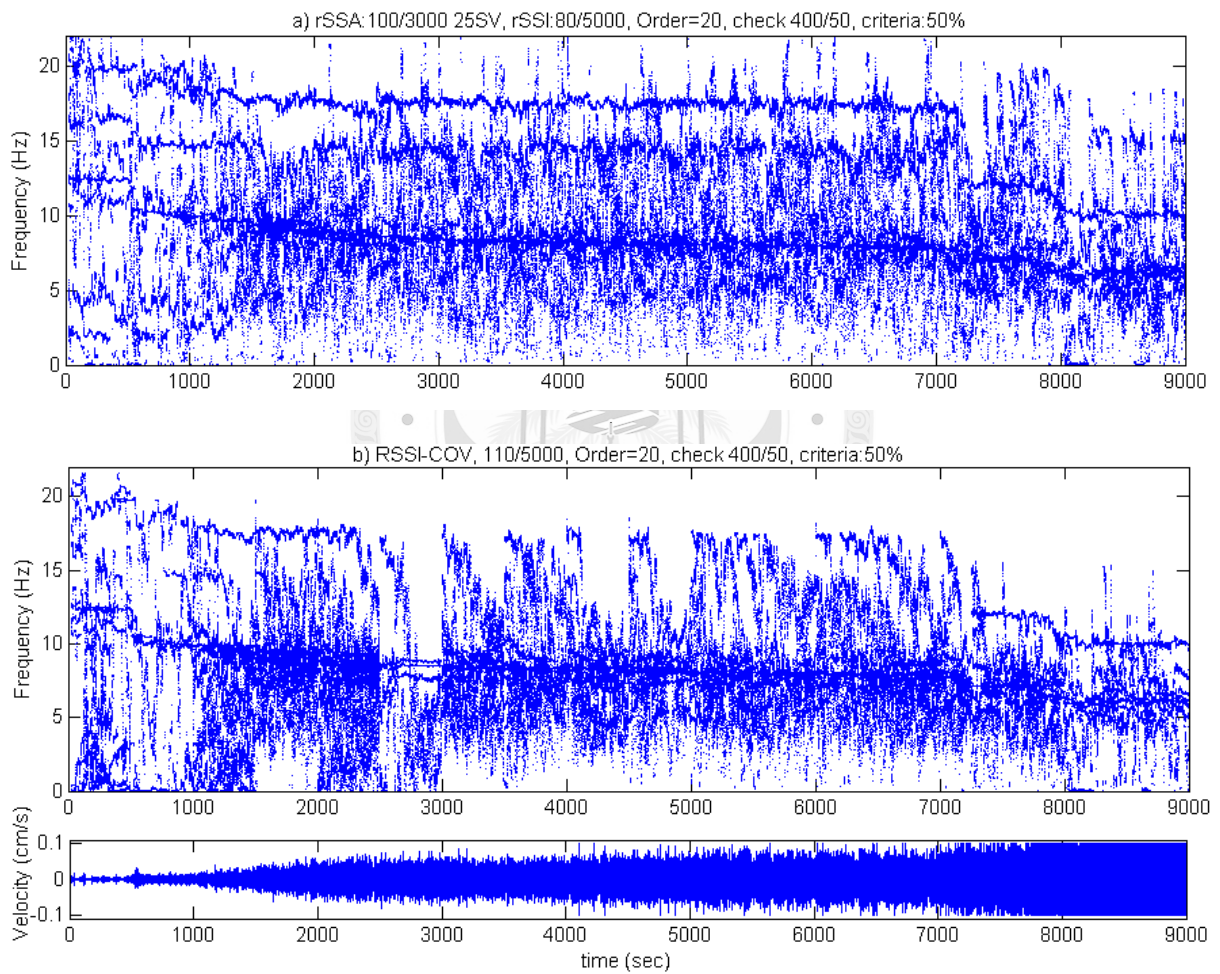
Figure 7-30 Variation of bridge modal frequencies traced by a) rSSA-SSI-COV and b) RSSI-COV.

a) rSSA:100/3000 25SV, rSSI:80/5000, Order=20, check 400/50, criteria:50%

b) Zoom in

blue: frequency stable poles (0.8%)
green: freq and mode shape stable poles (1%)
red: freq and damping stable poles (3%)

Arrival of water head Approx. at 485 s

Measurements at sensor No.9
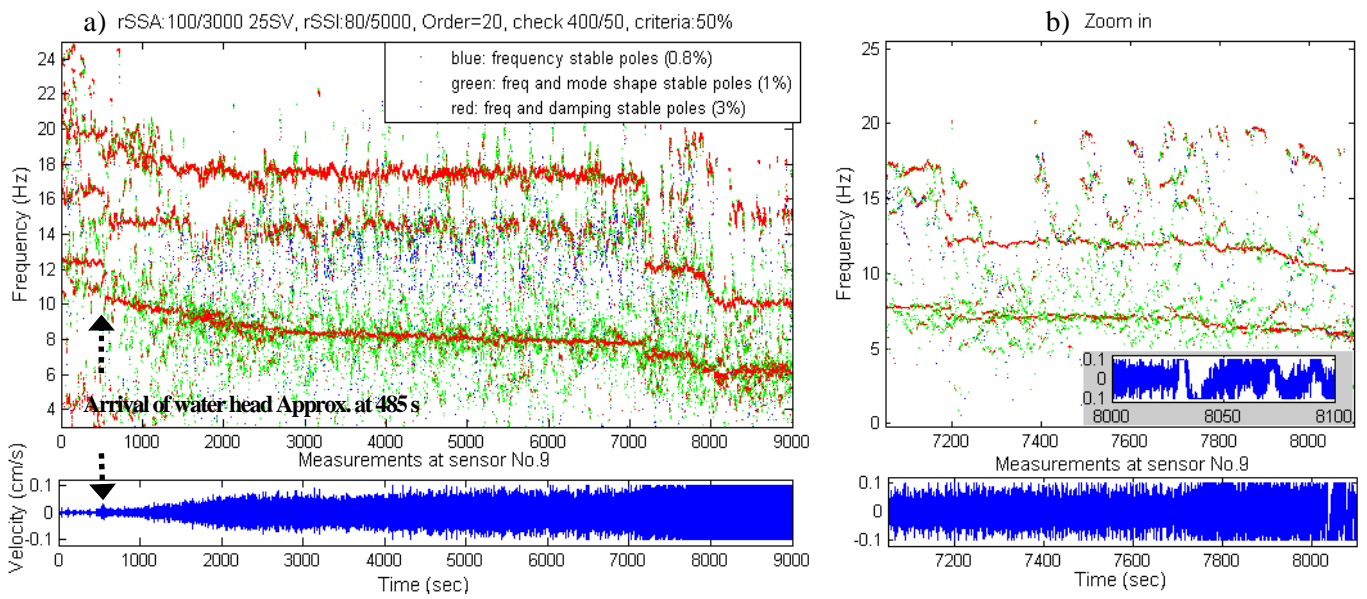
Figure 7-31. Application of stability criterion to the time-frequency plot of bridge modal frequencies, test conducted in 2011/01/24.

Scouring depth for 3 piers, 2011/01/19

Arrival of water head Approx. at 485 s

pier 1
pier 2
pier 3
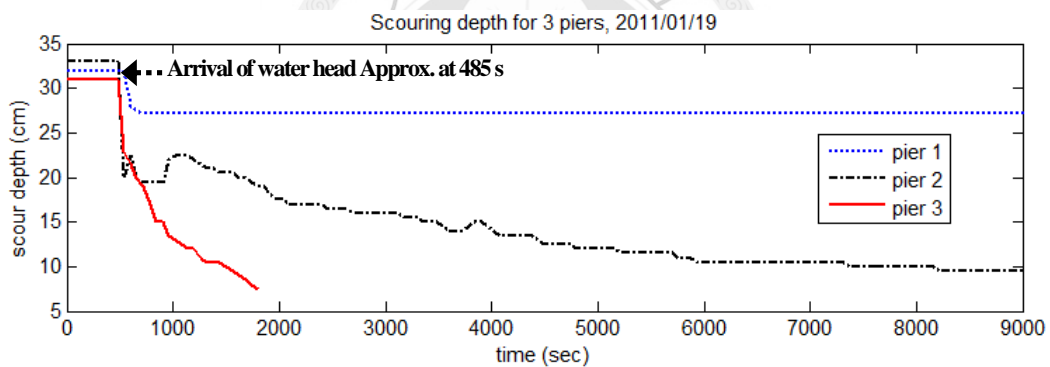
Figure 7-32   Scouring depth for 3 piers, test conducted in 2011/01/19.

a) SVD, rSSA

b) SVD at RSSI-COV, rSSA:40SV

c) SVD at RSSI-COV, rSSA:35SV

Order 34
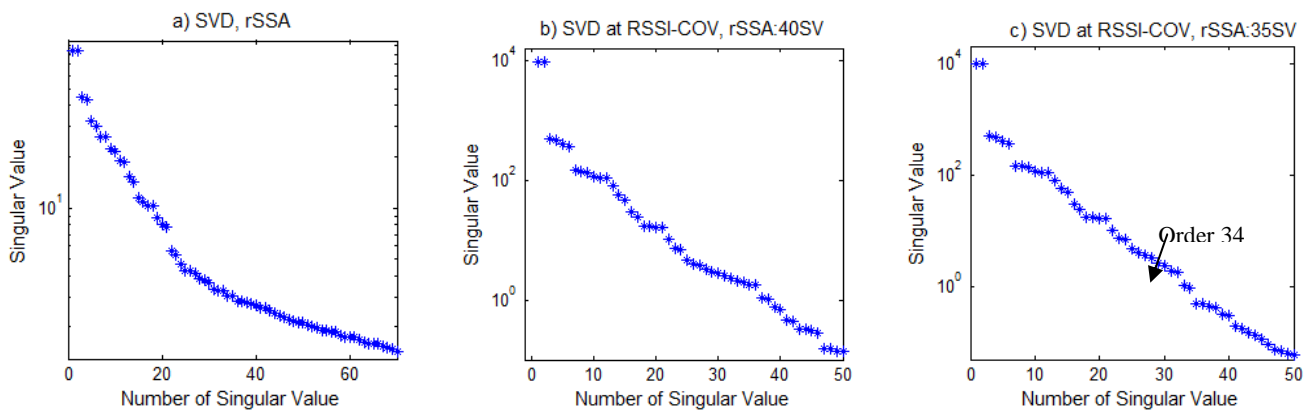
Figure 7-33   Singular spectrum for different choices of singular values in rSSA.
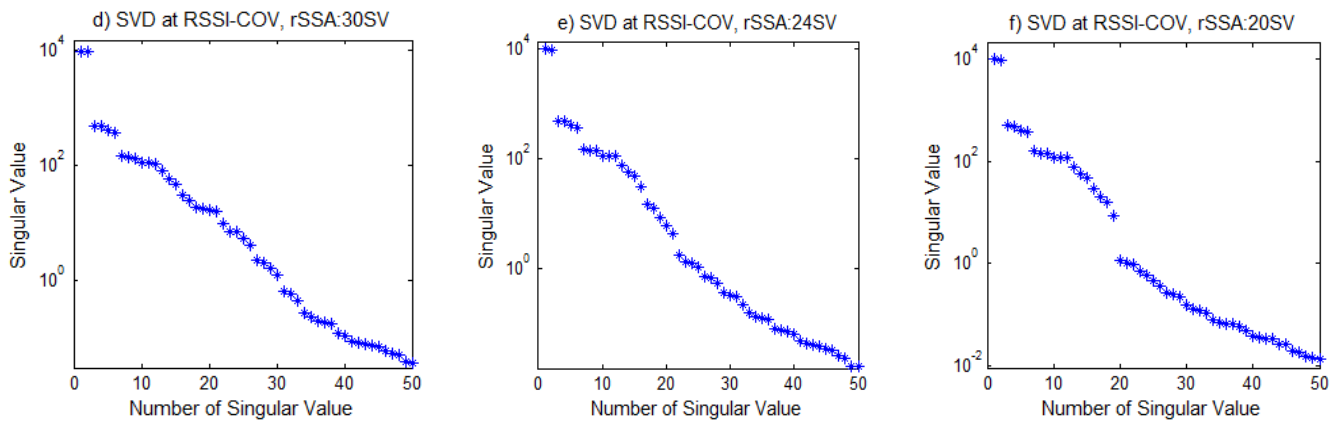
Figure 7-33 Singular spectrum for different choices of singular values in rSSA.
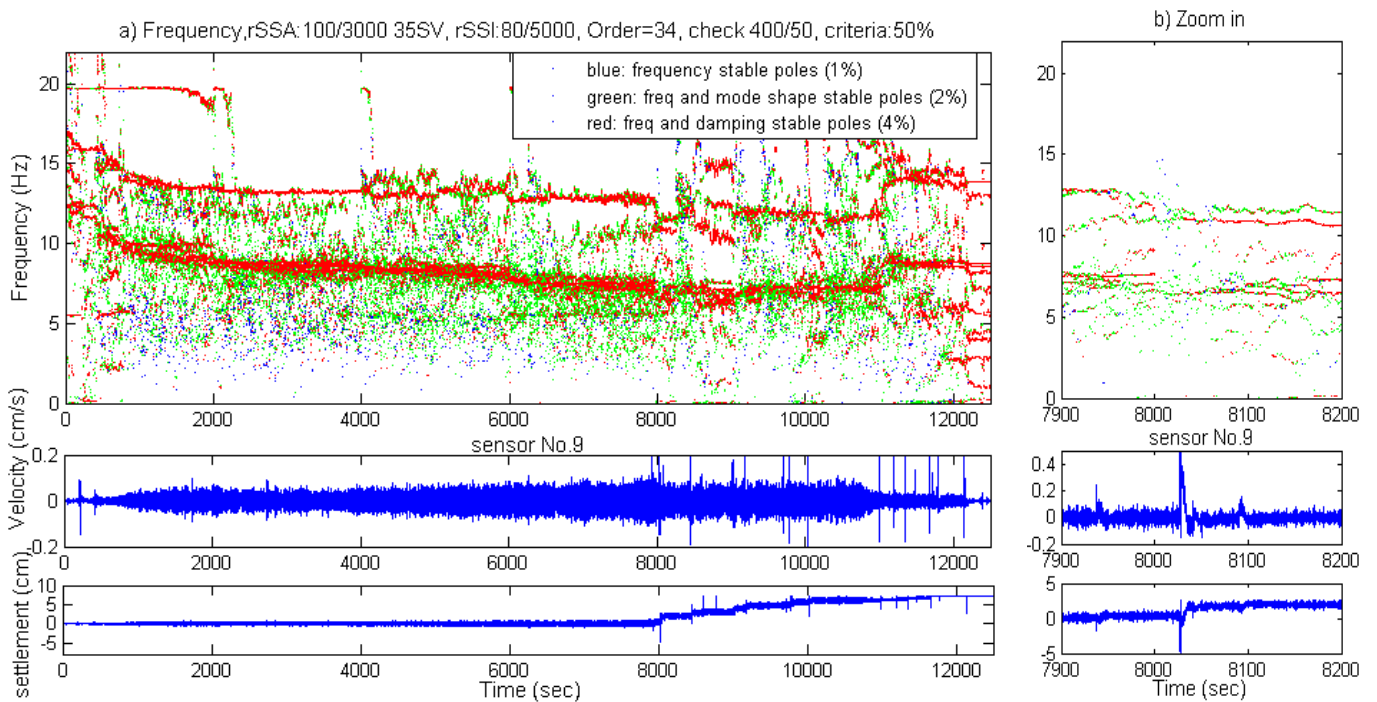
Figure 7-34 Evolution of bridge modal frequencies traced by rSSA-SSI-COV with applied stability criterion, test conducted in 2011/01/24.
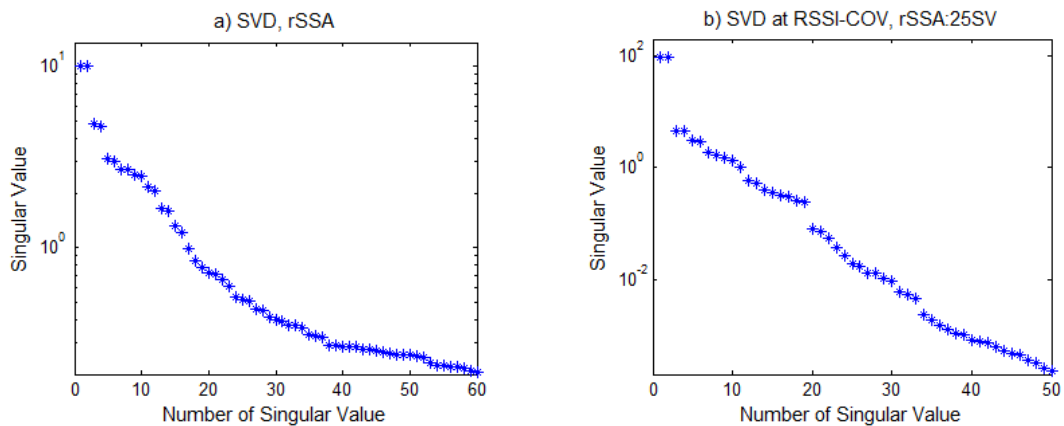
Figure 7-35 Singular spectrums: a) rSSA, b) RSSI-COV for the subspace order with 25 SV.
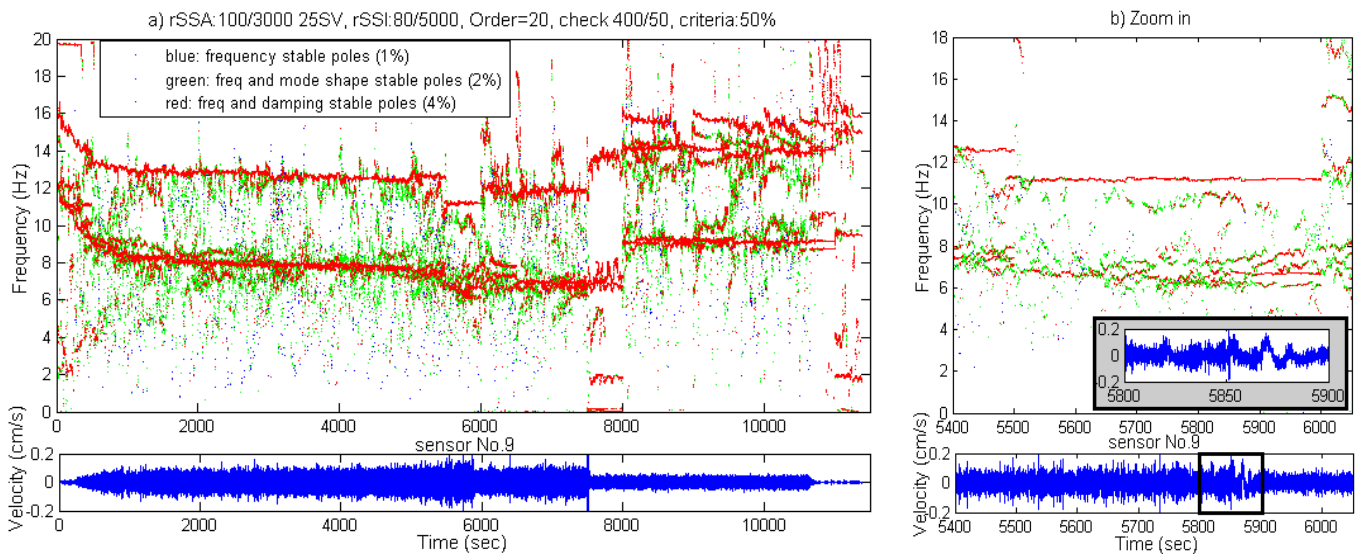
Figure 7-36 . Evolution of bridge modal frequencies traced by rSSA-SSI-COV with applied stability criterion, test conducted in 2011/01/26.
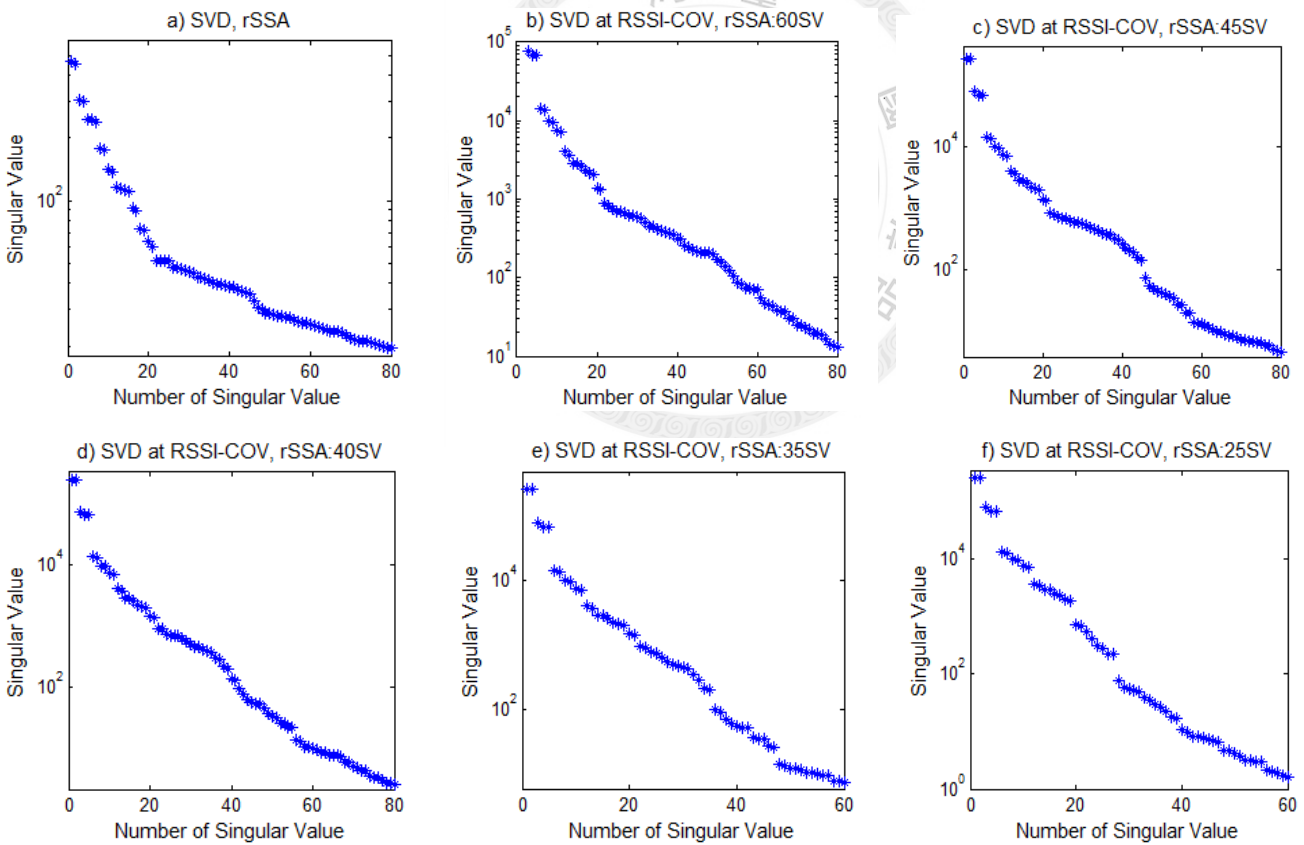
Figure 7-37 Singular spectrum for different choices of singular values in rSSA.
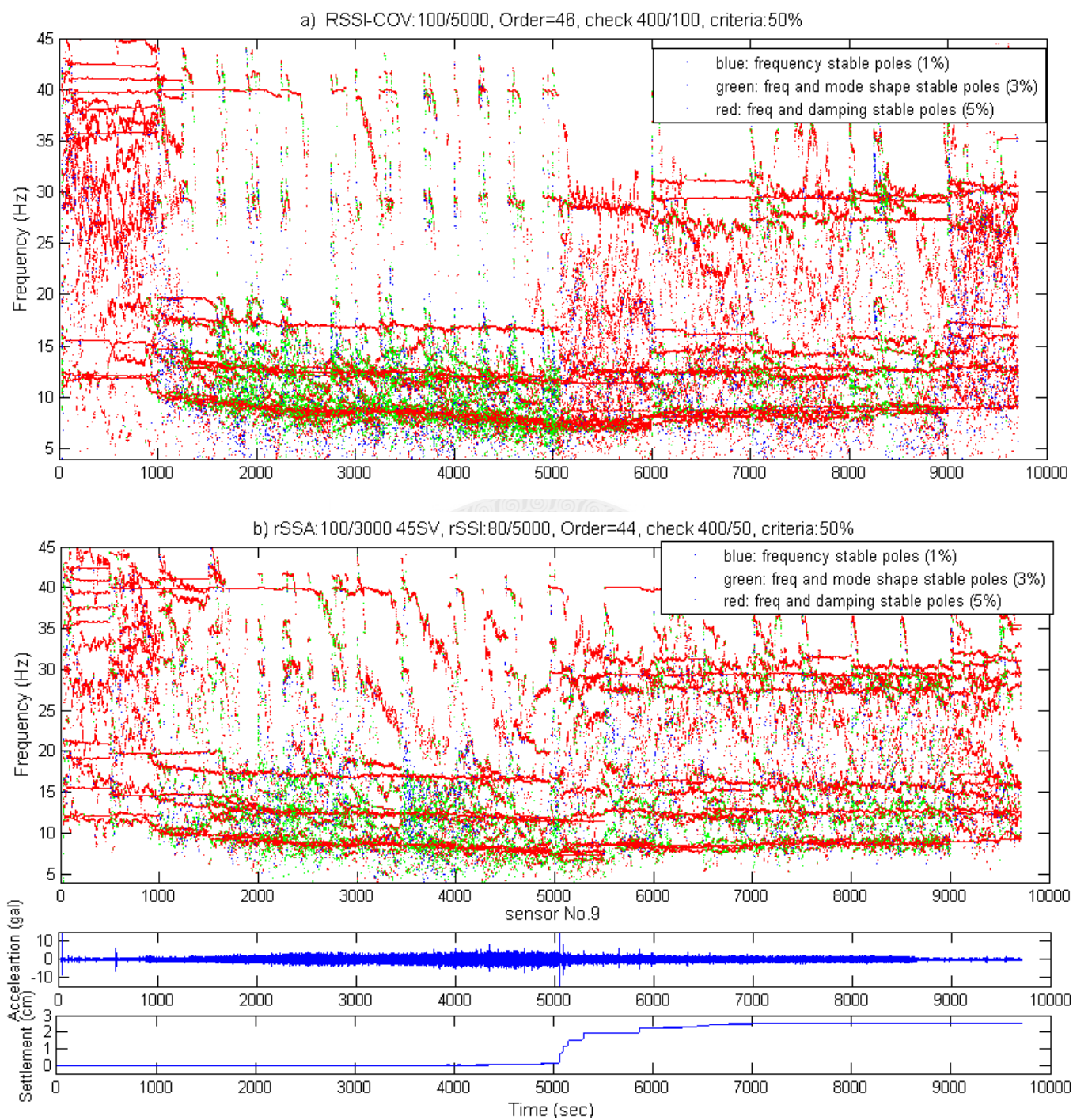
Figure 7-38 Evolution of bridge modal frequencies traced by both a) RSSI-COV and b) rSSA-SSI-COV, applying stability criterion, test conducted in 2011/03/29 measured by accelerometers.
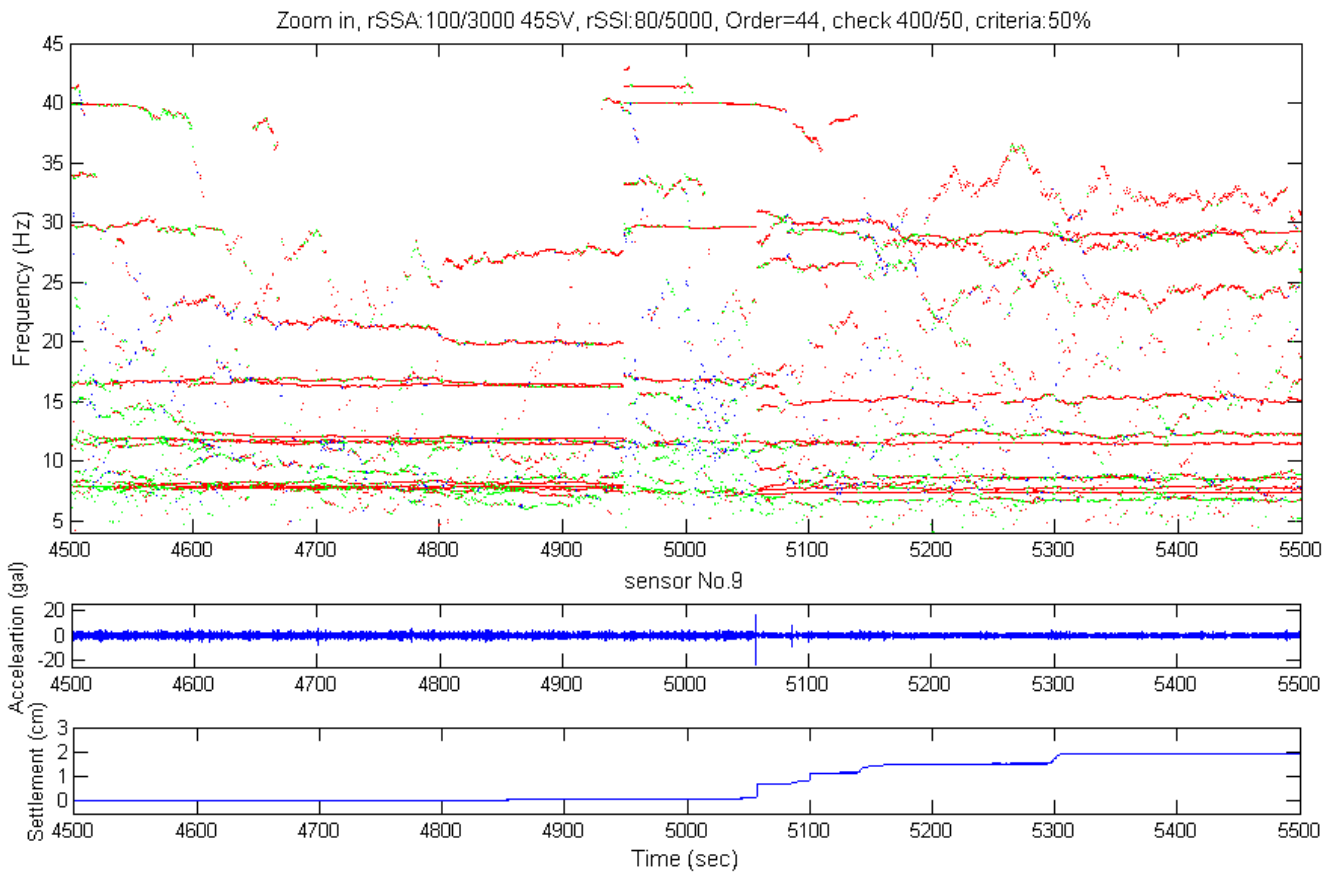
Figure 7-39   Zoom in the evolution of bridge modal frequencies between 4500 and 5500 seconds,

test conducted in 2011/03/29 measured by accelerometers.
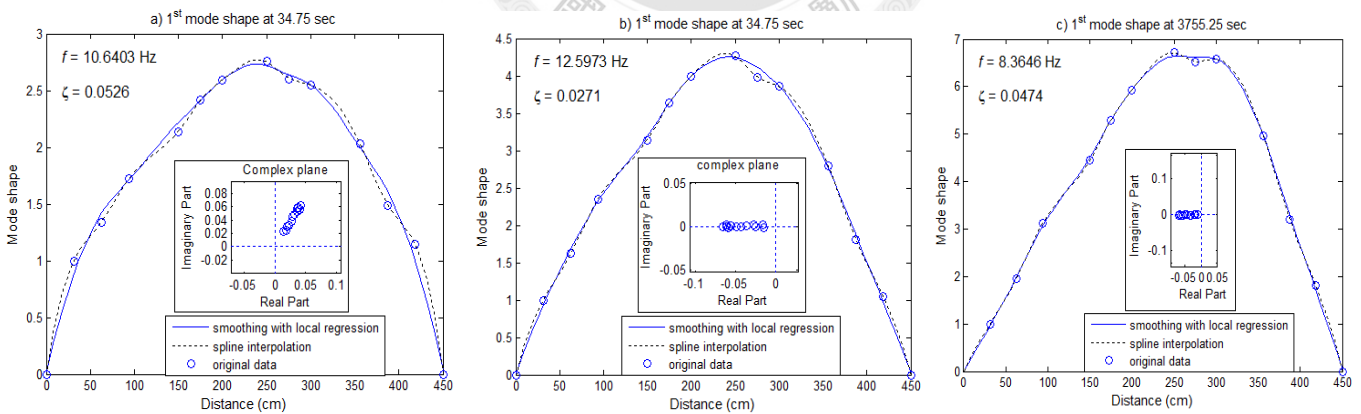
Figure 7-40   Identified 1st mode shapes from two time instants. Test in 2011/01/19.
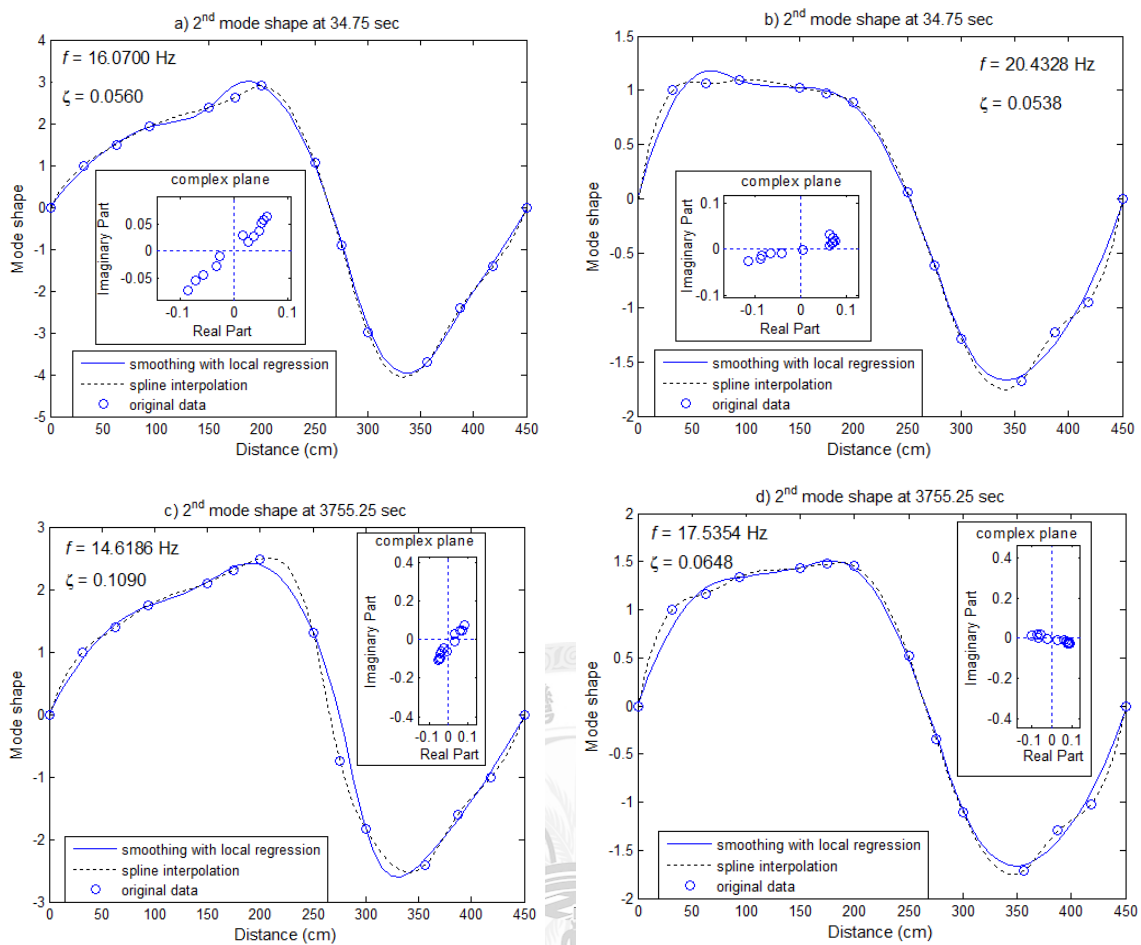
Figure 7-41 Examples of identified 2nd mode shapes from two time instants. Test in 2011/01/19.
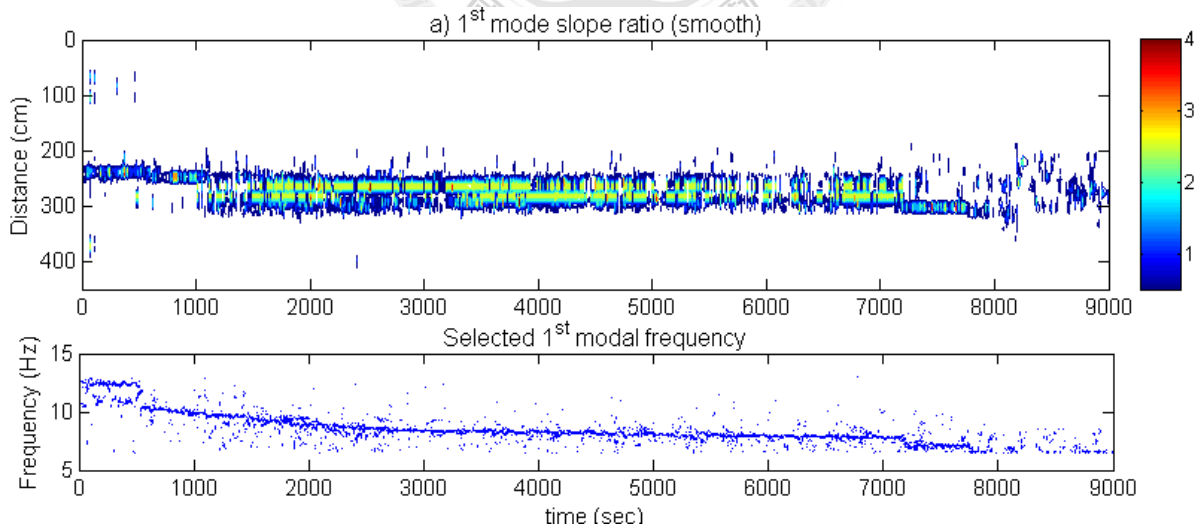
Figure 7-42 1st mode shape slope ratio for a) smoothed mode shapes. 2011/01/19 test.
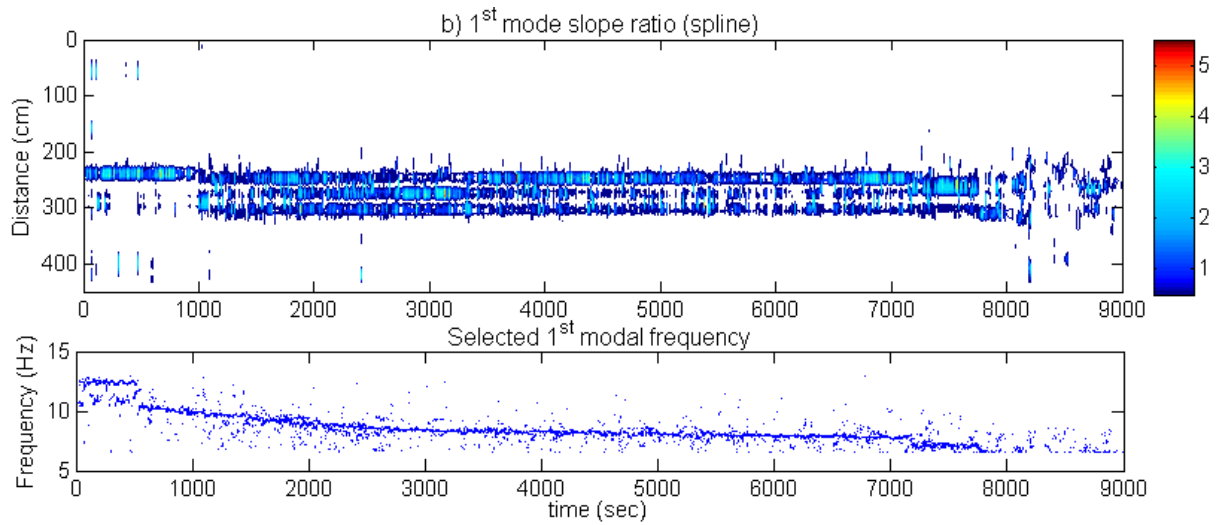
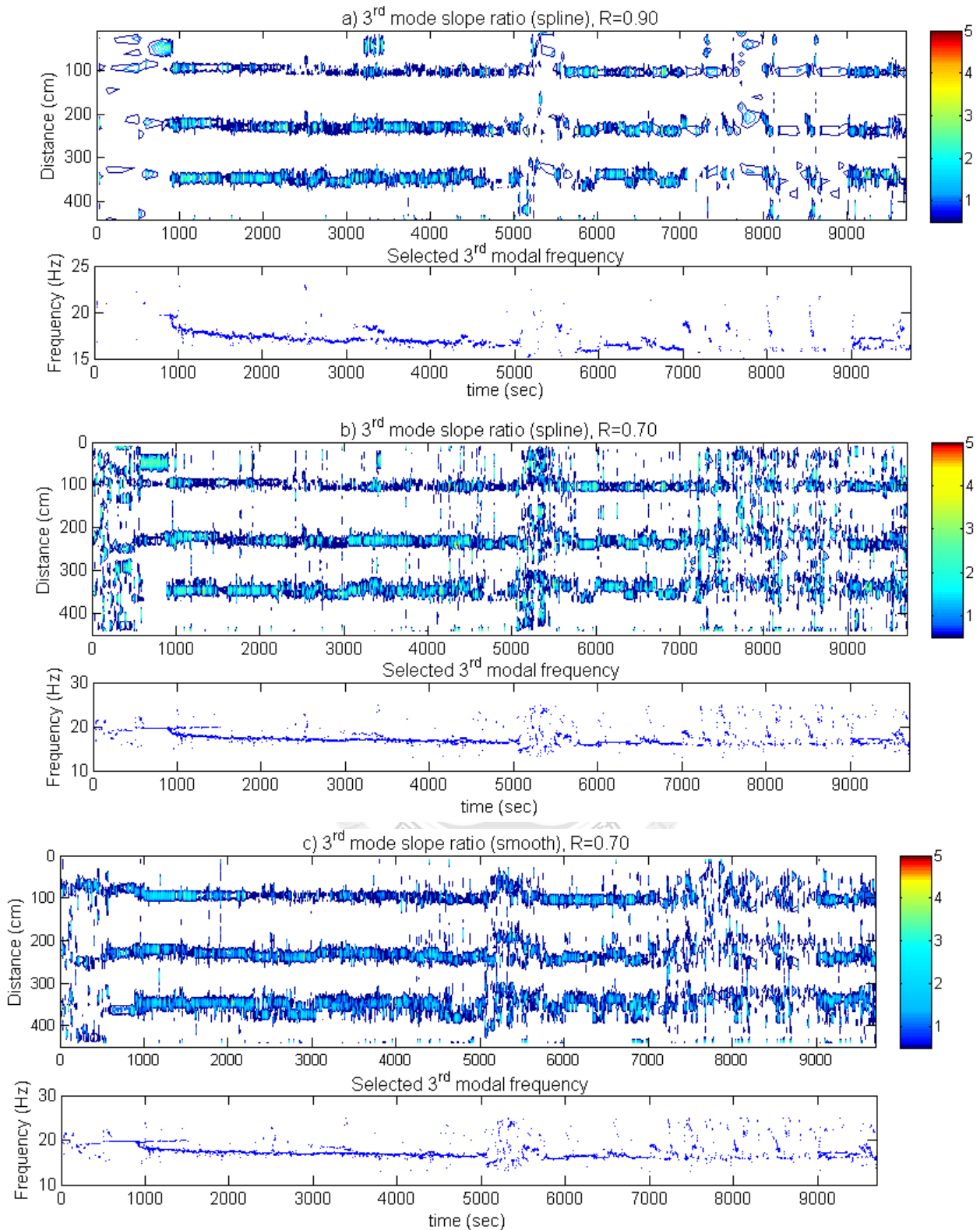**Figure 7-42** 1st mode shape slope ratio for b) non-smoothed mode shapes. 2011/01/19 test.
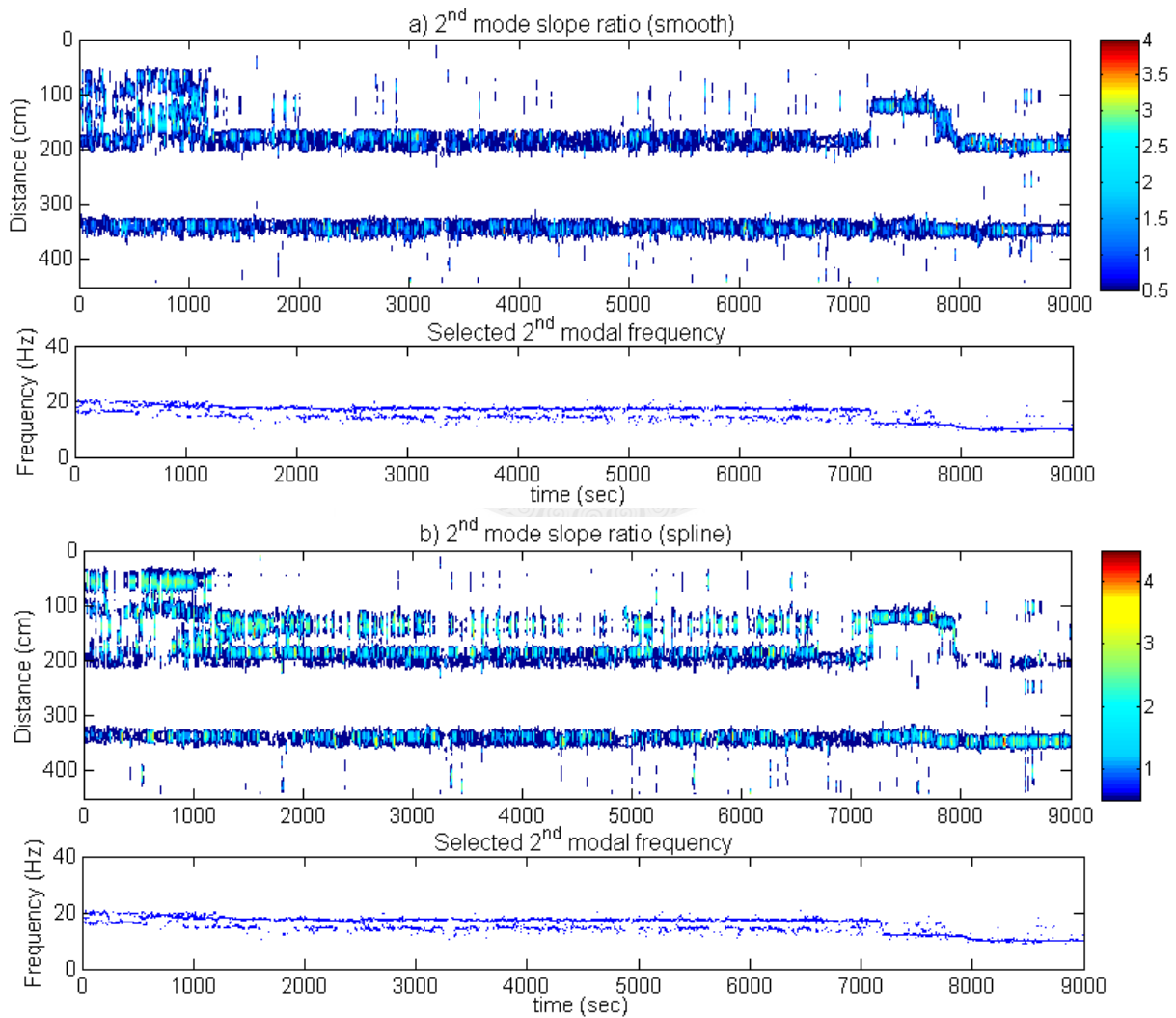
Figure 7-43 1st mode shape slope ratio for a) smoothed and b) non-smoothed mode shapes. 2011/01/19 test.
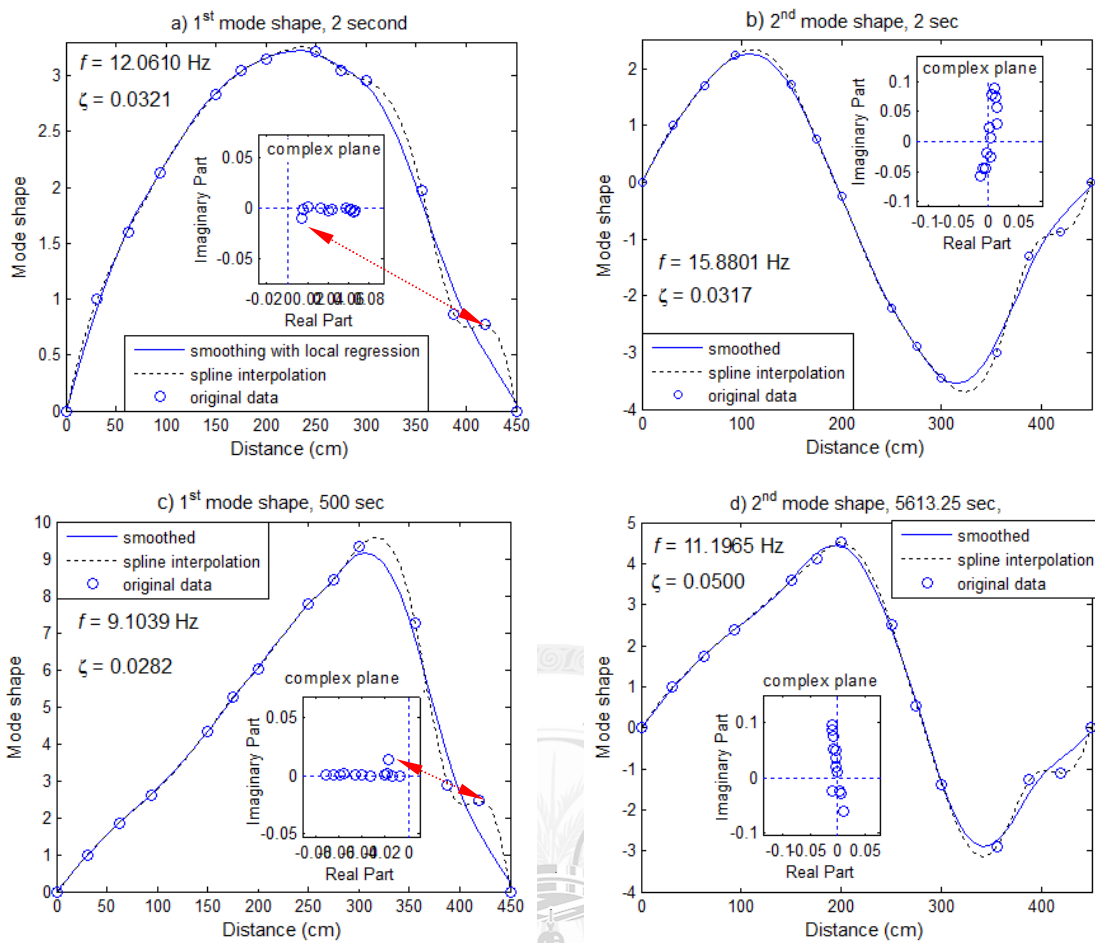
Figure 7-44 Examples of identified mode shapes from two time instants. Test in 2011/01/26.
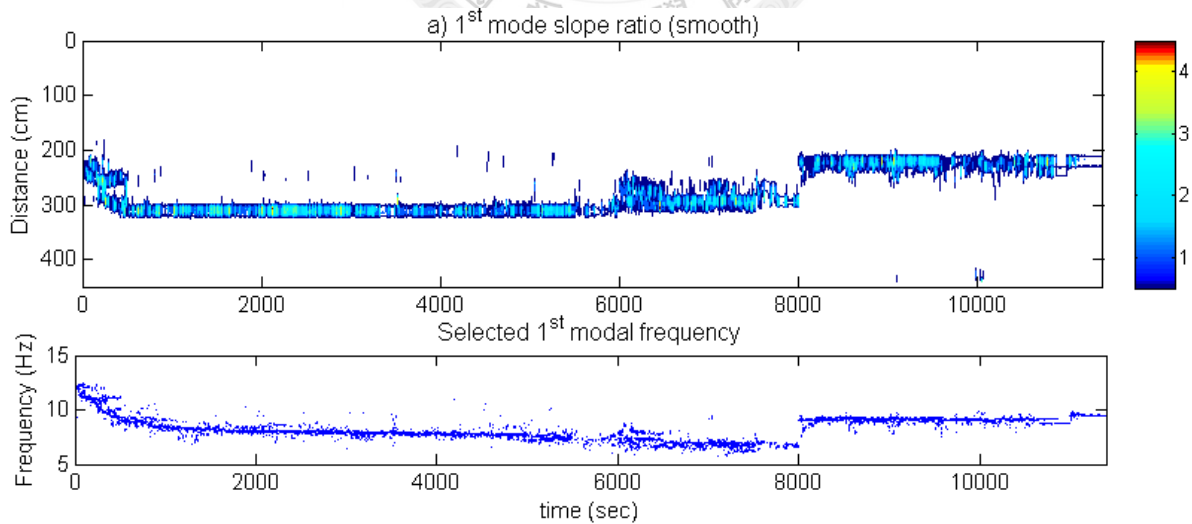
Figure 7-45   1st mode shape slope ratio for a) smoothed mode shapes. 2011/01/26 test.
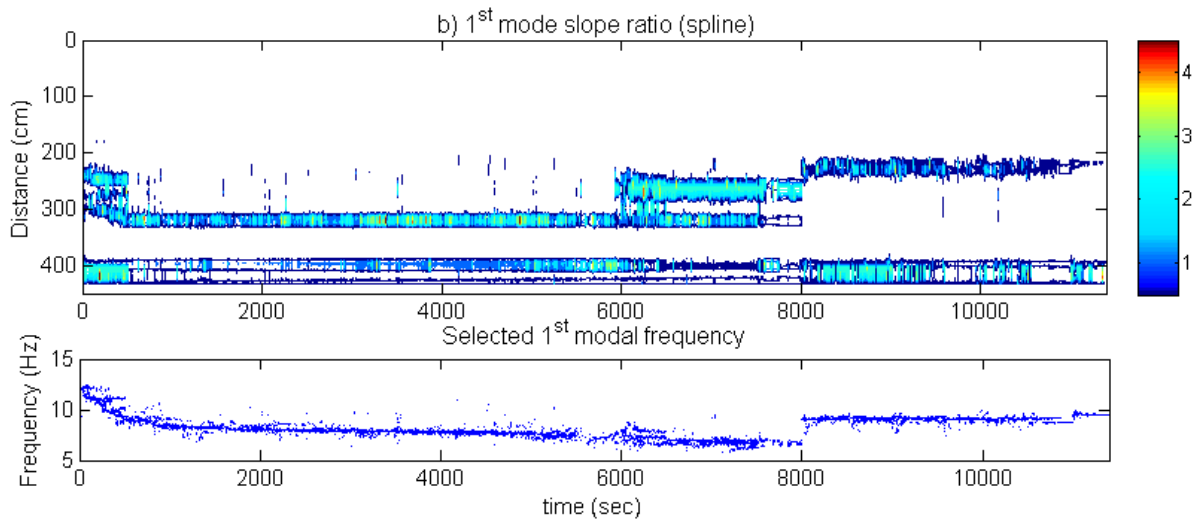
Figure 7-45 1st mode shape slope ratio for b) non-smoothed mode shapes. 2011/01/26 test.
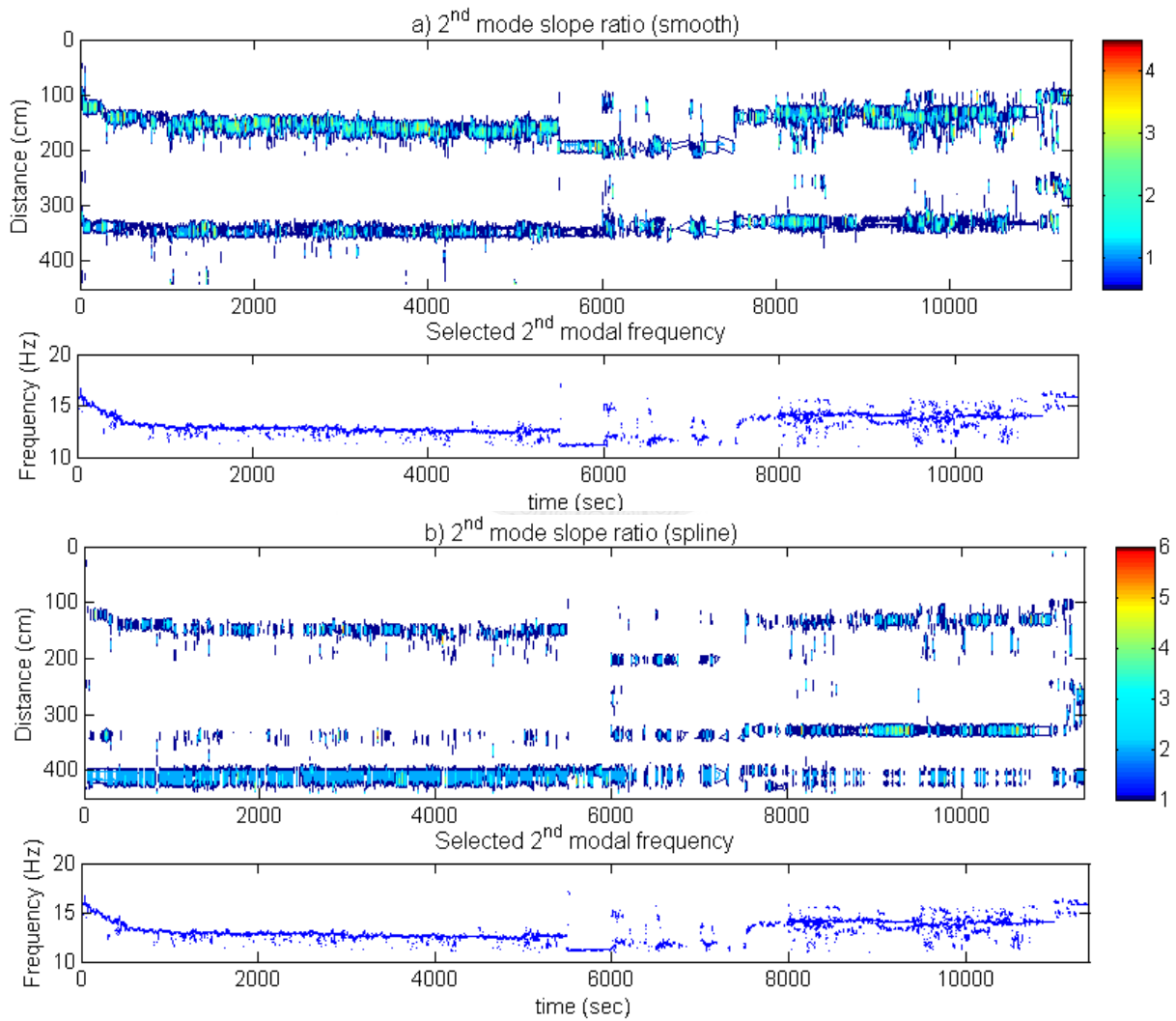
Figure 7-46   2nd mode shape slope ratio for a) smoothed and b) non-smoothed mode shapes. 2011/01/26 test.
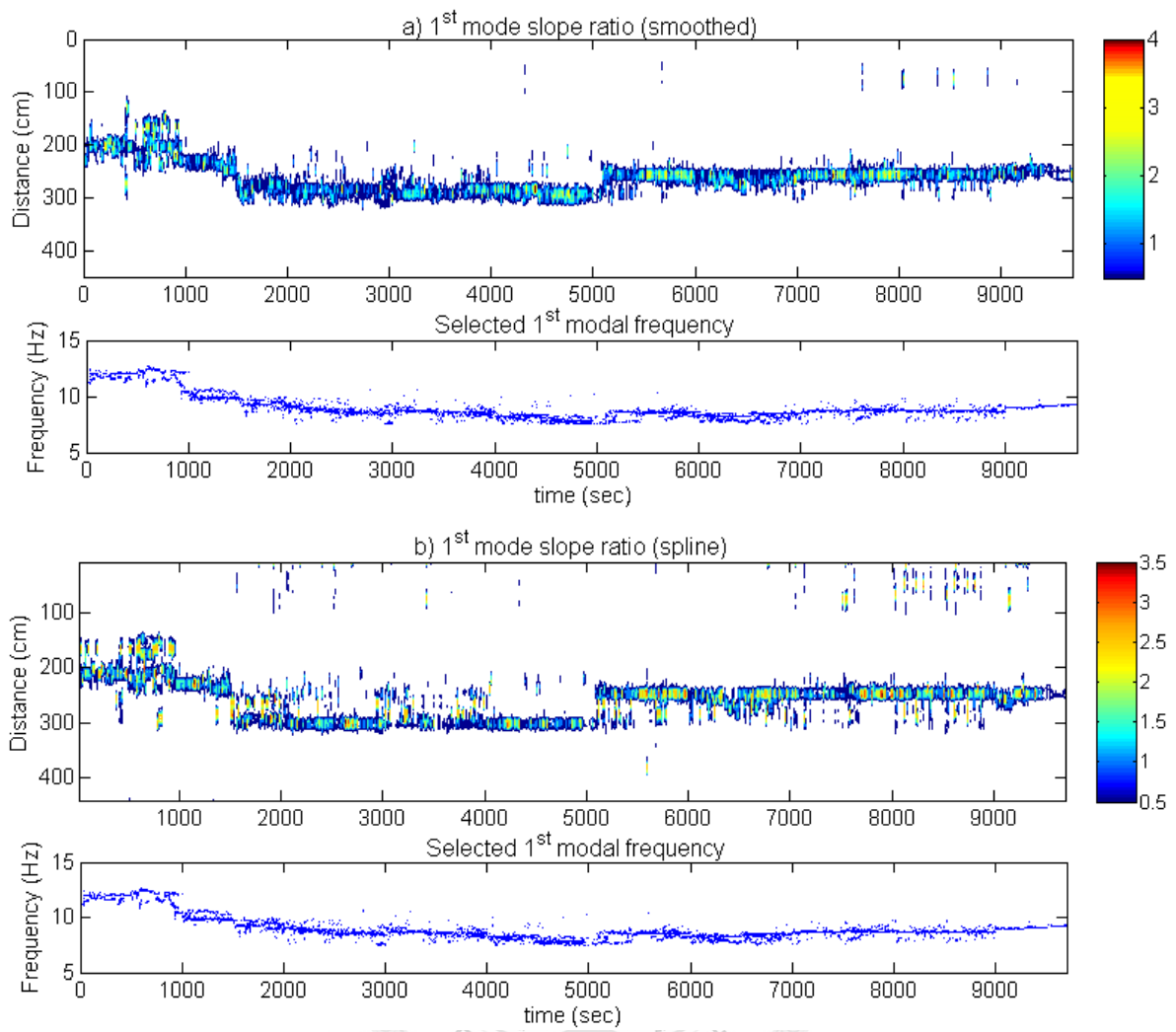
Figure 7-47 1st mode shape slope ratio for a) smoothed and b) non-smoothed mode shapes. 2011/03/29 test.

214
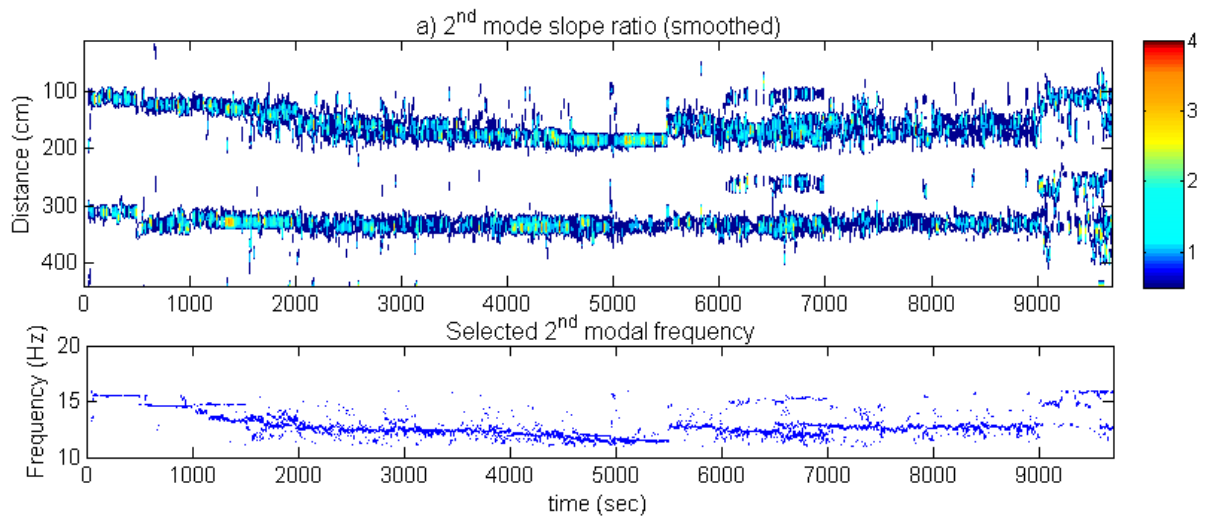
Figure 7-48 2nd mode shape slope ratio for a) smoothed mode shapes. 2011/03/29 test.
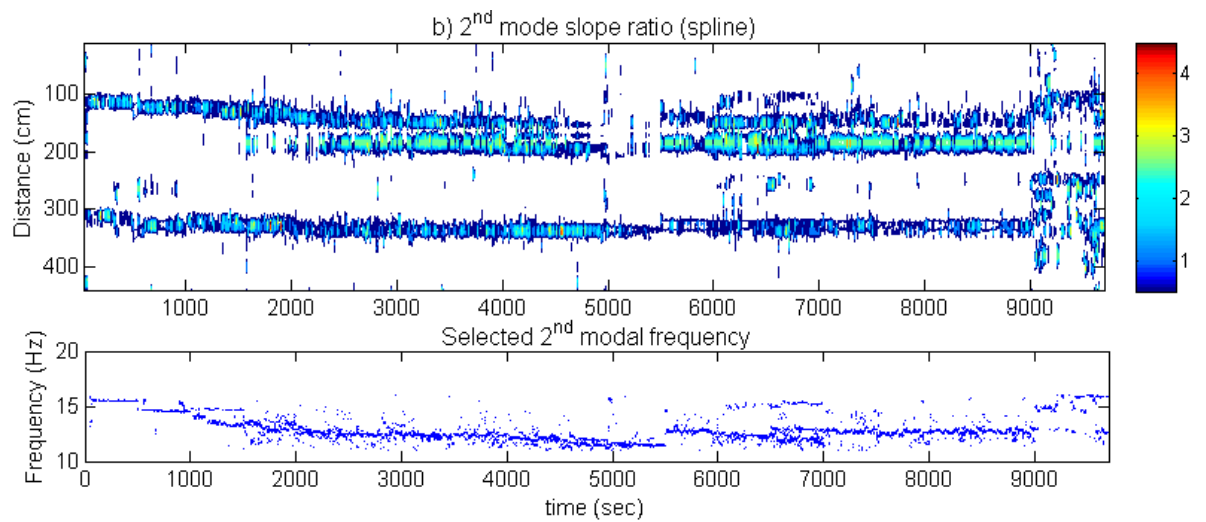
Figure 7-48 2nd mode shape slope ratio for b) non-smoothed mode shapes. 2011/03/29 test.

Figure 7-49 3rd mode shape slope ratio for a) non-smoothed, R=0.90; b) non-smoothed, R=0.70; and c) smoothed, R=0.70 mode shapes. 2011/03/29 test.
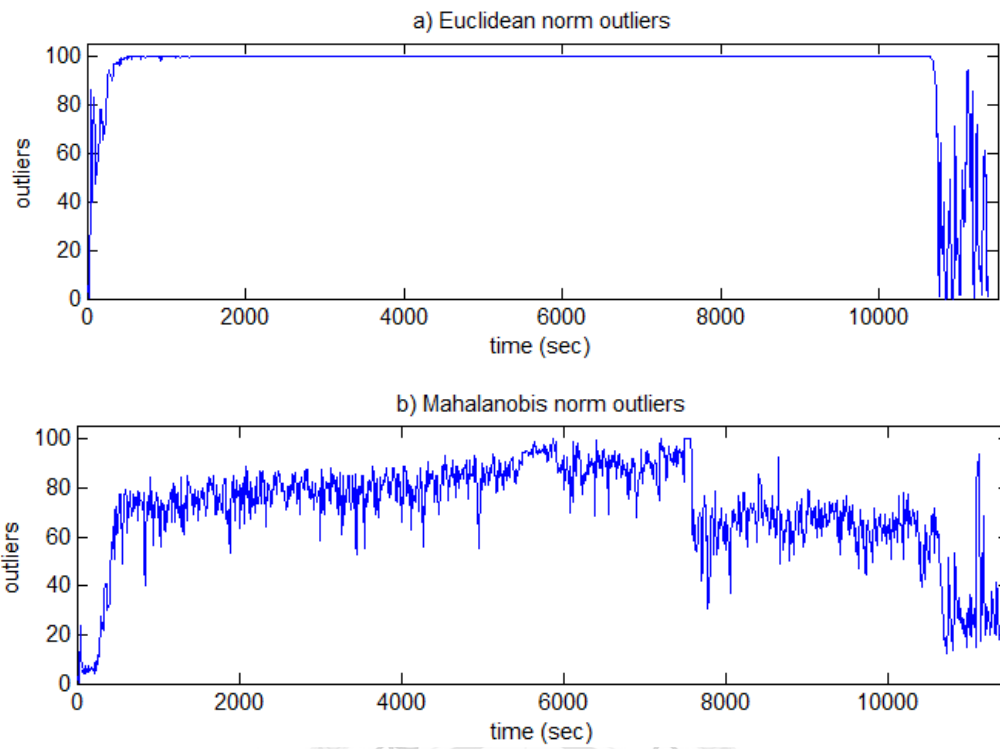
Figure 7-50 Outlier analysis for a) Euclidean norm and, b) Mahalanobis norm.
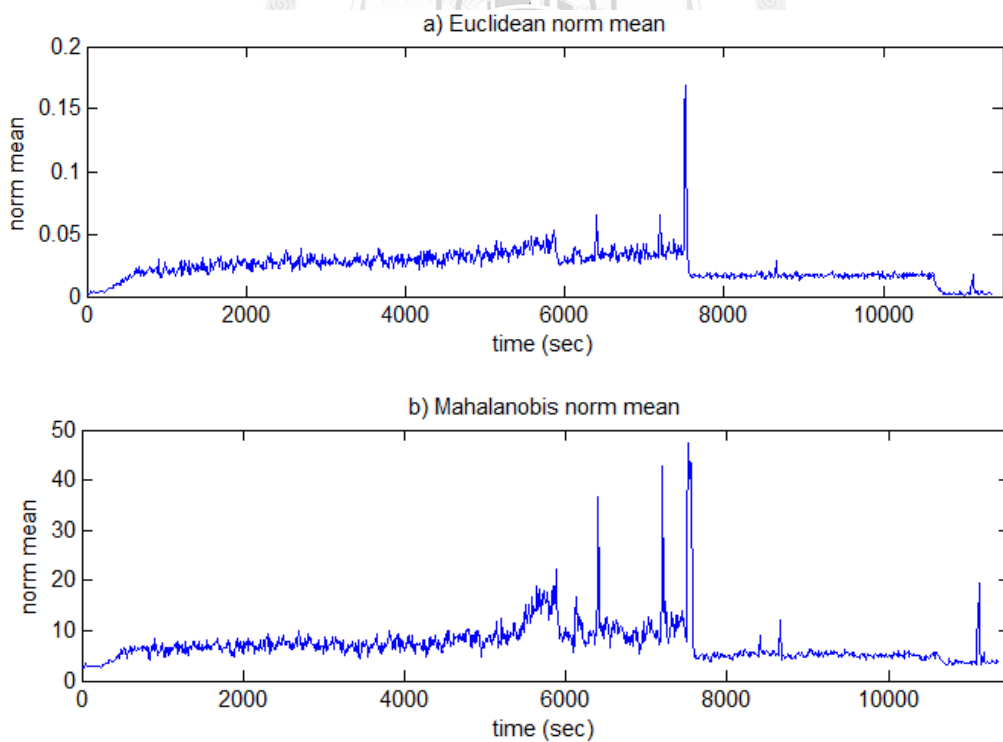
Figure 7-51 Error mean for a) Euclidean norm and, b) Mahalanobis norm.
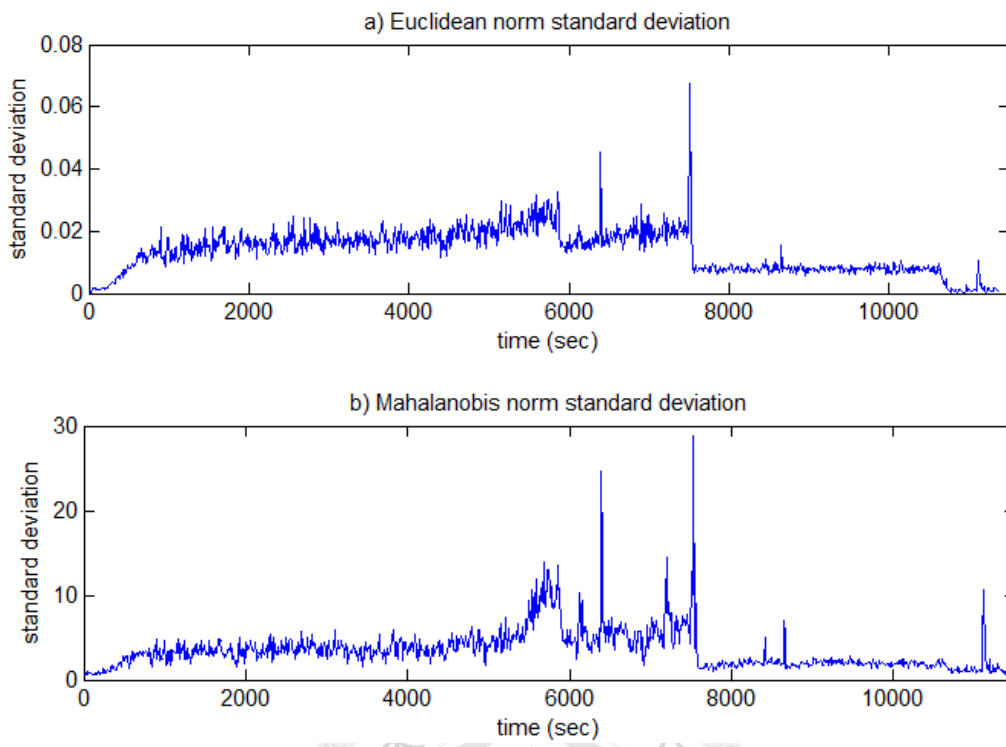
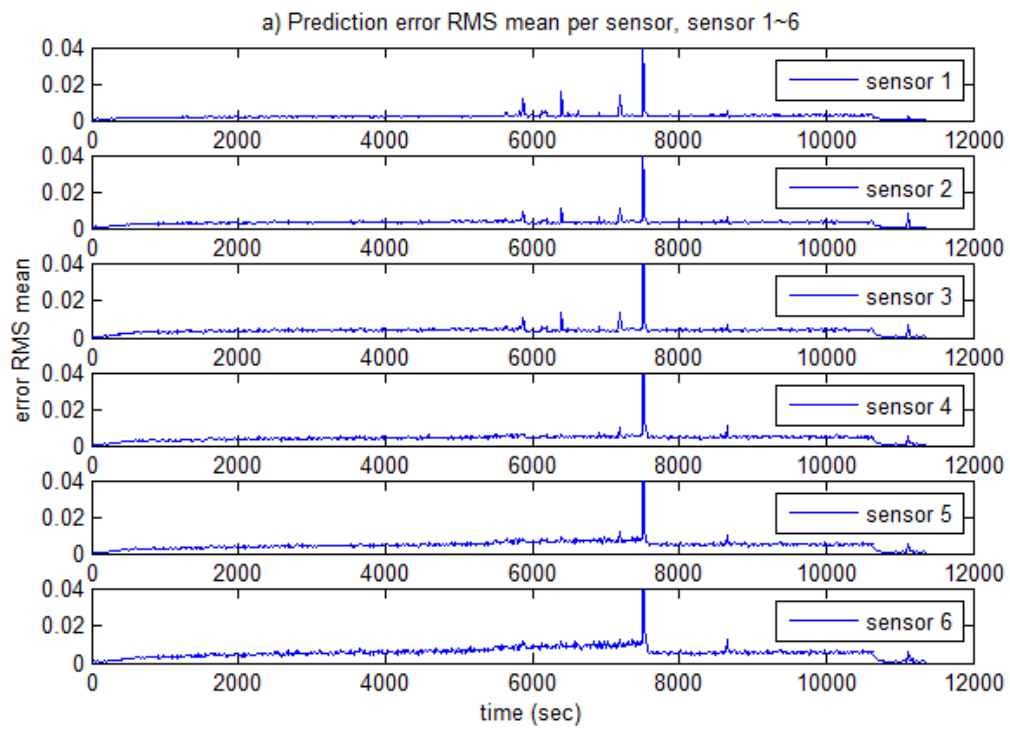**Figure 7-52**   Error standard deviation for a) Euclidean norm and, b) Mahalanobis norm.
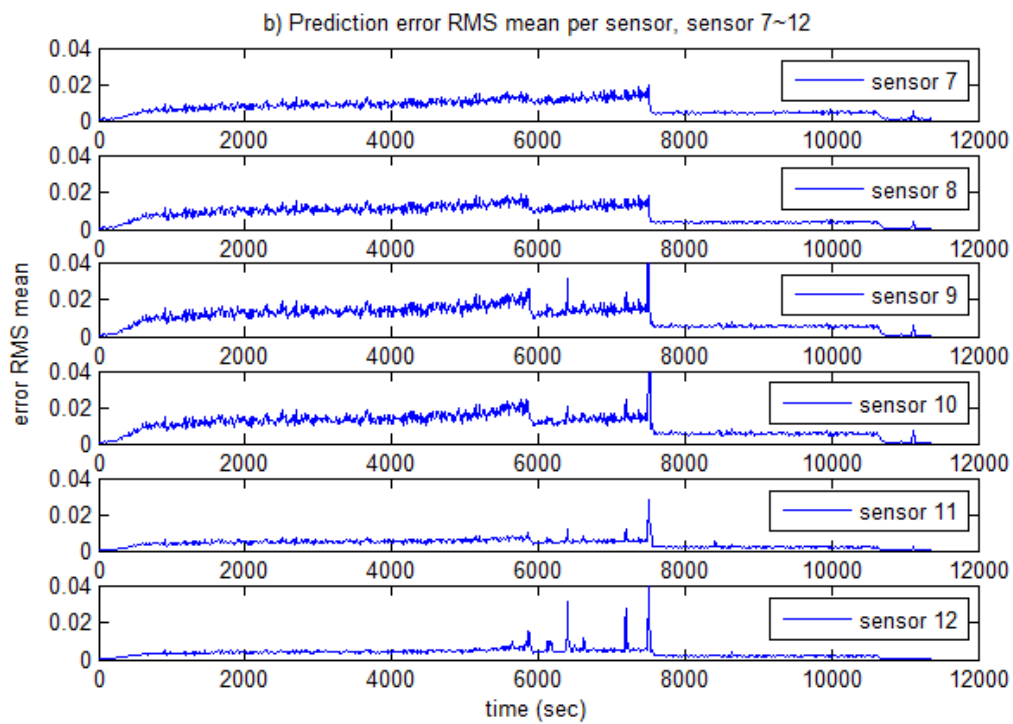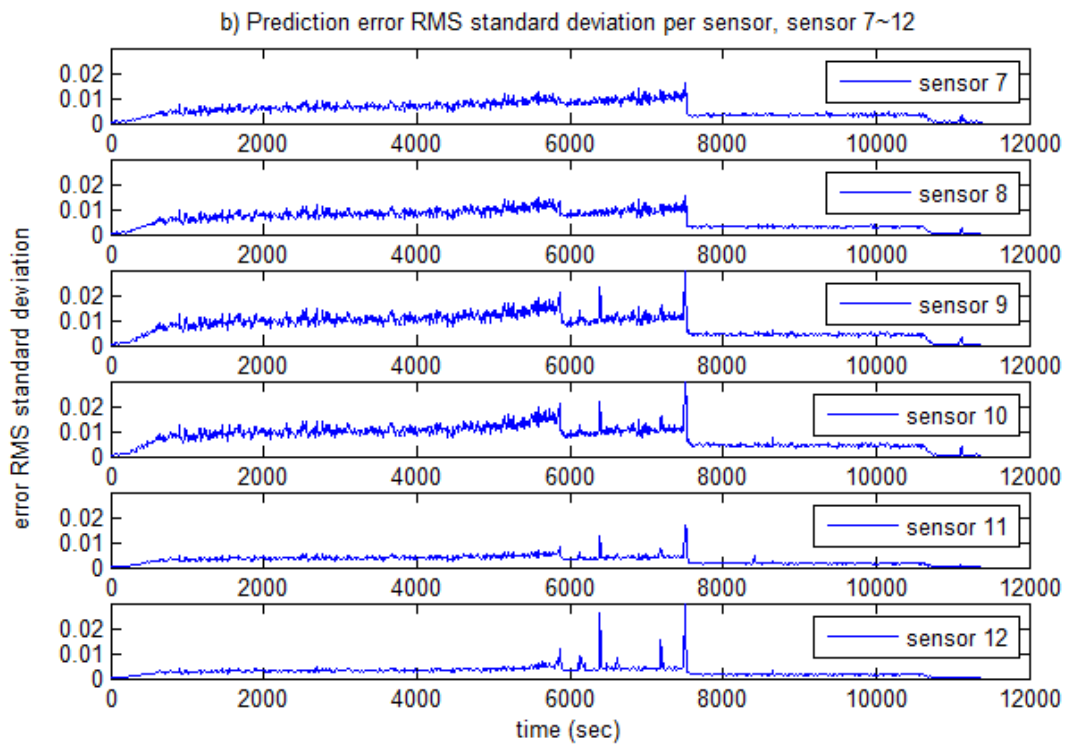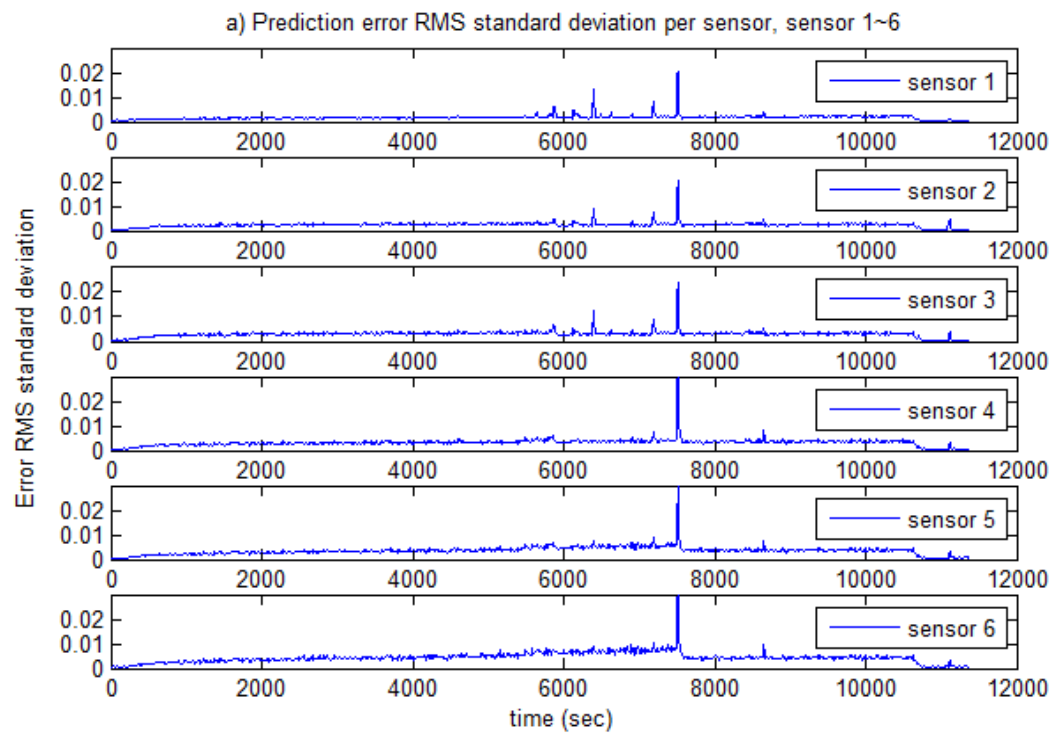
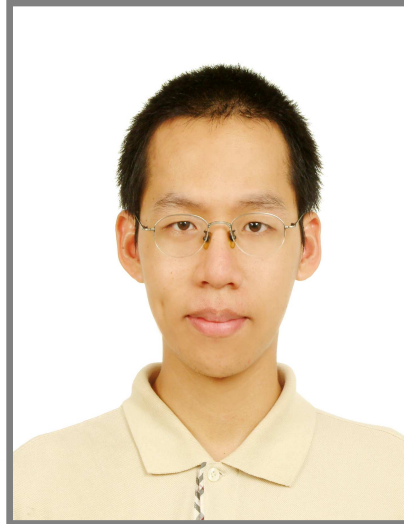**Figure 7-53** Error RMS mean per sensor.

Figure 7-54 Error RMS standard deviation per sensor.

簡　　歷

姓名: 劉奕成 (Yi-Cheng Liu)

籍貫: 台灣 台中市

生日: 民國73年1月8日

E-mail：r98521256@ntu.edu.tw

學歷 ：　國立台灣大學土木工程所結構工程組（2009.09 ～ 2011.06）

Universidad de Costa Rica, Licenciatura en Ingeniería Civil
（2001.02 ～ 2007.10）

Liceo Samuel Sáenz Flores, Costa Rica（1996.02 ～ 2000.12）

南投縣埔里鎮育英國民小學（1989.09 ～ 1995.07）